Site U1328[1]

Expedition 311 Scientists[2]

Chapter contents

[1] Expedition 311 Scientists, 2006. Site U1328. *In* Riedel, M., Collett, T.S., Malone, M.J., and the Expedition 311 Scientists. *Proc. IODP,* 311: Washington, DC (Integrated Ocean Drilling Program Management International, Inc.). doi:10.2204/iodp.proc.311.106.2006
[2] Expedition 311 Scientists' addresses.

Background and objectives

A number of cold vents characterized by near-vertical seismic blank (or wipeout) zones have been identified near Ocean Drilling Program (ODP) Sites 889/890 (Wood et al., 2000; Riedel, 2001; Riedel et al., 2002). The 2 km × 4 km cold vent field consists of at least four vents associated with near-surface faults. In addition to the main vent field, other vents have been identified by the presence of seismic blank zones ~4 km northwest of Site 889 and on the southeastern slope of an accreted ridge 8 km south-southwest of Site 889 (Riedel, 2001). The most prominent vent in this vent field, called Bullseye vent, has been the subject of intensive geophysical and geochemical studies since 1999, including

- Two-dimensional and three-dimensional (3-D) single-channel seismic and multichannel seismic (MCS) imaging (Riedel 2001; Riedel et al., 2002),
- High-resolution 3.5 kHz imaging (Riedel et al., 2002; Zühlsdorff and Spiess, 2004),
- Heat-probe measurements (Riedel et al., 2006),
- Piston coring with physical property measurements and geochemical pore water analyses (Novosel, 2002; Novosel et al., 2005; Solem et al., 2002),
- Seafloor video observations with the Remotely Operated Platform for Ocean Sciences of the Canadian Scientific Submersible Facility (ROPOS) (Riedel et al., 2002, 2006),
- Seafloor-towed controlled-source electromagnetic (CSEM) surveys (Schwalenberg et al., 2005), and
- Seafloor compliance studies (Willoughby et al., 2005).

Observations from seismic data

Blank zones associated with vents were first identified on Deep-Towed Acoustic Geophysics System (DTAGS) data in 1997 using intermediate frequencies from 250 to 650 Hz. Details of this study are described in Chapman et al. (2002) and Wood et al. (2002). The cold vent field associated with Integrated Ocean Drilling Program (IODP) Site U1328 (proposed Site CAS-06A; Collett et al., 2005) is characterized by numerous blank zones (Fig. **F1**). These subvertical zones of reduced seismic reflection amplitude have since been studied using different seismic recording systems and source frequencies, where the degree of blanking increases with higher seismic frequencies (Riedel et al., 2002). Several blank

doi:10.2204/iodp.proc.311.106.2006

zones have been recognized around Site U1328. The blank zones range from 80 m to several hundreds of meters in width, and blanking seems to be restricted to the upper slope sediment section above the bottom-simulating reflector (BSR). However, the majority of the deeper accreted sediments lack coherent reflectivity and blanking cannot be distinguished from the generally chaotic low reflectivity of the sediments at these depths.

The distinct surface expression of Bullseye vent (blank Zone 1) is evident, whereas blank Zones 2–4 have no equivalent surface expression (Fig. **F1**). A prominent high-amplitude layer at ~10 meters below seafloor (mbsf) is an apparent upward barrier for blank Zones 2 and 4 as identified in the 3.5 kHz data (Fig. **F1A**). A slight surface expression can be seen at blank Zone 2 but does not exceed 1 m. Blank Zone 3 extends to the seafloor but has little seafloor topographic expression. Bullseye vent has a near-vertical boundary to the southwest, but the zone widens with depth and its boundary is more diffuse to the northeast (Fig. **F2**).

The vents appear to be underlain by a continuous BSR (Figs. **F1, F2**), but the BSR is generally weak except for a bright spot associated with Bullseye vent (Fig. **F3A**). Reflection amplitudes beneath the BSR bright spot are enhanced, suggesting the existence of free gas. The location of the BSR bright spot also coincides with a deep trough of slope basin sediments between buried ridges of accreted material (Fig. **F3B**). The boundary between slope and accreted sediments is the strongest lithologic boundary observed in this area and could potentially be a barrier in upward fluid migration and in this case acts as a trap for free gas, creating the observed BSR bright spot.

All of the blank zones are observed to have an east–west trend, as identified from 3-D seismic time-slice analyses (Fig. **F4**), which is interpreted to be the result of the major margin-perpendicular compressional stress regime (Riedel et al., 2002). However, the area of blanking at blank Zone 1 is also elongated but trends more in an northeast–southwest direction. At Bullseye vent, 3-D time slices of instantaneous amplitude show an apparent ring structure that is interpreted to be the result of seismic diffractions at the shallow gas hydrate cap (Fig. **F5**). In 3-D, the gas hydrate is seen to form a cap, which dips away from the center of the vent (Fig. **F6**). Below the gas hydrate cap the amplitude of the seismic data is reduced.

Results from piston coring and heat-probe measurements

A total of 24 piston cores were collected over the area of the vent field in the year 2000, focusing on Bullseye vent and blank Zone 4 but also including reference locations outside the vent field (Novosel, 2002). The cored sediment mostly consists of finely laminated glaciomarine clays and silts with occasional layers of sands and silts. Occurrence of pyrite in the form of disseminated grains, framboidal fillings of small cavities, and complete replacement of foraminifers was limited to the cores located within the vents. Physical property analyses (*P*-wave velocity, density, magnetic susceptibility, and thermal conductivity) showed signs of sediment alteration from methane advection by the presence of increased reflection coefficients as well as higher thermal conductivities for cores inside the vent. Magnetic susceptibility was also significantly reduced by several orders of magnitude for cores taken inside the vent field relative to cores from outside the blank zone (Novosel et al., 2005). Similar observations were made on gas hydrate–bearing cores from the Mallik well site in the Mackenzie Delta, Northwest Territories, Canada (Lowe et al., 2005).

Coring investigations were complemented by heat flow measurements over the vent area to examine the thermal effect of fluid expulsion. Heat flow and thermal conductivity were measured at 11 core sites around Bullseye vent and at six sites at blank Zone 4 (Riedel et al., 2006). Heat flow is uniform over the vents with values of ~60 mW/m^2.

During piston coring operations, massive gas hydrate was recovered in the center of Bullseye vent from 1 to 8 mbsf. Often, gas hydrate stopped core penetration and was found in the core catcher. All recovered gas hydrate samples contained mostly CH_4, some H_2S and CO_2, and <0.5% of higher hydrocarbons (Solem et al., 2002; Riedel et al., 2006). The CH_4 isotopic $\delta^{13}C$ values were measured in two gas hydrate samples and two sections of free gas within the cores. Gas hydrate samples ranged from –65‰ to –70‰, and the void gas sampled had a slightly lighter isotopic composition, from –71‰ to –77‰. Studies using powder X-ray diffraction (XRD), nuclear magnetic resonance (NMR), and Raman spectroscopy showed that all samples recovered were Structure I gas hydrate, and hydration numbers were ~6 ± 0.2 (Lu et al., 2005).

Seafloor imaging and sampling with ROPOS

Two dives with the remotely operated vehicle ROPOS were conducted in 2000 and 2001 at Bullseye vent. The second dive was extended to cover the cold vent field along seismic Inline 27 from the 3-D MCS survey, which also was imaged with DTAGS in 1997. Large outcrops of carbonates were found at several locations (Fig. **F7A, F7B, F7C, F7D**). Typi-

cally, the 10–15 cm thick carbonate sheets cover an area of >10 m² of the seafloor and were located around relatively steep ridges ~3 m high. The carbonates often outcrop along multiple lineaments. The surface of the rocks is smooth and does not show any indication of alteration. The isotopic composition indicates that the carbonate is formed mainly by oxidation of biogenic methane (carbon isotopic values are about –45‰). Only a single, isolated living clam community (*vesicomyids*) associated with worms and bacteria mats was observed in the area around Bullseye vent in 2001 (Fig. **F7G, F7H**). The presence of these fauna indicates active methane venting and related sulfide emissions. The clams formed small colonies (1–2 m diameter) aligned around small carbonate ridges. Several water samples were taken with ROPOS in a vertical profile immediately above the clam colony (Solem et al., 2002; Riedel et al., 2006). Peak methane concentrations of ~20 nM were found at the seafloor and 100–200 m above the clam colony. Additional carbonate outcrops were observed at blank Zone 3, with carbonate formation being mainly flat, thin sheets embedded in the sediments (Fig. **F7E, F7F**).

Insights from seafloor compliance studies and CSEM surveys

Seafloor compliance studies

Gas hydrate that forms in sediments may have a cementing effect on grains and could significantly impact the shear properties of the sediment column. Seafloor compliance is the transfer function between pressure variations (from ocean surface, long-period gravity, or infragravity waves) and the associated displacement of the seafloor. The data are most sensitive to the shear modulus as a function of depth. Shear modulus is converted to shear wave velocity by assuming a density function that increases linearly with depth. Willoughby and Edwards (2000) published results of compliance studies near Site 889 and the implications for the shear wave velocity structure in the region. Newly gathered data over two of the gas hydrate cold vent structures show significant shear modulus anomalies (Fig. **F8**). Unlike reflection seismic data, compliance data are not hindered by the possible presence of free gas or other sources of scattering of seismic energy. The anomalous compliance results over the two vent sites indicate a large increase in shear modulus in the gas hydrate stability zone (GHSZ), particularly near the base, suggesting an increase in gas hydrate concentration with depth (Willoughby et al., 2005). There is no observed increase in velocities at the top of the section just below the seafloor; however, the sensitivity of the data to the uppermost sediments is limited by the cut-off frequency of gravity waves.

Controlled-source electromagnetic studies

The seafloor-towed CSEM system was developed at the University of Toronto and successfully deployed several times on the northern Cascadia margin over the past several years (Edwards, 1997; Yuan and Edwards, 2000; Schwalenberg et al., 2005). The CSEM array consists of a weight attached at the leading end of the cable followed by a 124 m long transmitter dipole and two receiver pairs (each 15 m long) that are located at 174 and 292 m from the transmitter, respectively. Received signals relate to depths comparable to half the transmitter–receiver separation.

Data from deployments of the CSEM system around Site 889 showed an average resistivity of ~2 Ωm for the 100 m thick layer overlying the BSR, which is in very good agreement with the downhole electrical resistivity logs from ODP Leg 146 (Yuan and Edwards, 2000). More recent deployments of the array over the cold vents showed dramatic anomalies associated with the vents (Schwalenberg et al., 2005), as illustrated in Figure **F9A.** The resistivity values within the anomalous zones are higher for the larger receiver separation and rise locally to >5 Ωm over the regional background resistivity of 1.1–1.5 Ωm. Like compliance data, this suggests that gas hydrate content may increase with depth. The measured resistivity values were then converted to gas hydrate concentrations (Fig. **F9B**) using different assumed Archie parameters by Hyndman et al. (1999) and Collett (2000). For both sets of coefficients, comparable amounts of gas hydrate are required within the entire blank zone (from seafloor to the BSR) to explain the observed resistivity anomalies and reach 50% of the pore space. It should be noted that these are average concentrations for the entire blank zone from the BSR to the seafloor and therefore even higher concentration could be encountered locally in small pockets.

Models of blanking

Several different mechanisms have been proposed for the origin of the seismic blanking observed in the Bullseye vent area and for the associated implications concerning the nature of the fluid venting. Riedel et al. (2002, 2006) suggested that much of the blanking is caused by near-surface carbonate or a massive shallow gas hydrate layer. Additional blanking may be caused by scattered accumulations of gas hydrate in fractures and veins in the deeper subsurface. Zühlsdorff and Spiess (2004) proposed that the oblong shape of the blank zone and its associated

surface mound were created by natural hydraulic fracturing induced by a local elevation in the seafloor and BSR; the blanking is produced by free gas bubbles within the fractures, particularly in the period following a fluid expulsion event. Wood et al. (2002) argued that the entire blank zone is a gas chimney produced by rising warm fluids that significantly perturb the base of the GHSZ upward. Seafloor compliance and CSEM surveys gave additional constraints to the nature of the cold vents and the possible cause of blanking as observed in the seismic data. The increased shear modulus and electrical resistivity suggest higher gas hydrate concentration over the entire depth of the blank zone and support the model proposed by Riedel et al. (2006), contradicting those by Zühlsdorff and Spiess (2004) and Wood et al. (2002). Even with the new constraints from seafloor compliance and CSEM studies, no final conclusion can be made if free gas is actually present in conjunction with gas hydrate.

Objectives

Site U1328 is unique relative to the other sites along the Expedition 311 coring transect in that it represents a location of focused fluid flow. Massive forms of gas hydrate were expected within the top few meters below the seafloor and sporadically throughout the depth of the blank zone in fractures and veins. Drilling and coring at this location will test the different models for the cold vent structure and associated causes of seismic blanking. It was important to obtain a high-resolution temperature profile for this area to assess any evidence of active fluid flow. Pressure coring using the Pressure Core Sampler (PCS) system will help answer the question if free gas is occurring within the GHSZ in this vent and contributing to seismic blanking. Pressure coring using the HYACINTH Fugro Pressure Corer (FPC) and HYACE Rotary Corer (HRC) recovered high-quality gas hydrate–bearing core for shore-based analyses.

The operational plan to achieve these objectives was based on a general three-hole concept, which included:

- A logging-while-drilling/measurement-while-drilling (LWD/MWD) hole;
- A continuously cored hole to characterize geochemical and microbiological baselines and proxies for gas hydrate;
- An additional "tools" hole for specialized pressure coring systems including the IODP PCS and the HYACINTH FPC/HRC systems, combined with selected spot-coring using the conventional extended core barrel (XCB) system; and
- A wireline logging program in the tools hole using the triple combination (triple combo) and Formation MicroScanner (FMS)-sonic tool strings and a vertical seismic profile (VSP).

An additional hole was drilled for near-seafloor high-resolution geochemical and microbiological studies of the sulfate/methane interface (SMI).

Operations

Hole U1328A

After completing LWD/MWD operations at Site U1327, we transited in dynamic positioning (DP) mode ~1.9 nmi to Site U1328 (proposed Site CAS-06A; Collett et al., 2005). The drill string was tripped to the seafloor and the vibration-isolated television (VIT) camera was deployed for a survey of the seabed to ensure that no chemosynthetic communities would be disturbed by operations. Hole U1328A was spudded at 1555 h on 24 September 2005, with an estimated seafloor depth of 1268.1 meters below sea level (mbsl; 1279.0 meters below rig floor [mbrf]). The hole was initiated with a controlled spud-in with 100 gallons per minute (gpm) circulation and 10–15 rpm rotation. At 10 mbsf, top drive rotation was increased to 40 rpm and then again to 60 rpm at 29 mbsf to maintain a 50 m/h rate of penetration (ROP) with a minimum circulation of 270 gpm. This controlled ramp-up was conducted to maintain hole stability and avoid blowing out the top of the hole. During drilling of Hole U1328A, no corrective action was required based on the safety protocol (see **"Downhole logging"** in the "Methods" chapter). At 0415 h on 25 September, the hole reached the total depth (TD) of 300 mbsf. After displacing the hole with weighted sepiolite mud, the drill string was tripped back to the ship, with the bit clearing the rotary table at 1100 h, ending operations in Hole U1328A. During the pipe trip, the ship moved 9.9 nmi in DP mode to Site U1329.

Hole U1328B

After completing operations at Site U1327, the ship was relocated ~1.9 nmi to Site U1328 and the VIT camera was deployed to inspect the seafloor for the occurrence of chemosynthetic communities. We conducted a 120 m camera survey along the proposed coring transect across the vent site (Fig. **F10**). We did not observe any living clam colonies; however, widespread carbonate outcrops were observed. Before spudding the first hole, we deployed the water-sampling temperature probe (WSTP) to collect a bottom water sample. Hole U1328B was spudded with the advanced piston corer (APC) system at 1310

h on October 11 2005. Recovery of 4.8 m of sediment indicated a successful mudline core. The estimated mudline seafloor depth and the visual observation of the seafloor tag during the camera survey agree within 0.3 m. Table T1 reports the visual seafloor tag depth of 1267.8 mbsl.

Core recovery in the second APC core was only 1.7 m with an incomplete stroke. The next core was taken with the XCB system to the target depth of the first PCS deployment (Core 311-U1328B-4P) at 14.5 mbsf. The APC core taken after Core 311-U1328B-4P was again an incomplete stroke, with only 1.89 m of core recovered. We switched back to XCB coring and advanced the hole to the target depth for the second PCS deployment (Core 311-U1328B-7P) at 26.0 mbsf. Both PCS deployments yielded core under pressure. Three additional APC cores were taken to 56.5 mbsf. Operations were suspended at 0315 h on 12 October because of strong winds and severe ship heave conditions. By 0745 h, conditions had deteriorated to a level (heave >8 m) that necessitated pulling out of Hole U1238B. Six APC, three XCB, and two PCS cores were collected in Hole U1328B with an average recovery of 73% (Table T1).

Hole U1328C

After waiting on the weather for 16 h, sea conditions improved enough to allow drilling and coring operations to continue. We offset the ship by 15 m from the location of Hole U1328B, spudded Hole U1328C at 2030 h on 12 October 2005, and drilled to the maximum depth of Hole U1328B (56.5 mbsf) to resume APC coring.

Hole U1328C was advanced to 75.5 mbsf with three APC cores, after which we switched to the XCB coring system and deepened the hole to 92.0 mbsf. A pressurized PCS core (311-U1328C-5P) was recovered from this depth and the rest of the hole was cored with the XCB system to 300 mbsf. The total average recovery for Hole U1328C was 80.3%. Temperature measurements were made on Cores 311-U1328C-2H, 3H, and 6H with either the Advanced Piston Corer Temperature (APCT) tool or the third-generation advanced piston corer temperature (APCT-3) tool (Table T1). Temperature measurements with the Davis-Villinger Temperature-Pressure Probe were carried out at 148.9 and 197.1 mbsf, but the data from both runs were degraded by an apparent electronic problem in the tool.

After reaching a TD of 300 mbsf at 1000 h on 14 October, the hole was prepared for wireline logging with a short wiper trip. At 1650 h, the triple combo tool string was lowered to 294 mbsf. The uphole triple combo run was completed without incident and the tool was back on the rig floor at 1940 h. Next, the FMS-sonic tool string was deployed at 2140 h, reaching the same depth as the triple combo logging run. Two passes of the FMS-sonic tool string were completed without incident and the tool was back on deck at 0245 h on 15 October. After rigging up for the VSP, the marine mammal watch began at 0730 h, followed by the 30 min ramp up of the generator-injector (GI) air gun at 0830 h. The VSP began at 0900 h with the first clamping position at 286 mbsf. The VSP was run successfully to the shallowest clamping position of 106 mbsf. Shallower positions were too noisy as a result of interference with the drill pipe, which had been set back to 76 mbsf. After pulling the tool back to the rig floor and rigging down logging, the drill string was pulled clear of the seafloor at 1615 h, ending operations in Hole U1328C.

Hole U1328D

The ship was offset 35 m to Hole U1328D for a high-resolution combined microbiology and geochemistry study of the SMI. The first two deployments of the APC system resulted in bent core barrels, so we switched to the XCB coring system. Hole U1328D was spudded with an XCB core at 1955 h on 15 October 2005, followed by a second XCB core, and then the deployment of the FPC at 14.0 mbsf. The FPC did not recover any core. The drill string was pulled clear of the seafloor at 2345 h, ending operations in Hole U1328D.

Hole U1328E

After offsetting 50 m from Hole U1328D, Hole U1328E was spudded with the XCB system at 0040 h on 16 October 2005. The primary focus of Hole U1328E was to recover pressure cores, with XCB spot cores from the top 40 mbsf. LWD data and previous scientific coring suggest that this interval contains the highest gas hydrate concentrations at this site. XCB coring advanced the hole to 8.5 mbsf, where the HRC was deployed with Core 311-U1328E-3E but did not return under pressure. Following an XCB core, a PCS core was deployed at 15.1 mbsf with Core 311-U1328E-5P but did not return pressurized. Another XCB core was taken and then the FPC was deployed with Core 311-U1328E-7Y, but it also failed to return a core under pressure. Two XCB cores advanced the hole to 46.0 mbsf, followed by deployment of the center bit to drill the hole to 92.0 mbsf. PCS Core 311-U1328E-10P was deployed and returned under pressure. A Davis-Villinger Temperature Probe (DVTP) temperature measurement followed. The center bit was redeployed and the hole was drilled to 197.0 mbsf. The FPC pressure core system was deployed with Core 311-U1328E-11Y, but it

improperly retracted into the autoclave and failed to yield a pressurized core. An additional DVTP survey was conducted at 198.0 mbsf after the last FPC core run. The hole was then drilled to 215.3 mbsf, where the HRC was deployed (Core 311-U1328E-12E) but recovered without pressure. The hole was then drilled to 233.0 mbsf for a PCS run (Core 311-U1328E-13P), which returned with a pressurized core (Table T1). With ship heave conditions increasing to 7 m, the planned DVTP deployment at the bottom of the hole was cancelled, ending operations in the hole at 235.0 mbsf. After the hole was displaced with weighted mud, the drill string was tripped to the surface and cleared from the seafloor, ending operations at Site U1328 at 0715 h on 17 October.

Lithostratigraphy

Site U1328 is located ~3.7 km southeast of Site U1327 on the mid-continental slope off Vancouver Island (~1267.9 mbsl) and has been identified as an active cold vent. Four of the five holes (Holes U1328B–U1328E) at this site were cored. Hole U1328B was cored to 56.5 mbsf (54.5 m recovered), Hole U1328C to 300 mbsf (242.5 m recovered), Hole U1328D to 15 mbsf (15 m recovered), and Hole U1328E to 235 mbsf (49 m recovered). Recovery was generally good, but lower in Holes U1328D and U1328E (Hole U1328B = 71.3%, Hole U1328C = 80.3%, Hole U1328D = 66.9%, and Hole U1328E = 25.3%).

We divided the 300 m thick sedimentary section recovered at Site U1328 into three lithostratigraphic units (Fig. F11) based on visual inspection of the recovered cores and analysis of smear slides. Other parameters, such as mineralogy data from XRD analyses, helped to better define the entire stratigraphic section. The results were also compared and correlated with seismic data, downhole LWD/MWD data, and physical property measurements.

Lithostratigraphic units

Lithostratigraphic Unit I

Intervals: Sections 311-U1328B-1H-1 through 10H-CC and 311-U1328C-1H-1 through 10X-2; Cores 311-U1328D-1H through 3P and 311-U1328E-1X through 10P

Depths: Hole U1328B: 0.00–56.98 mbsf, Hole U1328C: 56.50–132.60 mbsf, Hole U1328D: 0.00–15.00 mbsf, and Hole U1328E: 0.00–92.26 mbsf

Age: Pleistocene (<1.0 Ma)

Unit I is mainly composed of dark gray (N4) and dark greenish gray (5GY 4/1) clay and silty clay (Fig. F12). Fossils are very rarely observed in the major lithology; however, exceptions include diatoms in Core 311-U1328C-2H and 23% calcareous fossils (15% foraminifers and 7% nannofossils) in Section 311-U1328B-10H-1. The clay and silty clay is often interbedded with clayey silt, silt, sand-silt-clay, silty sand, and sand layers that have mostly sharp and sometimes erosional contacts (Figs. F12, F13). The single layers show varying thickness from a few millimeters to several centimeters. Sand layers are extremely abundant from Section 311-U1328B-8H-3 to the base of Unit I, often showing fining-upward sequences (Fig. F12). The major nonbiogenic components of Unit I are quartz, feldspar, clay minerals, opaque minerals, and accessory minerals (mainly amphibole). In Section 311-U1328E-8X-3 (29.54 mbsf), a 4 cm thick, glauconite-rich greenish layer is observed. A 2 cm thick layer of almost pure volcanic ash is observed in Section 311-U1328B-9H-5 (Figs. F14, F15).

Mostly rare sulfide mottling, appearing as dark gray (N4) stains, occurs in Unit I in Holes U1328B–U1328D. In Hole U1328E, however, we observe moderate to abundant sulfide mottles in Sections 311-U1328E-8X-2 and 9X-3 through 9X-5 (Fig. F16). Some sulfide concretions were observed at the bottom of Unit I in Cores 311-U1328C-1H, 3H, 6H, 7X, and 9X. Cores 311-U1328B-1H and 311-U1328E-8X are moderately to extremely bioturbated.

The biogenic components in the major lithology (clay and silty clay) have very low concentrations, if at all present, based on smear slide analyses (Fig. F11). From visible observations, some large foraminifers were observed in Cores 311-U1328B-9H, 10H, and 311-U1328C-7X. Some bivalve shell fragments are present in Cores 311-U1328B-10H, 311-U1328C-6H, 7X, and 311-U1328E-9X. A wood fragment was observed in Section 311-U1328C-3H-1.

Lithified and/or partly lithified carbonates are present in Sections 311-U1328B-1H-1, 1H-3, and 9H-CC, and unlithified carbonate cement is present in Section 311-U1328B-1H-2. A notable observation is that we often found lithified and/or partly lithified carbonates associated with soupy and mousselike sediment textures in Cores 311-U1328B-6X, 311-U1328D-1X, 2X, 311-U1328E-2X, 8X, and 9X (Fig. F17). Some of the carbonates seem to be cemented sediments, but we also observed some whitish crusts or coatings composed of pure carbonate, possibly calcite or aragonite. Sample 311-U1328-6X-1, 21–22 cm, revealed a mixed mineralogy of high-Mg calcite (17 mol% $MgCO_3$) and aragonite. These precipitates indicate carbonate formation directly related to the presence of gas hydrate (Bohrmann et al., 1998; Teichert et al., 2005).

Angular and rounded rock pebbles, 1–6 cm in size, are present in Cores 311-U1328B-1H, 10H, and 311-U1328C-4X. The pebble from Core 311-U1328B-10H is a well-rounded olivine basalt, which we interpret as a dropstone.

Soft-sediment deformation is present in Sections 311-U1328C-8X-1, 8X-4, and 9X-1 (Fig. F18), with only slightly tilted silt or sand layers, and in Sections 311-U1328C-2H-1, 2H-2, and 9X-2, with intermingled sand/silt and clay/silty clay layers.

The Unit I/II boundary is marked by a sharp decrease of sand and silt layers and by the onset of diatom-bearing intervals in Section 311-U1328C-10X-3 (20% diatoms estimated in Sample 311-U1328C-10X-3, 62 cm).

Lithostratigraphic Unit II

Intervals: Sections 311-U1328C-10X-3 through 16X-CC and 311-U1328E-11Y-1
Depths: Hole U1328C: 132.60–197.10 mbsf and Hole U1328E: 197.00–198.00 mbsf
Age: Pleistocene (>0.3 and <1.0 Ma)

Unit II is composed of dark greenish gray (5GY 4/1) and dark gray (N4) clay, clay with nannofossils, silty clay, silty clay with diatoms, diatom silty clay, and diatom ooze locally interbedded with sand and sandy silt layers or lenses. Some silty or sandy layers show fining-upward sequences. The amount of silty and sandy layers or lenses rapidly decreases in this unit compared to Unit I. The diatom-rich sections often display a dark greenish gray (5GY 4/1) color, whereas the sections barren in diatoms are dark gray (N4). The major nonbiogenic components of Unit II are quartz, feldspar, accessory minerals (mainly amphibole), clay minerals, opaque minerals, biotite, glauconite, and volcanic glass. Rare to abundant sulfide mottling is observed throughout Unit II. Rare sulfide concretions occur in Cores 311-U1328C-14X and 15X. Visible glauconitic green patches are found in Sections 311-U1328C-14X-1 and 16X-5. Rare to moderate bioturbation is observed in Sections 311-U1328C-14X-5 and 16X-3.

The presence of biogenic components characterizes Unit II, based on smear slide observations. The major lithology shows a high content of diatoms, on average 10% and as high as 45% in Sample 311-U1328C-14X-2, 81 cm (Fig. F19). The biogenic carbonate fraction is low, on average 4%. Locally high concentrations of foraminifers (25%) and nannofossils (18%) are found in Samples 311-U1328C-16X-3, 139 cm; and 16X-5, 90 cm, respectively. From visible observations, foraminifers are present in Cores 311-1328C-10X and 12X through 16X. Rare bivalve shell fragments are present in Cores 311-U1328C-14X and 16X. A wood piece is observed in Section 311-U1328C-14X-1. Siliceous spicules are present in Sections 311-U1328C-16X-1 and 16X-2. No unlithified carbonate cements or lithified carbonates occur in Unit II.

Mousselike textures related to the presence of gas hydrate are present in intervals 311-U1328C-11X-4, 37–46 cm; 13X-1, 34–39 cm; 13X-2, 6–7 and 26–27 cm; and 14X-3, 28–40 and 70–80 cm, although infrared (IR) camera temperature anomalies are not clear in those cores (see **"Physical properties"**).

Lithostratigraphic Unit III

Intervals: Sections 311-U1328C-17X-1 through 27X-CC
Depths: Hole U1328C: 197.10–300.00 mbsf
Age: Pleistocene (>0.3 to <1.6 Ma)

Unit III is mainly composed of dark greenish gray (5GY 4/1), dark gray (N4), and dark olive-gray (5Y 3/2) clay, silty clay, silty clay with diatoms, and diatom silty clay. In the upper part of Unit III, Sections 311-U1328C-17X-1 through 20X-CC (197.10–235.60 mbsf), dark greenish gray (5GY 4/1) silty clay and clay dominate. The middle part of the unit, Sections 311-U1328C-21X-1 through 25X-CC (235.60–283.70 mbsf), consists mainly of dark gray (N4) silty clay and clay, associated with dark greenish gray (5GY 4/1) clay in Sections 311-U1328C-23X-1 and 23X-2 and dark olive-gray (5Y 3/2) silty clay in Sections 311-U1328C-25X-1, 25X-2, 25X-6, and 25X-CC. Dark greenish gray (5GY 4/1) silty clay, silty clay with diatoms, and diatom silty clay are the main lithologies in the lower part of Unit III, Sections 311-U1328C-26X-1 through 27X-CC (283.70–300.00 mbsf). Coarser grained clayey silt, sandy silt, quartz sandy silt, and sand occur as minor lithologies in Cores 311-U1328C-18X through 22X, 26X, and 27X.

The Unit II/III boundary is distinguished by the sudden absence of diatoms in smear slides (see also **"Biostratigraphy"**), as well as the increase of induration of the sediments, characterized by the occurrence of drilling biscuits in Cores 311-U1328C-20X through 27X. Diatoms occur again (<30%) at the bottom of Unit III in Core 311-U1328C-27X. The major nonbiogenic components of Unit III are quartz, feldspar, accessory minerals, clay minerals, and opaque minerals. Sulfide concretions or sulfide mottling structures are present in Sections 311-U1328C-17X-2, 17X-5, 18X-1, 20X-2, 22X-6, 22X-7, 25X-2, and 27X-2. Glauconite-rich layers are observed in Sections 311-U1328C-17X-1, 17X-2, 17X-4, 17X-6, 18X-1, 19X-2, 20X-2, 20X-3, 25X-1, 27X-4, and 27X-7. A dark gray (N4) angular rock fragment (0.6 cm × 1.2 cm) is present in Section 311-U1328C-27X-1 and is probably a dropstone.

Visually observed foraminifers are very abundant in Cores 311-U1328C-17X through 20X, 21X, and 25X. Some bivalve shell fragments are present in Cores 311-U1328C-17X, 25X, 26X, and 27X. Bioturbation is not observed in Unit III.

Lithified carbonates and unlithified carbonate cements occur in Cores 311-U1328C-19X, 22X, and 25X. XRD analyses show a combination of high-Mg calcite (14–15 mol% $MgCO_3$), nonstoichiometric (probably Ca rich) dolomite (31–33 mol% $MgCO_3$) in Section 311-1328C-19X-4 (Figs. **F20, F21**), and almost stoichiometric dolomite (47 mol% $MgCO_3$) in Section 311-1328C-25X-2.

Sedimentary evidence of gas hydrate

At Site U1328, gas hydrate was sampled and evidence of gas hydrate was found in the recovered cores, in IR temperature anomalies in the unsplit cores on the catwalk (see **"Physical properties"**), and in the composition of the interstitial water (see **"Interstitial water geochemistry"**). It must be noted, however, that many intervals with gas hydrate were sampled and saved as whole rounds for postcruise analysis and could not, therefore, be observed in split core.

The presence of gas hydrate at Site U1328 is indicated in the split-core sediments by soupy and mousselike textures (Fig. **F22**). The term "soupy" refers to a sediment structure caused by dissociation of larger nodules or veins of gas hydrate. During dissociation, water is released, which liquifies the sediment (Figs. **F17, F23**). At Site U1328, soupy texture is only present within lithostratigraphic Unit I (<100 mbsf) in Sections 311-U1328B-2H-2, 6X-1, 6X-2, 311-U1328C-2H-1, 4X-3, 311-U1328D-1X-1 through 1X-6, 311-1328E-2X-1, 8X-1, and 9X-1. All interstitial water (IW) samples recovered from Hole U1328D indicate contamination with drilling fluid and seawater (see **"Interstitial water geochemistry"**). Analyses of soupy material by inorganic geochemists revealed seawater-like salinities, suggesting that a contribution of drilling fluid (seawater) may be causing some of the soupy appearance of the sediments. Nevertheless, IR temperature data clearly document the presence of gas hydrate in these sections (see **"Physical properties"**).

The term "mousselike" refers to a sediment structure caused by dissociation of disseminated gas hydrate. The dissociation of small grains of gas hydrate gives the sediment a mousselike texture with many small, roundish voids (Figs. **F23, F24**).

At Site U1328, mousselike textures are present occasionally within lithostratigraphic Units I–III (Fig. **F22**) in Sections 311-U1328B-1H-4, 2H-2, 6X-1, 6X-2, 311-U1328C-2H-1 through 2H-3, 4X-3, 7X-1, 10X-1, 11X-4, 13X-1, 13X-2, 14X-3, 18X-1, 20X-2, 311-U1328D-1X-6, 2X-1, 2X-2, 311-U1328E-2X-1, 8X-1, 9X-1, and 9X-2.

Authigenic carbonates are abundant within the soupy and mousselike intervals in Sections 311-U1328B-6X-1, 311-U1328D-1X-2 through 1X-6, 311-U1328E-2X-1, 8X-1, and 9X-1 (Fig. **F17**). These authigenic carbonates display varying shapes and colors: roundish shapes with light to dark gray color; thin gray chips; thin, even layers (sometimes showing layering); thin crusts with a rough, irregular surface and gray color; and thin crusts with a very irregular surface and a white coating. Further postcruise analyses will constrain the origin of the different shapes and might confirm formation related to the presence of gas hydrate.

Environment of deposition

Site U1328 recovered a sequence that corresponds to slope and slope basin sediments (see **"Background and objectives"**).

Lithostratigraphic Unit III is characterized by fine-grained (clay to silty clay) detrital sediments with very few silty interlayers from turbiditic deposits. We suggest that the sediments were deposited in an abyssal plain environment, as the agents of transport and deposition are distal, low-energy turbidity currents. The presence of authigenic unlithified carbonate cements shows that diagenetic processes are active in lithostratigraphic Unit III.

Lithostratigraphic Unit II is characterized by fine-grained (clay to silty clay) detrital sediments with some silty interlayers from turbiditic deposits and siliceous fossils (mainly diatoms; see also **"Biostratigraphy"**). The great abundance of marine diatoms along with resting spores of *Chaetoceros* within lithostratigraphic Unit II suggest blooming in a shallow-water shelf environment and coastal upwelling (see **"Biostratigraphy"**) followed by reworking by turbidity currents.

Lithostratigraphic Unit I is characterized by fine-grained detrital sediments (clay and silty clay), with abundant coarse-grained layers as thick as 6 cm, indicating turbiditic deposits. The large input of turbiditic deposits, as compared to lithostratigraphic Unit II, is reflected in an increase in sedimentation rate (from 24.6 to 37.5 cm/k.y.).

Biostratigraphy

Holes U1328B and U1328C contain a ~300 m thick Quaternary sedimentary sequence. The biostratigraphy determined for Site U1328 was based on an ex-

amination of all core catcher samples from Holes U1328B and U1328C (Table T2).

Diatoms

Diatoms are mostly very rare and poorly preserved in the upper stratigraphic section from the shallowest sample to ~128 mbsf and mostly rare to abundant but poorly to moderately preserved in the deeper section cored from ~134 to ~301 mbsf. Diatom assemblages are dominated either by marine species *Neodenticula seminae, Stephanopyxis* spp., *Thalassionema nitzschioides,* and *Thalassiosira* spp. or nonmarine diatoms *Aulacoseira granulata* s.l. and *Cyclotella* spp. The abundance of the dominant species varies significantly among samples. Abundant resting spores are frequently associated with marine diatom-dominant assemblages but are limited to the deeper section.

Marine- and nonmarine-dominant assemblages alternate throughout the cored section, suggesting terrigenous input by turbidites. Several distinct patterns in upward-increasing nonmarine diatoms are recognized at this site, especially in the lower part. These patterns might reflect sedimentary cycles, but detailed postcruise diatom analyses of more closely spaced samples are needed to ascertain if this hypothesis is true or an artifact caused by the coarsely spaced shipboard sampling.

The interval between the shallowest sample and Sample 311-U1328C-6H-CC (4.75–103.20 mbsf) contains *Neodenticula seminae* but lacks *Proboscia curvirostris* and was assigned to North Pacific Diatom (NPD) Zone 12 (*N. seminae* Zone; 0–0.3 Ma). The last occurrence (LO) of *P. curvirostris* was recognized in Sample 311-U1328C-7X-CC (110.07 mbsf), marking the NPD Zone 12/11 boundary (*P. curvirostris* Zone). The occurrence of *Actinocyclus oculatus* in this hole is very sporadic, and it is recognized only in Samples 311-U1328C-14X-CC (174.74 mbsf) and 25X-CC (281.99 mbsf). Its shallower occurrence is tentatively interpreted as reworked because it is separated from its deeper occurrence by as many as 10 samples that lack *A. oculatus*. The deeper occurrence was designated as the LO of *A. oculatus* in this hole, although detailed postcruise diatom analyses of more closely spaced samples are needed to confirm this interpretation. Based on the shipboard interpretation, the following zonation is made. The interval between the LO of *P. curvirostris* and 311-U1328C-24X-CC (110.07–272.18 mbsf) contains *P. curvirostris* but lacks *A. oculatus,* except for the reworked occurrence, and is assigned to NPD Zone 11 (*P. curvirostris* Zone; 0.3–1.0 Ma). The interval between the LO of *A. oculatus* and Sample 311-U1328C-27X-CC (281.99–301.97 mbsf) contains *P. curvirostris* and *A. oculatus* but lacks *Neodenticula koizumii* and is assigned to NPD Zone 10 (*A. oculatus* Zone; 1.0–2.0 Ma). Sample 311-U1328C-27X-CC (301.97 mbsf), the lowest in this hole, contains *P. curvirostris*. Therefore, the base of NPD Zone 10 in this hole, which is not the base of the entire NPD Zone 10, is younger than 1.6 Ma, the first occurrence of *P. curvirostris* (see Table T2).

Interstitial water geochemistry

The main objectives of the IW analyses at this site, located within an active vent, were to document the depth distribution of gas hydrate and their relationship to fluid chemistry, lithology, vent faults, and related fractures and to determine the fluid advection rate. Surprisingly, however, at this site diffusion controls the chemical profiles below ~30 mbsf, except perhaps in the deepest 50 m (250–300 mbsf) where chemistry seems to be controlled by advection, as suggested by the Cl and salinity data. The IW chemistry in the uppermost ~30 m is controlled by in situ gas hydrate formation from a methane-rich fluid transported through a network of faults and fractures.

A total of 90 IW samples were processed from four holes cored at Site U1328. From Hole U1328B, we processed 16 whole-round samples, 10–30 cm in length, which were collected with a sampling frequency of five per core in the first core and one to two samples per core in the remaining APC and XCB cores, depending on the length and condition of the retrieved core. In addition, six samples were collected from two pressure cores at ~15 and 26 mbsf (Cores 311-U1328B-4P and 7P). Hole U1328B was terminated at 56 mbsf because of strong winds and severe ship heave. Coring continued in Hole U1328C, which was offset from Hole U1328B by 15 m, from 58 mbsf to a TD of 300 mbsf.

From Hole U1328C we collected 48 whole-round IW samples, two of which were discarded because they were very disturbed and unsuitable for IW extraction. Three of the IW samples were divided into special sections based on IR images, generating three additional samples. Also, three samples were collected from pressure Core 311-U1328C-5P deployed at 92 mbsf. A total of 53 samples were processed from Hole U1328C.

Two XCB cores were retrieved from Hole U1328D, from which we collected and processed six samples, all of which were highly disturbed by drill water and gas hydrate dissociation during recovery. The three shallowest IW samples consisted of mostly drill water (Table T3).

Hole U1327E was drilled to deploy special tools and pressure coring systems. From this hole, we pro-

cessed five samples, one of which was divided to differentiate between "dry" sediment and "wet" material, which presumably has the larger signature from gas hydrate dissociation. Sample resolution was one or two samples per core, depending on the condition of the recovered sediment. Three pressure core deployments were conducted in this hole (see **"Pressure coring"**), and we collected three samples from pressure Core 311-U1328E-13P.

Because of the lithified nature of the formation and the presence of gas hydrate in the shallow sediments at this site, XCB coring was used for the collection of a large portion of IW samples. XCB coring yields relatively more disturbed cores, therefore these cores are more likely to be contaminated by drilling fluid than APC cores. Two whole-round samples showed extreme disturbance and were deemed unsuitable for IW extraction. They are marked by an asterisk in Tables **T3** and **T4.** Sulfate concentration below the depth of the SMI was used to identify and quantify occasional contamination by drilling fluid. In addition, samples collected from the first three sections of Core 311-U1328D-1X were highly disturbed but, because these whole-round samples contained gas hydrate, the samples were processed for analyses. As expected, these samples show very high contamination values, with sulfate values ranging from 22 to 26 mM (Table **T3**). These data are excluded from Figures **F25, F26,** and **F27.**

The IW data collected at Site U1328 are listed in Table **T3.** In addition, in Table **T4** we list sulfate-corrected data, which represent the composition of the IW corrected for drill-fluid contamination assuming zero sulfate concentration below the SMI. The sulfate-corrected data from Holes U1328B and U1328C and selected analyses from Hole U1328E are illustrated in Figures **F25, F26,** and **F27.**

In addition to IW whole-round samples and in coordination with gas analyses conducted by the organic geochemists (see **"Organic geochemistry"**), a total of nine gas hydrate samples (five from Hole U1328B, two from Hole U1328D, and two from Hole U1328E) were collected on the catwalk and allowed to dissociate for analyses of the lattice water. Because of the very low volumes of recovered water from the gas hydrate samples, shipboard analyses were confined to sulfate and Cl concentrations. Results of the gas hydrate–water analyses are listed in Table **T5.**

Salinity and chlorinity

The salinity and chlorinity profiles at this site show four distinct zones. In the uppermost ~60 m, the fluids collected from APC and PCS cores show a striking increase in both of these parameters, with maxima in the interval between 5 and 20 mbsf that reach salinity and chlorinity values of 48.9 and 855.2 mM, respectively. Values slightly above seawater were observed from 1.4 to 5 mbsf and from 20 to 60 mbsf (Fig. **F25**). Shallow gas hydrate is concentrated within the zone of salty, high-chlorinity fluids, which likely reflects recent and rapid formation of gas hydrate at shallow depth. The observed excess solutes result from salt exclusion from the water lattice structure during in situ gas hydrate formation and have not been removed by advective or diffusive processes.

A second zone, which extends from ~60 to ~150 mbsf, is characterized by relatively constant salinity values decreasing from 35 to 32 and a steady decrease in chlorinity from 570 to 538 mM. No gas hydrate was recovered from this zone, and no indication of gas hydrate dissociation was apparent in the IR images (see **"Physical properties"**).

A third zone, extending from ~150 to 250 mbsf across the BSR, shows discrete excursions to fresher salinity (~21 mM) and chlorinity values (~348 mM), suggesting that gas hydrate was present in the cores and dissociated prior to processing the samples. The salinity and chlorinity anomalies are consistent with observations of distinct negative thermal excursions in the IR scans (see **"Physical properties"**). Indeed, some of the lower salinity and chlorinity points shown in Figure **F25** represent samples collected to specifically target the more pronounced IR temperature anomalies. These samples were processed with the goal of establishing the relationship between lithology and hydrate accumulation. Our observations indicate a predominance (>90% of analyzed samples) of gas hydrate occupancy in the sandy layers. However, in the case of Sample 311-U1328C-13X-1, 0–10 cm, where the presence of gas hydrate was inferred by IR imaging and supported by salinity and chlorinity data, the sample consisted of a sizeable homogeneous clayey-silt biscuit. The fourth zone is observed from 250 mbsf to the TD of 300 mbsf. Here salinities remain constant with values ranging from 29.5 to 29.7. Chloride concentration is also relatively constant at 493 ± 3 mM, suggesting communication with a fluid at greater depth that is remarkably different in composition from the deep-seated fluid sampled at Sites U1327 and 889/890 (Westbrook, Carson, Musgrave, et al., 1994). At Site U1328, the Cl concentration of the deep fluid is ~495 mM, whereas at Sites U1327 and 889/890 it is 370 mM. This distinct difference in the deep fluid chlorinities suggests that at Site U1328 the temperature in the source region of the fluid is lower and, therefore, the fluid has undergone less freshening than at Sites U1327 and 889/890.

To form and maintain the shallow gas hydrate deposits, methane has to be supplied continuously. Furthermore, the high salinity and chlorinity values of 36–49 and 720–855 mM, respectively, observed between ~5 and 25 mbsf would dissipate rapidly if they were not continuously maintained by ongoing gas hydrate formation. However, the dissolved chlorinity profile below the subsurface brine is characteristic of a diffusion-controlled system. Assuming an average sediment diffusion coefficient of 5×10^{-6} cm^2/s, ~1.5 m.y. is required to establish the observed diffusion path length of 210 m observed in the chlorinity profile from 30 to 250 mbsf (Fig. **F25**). These observations indicate that in Hole U1328B the methane needed to sustain the shallow gas hydrate formation must be supplied from a laterally located source, most likely from a fault or fracture zone that intersects this site between 5 and 25 mbsf.

Below the high-salinity/chlorinity zone at 25–50 mbsf, Cl concentrations decrease from 572 to 560 mM. These values are slightly higher than the seawater value of 559 mM, suggesting diffusion from the high-chlorinity zone. Gas hydrate distribution at this site is bimodal: the first zone occurs close to the seafloor and the second zone is in a restricted depth interval above the BSR (from ~150 mbsf). Within these two zones, gas hydrate is mostly associated with sand horizons but also occurs in clayey-silt horizons, either in a disseminated mode or in thin layers parting the low-permeability clay-rich sediments, as observed in the X-ray scans of some pressure cores. Shore-based analyses should be able to show whether these two gas hydrate–bearing zones contain methane gas from the same source.

Sodium and potassium concentration profiles are overall very similar to the chlorinity profile.

Biogeochemical processes

Biological activity exponentially decays with depth, and in most cases limits its observable influence on IW chemistry to the upper part of the sediment. At Site U1328, the zone of highest biological activity coincides with the occurrence of gas hydrate and ongoing gas hydrate formation. Intense microbial activity at this site results in sulfate depletion in the upper ≤2 m, phosphate production, and significant accumulation of hydrogen sulfide in the interstitial water.

At this site, gas hydrate formation just below the seafloor results in the formation of highly saline fluids, caused by the exclusion of solutes from the gas hydrate and, therefore, increasing the solute concentrations in the interstitial water, including those affected by biological reactions. It is therefore difficult to delineate biogeochemical processes in the uppermost 30 m at this site (Fig. **F26**). Nevertheless, alkalinity values are significantly higher (up to 49.2 mM) than at Sites U1327 and U1329 than at Site U1328. This is a direct consequence of the higher organic matter accumulation rate, which in turn depends on the sedimentation rate. Compared to Sites U1329 (9.2 cm/k.y.) and U1327 (22 cm/k.y.), Site U1328 has a sedimentation rate of ~36 cm/k.y. (all rates refer to the uppermost unit; see **"Biostratigraphy"**) and consequently much higher alkalinity values.

Further downhole, the IW concentration profiles show extensive evidence of biological fluid/rock reactions (Fig. **F27;** Table **T4**). This is most evident in the Mg/Ca ratio, which shows a distinct maximum at ~220 mbsf, coincident with a minimum in Ca and Mg concentrations and the depth of BSR. In the upper part, where biological mediated reactions cause an increase in alkalinity and the subsequent precipitation of carbonate, primarily calcium carbonate is the precipitating phase, as indicated by the large increase in the Mg/Ca ratio. It is difficult to estimate how much carbonate has precipitated because at this shallow burial depth the interstitial water may be in communication with bottom seawater. If no communication with seawater is assumed, based on the alkalinity corrected for authigenic carbonate formation, the amount of authigenic carbonate formation seems insignificant between 0 and 30 mbsf (see Fig. **F28**). The first two sections in Core 311-U1328D-1X contained some authigenic carbonate in the form of small, disseminated, incipient micronodules.

Between 150 and 220 mbsf, two distinct authigenic carbonate reaction zones are observed. In the first zone, at the alkalinity maximum at ~150 mbsf, Ca also shows a maximum concentration. The Mg concentration, however, begins to decrease and the Mg/Ca ratio shows a broad minimum. These relations are indicative of authigenic carbonate formation that utilizes Mg and releases Ca. Such changes are typical of dolomitization of a precursor calcium carbonate. In the second zone, at ~220 mbsf and near the depth of the seismically inferred BSR, both alkalinity and Ca concentrations show minima. Here the Mg concentration remains equal to that of the deep fluid, and the Mg/Ca ratio shows a maximum, suggesting the formation of an authigenic carbonate enriched in Ca relative to Mg. Indeed, massive carbonate was recovered in Core 311-U1328C-19X, 216–226 mbsf. Iron is commonly involved in the formation of authigenic carbonates at greater burial depths. Shore-based analyses of the IW and diagenetic carbonates will indicate the involvement of Fe at this site.

Deep-seated fluid

The salinity and Cl, Na, K, and Li concentration profiles in Table **T4** provide important information on the nature of the deep-seated fluid at this site. As indicated in Figures **F25, F26,** and **F29,** the fluid is depleted in Cl, Mg, Na, and somewhat in K and enriched in Si and Ba. The Mg/Ca ratio is ~6, which is only slightly higher than the seawater ratio of 5.4, and the fluid has approximately seawater Sr, Li, and B concentrations. This is consistent with the Cl concentration data that show less dilution by hydrous mineral dehydration reactions, suggesting a lower temperature at the deep-fluid source. The other major and minor element concentrations also indicate a less-altered fluid source than at Site U1327.

Organic geochemistry

The organic geochemistry shipboard program for Site U1328 included analysis of the composition of volatile hydrocarbons (C_1–C_5) and nonhydrocarbon gases (i.e., O_2 and N_2) from headspace (HS) gas samples, void gas samples, gas samples recovered during PCS degassing experiments, and dissociated gas hydrate. Sediment from IW squeeze cakes was analyzed for inorganic carbon (IC; also expressed as weight percent $CaCO_3$), total carbon (TC), and total nitrogen (TN). Total organic carbon (TOC) was calculated as the difference between TC and IC. We collected 71 samples for HS and solid-state analysis at Site U1328. Most of the HS samples were collected from the cut end of core sections facing the IW samples so that the gas and IW data could be integrated. Gas hydrate dissociation during recovery of shallow cores (0–40 mbsf) affected the structural integrity of the sediments and allowed large volumes of drill fluid to contaminate the sediment IW. Consequently, we did not attempt to construct high-resolution vertical profiles of sulfate and methane in the near-surface sediments.

A total of 13 gas samples from gas hydrate pieces collected from the uppermost 40 m (seven from Hole U1328C, three from Hole U1328D, and three from Hole U1328E) were analyzed for gas composition. The lattice water from the dissociated gas hydrate was also collected for analysis (see **"Interstitial water geochemistry"**). We collected 49 void gas samples from depths where gas cracks in the cores were first observed (3.3 mbsf) to 299.5 mbsf. Finally, we analyzed the gas composition of five gas samples from PCS degassing experiments on cores from Holes U1328B, U1328C, and U1328E (see **"Pressure coring"**).

The primary objectives of the organic geochemistry sampling program at this site were to

- Characterize the composition of gas hydrate at the site;
- Determine the origin (microbial vs. thermogenic) of the gases recovered by HS, void, and gas hydrate gas and PCS degassing techniques;
- Investigate the relationship between the gas composition and the distribution of gas hydrate; and
- Compare the carbon and nitrogen contents to gas-related features in the sediments.

Hydrocarbons

Headspace and void gas composition

Hydrocarbon HS gas data from Holes U1328B, U1328C, and U1328D are listed in Table **T6.** Results are reported in parts per million by volume (ppmv) of methane, ethane, ethylene, and propane in the air headspace of a 25.41 ± 0.18 mL serum vial and as the millimolar concentration of dissolved C_1 in the interstitial water (see **"Organic geochemistry"** in the "Methods" chapter). Methane and ethane HS results from Site U1328 are plotted in Figure **F30** as the hydrocarbon gas component relative to depth. Methane content increased rapidly from 2.3 ppmv in the near-surface sample (0.5 mbsf) to a maximum concentration of ~65,500 ppmv at 5.3 mbsf. With the exception of a 3 m interval between 69 and 72 mbsf, where elevated HS concentrations of ~11,000 and 35,000 ppmv were observed, HS concentrations below 7.9 mbsf were fairly consistent and relatively low, ranging between ~1500 and 7000 ppmv. The apparent decrease in HS methane concentrations between 5.3 and 14.7 mbsf and the fairly consistent, relatively low concentrations below may be a sampling artifact that does not necessarily represent in situ trends. Postcruise stable carbon isotope analysis of the HS, void, and thermally desorbed gases will allow us to obtain a better understanding of which factors (degassing vs. preferential desorption from sediments) determine the composition and distribution of gas recovered by each method. A few air samples collected from the catwalk area during Site U1328 operations had a concentration of 1.81 ± 0.08 ppmv (n = 3) methane, which is similar to the current atmospheric methane concentration (~1.7 ppmv). The data reported in Table **T6** are uncorrected for the atmospheric contribution.

Ethane was present in the HS samples at all depths below 1.5 mbsf (Fig. **F30;** Table **T6**). Elevated C_2 was observed from near the surface (2–30 mbsf) where gas hydrate was recovered, and at or below the depth of the seismically inferred BSR (219 mbsf). Propane

was limited to a 27.8 m thick interval between 192.2 and 220 mbsf and above the BSR. It is noteworthy that ethane concentrations in this same interval were *not* elevated, especially when considering that chloride and IR temperature anomalies indicated that the interval contained gas hydrate (see **"Physical properties"** and **"Interstitial water geochemistry"**). Dissociation of gas hydrate with ethane is expected to enrich the surrounding gas with ethane because gas hydrate (especially Structure I gas hydrate) preferentially fractionates ethane relative to the source free-gas composition (Sloan, 1998). The same effect is observed with propane in Structure II gas hydrate (Sloan, 1998). Enrichment of propane, but not ethane, suggests an increased abundance of Structure II gas hydrate relative to Structure I gas hydrate in the interval above the BSR.

Gas composition expressed by the C_1/C_2 ratios of HS and void gas samples is plotted relative to sediment temperature in Figure **F31.** The sediment temperature was estimated assuming the calculated geothermal gradient of 54°C/km (see **"Physical properties"**). The monitoring of C_1/C_2 ratios in HS and void gas samples and its relationship to temperature was developed as a safety guideline by the Joint Oceanographic Institutions for Deep Earth Sampling Pollution Prevention and Safety Panel during ODP. C_1/C_2 ratios are described as either "normal" or "anomalous" depending upon where they plot relative to the slightly diagonal line in Figure **F31.** Some values from the HS and void gas samples were within the "anomalous" region (Pimmel and Claypool, 2001). The anomalous excursions, however, occurred in intervals where gas hydrate was either recovered or inferred. Because gas hydrate sequesters ethane and other higher hydrocarbons (Sloan, 1998), the C_1/C_2 values at this site were artificially deflated relative to the source signature. With this effect under consideration, it was determined that conditions were safe for drilling.

The composition of gas from voids in the core liner is shown in Table **T7.** With the exception of the near-surface samples, the void gas was ~90% methane. The surface samples contained slightly more air contamination and elevated H_2S in the shallow sediments. The calculated H_2S concentrations (as much as 4.5%) are based on calibration data from a previous cruise (H_2S standards above the detection limit of the gas chromatograph were not available during instrument calibration nor during finalization of this report) and will be verified postcruise. Carbon dioxide accounted for ~0.1%–1.5% of the total gas content. C_2–C_5 hydrocarbons constituted <0.2% of the total gas content in all samples; however, their relative abundances and distribution are valuable as tracers for fluid migration and interpreting the dynamics of the gas hydrate system.

The distribution of ethane and propane in the void gas samples was similar to the pattern observed in the HS data (Figs. **F30, F32**). Ethane concentrations were highest (~1600 ppmv at 38.2 mbsf in Hole U1328E) in the surface sediments where massive gas hydrate was recovered. Ethane was elevated from the BSR (219 mbsf) to the base of Hole U1328C.

Propane was present in trace amounts (0–5.3 ppmv) to 213 mbsf and then increased rapidly (maximum concentration = ~200 ppmv) in the 199–209 mbsf interval above the seismically inferred BSR. The highest *i*-butane concentration (170 ppmv) was observed in this same interval. Notably, ethane concentrations in this region of elevated propane and *i*-C_4 were not substantially elevated. The pattern of enriched Structure II gas hydrate–forming gases (C_3 and *i*-C_4) suggests that the gas hydrate inferred from the IR and chloride anomalies (see **"Physical properties"** and **"Interstitial water geochemistry"**) was enriched with Structure II gas hydrate relative to the near-surface (0–40 mbsf) gas hydrate.

The molecular ratios of C_1/C_2 and *i*-C_4/*n*-C_4 are consistent with the interpretation that the deep and shallow gas hydrate accumulations contain hydrocarbons from different sources. The C_1/C_2 ratios in the shallow interval (0–40 mbsf) were relatively low (~700–2900) and the *i*-C_4/*n*-C_4 ratios were slightly elevated (~6) (Fig. **F33**). These results indicate a slight contribution from Structure II gas hydrate. In contrast, the *i*-C_4/*n*-C_4 and C_1/C_2 ratios above the seismically inferred BSR (219 mbsf) were *both* elevated (Fig. **F33**). These data indicate the gas hydrate within that interval was enriched in propane and *i*-C_4, but not ethane.

Using a source gas composition similar to that present below the BSR (Table **T8**), the composition of Structure I and II gas hydrate at the in situ equilibrium conditions was calculated with the CSMHYD program (Sloan, 1998). These calculations did not include H_2S or CO_2. Both Structure I and II gas hydrate would have a C_1/C_2 ratio of ~2500. However, the Structure I gas hydrate would contain no propane or *i*-C_4, whereas the Structure II gas hydrate would have approximately twice as much propane as ethane (C_3/C_2 = 2.25) and approximately equal values of ethane and *i*-C_4 (*i*-C_4/C_2 = 1.25). Within the region of elevated propane and *i*-C_4 (199–209 mbsf), C_3/C_2 ratios ranged from 0.7 to 2.0 and *i*-C_4/C_2 ratios ranged from 0.2 to 1.4. By applying a two-source mixing model, where the end-members are Structure I and II gas hydrate with the molar percentages provided in Table **T8** and assuming that all void gas was a product of

gas hydrate decomposition, we calculated that ~50%–60% of the gas in the interval above the projected BSR may have come from Structure II gas hydrate.

Gas hydrate gas composition

The data from dissociated gas hydrate (HYD) gas from Site U1328 are listed in Table **T9.** The HYD gas samples were collected from the uppermost 40 m and therefore only reflect the composition of the shallow gas hydrate accumulations. Methane was the dominant gas recovered from the HYD gas samples. On average, C_1 accounted for ~99.4% of the total recovered gas, whereas C_2, CO_2, and H_2S comprised ~0.14%, 0.33%, and 0.12%, respectively. Although C_2 and CO_2 were present in most of the HYD gas samples, H_2S was limited to four HYD gas samples collected between the depths of 6.1 and 8.5 mbsf. The concentrations (~350 ppm to 1.8% H_2S) were similar to values reported from the southern summit of Hydrate Ridge (Milkov et al., 2005). The source of the H_2S is presumed to be from sulfate reduced during the anaerobic oxidation of methane. The concentration of ΣC_2–C_5 hydrocarbons was <0.001% of the total gas hydrate gas content and is consistent with a primary Structure I gas hydrate composition for the shallow gas hydrate.

Results from the analysis of gas samples collected during the PCS degassing experiments (see **"Pressure coring"**) are shown in Table **T10** and the C_1/C_2 ratios are plotted relative to depth with the HS, void, and gas hydrate gas data in Figure **F34.** The C_1/C_2 ratios of PCS gas samples are in agreement with the void gas sample trend at depths where direct comparisons were possible. Cores containing gas hydrate, the target for many PCS deployments, typically did not contain void gas that could be sampled. Gas hydrate dissociation degrades the mechanical stability of the sediments and allows air to flush the core liner. Therefore, opportunities to compare void gas from gas hydrate–bearing cores to gas from PCS cores are limited. The available direct comparisons of C_1/C_2 gas hydrate, PCS, and void gas generally agree within the shallow (0–40 mbsf) gas hydrate–bearing interval. The PCS samples from 92 mbsf (Cores 311-U1328C-5P and 311-U1328E-10P) did not fit the trend of the void gas C_1/C_2 data, but no void gas samples were collected within 10 m of the PCS samples. Low C_1/C_2 values in the HS data suggest the gas composition in that interval may be offset from the downhole void gas trend. The PCS gas sample from 230 mbsf (Core 311-U1328E-13P) agreed with the void gas data.

Biogeochemical processes

The depth of sulfate depletion was ~1.5 mbsf (see **"Interstitial water geochemistry"**), similar to the depth where dissolved methane concentrations begin to increase (Table **T6**). However, unlike the previous sites where the sulfate and C_1 profiles in the near-surface sediments showed clear zonation of the biogeochemical regions, high-resolution profiles from Site U1328 were not possible because of poor core recovery. Nevertheless, the shallow depth of sulfate depletion and occurrence of methane indicates a high flux of methane supporting the near-surface gas hydrate accumulations.

Sediment carbon and nitrogen composition

Sediment IC, carbonate ($CaCO_3$), TC, TOC, and TN concentrations and C/N ratios from Site U1328 are listed in Table **T11** and plotted relative to depth in Figure **F35.** Elevated IC was observed at two depths (9.7 wt% at 18.4 mbsf and 1.5 wt% at 43 mbsf) in the shallow Hole U1328B (52.8 mbsf). These elevated values suggest production of authigenic carbonate. In the deeper Hole U1328C, we observed a region of elevated carbonate between 190 and 210 mbsf. Within that region, the highest value of carbonate (1.1 wt%) occurred at 190.2 mbsf, and values declined gradually with depth to 0.62 wt% at 208 mbsf. There is no clear evidence for elevated carbonate from 216 to 226 mbsf, the interval where carbonate concretions and carbonate cements (see **"Lithostratigraphy"**) were observed. TOC ranged from 0.18 to 1.24 wt% (average = 0.5 wt%) and TN ranged from 0.02 to 0.14 wt% (average = 0.06 wt%) (Table **T11;** Fig. **F35**). TOC and TN contents were slightly lower in the uppermost 40 m relative to the deeper sediment at this site. C/N ratios ranged between 6.0 and 11.4 and averaged 8.3 for all samples. The values show no apparent trend with depth and indicate a primary marine source with limited terrestrial influence.

Microbiology

Site U1328 is an active cold vent located off the main transect of sites established by Expedition 311 across the northern Cascadia accretionary prism. It was the third site sampled for microbiology on this expedition. We anticipated a shallower SMI and a GHSZ that extended to a depth of ~220 mbsf. Efforts continued for obtaining live anaerobic methane oxidizers, unknown gas hydrate–associated microbial communities, high pressure adapted microorganisms, and methanogens. With the challenge of biological contamination from drilling, we also conducted tests

assess the level of microbial contamination from drilling slurry.

Microbiological sampling

Sampling from the mudline in Hole U1328B (Core 311-U1328B-1H-1, 0–3 cm) and the deepest core (Core 311-U1328C-27X-3, 55–70 cm; 297.0 mbsf) in Hole U1328C targeted microorganisms for aerobic and anaerobic high-pressure culturing. Sampling in the upper sedimentary section of Holes U1328D and U1328E targeted the SMI, where methane consumption is expected to exist. The upper part of Hole U1328B had limited recovery because of the difficulty penetrating hard layers near the seafloor with the APC and delays in core retrieval because of dangerous levels of hydrogen sulfide. Hole U1328C resumed coring where Hole U1328B ended (56 mbsf) and completed the targeted sedimentary section. The SMI was targeted for intensive, coupled microbiological and geochemical sampling in both Holes U1328D and U1328E (see **"Interstitial water geochemistry"** and **"Organic geochemistry"**). The SMI, however, was difficult to physically and chemically examine because of the challenges in recovering sediment that was highly disturbed by free gas and gas hydrate within the first several meters below the seafloor. The recovered cores were contaminated with seawater and appeared soupy in texture. Sediment quality was poor for geochemical analysis in both Holes U1328D and U1328E (see **"Interstitial water geochemistry"** and **"Organic geochemistry"**). Because LWD resistivity data and physical evidence (i.e., gas hydrate in the core catcher) indicated that gas hydrate was present within several meters below the seafloor, one 10 cm whole-round core from the uppermost 7 m was retained for microbiological study of gas hydrate–associated sediment.

Methanogenesis can exist in most anaerobic environments, but it becomes the major process when other electron donors such as nitrate, Fe(III), and sulfate are depleted. We sampled regularly downhole to below the depth of the predicted BSR to quantify methanogenesis in these sediments (see **"Microbiology"** in the "Methods" chapter).

Contamination tests

Perfluorocarbon tracer

Samples for perfluorocarbon tracer (PFT) and microsphere analyses were taken immediately from the ends of whole-round cut sections on the catwalk. Because the freshly cut sediment surface was potentially contaminated by PFT smeared along the core liner, the sediment surface at the sampling spots was scraped away using a clean spatula before sampling with a syringe. Subsamples (~5 cm^3) were taken from outer and inner layers from each core for gas chromatograph analysis as described in **"Microbiology"** in the "Methods" chapter. Samples were analyzed as described and the raw data are presented in Table **T12.** We also measured the catwalk air to confirm background PFT levels. When we processed the first APC core (Core 311-U1328B-1H-3), catwalk air contained PFT at 6.5 pg PFT/mL air. In the other cases, however, we found that PFT concentrations were below the detection level in catwalk air samples. Therefore, we could avoid false PFT contamination during the sampling process by taking subsamples for PFT measurements on the catwalk instead of in the Hold Deck reefer. Sampling the cores on the catwalk eliminated most of the background PFT contamination in measurements from Site U1328.

Fluorescent microspheres

Comparison of paired samples collected from the edges and centers of cores to assess fluorescent microsphere penetration is summarized in Table **T12.** Microscopic analysis of the outer portion of the APC cores showed detectable numbers of microspheres at 10^4 per gram of sediment, whereas microspheres were generally below the detection limit of 100 microspheres/g in samples taken from core interiors. Biscuit and sand layer samples obtained from XCB cores have a high possibility of contamination because of the nature of XCB coring or the porous structure of sand layers. In this hole, the quality of these characteristic samples was evaluated in detail. The samples were collected from the split cores because it is easy to identify the specific structures (Fig. **F36**). Numerous microspheres (10^3) were observed in the interior of one sand layer (Section 311-U1328C-16X-3), indicating contamination from drill fluid (Table **T12**). We also took samples from the inner and outer parts of biscuit and nonbiscuit (slurry) intervals at two different depths (Fig **F36**), but never observed microspheres in the inner portions of biscuits (Table **T12**). This observation suggests that the interiors of biscuits were biologically "clean."

Shipboard analysis

Samples were taken from the top (Sample 311-U1328B-1H-1, 0 cm) and bottom (Sample 311-U1328C-27X-3, 55–70 cm; 297.0 mbsf) of the sedimentary section for inoculation of enrichment cultures targeting high-pressure adapted heterotrophs and sulfate-reducing bacteria. Samples were maintained at low temperature, and dilution series were inoculated to culture for microorganisms at 55.1 MPa and 4°C. Only the sulfate reducers required preparation in the anaerobic chamber and were fed

formate, acetate, or lactate as a carbon source. Samples from Hole U1328D were collected from the mudline to ~15 mbsf.

Physical properties

Site U1328 is located within the Bullseye vent (Riedel et al., 2002). Seismic data suggest the presence of slope basin sediments deposited on older, accretionary complex material. This site was designed to probe the deep structure of this vent.

Physical properties were measured in cores recovered from Holes U1328B, U1328C, U1328D, and U1328E. Most of the samples discussed in this report were from Hole U1328B, which was sampled from 0.7 to 56.2 mbsf, and from Hole U1328C, which was sampled from 56.7 to 279.6 mbsf. Selected cores from gas hydrate–bearing zones were obtained from Hole U1328E, which was dedicated to special tools. Figure F37 presents an overview of the physical property data obtained at this site. Cores from this site were systematically scanned upon arrival on the catwalk to detect IR anomalies indicative of gas hydrate dissociation during core recovery. Many cold temperature anomalies were observed in the GHSZ, and catwalk sampling was conducted based on these scans. Notably, there were also cold thermal anomalies below the seismically inferred BSR at this site. In the following sections we discuss these data and compare them to data acquired at other sites.

Infrared images

All cores were scanned on the catwalk following the track-mounted IR camera procedures described in "Physical properties" in the "Methods" chapter. Portable Document Format images of the scans of all cores are available in the "Site U1328 core descriptions." Temperature arrays in the format of comma-separated value files were exported from the IR camera software and then concatenated for each core. The arrays were then further concatenated for all cores available in a given hole. Figure F38 shows cold thermal anomalies in the concatenated false-color IR images for Holes U1328B and U1328C. This figure also shows the Hole U1327B LWD/MWD resistivity image and the pore water saturation derived from these data for comparison.

As a precursor to quantitative studies on the temperature anomalies, downhole temperatures were averaged for each pixel row in the IR temperature array, excluding pixels ~1 cm from the edge of the image and 2 cm along the midline of the image to eliminate the major thermal artifacts in the images. Figure F39 shows a plot of temperature vs. depth for Holes U1328B and U1328C. These temperature profiles, and the definition of the baseline temperature of the core in the absence of gas hydrate, represent a first step toward quantifying the gas hydrate content of cores from IR data (Tréhu et al., 2004). Considerable effort was expended at this site on special experiments to calibrate the IR data by using it to target samples for IW chlorinity analyses.

Strong cold anomalies were detected in the shallowest cores from this site. A considerable amount of gas hydrate had been anticipated in the uppermost 40 m based on LWD/MWD resistivity measurements (see "Downhole logging"). Unfortunately, recovery was poor in this zone. Another zone of low IR temperature anomalies was observed from 105 to 115 mbsf. A high-resistivity zone was observed at a similar but slightly shallower depth in the LWD/MWD data; however, no chlorinity anomalies were detected in this zone. The strongest IR anomalies were detected just above the BSR, at 210–222 mbsf. Large chlorinity anomalies were also observed here. Finally, a few small but distinct cold anomalies were observed below the BSR, one of which was targeted for IW analysis, which showed pore water freshening indicative of gas hydrate. The possible presence of gas hydrate beneath the predicted BSR depth may indicate the presence of Structure II gas hydrate, which is stable to a depth of ~30 m below the base of the pure methane Structure I GHSZ. This hypothesis will be tested postcruise through analysis of chemical and physical property data obtained during Expedition 311.

Figure F40 shows a very strong temperature anomaly in an IR image taken immediately after the sample was removed from the catwalk to the Chemistry Laboratory, where it was extruded from the liner and split prior to analysis of pore water. The temperature in the interior of a gas hydrate–bearing sand layer was –3°C, an 18°C drop from the temperature at the outer edge of the core. This is one of the coldest gas hydrate–related anomalies documented during Expedition 311. The core liner temperature obtained from the IR scan on the catwalk was 6.5°C, a ΔT of 5.5°C. The chlorinity corresponding to this IR anomaly was 411 mM, indicating strong pore water freshening. An adjacent, slightly stronger anomaly (liner temperature = 5.5°C) had a Cl value of 347 mM (see Table T3; Samples 311-U1328C-18X-3, 67–72 and 72–82 cm).

Sediment density and porosity

Gamma ray attenuation (GRA) densities were measured on the multisensor track (MST), and bulk density, grain density, and porosity were calculated from the measured wet and dry weights and dry volume of the sediments (moisture and density [MAD] measurements; Table T13). Both estimates of density

were compared to in situ densities measured by the LWD/MWD tools (Fig. F37). The MAD data are compared to wireline data obtained in the same hole and to LWD/MWD data in Figure F41. The different data sets agree well. The agreement between the MAD and wireline data from the same hole below 100 mbsf is especially good, with matching trends in both data sets (see "Downhole logging" for further comparison of MAD and wireline density data). Low-porosity outliers are interpreted to represent sand-rich intervals. This hypothesis will be tested through postcruise grain-size analysis.

Accurate estimates of porosity are very important for obtaining accurate estimates of the in situ gas hydrate content of sediments recovered in pressure cores, and pressure cores represent the most direct means of determining the absolute amount of gas hydrate. During ODP Leg 204, it was reported that MAD samples from pressure cores sometimes yielded lower porosity estimates than adjacent APC or XCB cores. We tested that observation at this site (Fig. F42). No such correlation was found in seven samples from three different pressure cores.

Magnetic susceptibility

Magnetic susceptibility at this site was generally higher and more variable than at Sites U1327 and U1329 cored previously during Expedition 311 (Fig. F41C). Causes for the intersite variability in magnetic susceptibility will be a topic for postcruise research. It is likely that the variability is related to differences in the amount of silty and sandy turbidites, reflecting different sedimentary environments.

A decrease in magnetic susceptibility was previously reported by Novosel et al. (2005) for shallow sediments within Bullseye vent, compared to shallow sediments on the flanks of the vent. This has been attributed to chemical processes related to gas hydrate formation. At Site U1328, the average magnetic susceptibility in cores from the uppermost 30 m, while strong, is lower than in cores from 30 to 70 mbsf. Whether this is due to gas hydrate or to lithological variability will be examined postcruise.

Compressional wave velocity from the multisensor track and Hamilton frame

Because of the high gas content and limited recovery from the shallow section at this site, only a few poor quality *P*-wave velocity data were obtained (Table T14).

Shear strength

Shear strength measurements were made routinely throughout Holes U1328B and U1328C using the handheld Torvane (Table T15). A limited number of measurements were also made with the automated vane shear (AVS) system (Table T16). Measurements were made on the working half of the split core after resistivity and velocity measurements had been completed and after MAD samples had been taken. Measurements were taken in areas of the core where the sediment was undisturbed and as close as possible to where the MAD samples had been extracted. At least two Torvane shear strength measurements were taken per section, and often more where there were visual changes in the sediments (i.e., color and grain size). Two AVS measurements were taken per core.

AVS shear strength measurements were similar to, but generally slightly lower than, those obtained with the handheld Torvane (Fig. F43A; see also "Physical properties" in the "Site U1327" chapter). Shear strength values generally increase with depth and range from 15 kPa at the top of the hole to 120 kPa at the bottom. The ratio of shear strength to overburden pressure is a measure of the consolidation state of the sediments (Fig. F43C). A ratio >0.25 indicates overconsolidation and a ratio <0.25 indicates underconsolidation (Riedel et al., 2006). Except for the uppermost 5 m of the hole, the sediments are underconsolidated. The apparent overconsolidation of sediments in the upper 5 m may be caused by high carbonate content.

Electrical resistivity

Electrical resistivity was measured on core samples by both contact and noncontact methods. The contact resistivity measurement interval varied depending on core quality. MST noncontact resistivity measurements were made every 2.5 cm. Values obtained were very scattered because of gas expansion in the core. Contact resistivity measurements were made to a depth of 260 mbsf and ranged in value from 0.3 to 2.2 Ωm (Table T17; Fig. F44A). Higher resistivities were recorded but these were caused by cracks in the sediment. Resistivity increases with depth but becomes more scattered.

Pore water resistivities were calculated from the IW salinities using equations developed by Fofonoff (1985) and corrected to 20°C (Fig. F44A). These were used to calculate the formation factor (ratio of saturated sediment resistivity to pore fluid resistivity) from the contact resistivities (Fig. F44B). Archie's parameters were then determined by fitting Archie's equation to the formation factor and MAD porosity data (Fig. F44D). The cementation coefficient m = 1.36 and the tortuosity coefficient a = 1.58. Measurements made in sand intervals were not included in the estimation of Archie's parameters. These parameters were then used to determine porosities, which

were compared to the porosities measured from the MAD samples. Archie's parameters give a good fit to the data to a depth of 175 mbsf. Below this depth, the Archie's porosities underestimate the MAD porosities, suggesting a change in lithology that requires the calculation of a new set of Archie's parameters.

Thermal conductivity

Thermal conductivity values range from 0.6 to 1.3 W/(m·K) and show no consistent trend with depth (Table **T18;** Fig. **F37**). Although we tried to avoid disturbed portions of the core, gas expansion cracks were pervasive. The highest values follow the regional trend defined by Davis et al. (1990). For determination of in situ temperature and heat flow, a constant thermal conductivity value of 1.1 W/(m·K) was assumed. The depth interval from 110 to 140 mbsf, which has high thermal conductivity, high shear strength, high density, and low porosity, may be a more lithified zone similar to that observed from 75 to 90 mbsf at Site U1327. In contrast to Site U1237, however, the magnetic susceptibility is high in this interval.

In situ temperature profile

Although nine deployments of temperature tools were attempted at Site U1328, only three provided reliable data (Table **T19**). Unfortunately, one tool failed three times before a loose connection was found. The data are shown in Figure **F45.** Four deployments were seriously degraded by ship heave (56.5, 85.0, 93.0, and 103.0 mbsf), which reached ~9 m during operations in Hole U1328E. During the 93.0 mbsf deployment, the DVTP appears to have broken loose from the seafloor prematurely, so that it primarily measured the temperature of fluid in the drill pipe. Even the best data obtained at this site were affected by heave. The APCT16 deployment at 75.5 mbsf, while providing a "good" in situ temperature estimate (Table **T19**), has an unusual temperature profile with a very high initial temperature and anomalously fast decay rate.

Extrapolated temperatures are plotted and compared to data from Site U1327 and from Site 889 in Figure **F46.** The temperatures determined for Site U1328 are generally similar to those at Site U1327 and slightly higher than those determined at similar depths for Site 889 (Westbrook, Carson, Musgrave, et al., 1994). The temperature gradient at Site U1328 was determined to be 53.6 ± 0.4°C/km (Fig. **F46**). The remarkably good fit of the line to the three reliable (and, coincidentally, one unreliable) data points clearly underestimates the uncertainty in the determination of the subsurface temperature profile. The line falls within the region delimited by the standard error in the slope and intercept of the line fit to all reliable data points from Sites 889, U1327, and U1328, except for at the seafloor, where the intercept of the line fit to three Site U1328 reliable points is ~0.5°C higher than the expected bottom water temperature of ~3.0°C. Although the scatter in the combined data slightly exceeds the scatter expected based on the estimated measurement uncertainties for good- to excellent-quality data, we do not have enough data to constrain the vertical and lateral temperature gradients.

The combined temperature gradient predicts the base of methane hydrate stability at 220–245 mbsf. For the measured background pore water salinity of 3%, the predicted base of the GHSZ drops by ~2 m to 222–247 mbsf. For comparison, the seismic BSR depth in estimated to be 219 mbsf.

Advanced piston corer methane tool

Note: Derryl Schroeder (Integrated Ocean Drilling Program, Texas A&M University, 1000 Discovery Drive, College Station TX 77845, USA) provided the advanced piston corer methane (APCM) tool shipboard data and plots.

Pressure, temperature, and electrical conductivity histories of Cores 311-U1328C-2H, 3H, and 6H were logged using the APCM tool (Ussler et al., in press). Similar measurements were also made during deployment of the PCS (see **"Pressure coring"**). Results of the APCM tool deployments are shown in Fig. **F47.** Pressure, temperature, and conductivity are plotted continuously for all three deployments (Fig. **F47A**). The principal purpose of the conductivity probe is to detect the presence or absence of gas in the headspace above the core. Conductivity shows a dramatic drop at the time of the APC shot for Cores 311-U1328C-2H and 6H but not 3H, suggesting either that the headspace remained filled with drilling fluid (i.e., there was less methane at this depth) or that the conductivity probe malfunctioned, possibly as a result of clogging of the sensor by sediment. Pressure data show the descent, pause at the seafloor, lowering into the hole, shot of the APC, hold at the bottom of the coring position, pull to and pause at the seafloor, finally followed by ascent to the rig floor. All three deployments were coincident with APCT or APCT-3 measurements of temperature at the cutting shoe of the core. The APCT-3 data are compared to the APCM data in Figure **F47B.** The two temperature records show both positive and negative correlations. We note that the APCM shows cooling as the tool is fired and the APCT-3 shows the onset of frictional heating. This may be caused by cooling of the core as a result of pumping of fluid through the

drill pipe. XCB cores require continuous pumping, typically leading to a cooler core top and a steeper gradient from top to bottom than is obtained with APC coring (Tréhu et al., 2004).

Additional analysis of these data will be conducted postcruise, including integration with core line measurements made on the rig floor (Ussler et al., in press) to precisely reconstruct the pressure and temperature history of the core. The data should ultimately be of great value for understanding processes that affect core recovery, and for providing temperature and pressure boundary conditions for modeling the dissociation of gas hydrate during core recovery. Such modeling is critical for more sophisticated interpretation of IR anomalies.

Paleomagnetism

Note: This section was contributed by Jennifer Henderson and Katerina Petronotis (Integrated Ocean Drilling Program, Texas A&M University, 1000 Discovery Drive, College Station TX 77845, USA).

Alternating-field (AF) demagnetization of the sedimentary archive-half sections was used to determine the remanent magnetization components recorded in the recovered core (Fig. **F48**). The paleomagnetic data will be used postcruise to characterize the magnetic properties of the sediments and to construct a magnetostratigraphy of the sedimentary section recovered at Site U1328. The AF demagnetization applied at 10 and 20 mT should have removed most of the drill string magnetic overprint, but postcruise demagnetization at higher fields will most likely be required.

Questionable data may be associated with remanence measurements over intervals disturbed or deformed by coring. Similarly, magnetic edge effects, which can be large when measurements are within ~5 cm of the edge of a section or edge of a void, can give biased results. To avoid interpreting results in these regions, we manually noted the disturbed intervals and voids in the cores. Data from these intervals will be removed prior to postcruise interpretation.

Pressure coring

The main objectives of pressure coring during Expedition 311 were to quantify natural gas composition and concentration in sediments and to determine the nature and distribution of gas hydrate and free gas within the sediment matrix. To achieve these objectives, we

- Measured the quantity and composition of gases released during controlled degassing experiments,
- Conducted nondestructive measurements (X-ray imaging, *P*-wave velocity, gamma ray density) at in situ pressure and during degassing, and
- Preserved gas hydrate–bearing sediments at in situ pressure for more comprehensive shore-based investigations.

The nondestructive measurements not only provide a direct indication of the existence of gas hydrate, but the resulting data (acoustic impedance) can be used to help interpret regional seismic data. Site U1328 is situated at the Bullseye cold vent, where seismic records show a blank zone beneath the seep and a weak BSR (219 mbsf). Massive gas hydrate had previously been found at the surface of this site (Riedel et al., 2002, 2006). The presence of massive forms of gas hydrate was also inferred from LWD data in Hole U1328A, where very high resistivity layers associated with low densities occur from 0 to 46 mbsf and near 95 mbsf (see **"Gas hydrate and free gas occurrence"**). LWD resistivities did not show evidence of free gas below the BSR, but there was indication of gas below the BSR in the sonic waveform coherence (see **"Gas monitoring with real time logging-while-drilling/measurement-while-drilling data"**). Specific objectives at this site were to determine the concentration of gas hydrate in the sediment column, determine the concentration of free gas below the BSR, and retrieve samples of massive gas hydrate.

Operation of pressure coring systems

Pressure coring tools were deployed 11 times at Site U1328 (Table **T20**): two PCS cores in Hole U1328B, with the top core targeting massive gas hydrate; one PCS core in Hole U1328C, which targeted the high-resistivity layer near 95 mbsf; one FPC core in Hole U1328D, which targeted massive gas hydrate near the seafloor; and two deployments each of the HRC and the FPC along with three deployments of the PCS in Hole U1328E, with the top HRC and FPC cores targeting massive gas hydrate, the middle PCS core targeting the ~95 mbsf high-resistivity layer, and the bottom PCS core targeting free gas below the BSR. Figures **F49** and **F50** show the pressure history of the cores during deployment, coring, recovery, and chilling in the ice shuck. The ice shuck had no ice in it when Core 311-U1328-10P was immersed.

Five of the six PCS runs recovered full cores at some pressure (Table **T20**). The first two deployments (Cores 311-U1328B-4P and 7P) had particularly unusual pressure profiles (Fig. **F49**). Despite immersion

of the autoclave in the ice shuck, the pressures rose rapidly and peaked sharply at pressures well above in situ pressures (20 and 24 MPa, respectively), before rapidly falling again prior to the tool being removed from the ice. Pressures were still decreasing rapidly when the data loggers were removed. The other PCS deployments recovered cores with only ~30%–80% of in situ pressure (Table **T20**). After the PCS cores were degassed and X-rayed (see "**Degassing experiments**"), they were extruded using a hydraulic pump, curated, and samples for IW, porosity and headspace gas analyses were taken.

The first FPC (Core 311-U1328D-3Y) and HRC (Core 311-U1328E-3E) deployments targeted massive gas hydrate. Core 311-U1328D-3Y returned empty and showed no evidence of penetrating the formation. Core 311-U1328E-3E penetrated massive gas hydrate that was not retained as an intact core. The depth of Core 311-U1328E-3E was determined by the previous partial XCB core, which had been drilled until a hard formation was reached. The recovered pressure in Core 311-U1328E-3E (4 MPa) was below in situ pressure (12.8 MPa) because the side valve on the HRC had failed; the core was returned to full in situ pressure and quickly X-rayed, but the core liner was nearly empty. When the autoclave was depressurized and inspected, gas was released and small pieces of gas hydrate were found in the autoclave, though there was very little associated sediment.

The remaining FPC and HRC deployments (Cores 311-U1328E-7Y, 11Y, and 12E) all failed because of adverse heave and weather conditions. The FPC deployments that recovered Cores 311-U1328E-7Y and 11Y suffered from large tensions on the sand line during coring (as confirmed subsequently from the rig data), when during normal operation the sand line should be slack. The HRC deployment was terminated by an ill-timed 4 m heave that lifted the drill string and tool off the bottom during the crucial coring stroke, returning the corer with an empty and shattered liner.

Degassing experiments

At Site U1328, the five PCS cores that were successfully recovered under pressure were investigated by controlled shipboard degassing experiments (Table **T21**). Two PCS cores were taken within the near-surface gas hydrate–bearing section from 0 to 46 mbsf (Cores 311-U1328B-4P at 14.5 mbsf and 7P at 26.0 mbsf). PCS Cores 311-U1328C-5P and 311-U1328E-10P were both recovered from 92.0 mbsf where very high resistivity layers associated with low densities were seen in the LWD data. The deepest PCS core was taken at a depth of 233.0 mbsf, very close to the seismically inferred BSR depth (Core 311-U1238E-13P).

All degassing experiments included the following steps. First, the volume and density of sediment inside the inner core barrel of the PCS was monitored by X-ray analysis. Next, the PCS was slowly degassed in a temperature-controlled van (7°C), and the volume and composition of released gas and water, the pressure inside the core, and the ambient air pressure and temperature were monitored (Table **T22**) as described in **"Pressure coring"** in the "Methods" chapter. During the degassing procedure, the vertical density distribution of the PCS cores was repeatedly determined by GRA scans to examine the evolution of gas voids within the sediment. After degassing was completed, we X-rayed the PCS cores again, collected the water remaining in the outer core barrel for mass balance considerations, curated the sediment that was extruded from the cores, and subsampled it for IW chemistry, dissolved gases, and physical property analyses.

Degassing the five PCS cores from this site yielded 2.7–61.6 L of gas and showed variable methane concentrations with depth (Table **T22**). Mass balance calculations yield pore space methane concentrations of 123–3775 mM. They indicate 2%–15% of gas hydrate in the pore space of shallow Cores 311-U1328B-4P (14.5 mbsf) and 7P (26.0 mbsf), gas hydrate pore space concentrations of 0.7%–38% for Cores 311-U1328C-5P and 311-U1328E-10P (92.0 mbsf), and a free gas concentration of 58% in the pore space of Core 311-U1328E-13P (233.0 mbsf) from below the depth of the BSR (Tables **T23, T24;** Fig. **F51**).

Methane was the major component of the released gas for all PCS cores (Table **T22**). In Cores 311-U1328C-5P and 311-U1328B-7P with low gas hydrate contents, methane accounted on average for 70% ± 8% and 76% ± 4% of the emitted gas, respectively. In all other cores, methane concentrations ranged from 91% ± 5% to 98% ± 1%. Nitrogen was the second most abundant gas, contributing 0.7% ± 0.3% to 23% ± 9% to the gas released. Carbon dioxide, ethane, and higher hydrocarbon concentrations were below the detection limit of the Agilent gas chromatograph used for continuous gas analysis during the degassing experiments. A subset of gas samples from each core was analyzed using methods described in **"Organic geochemistry"** in the "Methods" chapter and yielded 337–1052 ppmv ethane.

During four degassing experiments, the pressure inside the PCS cores dropped below the predicted gas hydrate stability conditions when the port valve of

the PCS was first opened and water expanded from the outer core barrel into the manifold system. Therefore, no pressure plateaus or rebounds from gas hydrate dissociation could be expected and a steady decrease of core pressure vs. removed gas volume was observed (Fig. F52). In contrast, during the degassing of Core 311-U1328E-13P from below the depth of the BSR, the pressure inside the PCS remained at a constant high level of 5 MPa while the initial 25 L of gas was released. This pressure indicates gas hydrate stability, and the observed pressure plateau and rebound of pressure are typical for gas hydrate dissociation. However, X-ray images and repeated gamma ray density profiles of Core 311-U1328E-13P show no evidence for gas evolution within the sediment, and IW analysis does not indicate pore water freshening caused by decomposition of gas hydrate. Therefore, we conclude that the observed gas hydrate was artificially formed from free gas when the PCS was brought into the gas hydrate stability field upon entering the temperature-controlled laboratory.

X-ray scans before and after degassing, as well as gamma ray density scans during degassing experiments (Fig. F53), confirmed the presence of gas hydrate within some of the cores. The initial X-ray scan of Core 311-U1328B-4P shows low-density layers that correspond to large gas cracks in the final X-ray image, which also shows a large void in the bottom of the core barrel (Fig. F53). The time series of density profiles (Fig. F54) shows the formation of this void in the core barrel as gas and sediment were forced down and out of the bottom of the inner core barrel. IW chlorinities from this core are extremely high, indicating current gas hydrate formation (see "Interstitial water geochemistry"). It is not possible to quantify gas hydrate through pore water freshening in this core because no background chlorinity can be assumed.

Differential density profiles (i.e., gamma ray density profiles from which the initial profile has been subtracted) of Core 311-U1328B-7P show expansion throughout the core, with movement of pieces of sediment out of the bottom of the barrel (Fig. F53B). The final X-ray scan shows a low-density, highly expanded core. Based on the gamma ray density measurements and the X-ray image, this core was initially 95 ± 3 cm long. An IW sample taken in a less expansive portion of the core had chlorinities that agreed with the general background value for Hole U1328B.

Core 311-U1328C-5P, in contrast to most of the other pressure cores from Site U1328, showed only a small amount of expansion, all of which occurred between the first and second gamma ray density scans (Fig. F53C). This core also had chlorinities that agreed with the background value for Hole U1328B.

Core 311-U1328E-10P, collected in a steel barrel, originally contained ~35 ± 5 cm of core, based on the gamma ray density scans (Fig. F55). However, this core was completely homogenized during the degassing process as sediment and gas forced their way down and out of the inner core barrel. No IW sample was taken from this destroyed core.

The X-ray images and repeated gamma ray density profiles of Core 311-U1328E-13P (Fig. F53E), which yielded 62 L of gas, show little evidence for gas evolution from the sediments during degassing. Although some expansion took place in the lowermost 10 cm of the core, the overall density decrease in the core was less than that seen in Core 311-U1328C-5P, which only released 2.74 L of gas. None of the three IW samples taken showed evidence of pore water freshening. It is concluded that little of the gas released from Core 311-U1328E-13P during the degassing experiment actually comes from the sediments in the core.

Gas hydrate concentration, nature, and distribution

Based on mass balance calculations from pressure coring, Site U1328 contained highly variable amounts (0.7%–38.0%) of methane hydrate in the sediment column (Table T24; Fig. F51). This cold vent site was expected to contain large amounts of gas hydrate but also to be laterally heterogeneous. Both of these expectations were confirmed from the pressure coring results. The single core (Core 311-U1328B-13P) from below the BSR, which may or may not have been below the base of the GHSZ given the uncertainty of the temperature data (see "In situ temperature profile"), contained evidence for free gas.

The highest concentrations of gas hydrate were found not near the seafloor, as expected, but in a core from 92 mbsf (Core 311-U1328E-10P), which corresponds to a zone of very high resistivity in the LWD data from Hole U1328A. A pressure core taken at the same depth in Hole U1328C (Core 311-U1328C-5P) contained almost no gas hydrate, and the IR images (Fig. F38) and salinity and chlorinity profiles (Fig. F25) show no anomalies near 90–100 mbsf. The targeted resistivity feature might be a steeply dipping fracture in Hole U1328A (see "Logging-while-drilling borehole images"), in which case any attempt to correlate this feature with other holes would be futile. There is also evidence for general lateral heterogeneity from LWD and wireline logs from different holes at Site U1328 (see "Log-

ging-while-drilling and wireline logging comparison").

On two occasions during Expedition 311, the PCS returned a significant amount of natural gas that could not be attributed to the recovered core (Cores 311-U1328E-13P and 311-U1329C-23P). We suggest that during these deployments, free gas from the formation was collected directly in the outer core barrel of the PCS. During the coring operation, the outer barrel of the PCS is unlikely to collect gas because drilling fluids are flowing down the outer core barrel. However, when coring is completed, this flow is stopped and the actuator raises the inner barrel, enlarging the opening from the formation to the outer core barrel. At this stage in the recovery of the PCS core, gas in the formation could freely bubble into the outer core barrel prior to the ball valve being closed. If cuttings were to block the main hole, the actuator would "swab" any gases trapped in the bottom of the hole into the outer core barrel. In this way the outer barrel may end up as a "gas sampler" for free gas that has either been released from the formation during drilling or released by the dissociation of gas hydrate during the heating caused by drilling.

The abrupt pressure rise that Cores 311-U1328B-4P and 7P experienced in the ice shuck (Fig. F49) might be associated with gas hydrate dissociation, assuming a thermal lag between the core and the recording thermistor above the autoclave. The equally abrupt pressure decrease would then correspond to the reformation of gas hydrate. However, such a pressure increase (or decrease) was not shown by similar cores that contained large amounts of gas hydrate (e.g., Cores 311-U1327D-10P and 311-U1328E-10P) and were near the gas hydrate phase boundary. Pressure increases of this type were seen in other gas hydrate–bearing pressure cores during Leg 204 (Tréhu, Bohrmann, Rack, Torres, et al., 2003) and might contain kinetic information about the distribution and surface area of the gas hydrate.

Downhole logging

Logging while drilling

Operations

Hole U1328A was spudded at 1279 mbrf water depth (drillers depth) at 0455 h on 24 September 2005. Hole U1328A was drilled after completing Hole U1327A by pulling the drill string clear of the seafloor and moving the ship in DP mode. LWD tools included the GeoVISION resistivity tool, the EcoScope tool, the SonicVISION tool, the TeleScope MWD tool, the ProVISION NMR tool, and the ADN-VISION tool. For details on each tool and the measurements it makes, see "Downhole logging" in the "Methods" chapter.

Drilling in Hole U1328A began after a VIT camera survey established that no living chemosynthetic communities were present at the seafloor. Because massive gas hydrate was suspected near the surface, Hole U1328A was initially drilled more slowly than the other LWD holes of Expedition 311. The first 10 m of Hole U1328 was drilled with a rotation rate of 10 rpm, a pump flow rate of 100 gpm, and an ROP of 10–15 m/h. We then increased the rotation rate to 40 rpm while keeping the low pumping rate of 100 gpm until 30 mbsf, and then to 60 rpm and 270 gpm (to start the MWD telemetry), keeping the instantaneous ROP below 50 m/h with depth. The target depth of 300 mbsf (1633 mbrf) was reached at 0415 h on 25 September. The LWD tool string was then brought back to the surface, and rig down and data download for Holes U1326A, U1327A, and U1328A was completed by 1050 h on 25 September 25.

Gas monitoring with real time logging-while-drilling/measurement-while-drilling data

The LWD logs were acquired to plan coring and pressure coring operations in subsequent holes at Site U1328. As Hole U1328A was drilled without coring, the LWD data had to be monitored for safety to detect gas entering the borehole. As explained in "Downhole logging" in the "Methods" chapter, the primary measurement we used in gas monitoring was annular pressure while drilling (APWD) measured by the EcoScope tool in the borehole annulus. We looked for sudden decreases of >100 psi in the annular pressure, which could be caused by low-density gas entering the borehole. We also monitored pressure increases of the same magnitude, which could be the result of fluid acceleration caused by a gas kick (Aldred et al., 1998).

Figure F56 shows the measured borehole fluid pressure profile in Hole U1328A after subtraction of the best-fit linear trend. The borehole fluid pressure shows only small fluctuations over the trend, except for two negative pressure anomalies of almost 20 psi at 245–255 mbsf and ~10 psi at 263–270 mbsf. These fluid pressure anomalies were well below the 100 psi level that would have required preventive action.

We also monitored the coherence of the sonic waveforms acquired by the SonicVISION tool, focusing on the velocity of fluid in the borehole. Loss of coherence in the waveforms and a slower velocity for the drilling fluid indicate the presence of gas. The sonic waveform coherence image in Figure F56 shows a generally well defined fluid arrival with a slowness of ~200 µs/ft, which corresponds to the expected fluid

velocity of ~1500 m/s. There is an anomalous interval at 222–240 mbsf, which is probably below the GHSZ at this site, and if excess gas was present in the formation it had to be free gas. The sonic waveform coherence suggests that the fluid velocity decreased in this interval and that the slowness was higher than the upper bound of 240 µs/ft used in the processing. The ultrasonic caliper shows a smaller hole diameter at 233–250 mbsf, roughly coinciding with the interval of negative fluid pressure anomalies. The apparent offset between the pressure anomaly and the low-coherence interval could be caused by the spacing between the pressure and sonic sensors, with both reacting at the same time to the release of free gas in the borehole. These results suggest that the fluid velocity measured while drilling may indicate layers containing free gas and warrant further study. Even if the low coherence and low drilling fluid velocities were caused by free gas it is important to stress that the fluid pressure anomalies were small and that if gas was in the drilling fluid at ~223–250 mbsf, it had to be in low concentrations.

Logging quality

Figure **F56** also shows the quality control logs for Hole U1328A. The ROP was generally 60 m/h or less in the interval from the seafloor to TD. This is sufficient to record one measurement every 4 cm (~25 measurements/m) with the GeoVISION resistivity tool, and no significant resolution loss was observed with variation in ROP. The ultrasonic caliper log, which is a direct measurement of the borehole diameter recorded by the EcoScope tool, is our best indicator of borehole size. Most of the hole had a diameter slightly >10 inches (25 cm), with larger washouts slightly above 11 inches (28 cm) restricted to the uppermost 70 m of the hole. The density correction, calculated from the difference between the short- and long-spaced density measurements, generally varies from 0 to 0.2 g/cm^3 (Fig. **F56**), showing the good quality of the density measurements. Figure **F57** is a summary of the main LWD logs with density and porosity measurements from cores from Holes U1328B, U1328C, and U1328E superimposed (see **"Physical properties"**).

The depth relative to the seafloor was fixed for all LWD logs by identifying the step change in the gamma ray log associated with the seafloor. For Hole U1328A, the gamma ray logging pick for the seafloor was at a depth of 1279 mbrf.

Wireline logging

Operations

Hole U1328C was continuously cored to a depth of 300 mbsf, which was reached at 1000 h on 14 October 2005. A short wiper trip was made in the bottom 40 m, and the hole was displaced with 10.5 ppg mud. Wireline logging operations in Hole U1328C began with the deployment of the triple combo tool string (resistivity, density, and porosity measurements), which consists of the Hostile Environment Gamma Ray Sonde, the Dual Induction Tool, the Hostile Environment Litho-Density Tool, the Accelerator Porosity Sonde (APS), and the Lamont-Doherty Earth Observatory high-resolution Temperature/Acceleration/Pressure (TAP) tool. For details on the different tools, see **"Downhole logging"** in the "Methods" chapter. Rig up of the triple combo tool string started at 1415 h and was completed at 1605 h. The tool string reached the bottom of the hole at 1573 mbrf (294 mbsf) without difficulty by 1735 h, and we started to log up. During the run, the minitron (neutron generator) on the APS tool started to malfunction at ~1380 mbrf (101 mbsf). Consequently, when the tool reached the seafloor we decided not to run a second pass. The triple combo tool string was returned to the rig floor at 1930 h. When the TAP tool was brought back to the Downhole Logging laboratory to download the data, we discovered that it had not functioned properly, and there are no downhole temperature data available for Site U1328.

After rig down of the triple combo tool string was complete, rig up of the FMS-sonic tool string began and was finished at 2110 h on 14 October. The FMS-sonic tool string consists of the FMS, the General Purpose Inclinometer Tool, the Scintillation Gamma Ray Tool, and the Dipole Sonic Imager (DSI). The tool string was lowered into the hole and reached the bottom (1574 mbrf; 295 mbsf) at 2318 h when the first FMS pass started. After reaching the seafloor, we lowered the tool string to the bottom of the hole for a second pass, which began at 0030 h on 15 October. The second pass ended at 1346 mbrf (67 mbsf) and was followed by a third, short pass between 1480 and 1450 mbrf (201–171 mbsf) to test the Schlumberger heave compensator, which worked well. Rig down of the FMS-sonic tool string was completed at 0315 h, when rigging for the VSP operations started (see **"Vertical seismic profile"**).

Logging quality

Wireline logging data from the triple combo and FMS-sonic tool string runs in Hole U1328C were compromised to some extent by poor hole conditions typical of these unconsolidated formations (Fig. **F58**). The two FMS calipers measure the hole diameter in two orthogonal directions, and Figure **F58** shows that the hole was particularly elongated with a consistent difference of ~3 inches between the two calipers. The larger measurement was beyond the

maximum range of 15 inches (38 cm) in most of the hole. As a consequence, there was often poor contact between some of the FMS pads and the borehole wall, which degraded the quality of the resistivity images.

On the other hand, the density tool caliper measured less than its maximum range of 20 inches (51 cm) in most of the hole, and the density pad was generally in good contact with the formation. The density log in Figure **F58** is of good quality and shows only a few intervals where the logged densities are erroneously low (below ~1.5 g/cm^3) because of hole enlargements. The excellent quality of the density log and the derived porosities is also supported by the close fit with core measurements, which is especially good at 128–200 mbsf where resistivity was low and uniform. This suggests that little or no gas hydrate was present, and that formation disturbance after coring caused by hydrate dissociation had to be minimal. It should also be stressed that the core measurements plotted in Figure **F58** were obtained on samples taken from the same hole that was logged, and that the comparatively poor fit between the LWD density log and the core data (Fig. **F57**) may be due at least in part to lateral heterogeneity.

Porosities measured by the neutron log are close to those computed from the density log at 100–130 mbsf, but are markedly higher than the density porosities at depths >128 mbsf. This difference is probably caused by sediments with a greater clay content below 128 mbsf because the neutron log measures hydrogen abundance and it tends to overestimate porosity in clay-rich formations where hydrogen in clay minerals is counted as porosity. The induction log resistivities are generally not affected by hole conditions as much as the nuclear logs, and the resistivity logs in Figure **F58** are of very good quality. The only exception is at depths above 92 mbsf, where the logged resistivities are variable and locally anomalously low. We have no caliper information in this interval, but hole enlargements are probably the reason for the poor measurement quality.

The acoustic data measured in Hole U1328C appear to be of excellent quality. The acoustic waveforms and slowness-time coherence projection are shown in Figure **F59.** The velocity profiles acquired are very robust, and almost no additional processing was required to derive reliable compressional (V_P) and shear (V_S) wave velocities.

The depth relative to the seafloor for all wireline logs was fixed by identifying the step change in the gamma ray log associated with the seafloor. The gamma ray pick for the seafloor was at 1279 mbrf in Hole U1328C.

Logging-while-drilling and wireline logging comparison

Figure **F60** shows a comparison of LWD (Hole U1328A) and wireline (Hole U1328C) data using the gamma ray, neutron porosity, density, and resistivity logs. In general, the LWD and wireline data from each hole match relatively well, exhibiting similar curve shapes and absolute logging values. For example, the LWD and wireline density logs give generally similar values except for a few intervals where the hole is enlarged and the wireline density log gives anomalously low readings (compare the wireline density log to the wireline caliper track in Fig. **F60**).

A notable difference between LWD and wireline measurements is the gamma ray log, where the LWD log gives higher readings (100 gAPI on average) than the wireline log (50 gAPI on average). The LWD and wireline gamma ray curves have similar character and correlate well in some intervals (e.g., 95–115 mbsf), but in much of the drilled sequence there is no obvious correlation between the two. The cause of the discrepancy is not fully understood; however, the wireline data are consistent with the logs recorded during Leg 146.

Except for some anomalies caused by the enlarged hole, LWD and wireline neutron porosities are similar between and 102 and 128 mbsf. Below 128 mbsf, however, the neutron wireline log gives higher porosities than the LWD log and the core measurements. As noted above, this is most likely caused by an increase in the clay content of the formation, which is supported by a small increase in both the LWD and wireline gamma ray readings below 128 mbsf. The LWD neutron porosity shown in Figure **F60** is not affected by this increase in clay content below 128 mbsf because it is the "best thermal neutron porosity" measured by the EcoScope tool, which has been corrected for the effect of clay so that it is only slightly higher than the density porosity.

Comparison of LWD and wireline resistivities shows a similar overall trend. The low resistivities measured by the wireline logs in the shallow interval above 92 mbsf are probably the result of washouts in Hole U1328C. There are differences between LWD and wireline logs, however, in resistivity peaks that may be caused by the presence of gas hydrate. The LWD resistivities show peaks where resistivity reaches 2–3 Ωm at 90–98, 125, 160, 170–178, 183–191, and 195–206 mbsf. The wireline resistivities do not contain any of these LWD peaks but instead display two other peaks at 217 and 231–237 mbsf that are not seen in the LWD resistivity logs.

Given the evidence for lateral heterogeneity at nearby Site U1327 (see **"Downhole logging"** in the "Site U1327" chapter), the observed differences between the LWD and wireline resistivity logs at Site U1328 are consistent with similar lateral variability in gas hydrate distribution and/or lithology. This implies that one should be cautious when comparing measurements taken in different holes (e.g., LWD logs from Hole U1328A and core analyses from Hole U1328B or U1328C).

Logging units

The logged section in Holes U1328A and U1328C can be divided into three logging units based on obvious changes in LWD and wireline gamma ray, density, electrical resistivity, and acoustic measurements (Figs. **F57, F58, F59**). Except for minor differences in the boundary depths (3–5 m), these three logging units correspond to lithostratigraphic Units I, II, and III (see **"Lithostratigraphy"**).

Logging Unit 1 (0–128 mbsf) is characterized by a well-defined increase in density with depth (from 1.7 g/cm^3 near the seafloor to 2 g/cm^3 at 128 mbsf), and a decrease in porosity (from 70% near the seafloor to 45% at 128 mbsf). The *P*-wave velocities average ~1550 m/s. The most striking features are seen in the LWD logs between the seafloor and 46 mbsf, where high resistivities (>25 Ωm) alternate with intervals of much lower resistivity (1–2 Ωm). These high resistivities are not associated with high densities (at most 1.7 g/cm^3) and are, therefore, likely to indicate gas hydrate and not cemented sands or carbonates. The low resistivities are closer to the background values observed in the rest of the section, and Unit 1 is likely to contain layers with high gas hydrate content intercalated with sediments that have little or no gas hydrate in the 0–45 mbsf interval.

Logging Unit 2 (128–200 mbsf) is marked by a clear decrease in density (from 2 to 1.75 g/cm^3) at the top, compared to the bottom of Unit 1. Unit 2 is also characterized by a constant background resistivity value just above 1 Ωm and no resistivity peaks attributable to gas hydrate; however, an exception may be at 160 mbsf in the LWD resistivity logs. Porosity and V_P average ~50% and ~1600 m/s, respectively.

Logging Unit 3 (200–300 mbsf) displays a small increase in background resistivity and a markedly higher variability in resistivity (1–4 Ωm) and V_P (1500–1800 m/s) compared to Unit 2. Density and porosity are otherwise similar to those in Unit 2.

Logging-while-drilling borehole images

The GeoVISION, ADNVISION, and EcoScope LWD tools generate high-resolution images of borehole log data. The ADNVISION and EcoScope tools produce images of density and hole radius (computed on the basis of the density correction, which depends on the borehole standoff). The GeoVISION tool produces a gamma ray image and shallow, medium, and deep depth of investigation resistivity images.

Figure **F61** shows some of the LWD images collected by the EcoScope and GeoVISION tools. It should be noted that the display in Figure **F61** is highly compressed in the vertical direction. The unwrapped images are ~90 cm wide (for an 11 inch diameter borehole), and the vertical scale is compressed by a factor of ~37:1. These high-resolution images can be used for detailed sedimentological and structural interpretations and to image gas hydrate distribution in sediments (e.g., in layers, nodules, or fractures). Gas hydrate–bearing sediments exhibit high resistivities within intervals of uniform or low bulk density. Layers with high resistivities and high densities are likely to be low-porosity, compacted, or carbonate-rich sediments.

High concentrations of gas hydrate is evident from 0 to 46 mbsf in Hole U1328A, where densities are generally low and high-resistivity, gas hydrate–rich layers (bright in the resistivity images of Fig. **F61**) alternate with low-resistivity layers (dark in the images of Fig. **F61**) that are likely to contain little or no gas hydrate. Other points of interest in the resistivity images are at 25–45 and 92–97 mbsf, where roughly sinusoidal, bright features can be interpreted as dipping fractures containing gas hydrate (Fig. **F62**). These fractures have steep dips. For example, the top and bottom of the fracture at 92–97 mbsf are 3 m apart vertically, and for a borehole of 10.5 inch diameter (27 cm) this implies a dip of 85°. These near-vertical fractures may act as gas-migration conduits that feed the gas hydrate accumulation observed near the seafloor at Site U1328.

Logging porosities

Sediment porosities can be determined from analyses of recovered cores and from downhole measurements (see **"Physical properties"** and **"Downhole logging"** in the "Methods" chapter). Data from the LWD density and neutron logs were used to calculate sediment porosities from Hole U1328A. Core-derived physical property data, including porosities (see **"Physical properties"**), were used to calibrate and evaluate the log-derived sediment porosities.

The LWD log–derived density measurements were used to calculate sediment porosities (ϕ) using the standard density-porosity relation

$$\phi = (\rho_g - \rho_b)/(\rho_g - \rho_w).$$

We used a constant water density (ρ_w) of 1.03 g/cm³ and a grain/matrix density (ρ_g) of 2.76 g/cm³, which is the average grain density measured in the core samples (see **"Physical properties"**). The density log–derived porosities range from ~70% at 10 mbsf to ~45% at 300 mbsf (Fig. **F63**).

The LWD neutron porosity log (Fig. **F63**) yielded sediment porosities ranging from an average value of ~70% at 20 mbsf to ~45% at 300 mbsf. As noted earlier, porosities measured by the neutron log are expected to be higher than those computed from the density log in clay-rich sediments because the neutron log essentially measures hydrogen abundance, and hydrogen in clay minerals is counted as porosity. The neutron porosity measured by the EcoScope tool (Fig. **F63)** has been corrected for the effect of clay, so that it is only slightly higher than the density porosity.

The comparison of core- and LWD-derived porosities in Figure **F63** reveals that the log-derived porosities agree with the core-derived values throughout the logged interval, with the density porosities being slightly lower and the neutron porosities slightly higher than the core porosities.

Gas hydrate and free gas occurrence

As previously discussed (see **"Downhole logging"** in the "Methods" chapter), the presence of gas hydrate is generally characterized by increases in electrical resistivity and acoustic velocity that are not accompanied by a corresponding decrease in porosity. A decrease in porosity alone in a water-saturated sediment can result in an increase in resistivity and acoustic velocity. Resistivities logged in Holes U1328A and U1328C show a number of positive anomalies over a general increase of resistivity with depth without a corresponding decrease in porosity (Figs. **F57, F58**), suggesting that there are several intervals where gas hydrate may be present.

Water saturations from Archie's equation

To estimate the amount of gas hydrate at Site U1328, we used the Archie relation (e.g., Collett and Ladd, 2000)

$$S_w = [(a \times R_w)/(\phi^m \times R_t)]^{1/n},$$

where

- S_w = water saturation,
- a = tortuosity coefficient,
- R_w = formation water resistivity,
- ϕ = density porosity computed from the adnVISION enhanced resolution bulk density,
- m = cementation coefficient,
- R_t = GeoVISION high-resolution button deep average resistivity, and
- n = saturation coefficient.

We use the button deep resistivity instead of the ring resistivity because the button deep resistivity matches the resistivities with the greatest depth of investigation measured by the LWD EcoScope tool (except for having a higher resolution), whereas the ring resistivity is generally lower than the EcoScope deep resistivities.

Gas hydrate saturation (S_h) is the percentage of pore space in sediment occupied by gas hydrate, which is the complement of the water saturation S_w

$$S_h = 1 - S_w.$$

The procedure followed to estimate S_w with Archie's relation is illustrated in Figure **F64.** We first computed porosity from the density log as described above with a water density ρ_w of 1.03 g/cm³ and a grain/matrix density ρ_g of 2.76 g/cm³ (see **"Physical properties"**).

To estimate the formation water resistivity (R_w), we started by constructing a salinity versus depth function based on the IW salinity measurements (see **"Interstitial water geochemistry"**). This salinity versus depth function consists of three linear segments fitted to the data (0–110, 110–230, and below 230 mbsf) plus a Gaussian peak centered at 12 mbsf that reproduces a shallow high-salinity anomaly. At every logging depth, we combined the salinity value with a formation temperature obtained from the geothermal gradient estimated from the downhole formation temperature measurements (see **"In situ temperature profile"**), and used the formulas of Fofonoff (1985) to obtain the corresponding value of the water resistivity R_w.

To estimate the water saturation S_w, we also need to choose values for the Archie coefficients a and m. One way to do this is to choose a logged interval where the sediments can be assumed to be water saturated and fit a and m to a plot of measured resistivity versus porosity, known as a "Pickett plot" (e.g., Doveton, 1994). In marine sediments, however, the range of porosity is relatively small and it is not possible to obtain a robust estimate of both a and m. We prefer to set $a = 1$, which is physically the most realistic value because it gives a resistivity equal to the formation water resistivity when the porosity is 100%. We then compute a log of "estimated m" given by

$$m_{est} = -\log(F)/\log(\phi),$$

where $F = (R_t/R_w)$ is the formation factor. This m_{est} curve should give the appropriate value to be used in Archie's law in water-saturated intervals and will give anomalously high values in intervals that contain hydrocarbons. A reasonable value of $m = 2.6$ can

be chosen from the baseline trend of the m_{est} curve in Figure F64.

The next step is to compute the resistivity R_0 predicted by Archie's equation for a water-saturated formation of a given porosity, which is given by:

$$R_0 = (a \times R_w)/\phi^m.$$

Using Archie coefficients of a = 1 and m = 2.6, we computed an R_0 curve that generally follows the measured resistivity R_t, but is significantly lower than R_t in several intervals of logging Unit 1 (Fig. F64). Finally, we computed the water saturation S_w using a saturation coefficient n = 2.

The most notable intervals in logging Unit 1 that show a measured resistivity R_t greater than the resistivity R_0 predicted for water-saturated conditions are between the seafloor and 46 mbsf. In the first 15 m below the seafloor, porosities are 75% or higher and the inferred water saturations S_w are as low as 5%. Archie's relation suggests that where the measured resistivities are highest at 0–15 mbsf, most of the formation is composed of gas hydrate, with small amounts of sediment and pore water. These layers of high hydrate concentration alternate with layers of much higher water saturations, which are predicted to contain only small amounts of gas hydrate. Another interval where R_t is greater than the predicted water-saturated resistivity R_0 is at 92–97 mbsf, which is where the LWD resistivity images show a steeply dipping fracture that contains gas hydrate (see **"Logging-while-drilling borehole images"**).

Comparison with infrared images

The IR core images taken on the catwalk measure the core liner temperature, and cold anomalies in the IR images caused by gas hydrate dissociation give an independent "map" of gas hydrate concentrations (see **"Physical properties"**). Figure F65 shows a comparison of the LWD and wireline resistivity logs with the IR image results. There are a number of correlations between temperature anomalies and layers of high resistivity. For example, the IR images show a cold interval at 215–222 mbsf that corresponds to a high-resistivity interval both on the LWD and wireline logs. There is also a 4 Ωm high-resistivity peak at 217 mbsf in the wireline spherically focused resistivity log. This peak is unlikely to correspond to gas hydrate, however, because it is matched by a high-density peak (2.3 g/cm³; Fig. F58). The thin layer at 217 mbsf may be authigenic carbonate, which is occasionally found in gas hydrate–rich intervals (e.g., Medioli et al., 2005).

On the other hand, the layer with high resistivity and low water saturation from Archie's relationship observed in the Hole U1328A LWD logs at 90–98 mbsf is not seen on either the IR images or the wireline logs, both from Hole U1328C. The IR data may have missed this interval because of poor core recovery, but the lack of a high-resistivity layer in the wireline log points to horizontal variation. This is not unexpected, as the high-resistivity layer in the LWD image contains a steeply dipping fracture that is unlikely to be intersected at the same depth by Hole U1328C.

Analysis of sonic logging waveforms

The combined analysis of sonic velocities and waveform amplitudes (Fig. F59) can also help identify the occurrence of gas hydrate and/or free gas. In the interval between 210 and 220 mbsf, where resistivity data show a peak of ~2 Ωm, V_P drops slightly while V_S derived from the upper dipole increases. This could be the result of the coexistence of free gas and gas hydrate in the vicinity of the BSR, which has been observed on the Blake Ridge (Guerin et al., 1999) and Hydrate Ridge (Tréhu, Bohrmann, Rack, Torres, et al., 2003). The presence of gas hydrate increases V_S, whereas V_P is affected by free gas in the pore fluid. The low amplitude of the high-frequency (~2.5 kHz) lower dipole waveforms over most of the interval above ~220 mbsf is similar to data recorded on the Blake Ridge and Hydrate Ridge, and could indicate the particularly strong effect of gas hydrate on shear attenuation in the higher dipole frequency range (Guerin and Goldberg, 2005).

Identification of free gas

The Archie-based analysis of Figure F64 does not show any clear evidence for free gas below the BSR (~219 mbsf) at Site U1328. There are some indications of free gas, however, if we integrate information from the LWD sonic coherence and fluid pressure, and from the wireline V_P, resistivity, density, and neutron logs. Three intervals (219–222, 230–236, and 260–265 mbsf) in the wireline sonic log show a low *P*-wave velocity of ~1500 m/s, and the shallower of these intervals corresponds to a peak of ~2 Ωm in the wireline resistivity (Fig. F58). These two intervals coincide with negative fluid pressure anomalies in the LWD/MWD APWD log, and the shallower interval also displays a significant loss in coherence for the drilling fluid arrivals in the LWD/MWD sonic waveforms (Fig. F56). Moreover, in these two intervals the neutron porosity, which normally is well above the density porosity, decreases and converges to values near those of the density porosity (Fig. F58). This may be a manifestation of "neutron-density crossover," a gas effect well known in logging operations (e.g., Schlumberger, 1989). If the formation contains free gas, its bulk density will de-

crease and the density porosity calculated assuming water is in the pores will increase. At the same time, the porosity measured by the neutron log, which depends on hydrogen density, will decrease because gas has much less hydrogen per unit volume than water. The neutron porosity and the density porosity will cross over and clearly mark the free gas zone.

The evidence for free gas from the wireline logs at 219–222, 230–236, and 260–265 mbsf, however, is not conclusive. Neutron porosity does decrease as predicted by the gas effect, but the density porosity does not show a corresponding increase (Fig. **F58**). The convergence between neutron and density porosity may be caused by a decrease in clay content, which also affects the neutron log. In addition, the low V_P observed in these two intervals coincides with a low V_S, which should not be affected by free gas. Nevertheless, low V_P and V_S have been observed in well-defined, gas-bearing intervals and might be the result of loss of cohesion induced by drilling in a slightly overpressured interval. The most convincing evidence for free gas between 230 and 265 mbsf comes from the LWD drilling fluid pressure and sound velocity (Fig. **F56**).

Vertical seismic profile

Operations

VSP operations in Hole U1328C started with rig up of the WST, which was completed at 0335 h on 15 October 2005. After rig up, the WSTP was lowered in the drill pipe just above the mudline (~1280 mbrf), awaiting daybreak. The first GI air gun shots were fired at 0830 h, 1 h after the start of marine mammal observations, ramping up to the desired operational intensity over 30 min. After a short delay to troubleshoot the air gun triggering, the WSTP was lowered below the mudline at 0952 h, reaching a maximum depth of 1569 mbrf (290 mbsf) at 1009 h.

The first downhole VSP shots were fired at 1016 h, with a plan to try a station every 5 m and move along if there was no success in obtaining good coupling between the tool and the borehole wall. We fired a total of 305 shots and recorded 35 successful stations between 1565 and 1385 mbrf (286 and 106 mbsf), shooting seven times or more at each station for subsequent stacking. Only two 5 m intervals were missed (Table **T25**), where a good coupling could not be achieved because of enlarged borehole conditions (see the caliper log in Fig. **F58**). The ship's heave stayed between 2.5 and 3 m, and did not affect data acquisition. At depths shallower than 1385 mbrf (106 mbsf), the tool still achieved good coupling with the borehole wall, as shown by the tension decrease when the cable was slacked. Nevertheless, noise probably transmitted through the drill pipe (the bit was at 1339 mbrf or 60 mbsf), and/or the cable made it impossible to measure waveforms of acceptable quality. We decided to terminate VSP data acquisition at 1402 h, and brought the WSTP back to the rig floor at 1445 hr. Rig down was completed by 1545 h on 15 October 15.

Time versus depth relationship, interval velocity estimation, and depth to the bottom-simulating reflector

The VSP provides a direct measurement of the time versus depth relationship in the first break of the direct compressional wave arrival. Figure **F66** shows the stacked waveforms at the 35 stations successfully recorded. Stacking was accomplished by taking the median of the seven or more waveforms recorded at each station. The first break times can be easily seen, and are marked by red crosses in Figure **F66.** Table **T25** lists the first break times and the times corrected for the 50 m horizontal offset of the source, the depth of the gun 2 m below sea level, and the delay between triggering and firing. Corrected first break times are traveltimes from the sea surface to each receiver along a vertical path.

The corrected first break times are plotted in Figure **F67** versus the depth of the receivers. The error bars show an uncertainty in the picked first break times of ±1 ms, which combines traveltime errors caused by uncertainties in the depth of the receiver and fluctuations in the vertical source position caused by waves (the latter errors are reduced but not eliminated by stacking). In a medium where the velocity is constant over the vertical range spanned by the receivers, the first break times follow a straight line whose slope gives the velocity. The first break times of Figure **F67** follow a line within the ±1 ms error defining a velocity of 1645 m/s for all receivers between 106 and 286 mbsf. This uniform velocity is in contrast with the results from the Hole U1327D VSP, which clearly showed a high-velocity layer (1843 m/s) above a layer with low velocities characteristic of free gas (1281 m/s), separated by a discontinuity at 245–260 mbsf that defines the location of the BSR (see **"Vertical seismic profile"** in the "Site U1327" chapter). In the Hole U1328C VSP, there is no clear velocity contrast around the expected depth of the BSR (~219 mbsf).

To compare the VSP results to other velocity measurements, it is useful to translate the first break times into interval velocities. In principle, the vertical distance between two receivers divided by the difference between the two first break traveltimes should give an immediate estimate of the interval velocity. In practice, the first break picks are not exact, and small errors in time picking can translate to

large errors in the estimated velocities. A reliable estimate of interval velocity requires an inversion that combines the first break measurements and some smoothness constraint. We use here a Bayesian inversion method where the smoothness of the final solution is determined by the data, whereas the standard deviation of the traveltime measurements is fixed to 1 ms (see above). For method details, see Malinverno and Briggs (2004). The inversion is applied to determine the interval velocity in a layered medium with 5 m thick layers.

The results are shown in Figure **F68,** which compares interval velocities from the VSP in Hole U1328C with *P*-wave velocities from the sonic log in the same hole. In the VSP interval velocity inversion (Fig. **F68A**), the solid line shows the best estimate of compressional wave velocity and the dashed lines show its uncertainty defined by the posterior standard deviation. The posterior standard deviation measures the uncertainty in the estimated velocity caused by uncertainty in the traveltime picks. Figure **F68B** compares the *P*-wave velocities measured in two passes of the DSI tool to the best estimate of *P*-wave velocity from the VSP first breaks. The sonic log and VSP velocities are generally similar, with the VSP measuring a slightly higher velocity than the sonic log between 120 and 155 mbsf. This could be the result of the VSP being affected by velocities farther away from the borehole compared to the shallow depth of investigation of the sonic tool. In any case, both the sonic log and VSP data agree in showing only small *P*-wave velocity variations between 105 and 290 mbsf, and no sign of the sizable 36% velocity decrease associated with free gas at Site U1327.

References

Aldred, W., Cook, J., Bern, P., Carpenter, B., Hutchinson, M., Lovell, J., Rezmer-Cooper, I., and Leder, P.C., 1998. Using downhole annular pressure measurements to improve drilling performance. *Oilfield Rev.,* 10(4):40–55

Bohrmann, G., Greinert, J., Suess, E., and Torres, M., 1998. Authigenic carbonates from the Cascadia subduction zone and their relation to gas hydrate stability. *Geology,* 26:647–650.

Chapman, N.R., Gettrust, J.F., Walia, R., Hannay, D., Spence, G.D., Wood, W.T., and Hyndman, R.D., 2002. High-resolution, deep-towed, multichannel seismic survey of deep-sea gas hydrates off western Canada. *Geophysics,* 67(4):1038–1047. **doi:10.1190/1.1500364**

Collett, T.S., 2000. Quantitative well-log analysis of in-situ natural gas hydrates [Ph.D. dissert.]. Colorado School of Mines, Golden.

Collett, T.S., and Ladd, J., 2000. Detection of gas hydrate with downhole logs and assessment of gas hydrate concentrations (saturations) and gas volumes on the Blake Ridge with electrical resistivity log data. *In* Paull, C.K., Matsumoto, R., Wallace, P.J., and Dillon, W.P. (Eds.), *Proc. ODP, Sci. Results,* 164 [Online]. Available from World Wide Web: **http://www-odp.tamu.edu/publications/164_SR/chap_19/chap_19.htm.**

Collett, T.S., Riedel, M., Malone, M.J., and the Expedition 311 Project Team, 2005. Cascadia margin hydrates. *IODP Sci. Prosp.,* 311. **doi:10.2204/iodp.sp.311.2005**

Davis, E.E., Hyndman, R.D., and Villinger, H., 1990. Rates of fluid expulsion across the northern Cascadia accretionary prism: constraints from new heat flow and multichannel seismic reflection data. *J. Geophys. Res.,* 95:8869–8889.

Doveton, J.H., 1994. Geologic log analysis using computer methods. *AAPG Comp. Appl. Geol.,* 2:169.

Edwards, R.N., 1997. On the resource evaluation of marine gas hydrate deposits using sea-floor transient electric dipole-dipole method. *Geophysics,* 62:63–74. **doi:10.1190/1.1444146**

Fofonoff, N.P., 1985. Physical properties of seawater: a new salinity scale and equation of state for seawater. *J. Geophys. Res.,* 90:3332–3342.

Guerin, G., and Goldberg, D., 2005. Modeling of acoustic wave dissipation in gas hydrate–bearing sediments. *Geochem., Geophys., Geosyst.,* 6. **doi:10.1029/2005GC000918**

Guerin, G., Goldberg, D., and Meltser, A., 1999. Characterization of in situ elastic properties of gas-hydrate bearing sediments on the Blake Ridge. *J. Geophys. Res.,* 104:17781–17796. **doi:10.1029/1999JB900127**

Hyndman, R.D., Yuan, T., and Moran, K., 1999. The concentration of deep sea gas hydrates from downhole electrical resistivity logs and laboratory data. *Earth Planet. Sci. Lett.,* 172:167–177. **doi:10.1016/S0012-821X(99)00192-2**

Lowe, C., Enkin, R.J., Baker, J., and Dallimore, S.R., 2005. Investigation of airborne magnetic data and magnetic properties of cored rocks from the Mallik gas hydrate field. *In* Dallimore, S.R., and Collett, T.S. (Eds.), *Scientific Results from the Mallik 2002 Gas Hydrate Production Research Well Program, Mackenzie Delta, Northwest Territories, Canada.* Bull.—Geol. Surv. Can., 585.

Lu, H., Moudrakovski, I., Riedel, M., Spence, G., Dutrisac, R., Ripmeester, J., Wright, F., and Dallimore, S., 2005. Occurrences and structural characterizations of gas hydrates associated with a cold vent field, offshore Vancouver Island. *J. Geophys. Res.,* 110(B10):B10204. **doi:10.1029/2005JB003900**

Malinverno, A., and Briggs, V.A., 2004. Expanded uncertainty quantification in inverse problems: hierarchical bayes and empirical bayes. *Geophysics,* 69:100–1016. **doi:10.1190/1.1778243**

Medioli, B.E., Wilson, N., Dallimore, S.R., Paré, D., Brennan-Alpert, P., and Oda, H., 2005. Sedimentology of the cored interval, JAPEX/JNOC/GSC et al. Mallik 5L-38 gas hydrate production research well. *In* Dallimore, S.R., and Collett, T.S. (Eds.), *Scientific Results from the Mallik 2002 Gas Hydrate Production Research Well Program, Mackenzie Delta, Northwest Territories, Canada.* Bull.—Geol. Surv. Can., 585.

Milkov, A.V., Claypool, G.E., Lee, Y.-J., and Sassen, R., 2005. Gas hydrate systems at Hydrate Ridge offshore Oregon inferred from molecular and isotopic properties of gas hydrate-bound and void gases. *Geochim. Cosmochim. Acta,* 69(4):1007–1026. **doi:10.1016/j.gca.2004.08.021**

Novosel, I., 2002. Physical properties of gas hydrate related sediments, offshore Vancouver Island [M.Sc. Thesis]. Univ. Victoria, Canada.

Novosel, I., Spence, G.D., and Hyndman, R.D., 2005. Reduced magnetization produced by increased methane flux at a gas hydrate vent. *Mar. Geol.,* 216:265–274. **doi:10.1016/j.margeo.2005.02.027**

Pimmel, A., and Claypool, G., 2001. Introduction to shipboard organic geochemistry on the *JOIDES Resolution. ODP Tech. Note,* 30 [Online]. Available from World Wide Web: **http://www-odp.tamu.edu/publications/tnotes/tn30/INDEX.HTM.**

Riedel, M., 2001. 3D seismic investigations of northern Cascadia marine gas hydrates [Ph.D. dissert.]. Univ. Victoria, Canada.

Riedel, M., Novosel, I., Spence, G.D., Hyndman, R.D., Chapman, N.R., and Lewis, T., 2006. Geophysical and geochemical signatures associated with gas hydrate–related venting in the northern Cascadia margin. *Geol. Soc. Am. Bull.,* 118:23–38. **doi:10.1130/B25720.1**

Riedel, M., Spence, G.D., Chapman, N.R., and Hyndman, R.D., 2001. Deep sea gas hydrates on the northern Cascadia margin. *The Leading Edge,* 20(1):87–91.

Riedel, M., Spence, G.D., Chapman, N.R., and Hyndman, R.D., 2002. Seismic investigations of a vent field associated with gas hydrates, offshore Vancouver Island. *J. Geophys. Res.,* 107(B9):2200. **doi:10.1029/2001JB000269**

Schlumberger, 1989. *Log Interpretation Principles/Applications:* Houston (Schlumberger Educ. Services), SMP–7017.

Schwalenberg, K., Willoughby, E.C., Mir, R., and Edwards, R.N., 2005. Marine gas hydrate signatures in Cascadia and their correlation with seismic blank zones. *First Break,* 23:57–63.

Sloan, E.D., 1998. *Clathrate Hydrates of Natural Gases* (2nd ed.): New York (Marcel Dekker).

Solem, R.C., Spence, G.D., Vukajlovich, D., Hyndman, R.D., Riedel, M., Novosel, I., and Kastner, M., 2002. Methane advection and gas hydrate formation within an active vent field offshore Vancouver Island. *Fourth Int. Conf. Gas Hydrates,* 19023.

Teichert, B.M.A., Gussone, N., Eisenhauer, A., and Bohrmann, G., 2005. Clathrites: archives of near-seafloor pore-fluid evolution ($\delta^{44/40}$Ca, δ^{13}C, δ^{18}O) in gas hydrate environments. *Geology,* 33:213–216. **doi:10.1130/G21317.1**

Tréhu, A.M, Bohrmann, G., Rack, F.R., Torres, M.E., et al., 2003. *Proc. ODP, Init. Repts.,* 204 [Online]. Available from World Wide Web: **http://www-odp.tamu.edu/publications/204_IR/204ir.htm.**

Tréhu, A.M., Long, P.E., Torres, M.E., Bohrmann, G., Rack, F.R., Collett, T.S., Goldberg, D.S., Milkov, A.V., Riedel, M., Schultheiss, P., Bangs, N.L., Barr, S.R., Borowski, W.S., Claypool, G.E., Delwiche, M.E., Dickens, G.R., Gracia, E., Guerin, G., Holland, M., Johnson, J.E., Lee, Y.-J., Liu, C.-S., Su, X., Teichert, B., Tomaru, H., Vanneste, M., Watanabe, M., and Weinberger, J.L., 2004. Three-dimensional distribution of gas hydrate beneath southern Hydrate Ridge: constraints from ODP Leg 204. *Earth Planet. Sci. Lett.,* 222:845–862. **doi:10.1016/j.epsl.2004.03.035**

Ussler, W., III, Paull, C.K., McGill, P., Schroeder, D., and Ferrell, D., 2006. A test of the temperature, pressure, and conductivity tool prototype at Hydrate Ridge. *In* Tréhu, A.M., Bohrmann, G., Torres, M.E., and Colwell, F.S. (Eds.), *Proc. ODP, Sci. Results,* 204 [Online]. Available from World Wide Web: **http://www-odp.tamu.edu/publications/204_SR/112/112.htm.**

Westbrook, G.K., Carson, B., Musgrave, R.J., et al., 1994. *Proc. ODP, Init. Repts.,* 146 (Pt. 1): College Station, TX (Ocean Drilling Program).

Willoughby, E.C., and Edwards, R.N., 2000. Shear velocities in Cascadia from seafloor compliance measurements. *Geophys. Res. Lett.,* 27:1021–1024. **doi:10.1029/1999GL010481**

Willoughby, E.C., Schwalenberg, K., Edwards, R.N., Spence, G.D., and Hyndman, R.D., 2005. Assessment of marine gas hydrate deposits: a comparative study of seismic, electromagnetic and seafloor compliance methods. *Fifth Int. Conf. Gas Hydrates,* 3:802–811.

Wood, W.T., Gettrust, J.F., Chapman, N.R., Spence, G.D., and Hyndman, R.D., 2002. Decreased stability of methane hydrates in marine sediments owing to phase-boundary roughness. *Nature (London, U. K.),* 420:656–660. **doi:10.1038/nature01263**

Wood, W.T., Lindwall, D.A., Gettrust, J.F., Sekharan, K.K., and Golden, B., 2000. Constraints on gas or gas hydrate related wipeouts in seismic data through the use of physical models. *Eos, Trans., Am. Geophys. Union,* 81(48):F639.

Xu, W., 2002. Phase balance and dynamic equilibrium during formation and dissociation of methane gas hydrate. *Fourth Int. Conf. Gas Hydrates:* 19023:199–200.

Xu, W., 2004. Modeling dynamic marine gas hydrate systems. *Am. Mineral.,* 89:1271–1279.

Yuan, J., and Edwards, R.N., 2000. The assessment of marine gas hydrates through electrical remove sounding: hydrate without a BSR?, *Geophys. Res. Lett.,* 27:2397–2400. **doi:10.1029/2000GL011585**

Zühlsdorff, L., and Spiess, V., 2004. Three-dimensional seismic characterization of a venting site reveals compelling indications of natural hydraulic fracturing. *Geology,* 32(2):101–104. **doi:10.1130/G19993.1**

Publication: 28 October 2006
MS 311-106

Figure F1. (**A**) 3.5 kHz subbottom profiler data and (**B**) multichannel seismic (MCS) data along Inline 27 of the 1999 3-D survey. Note distinct seafloor expression at blank Zone 1 and strong edge–diffractions from the boundaries of the blank zones (from Riedel, 2001). BSR = bottom-simulating reflector, B.Z. = blank zone, CDP = common depth point.

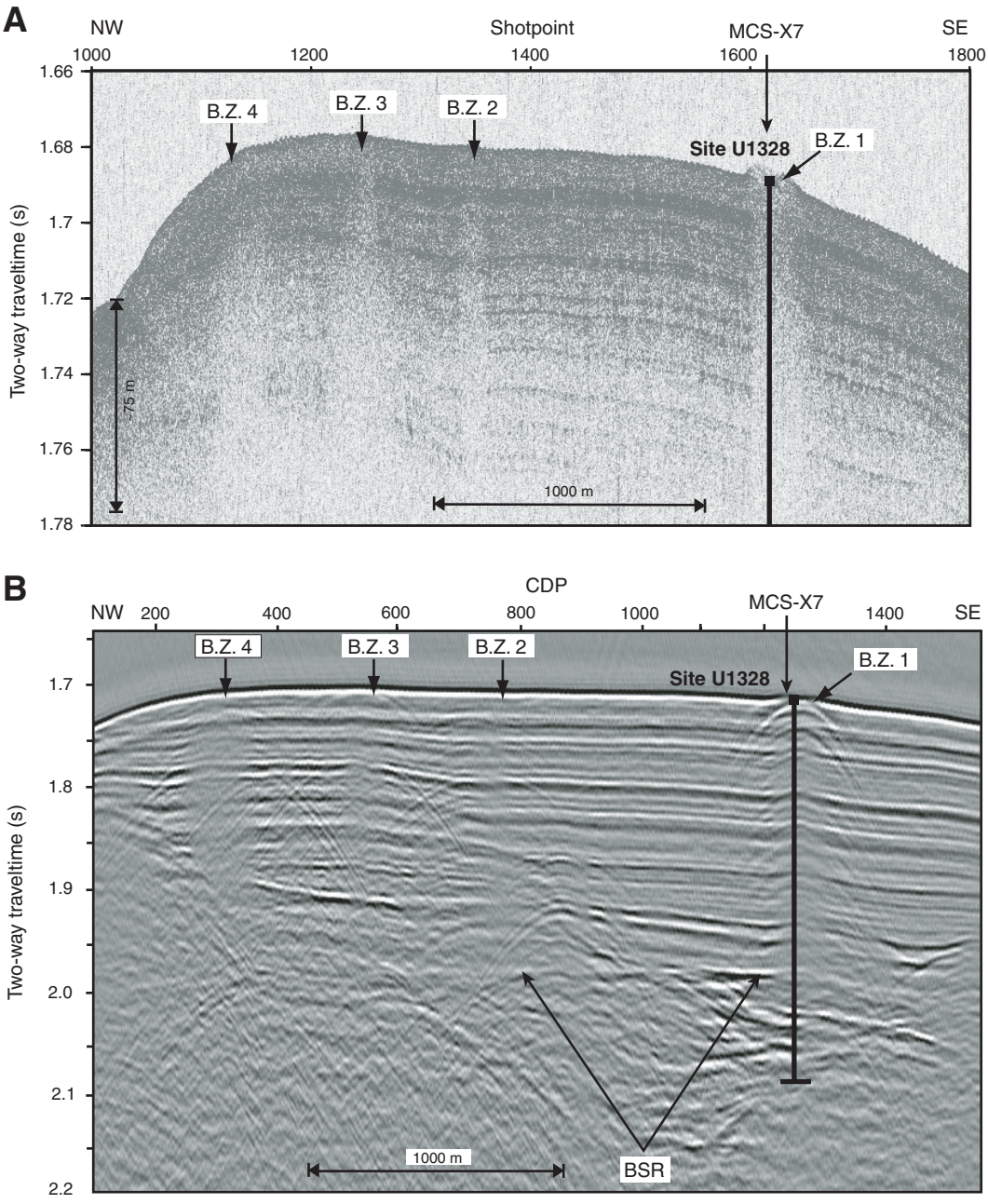

Figure F2. (**A**) 3.5 kHz subbottom profiler data along Inline 16 of the 2000 3-D single-channel seismic survey and (**B**) multichannel seismic Line XL07 of the 1999 survey (from Riedel, 2001). BSR = bottom-simulating reflector, CDP = common depth point, V.E. = vertical exaggeration.

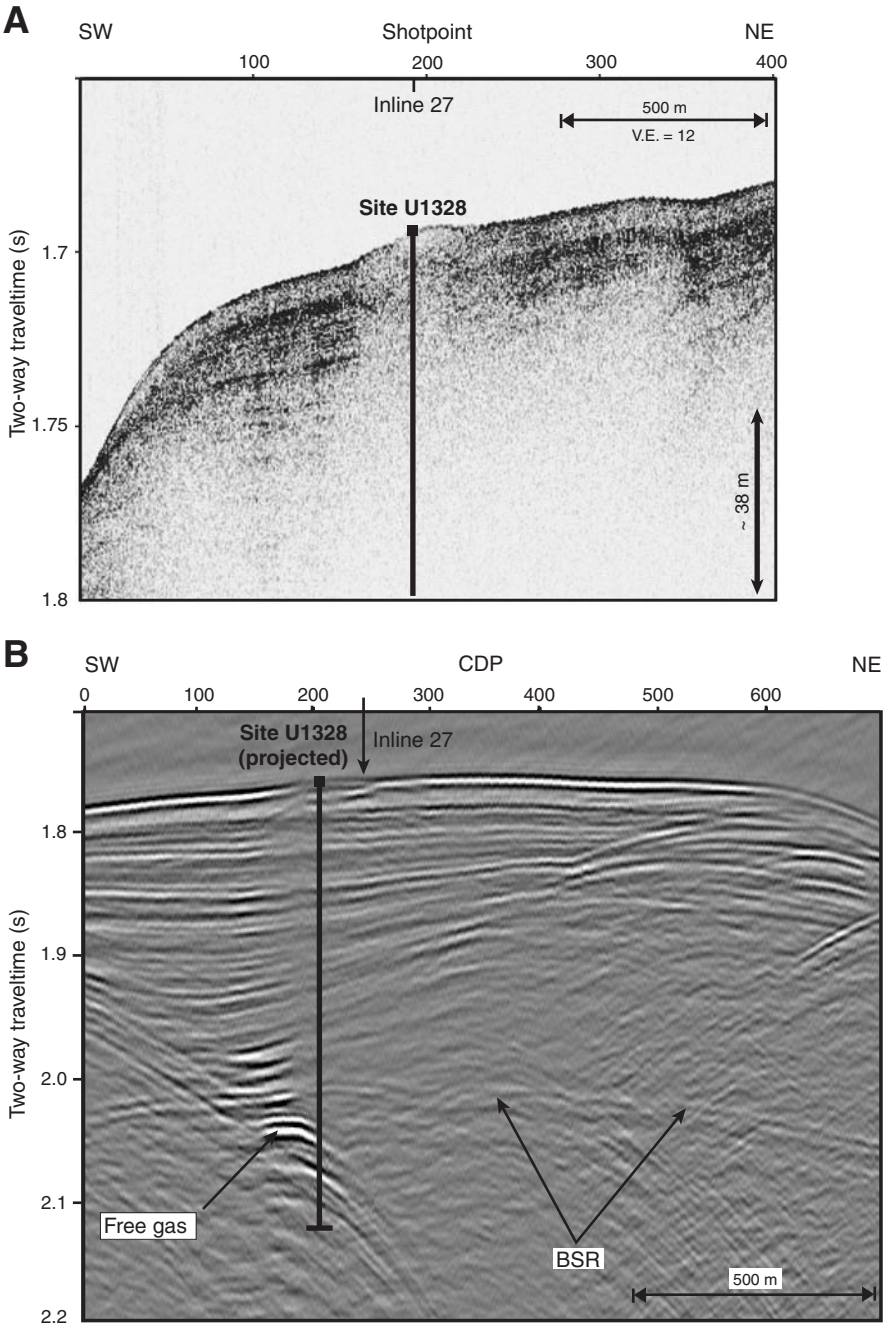

Figure F3. A. Bottom-simulating reflector (BSR) reflection coefficient determined from the 1999 3-D multichannel seismic survey. **B.** Interpreted seismostratigraphic boundary between accreted and slope basin sediments showing the coincidence of the BSR bright spot near Site U1328 and a trough in the boundary.

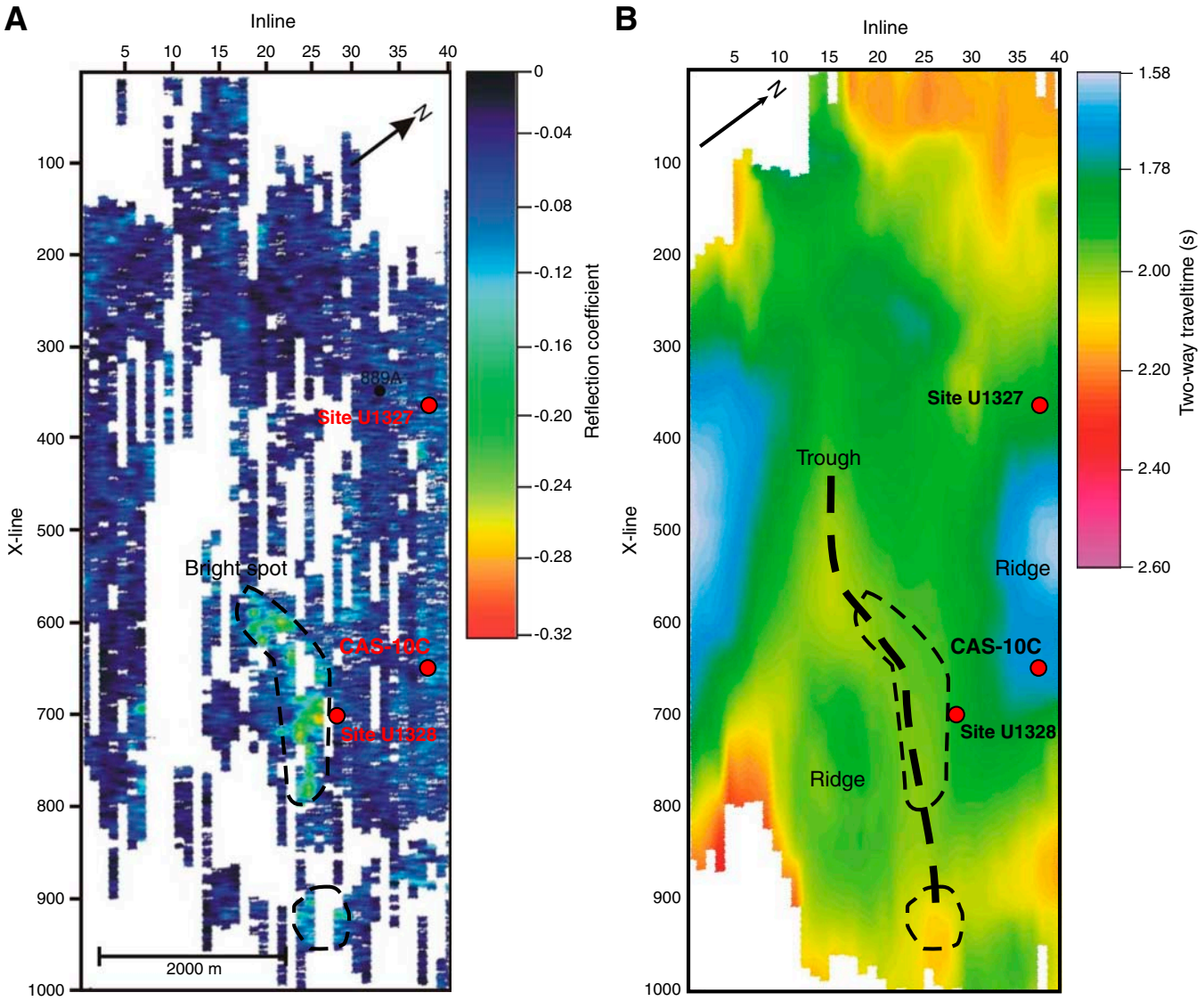

Figure F4. Time slices of seismic reflection and instantaneous amplitude from the 1999 3-D single-channel seismic survey showing an apparent east–west trend in blank zones. The edges of blank zones appear as bright reflections, as a result of diffractions. Blank Zone 1 (Bullseye vent) appears as a circular feature (after Riedel et al., 2001). msbsf = milliseconds below seafloor.

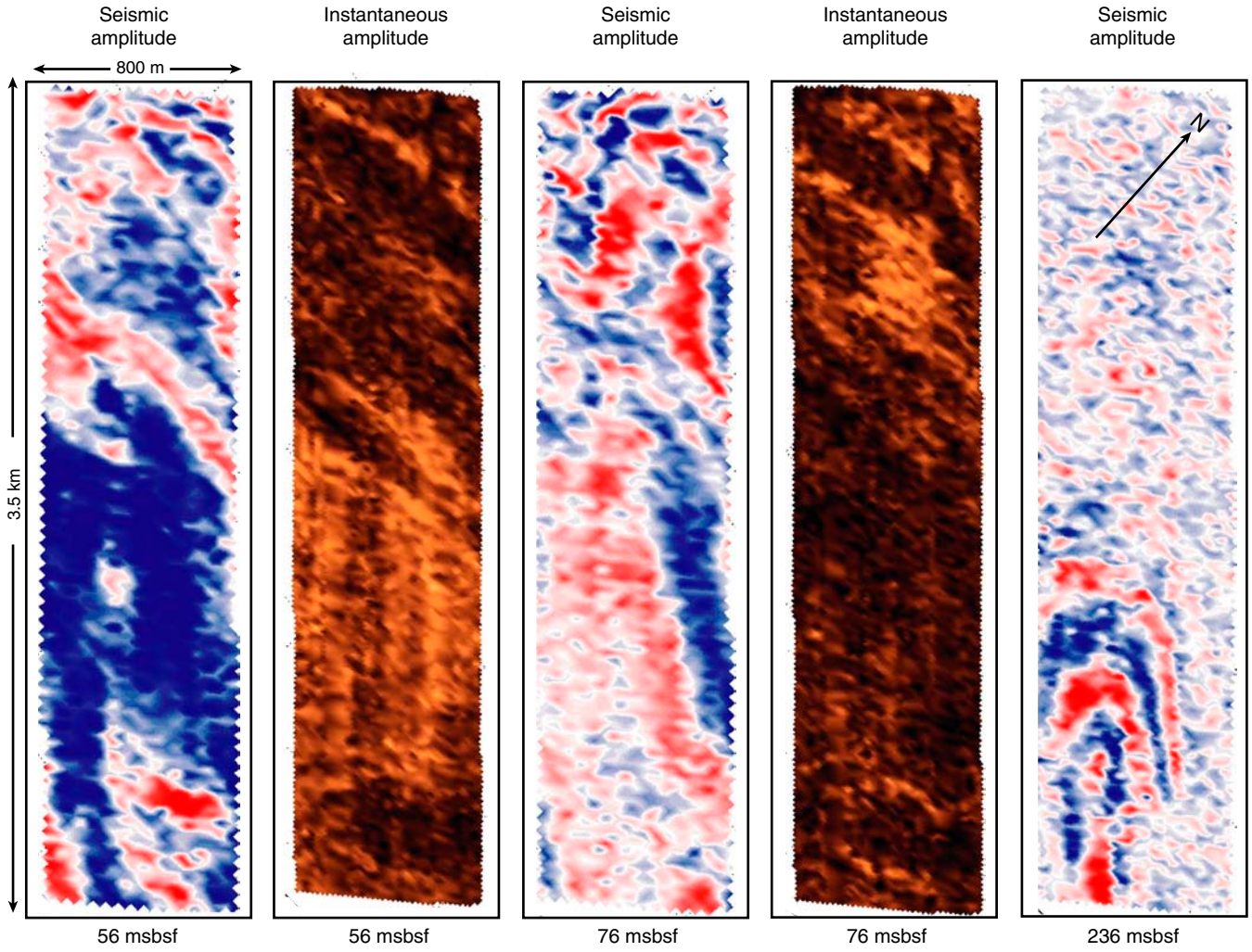

Figure F5. Time slices of instantaneous amplitude from unprocessed 2000 3-D single-channel seismic survey data showing ring structures that are the result of diffraction at shallow gas hydrate cap (after Riedel et al., 2002).

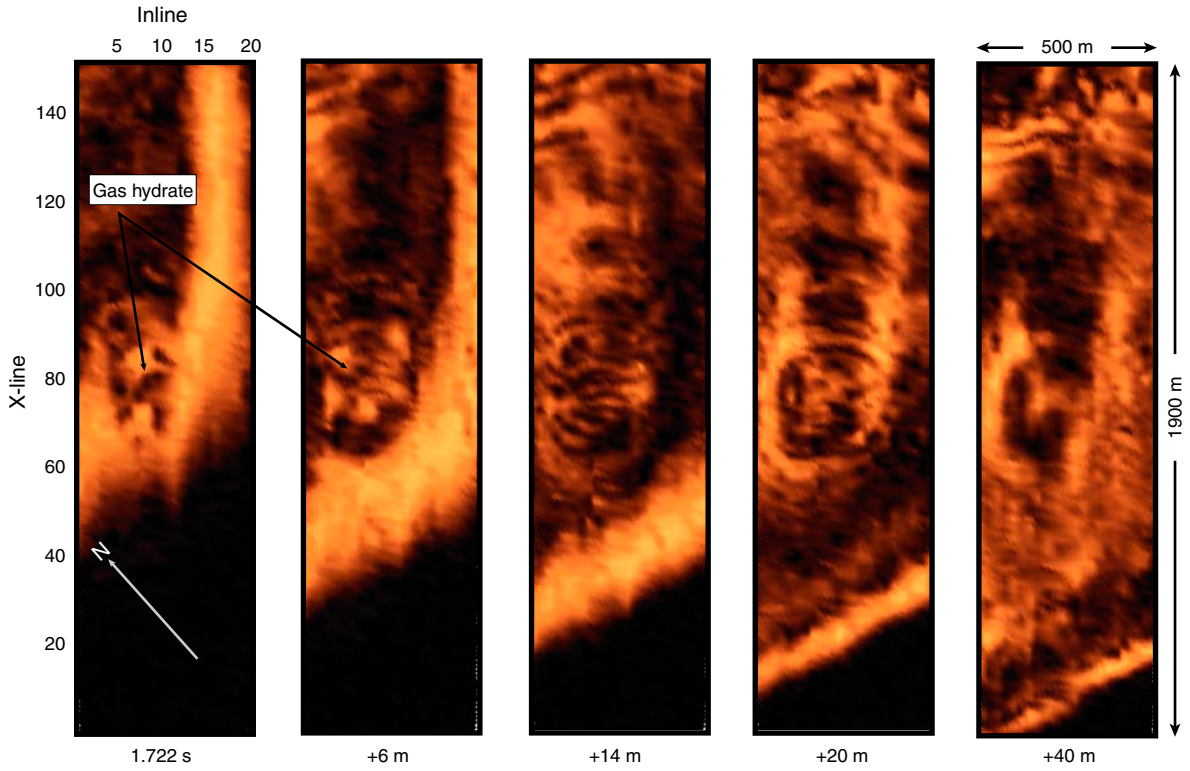

Figure F6. A. Time slice of instantaneous amplitude at 1.755 two-way traveltime superimposed on depths to the top of gas hydrate and various core locations. Axes are universal transverse Mercator (UTM) projection easting and northing coordinates using the WGS-84 reference. CTD = conductivity-temperature-depth, MCS = multi-channel seismic. **B.** Seismic section identifying the top of the gas hydrate occurrence at Bullseye vent as a cap reflector (after Riedel et al., 2006). XL = cross line.

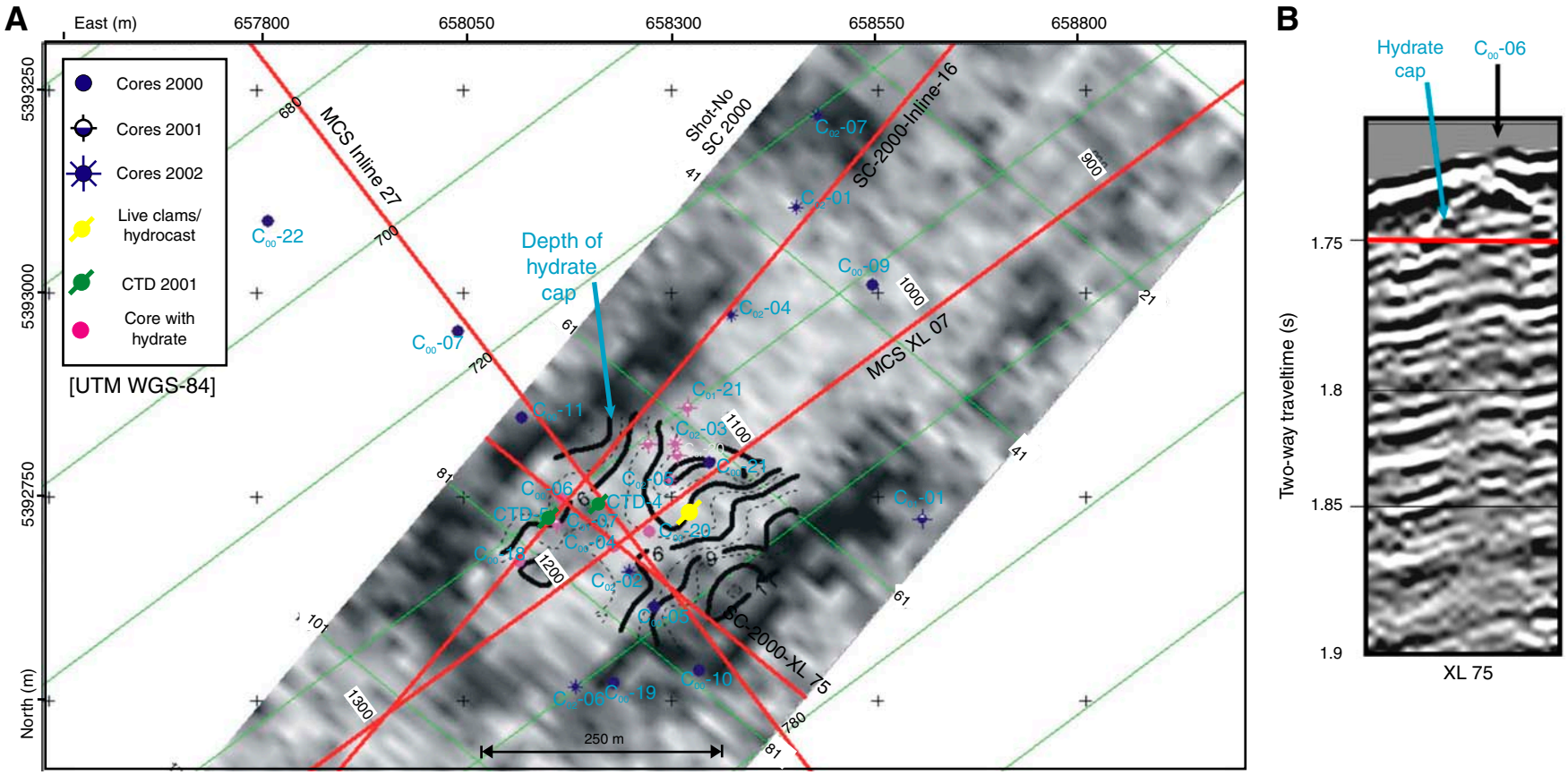

Figure F7. (**A, B, C, D**) Examples of carbonate outcrops, (**E, F**) blank Zone 3, and (**G, H**) chemosynthetic communities at Bullseye vent (from Riedel, 2001).

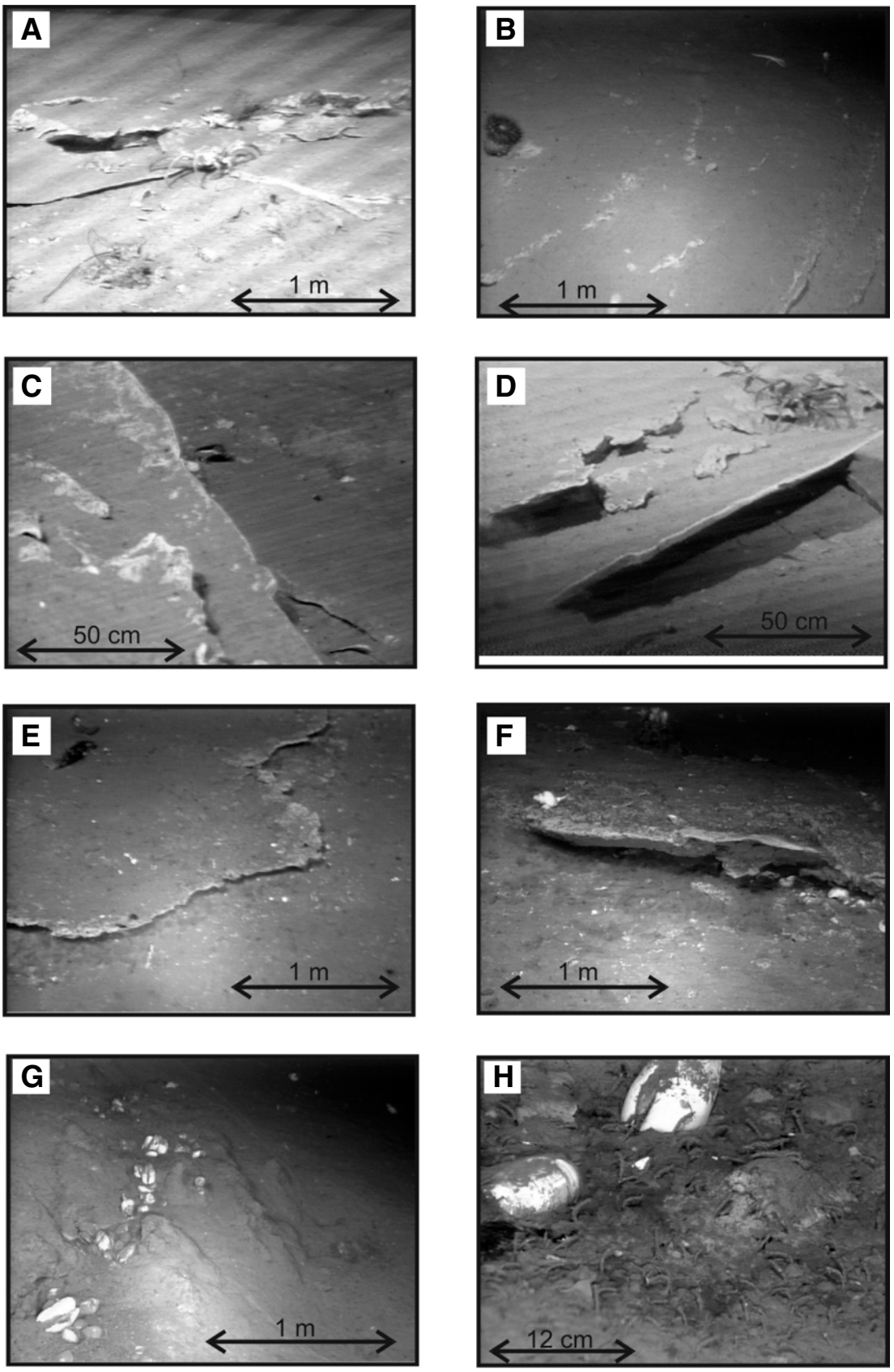

Figure F8. A. Normalized seafloor compliance data. 1-D = one-dimensional, 3-D = three-dimensional. **B.** Coherence of frequency data. **C.** Inferred shear wave velocity profile at Bullseye vent (from Willoughby et al., 2005).

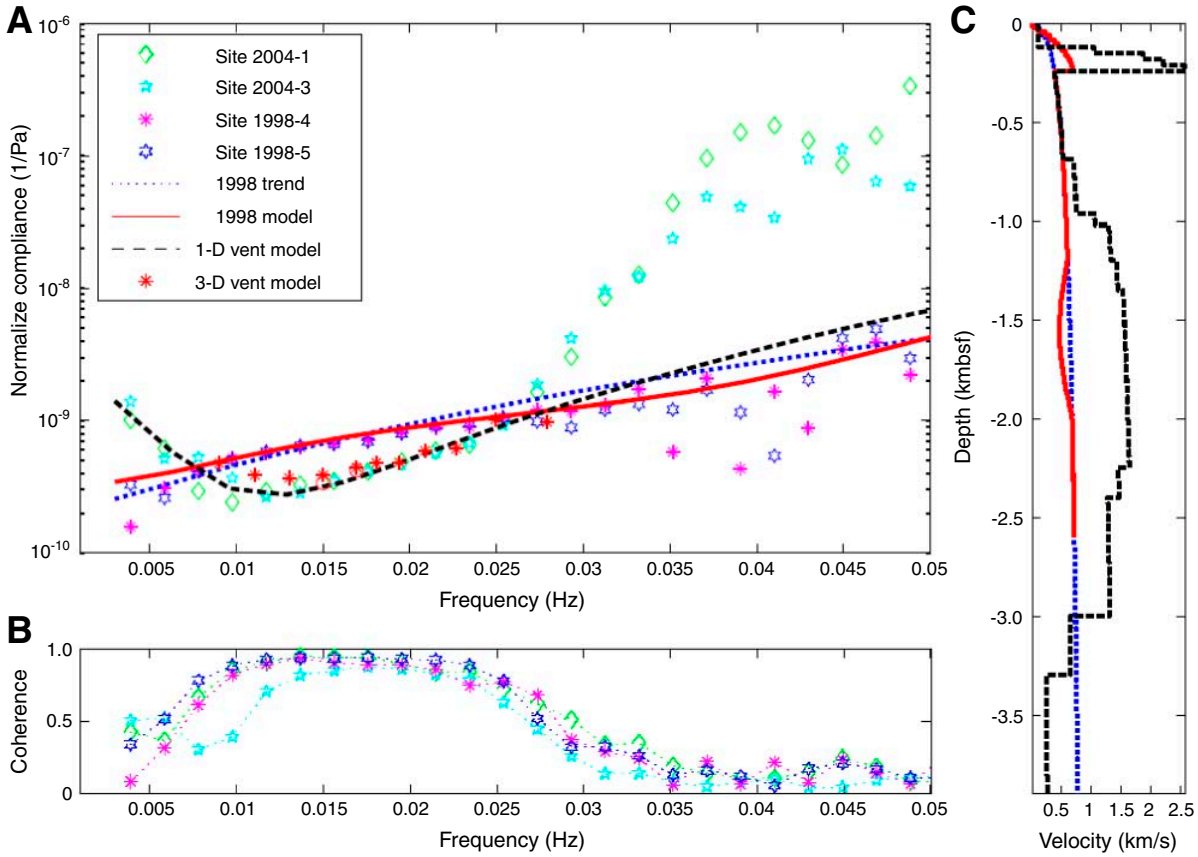

Figure F9. Profile of (**A**) electrical resistivity and (**B**) inferred gas hydrate concentration along a profile across the cold vent field (from Schwalenberg et al., 2005). Blank zones are denoted by the numbered ovals.

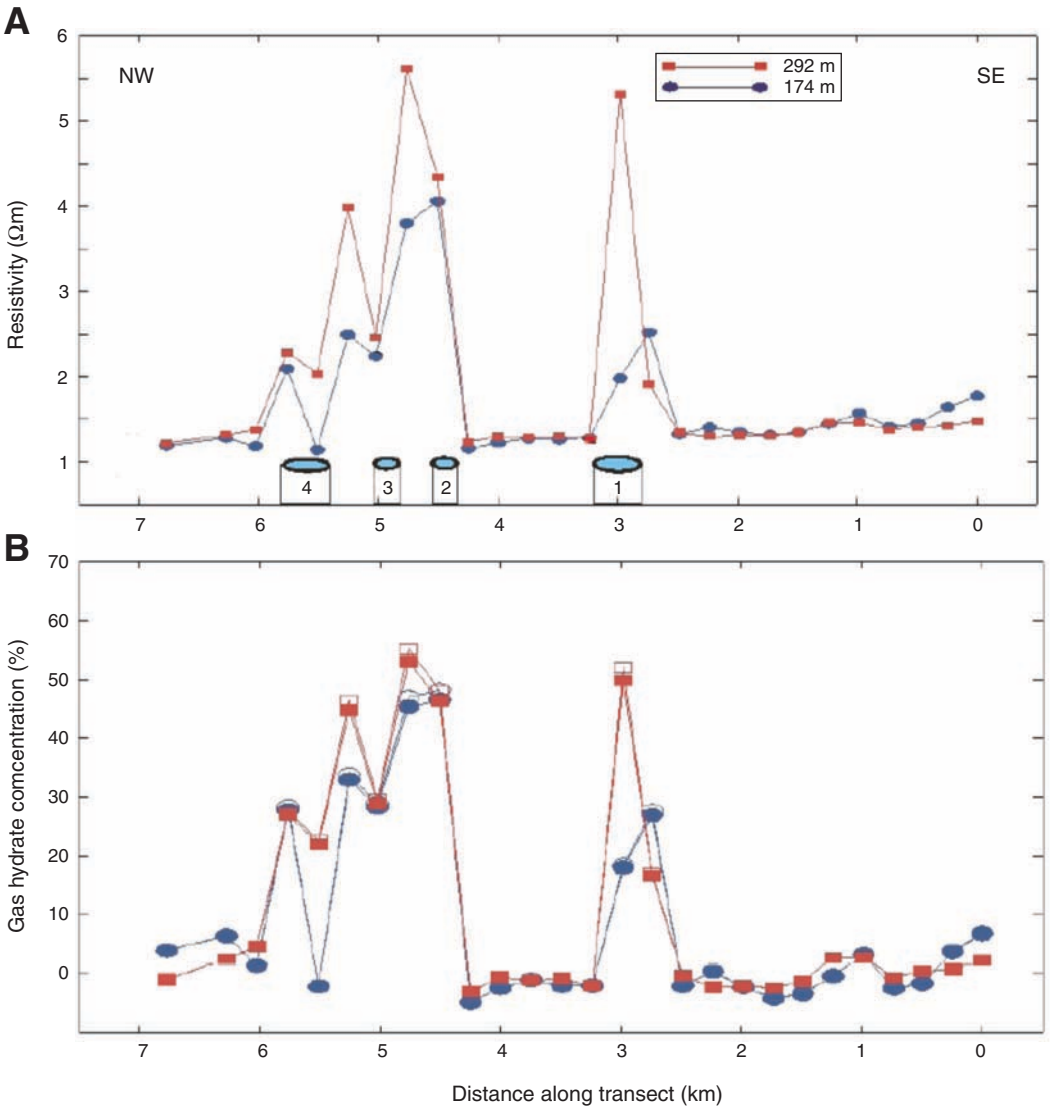

Figure F10. Location holes drilled at Site U1328 showing track lines with seismic survey shotpoints. Axes are universal transverse Mercator (UTM) projection easting and northing coordinates using the WGS-84 reference. MCS = multichannel seismic.

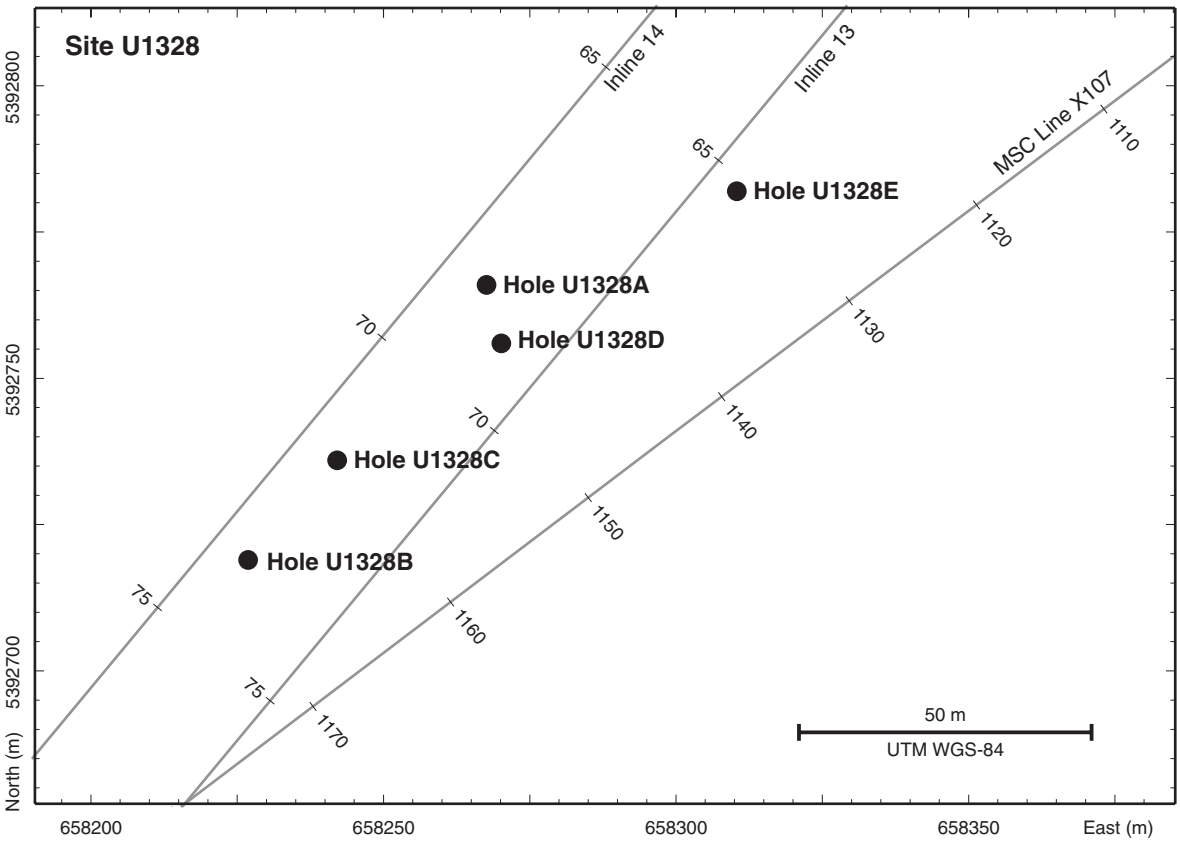

Figure F11. Lithostratigraphic summary for Holes U1328B (solid circles) and U1328C (solid squares) showing the percentage of clay, silt, sand, biogenic opal (diatoms, radiolarians, siliceous spicules, silicoflagellates), foraminifers, and nannofossils in the major lithology; clay, silt, and sand in the minor lithology; and AMST color reflectance (a*).

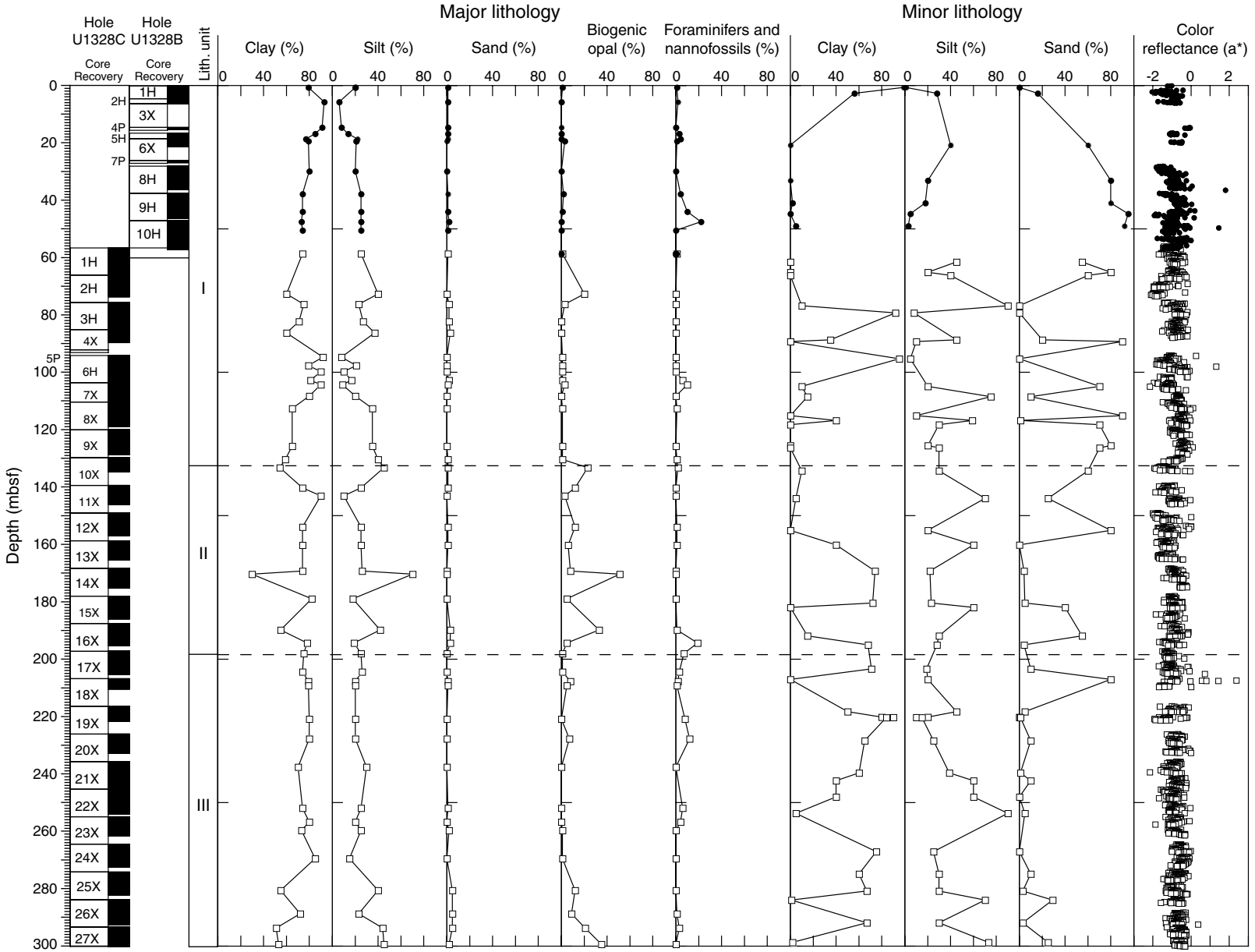

Figure F12. Dark gray silty clay with multiple sand layers showing fining-upward sequences in lithostratigraphic Unit I (interval 311-U1328B-9H-3, 55–75 cm).

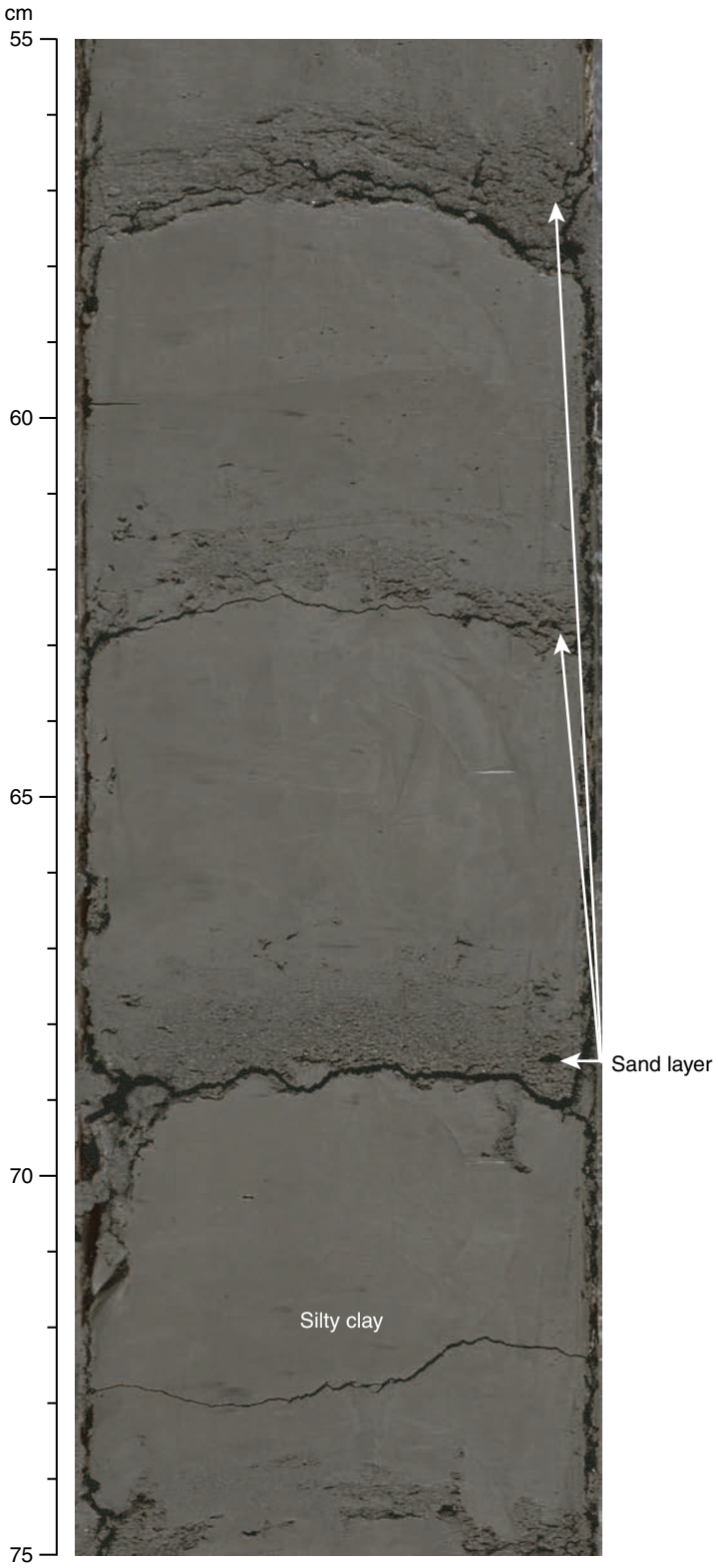

Figure F13. Dark gray silty clay with multiple, thin interlayers of sand in lithostratigraphic Unit I (interval 311-U1328C-9X-7, 35–55 cm).

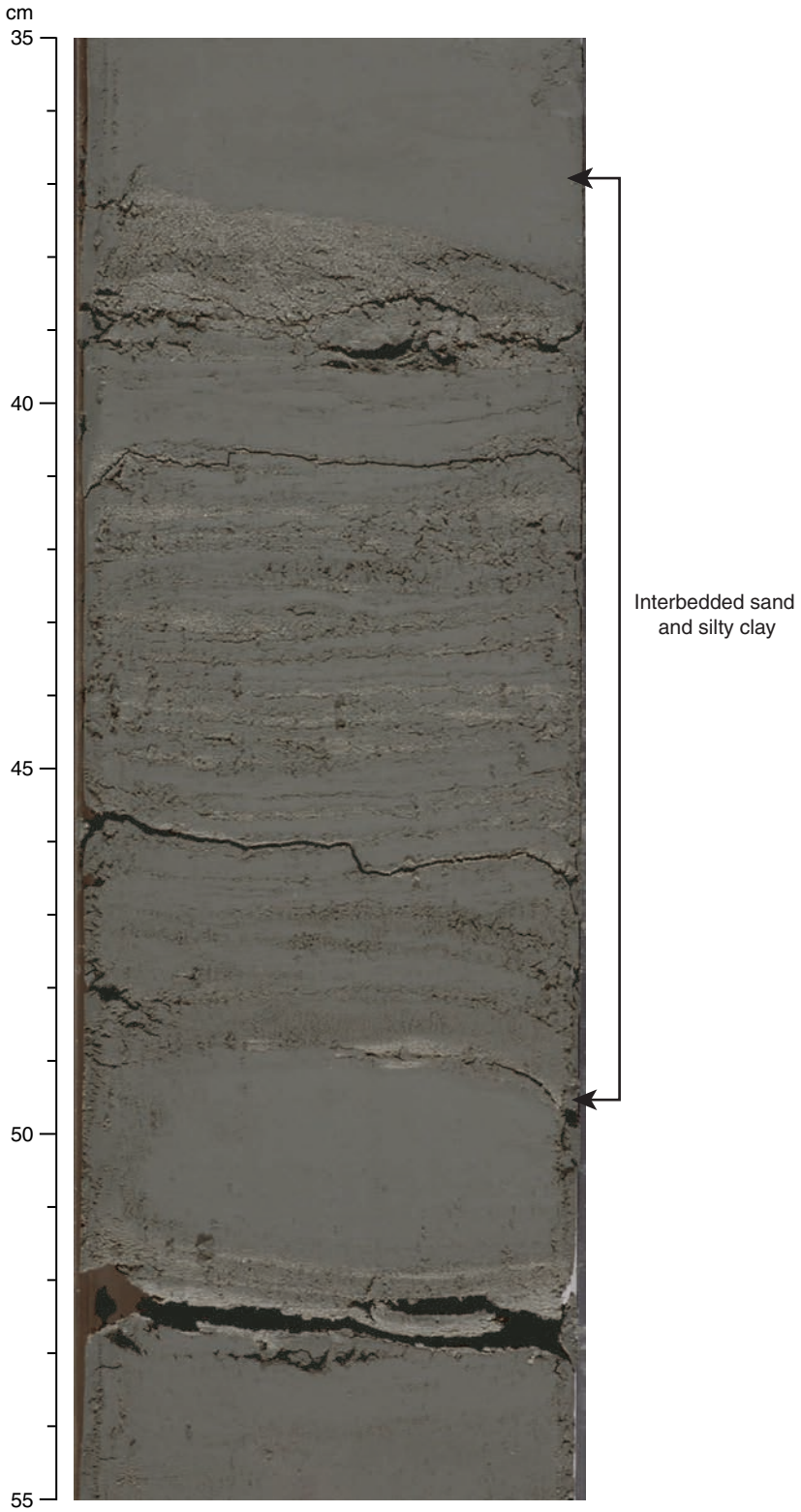

Figure F14. Dark greenish gray silty clay with a 1 cm thick, light colored volcanic ash layer in lithostratigraphic Unit I (interval 311-U1328B-9H-5, 138–150 cm).

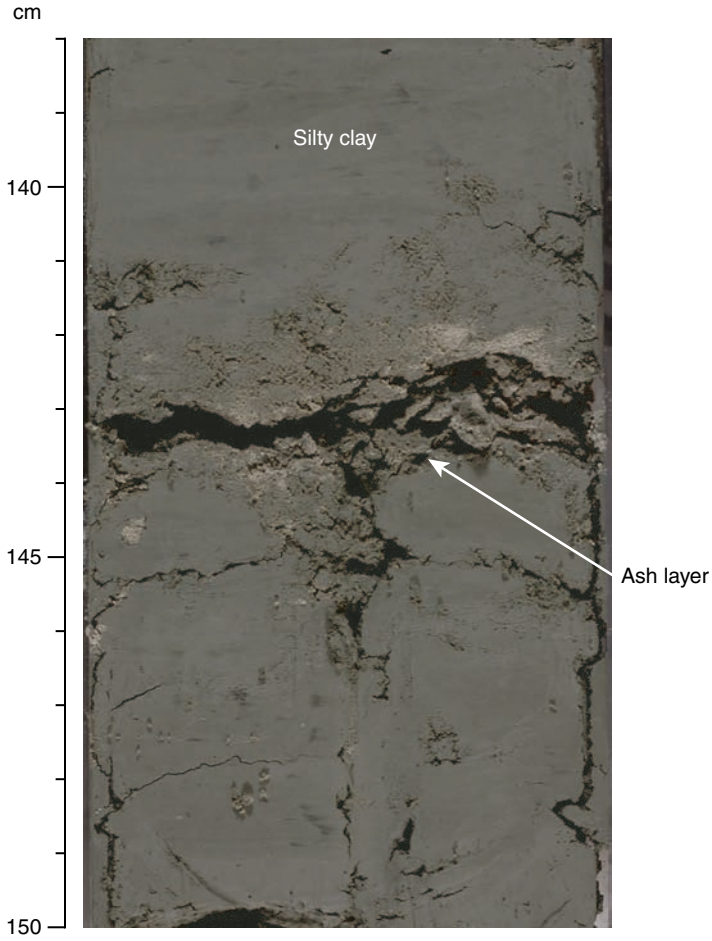

Figure F15. XRD record from the volcanic ash layer in lithostratigraphic Unit I (Sample **311-U1328B-9H-5, 142–143 cm**) showing the typical bulge from amorphous silica.

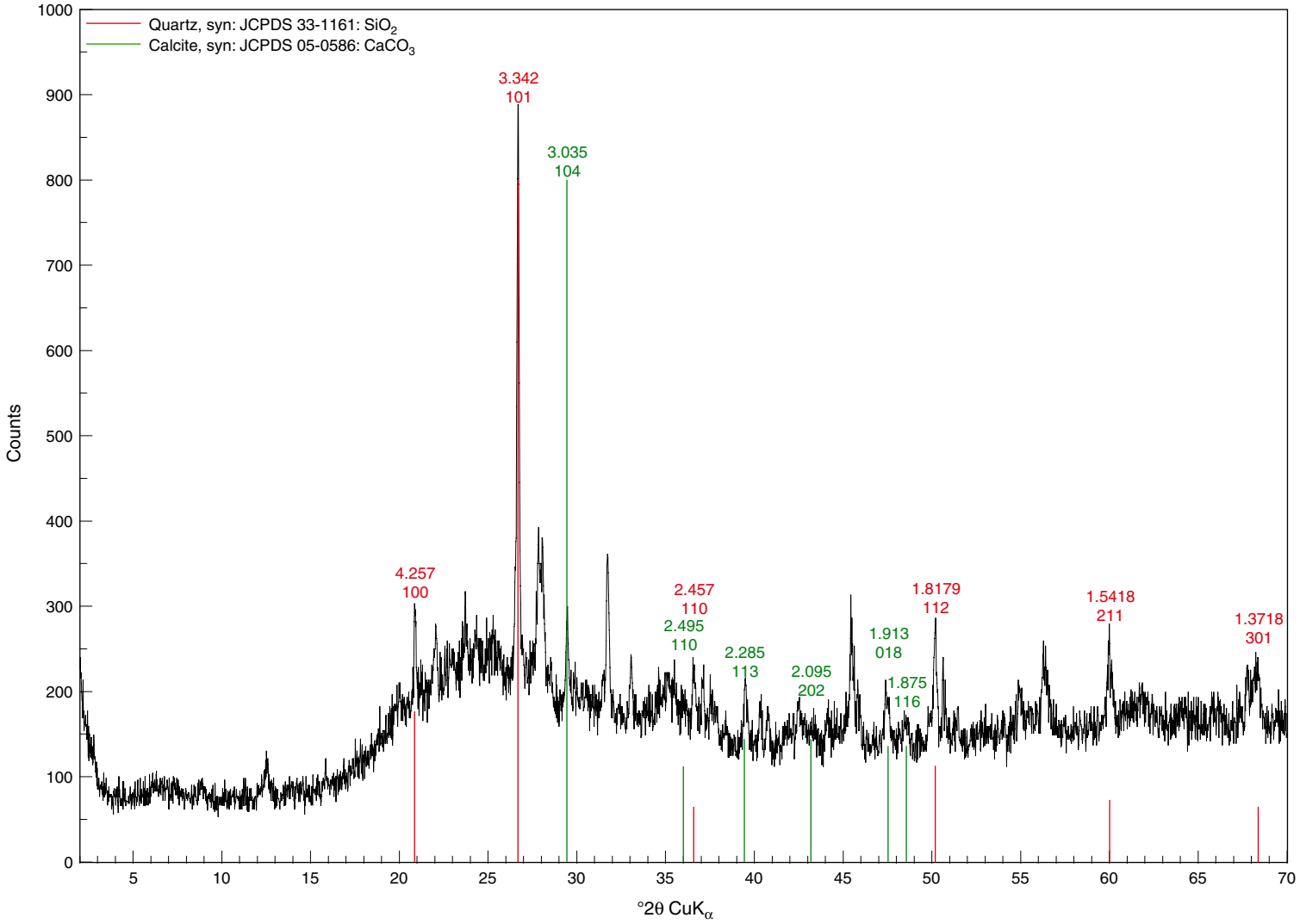

Figure F16. A. Bivalve shell (interval 311-U1328E-9X-3, 25–46 cm) and abundant sulfide mottling and bioturbation structures. This photograph is from the digital imaging system and was taken right after splitting and scraping the core. **B.** Same interval as in (A) one day later. The core was accidentally not scraped before the photograph was taken. The comparison shows clearly that sulfide structures fade very quickly.

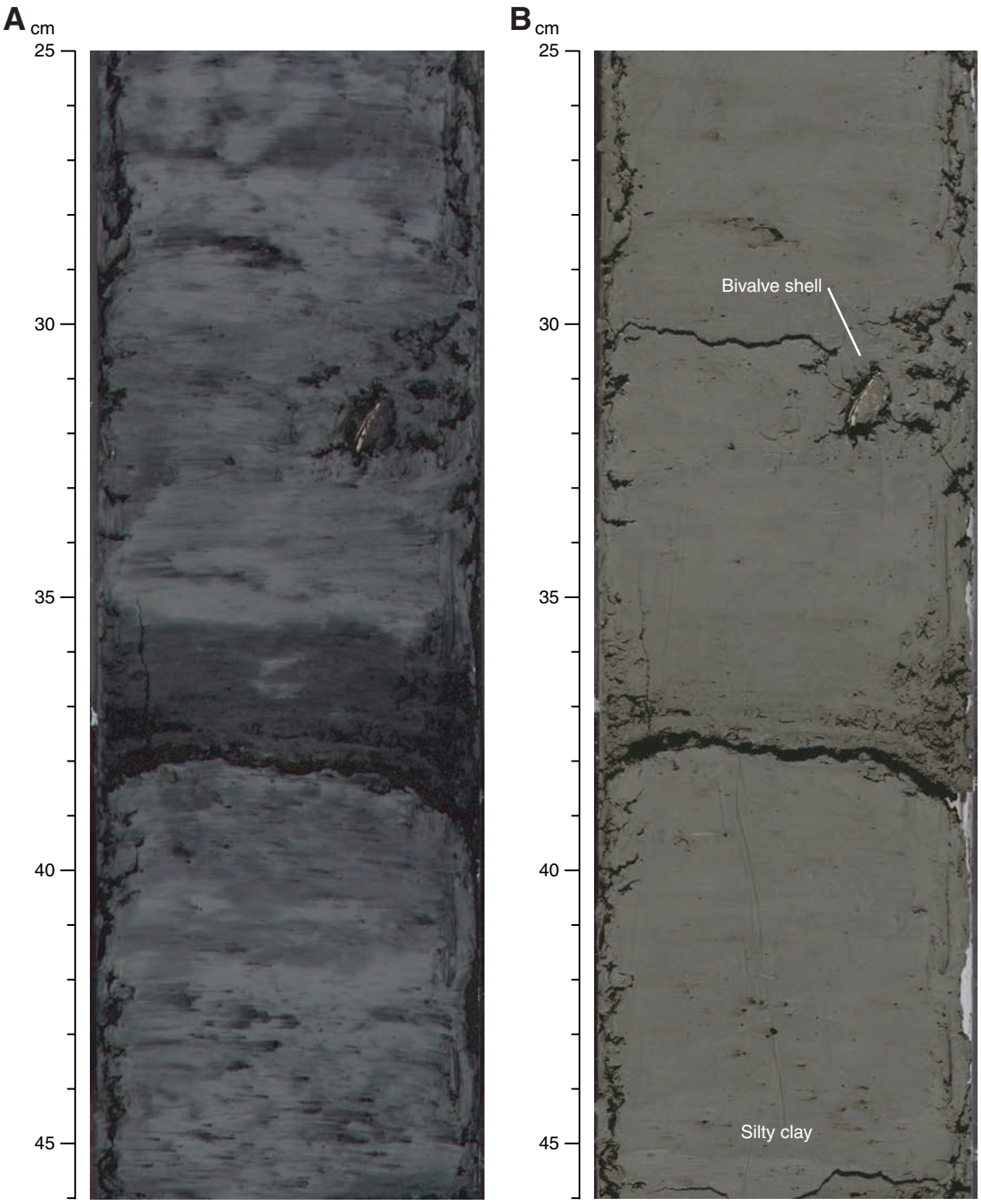

Figure F17. Soupy sediment texture in dark greenish gray clay with pieces of irregularly shaped lithified authigenic carbonates in lithostratigraphic Unit I (interval 311-U1328B-6X-1, 20–50 cm).

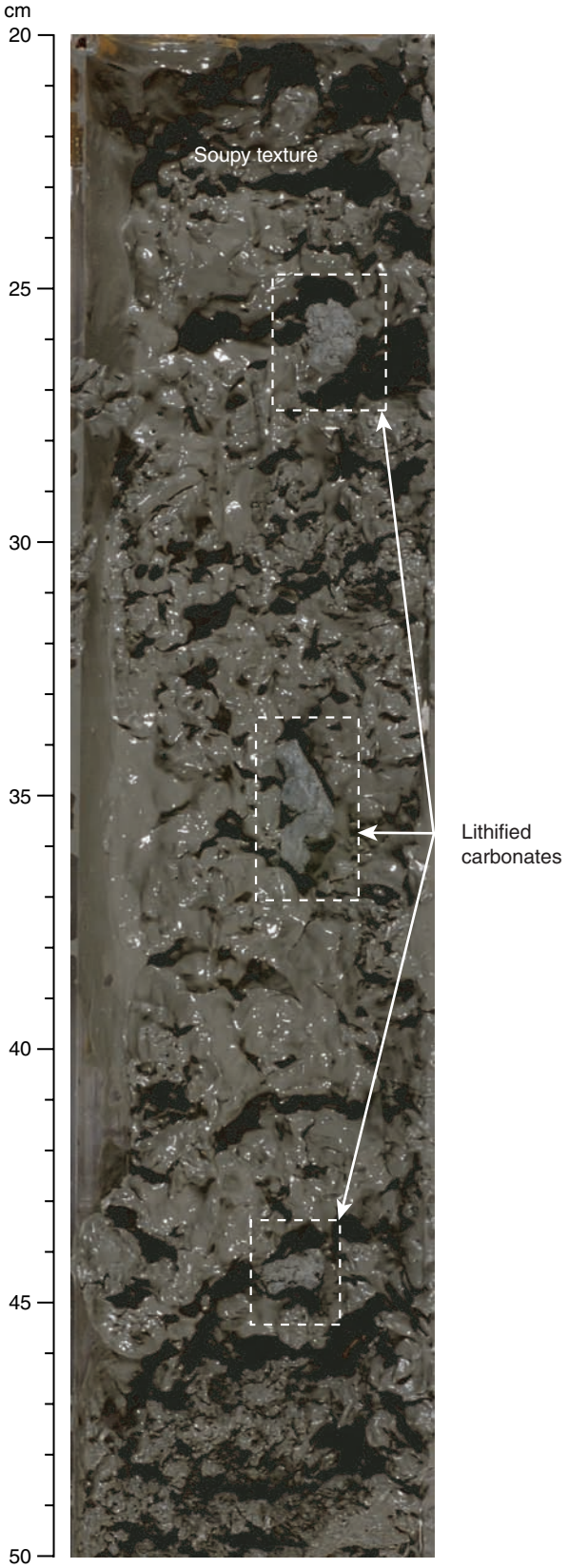

Figure F18. Interpreted natural soft-sediment deformation showing dark gray silty clay as the major lithology and distorted sand layers in lithostratigraphic Unit I (interval 311-U1328C-9X-1, 102–135 cm).

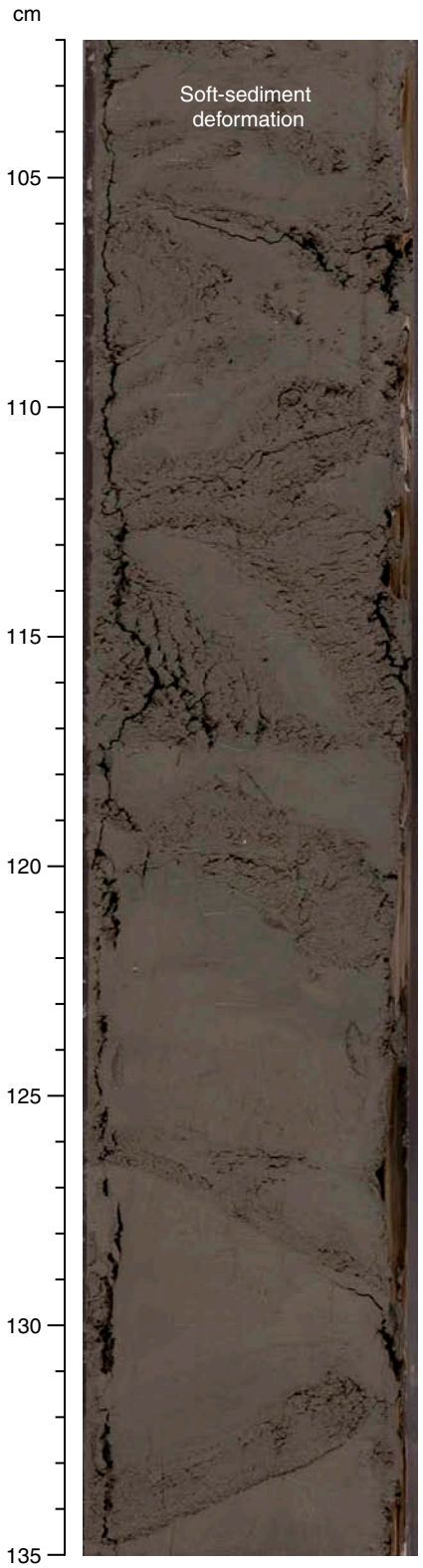

Figure F19. Diatom silty clay in lithostratigraphic Unit II (Sample **311-U1328C-16X-2, 80 cm**).

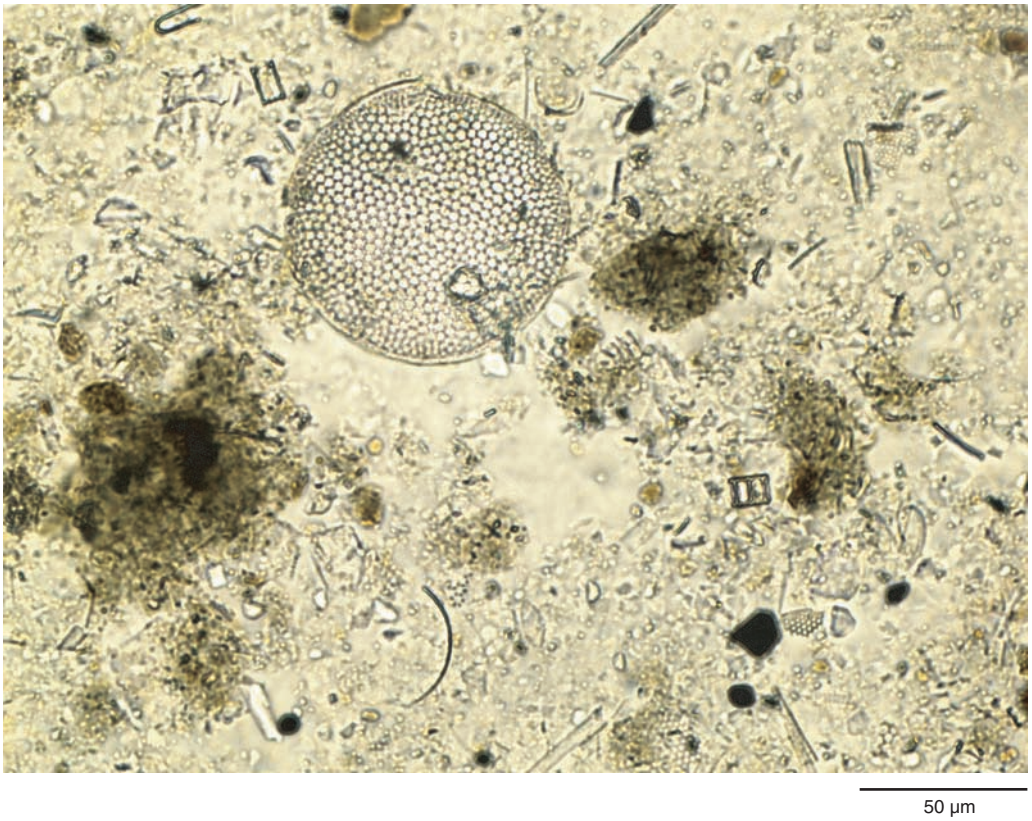

Figure F20. Three differently colored carbonate cements in dark greenish gray clay in lithostratigraphic Unit III (interval 311-U1328C-19X-4, 6–39 cm). A smear slide sample was taken from the brownish unlithified carbonate cement (interval 311-U1328C-19X-4, 18–20 cm; labeled "Carbonate"). At the bottom of the light colored unlithified carbonate cement (interval 311-U1328C-19X-4, 22–25 cm; labeled "HMC + Ca-dolomite"), a partly lithified carbonate piece is present in the working half. Right below, there is a dark gray sand layer (interval 311-U1328C-19X-4, 25–29 cm). Within the crumbly looking interval underneath the sand layer (interval 311-U1328C-19X-4, 29–34 cm; labeled "HMC + Ca-dolomite"), a piece of lithified dark gray carbonate was found in the working half, which completely filled the width of the core, suggesting a more extensive layer of carbonate.

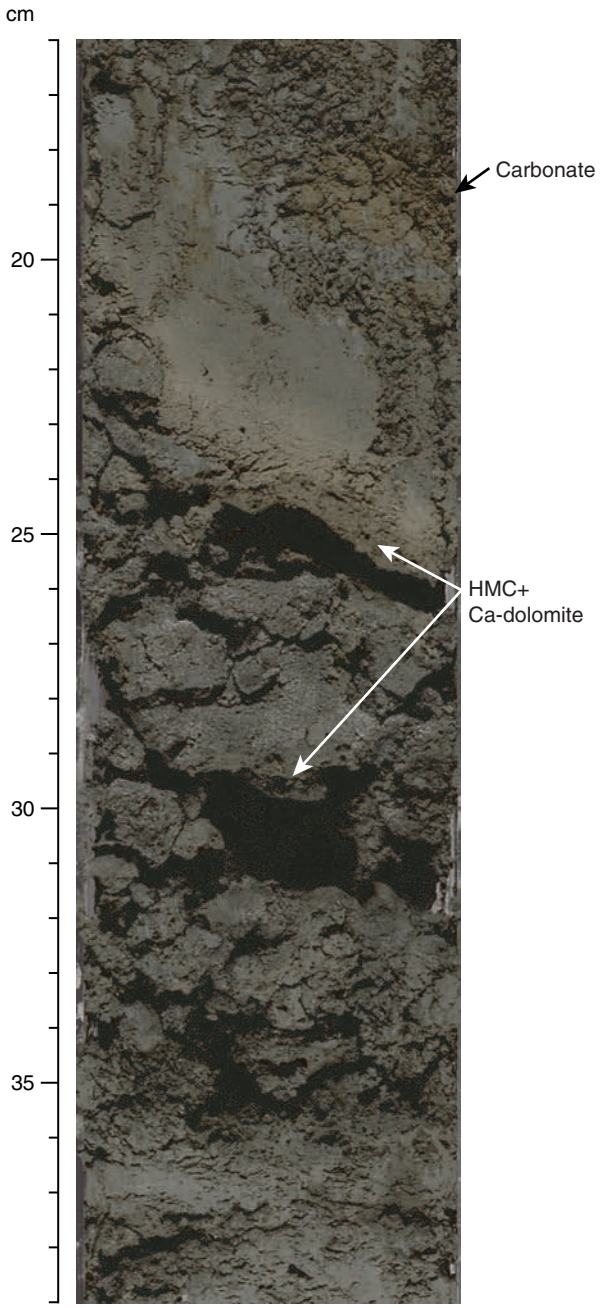

Figure F21. Elongated 5–15 µm carbonate crystals in a brownish unlithified carbonate cement in lithostratigraphic Unit III (Sample **311-U1328C-19X-4, 20 cm**).

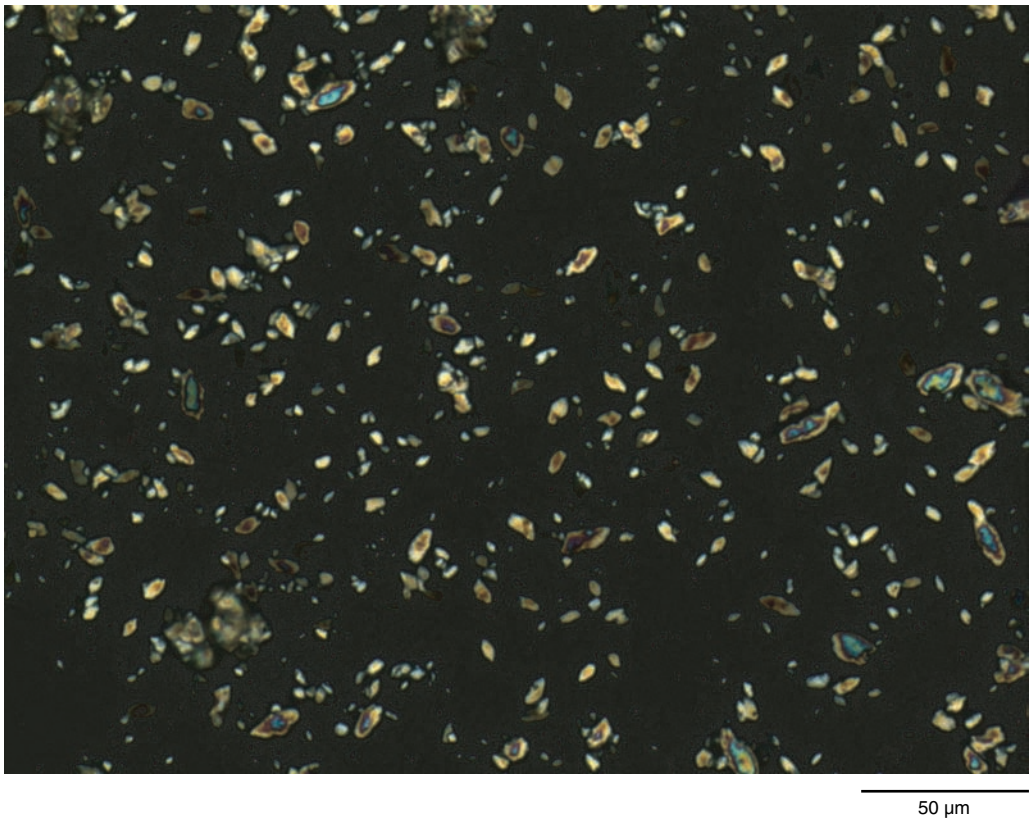

Figure F22. Distribution of soupy and mousselike sediment textures at Site U1328.

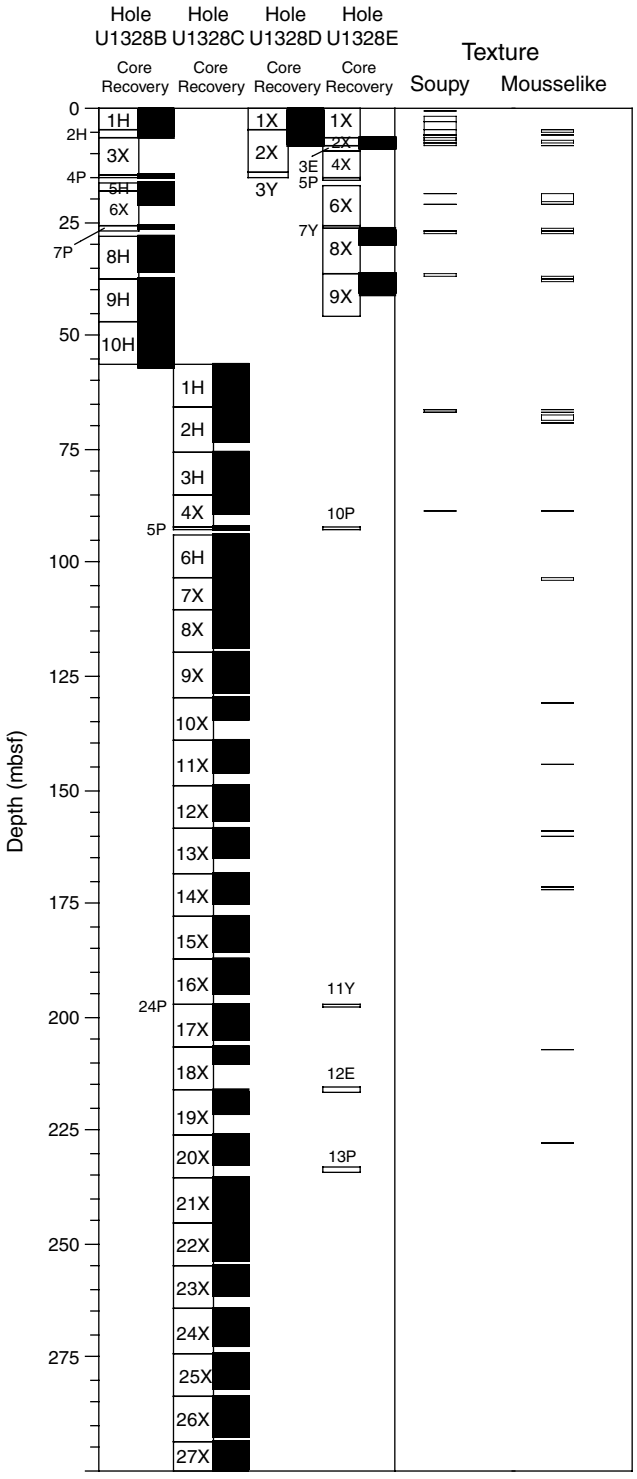

Figure F23. Soupy and mousselike sediment texture in dark greenish gray silty sand of lithostratigraphic Unit I (interval 311-U1328C-2H-1, 33–58 cm).

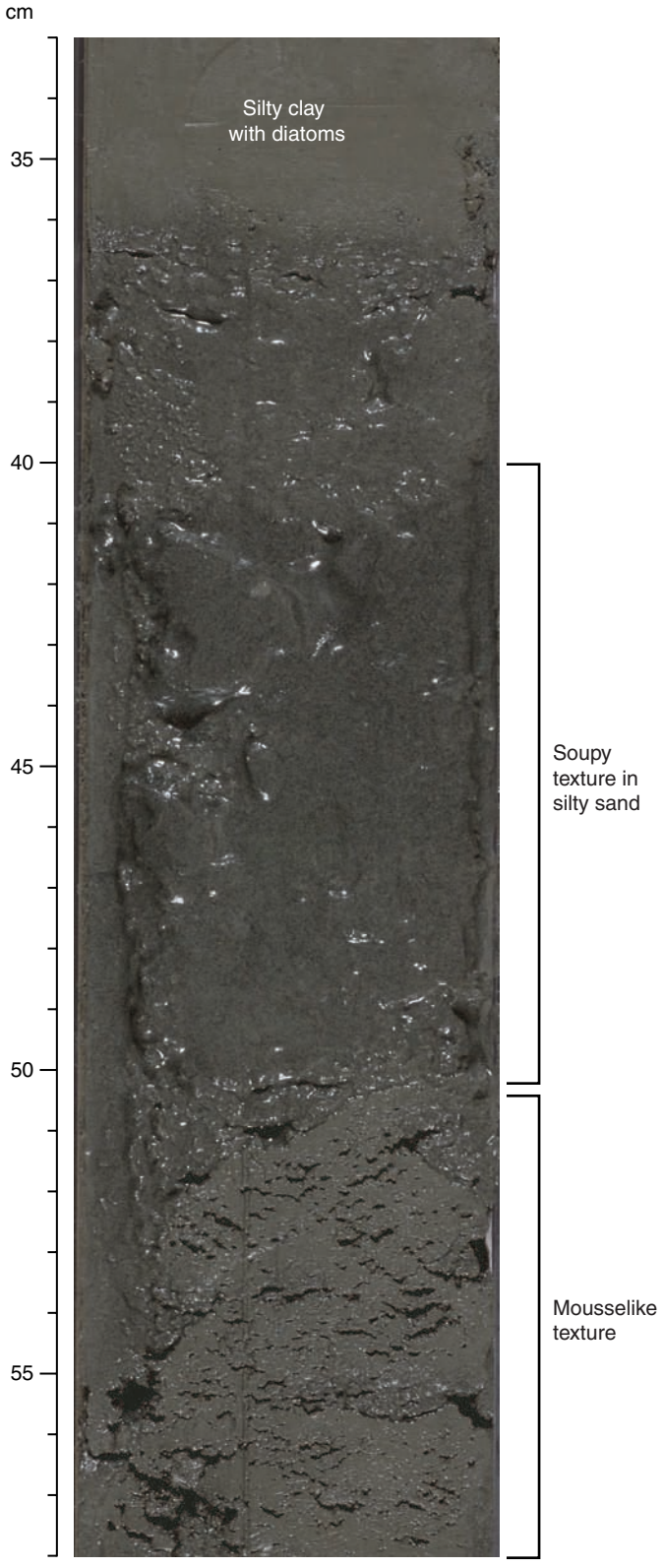

Figure F24. Mousselike sediment texture in dark greenish gray silty clay of lithostratigraphic Unit I (interval 311-U1328C-10X-1, 119–140 cm).

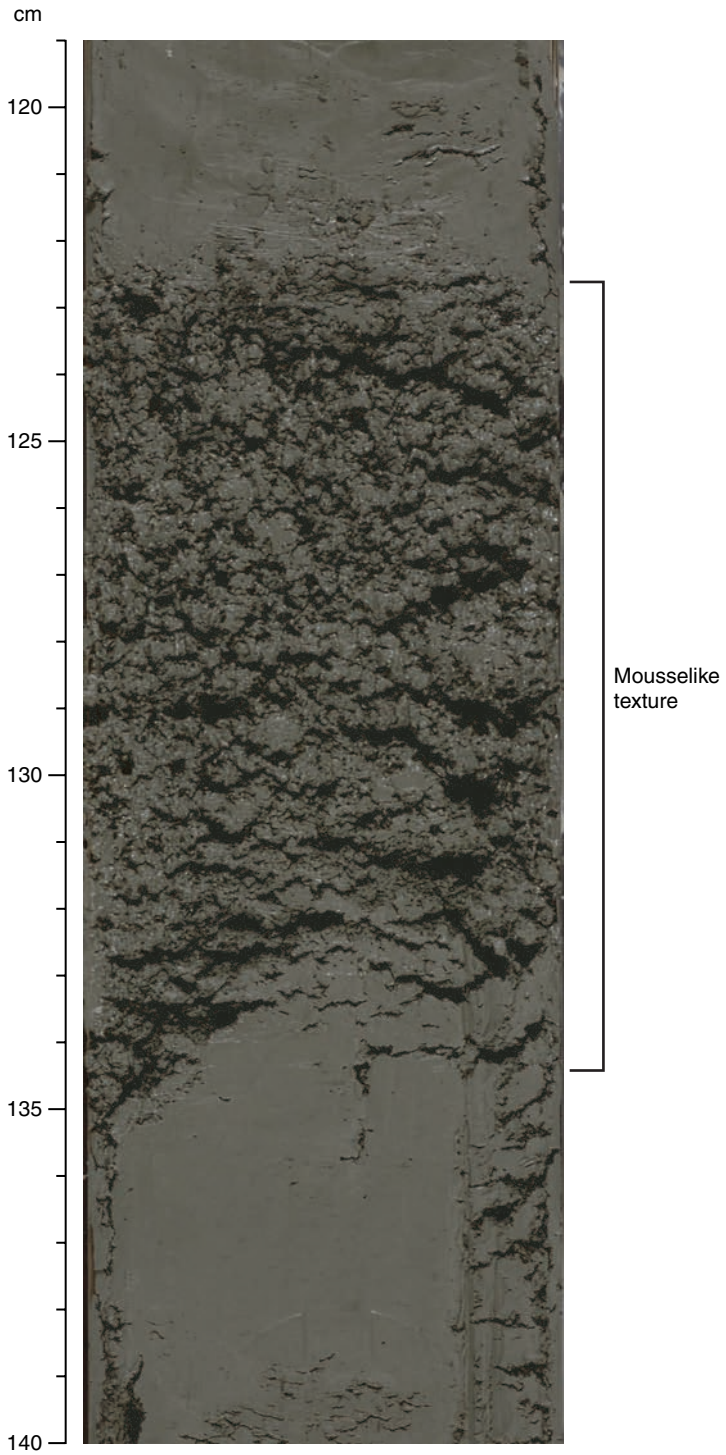

Figure F25. Concentration vs. depth profiles of salinity, chloride, sodium, and potassium in interstitial waters from Holes U1328B, U1328C, and U1328E. SW = seawater, BSR = seismically inferred bottom-simulating reflector.

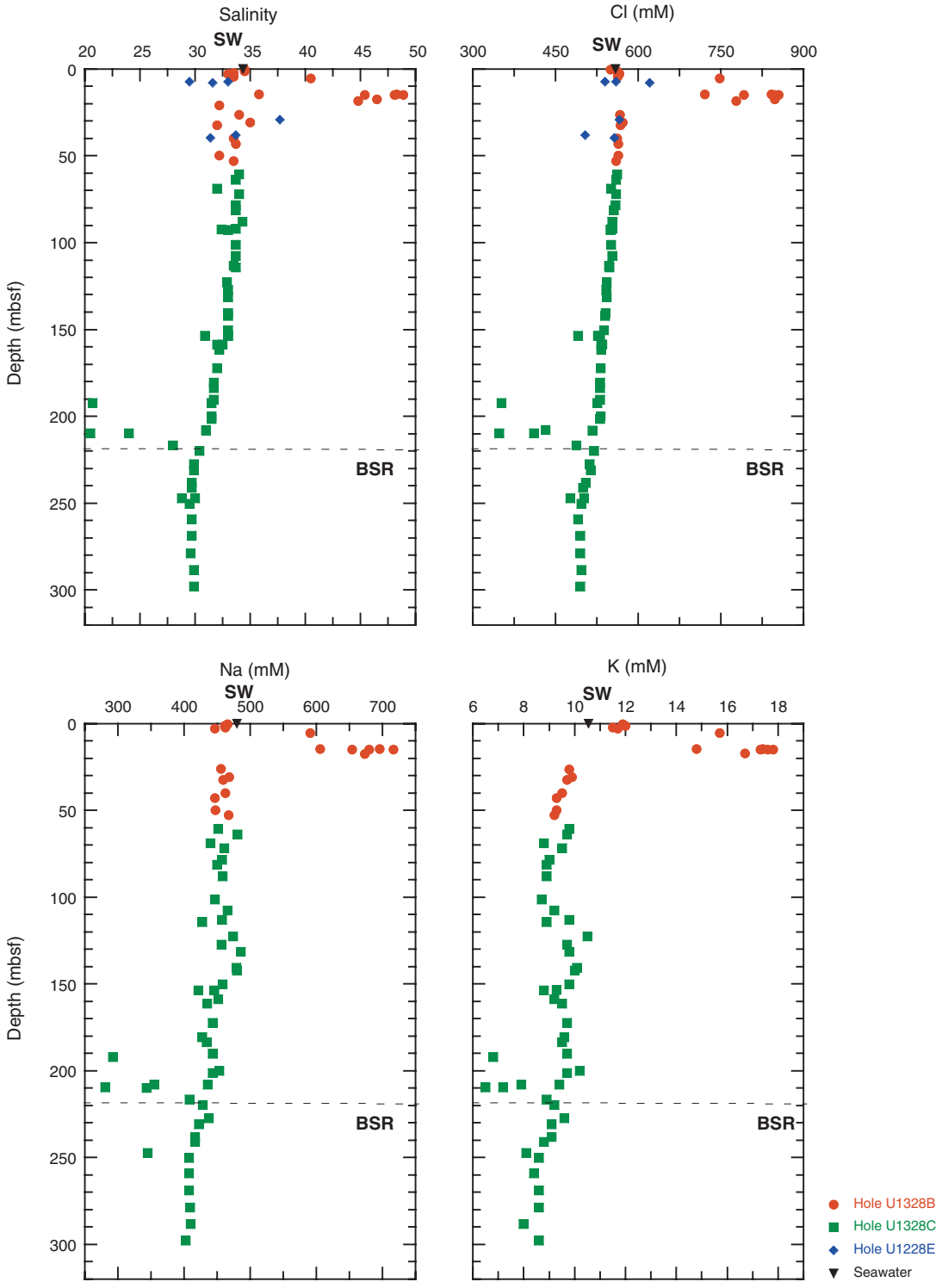

Figure F26. Concentration vs. depth profiles of alkalinity, sulfate, ammonium, and phosphate in interstitial waters from Holes U1328B, U1328C, and U1328E. SW = seawater, BSR = seismically inferred bottom-simulating reflector.

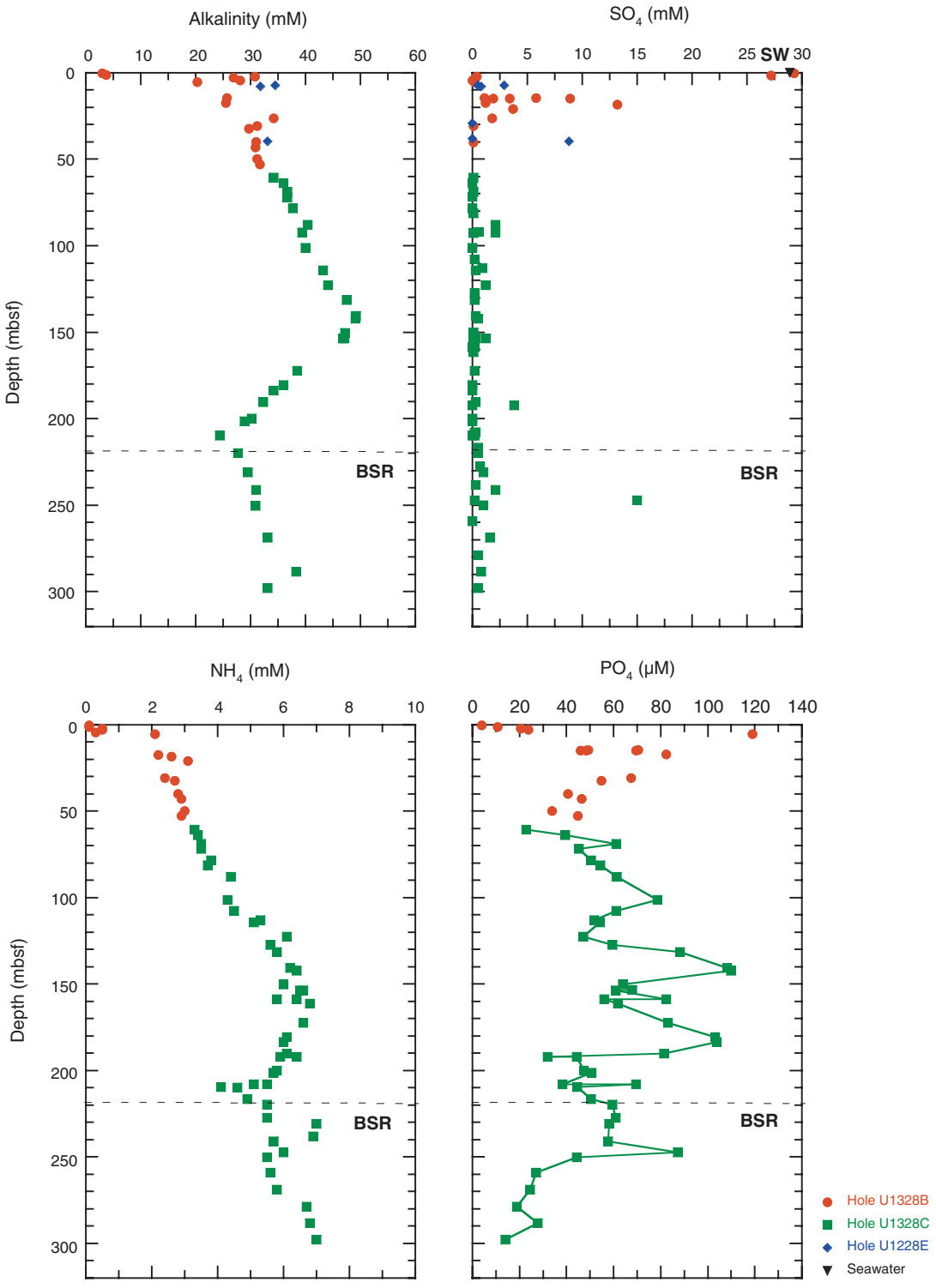

Figure F27. Concentration vs. depth profiles of calcium, magnesium, Mg/Ca ratios, and strontium in interstitial waters from Holes U1328B and U1328C. SW = seawater, BSR = seismically inferred bottom-simulating reflector.

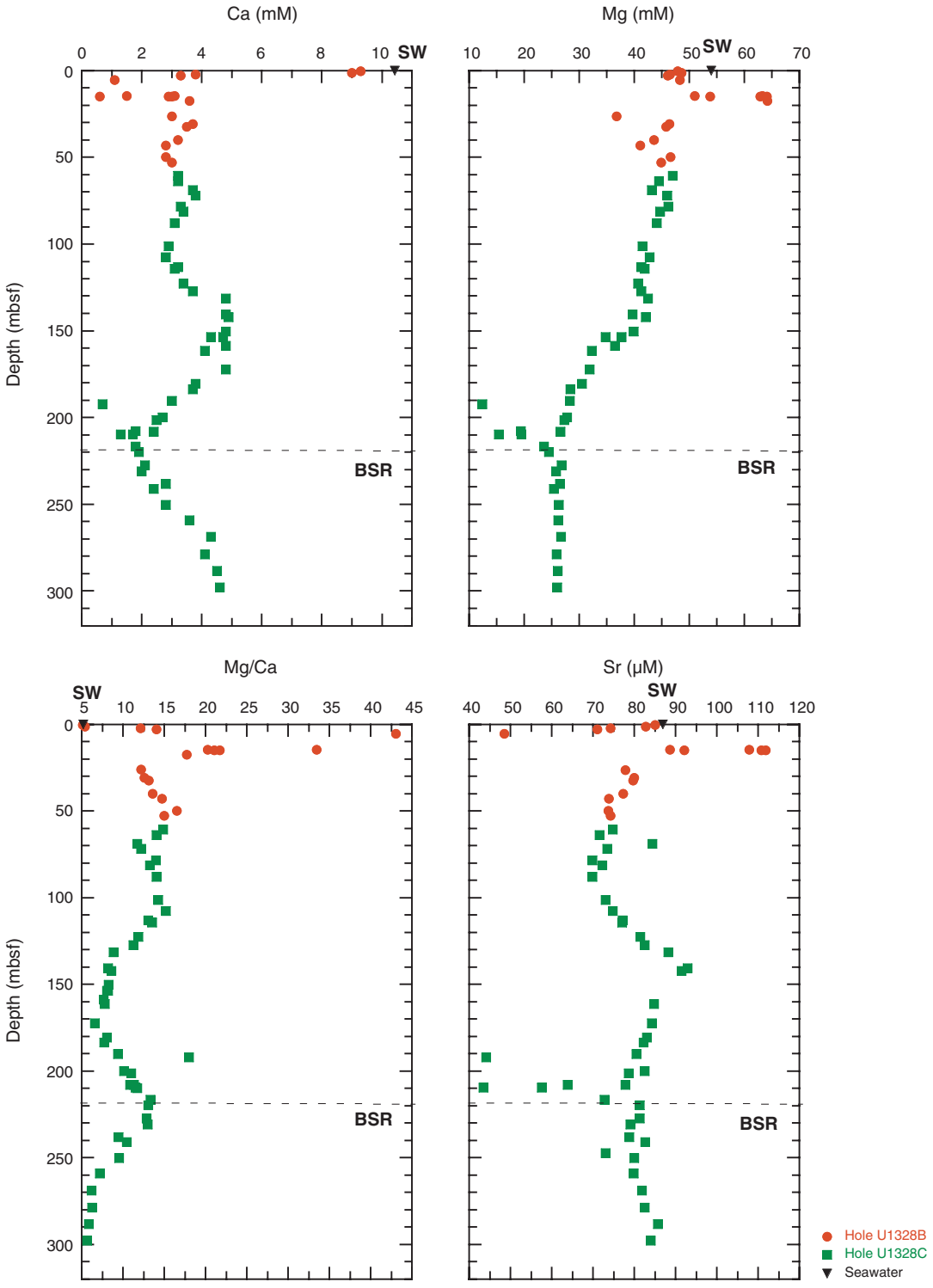

Figure F28. Concentration vs. depth profile of alkalinity values corrected for carbonate formation using calcium and magnesium data as proxies for the amount to dissolved inorganic carbon consumed by carbonate diagenesis.

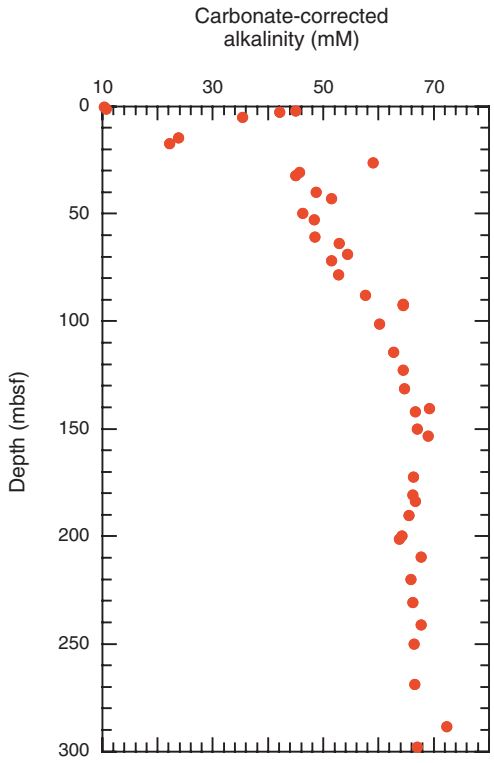

Figure F29. Concentration vs. depth profiles of dissolved lithium, boron, H_4SiO_4, and barium from Holes U1328B and U1328C. SW = seawater, BSR = seismically inferred bottom-simulating reflector.

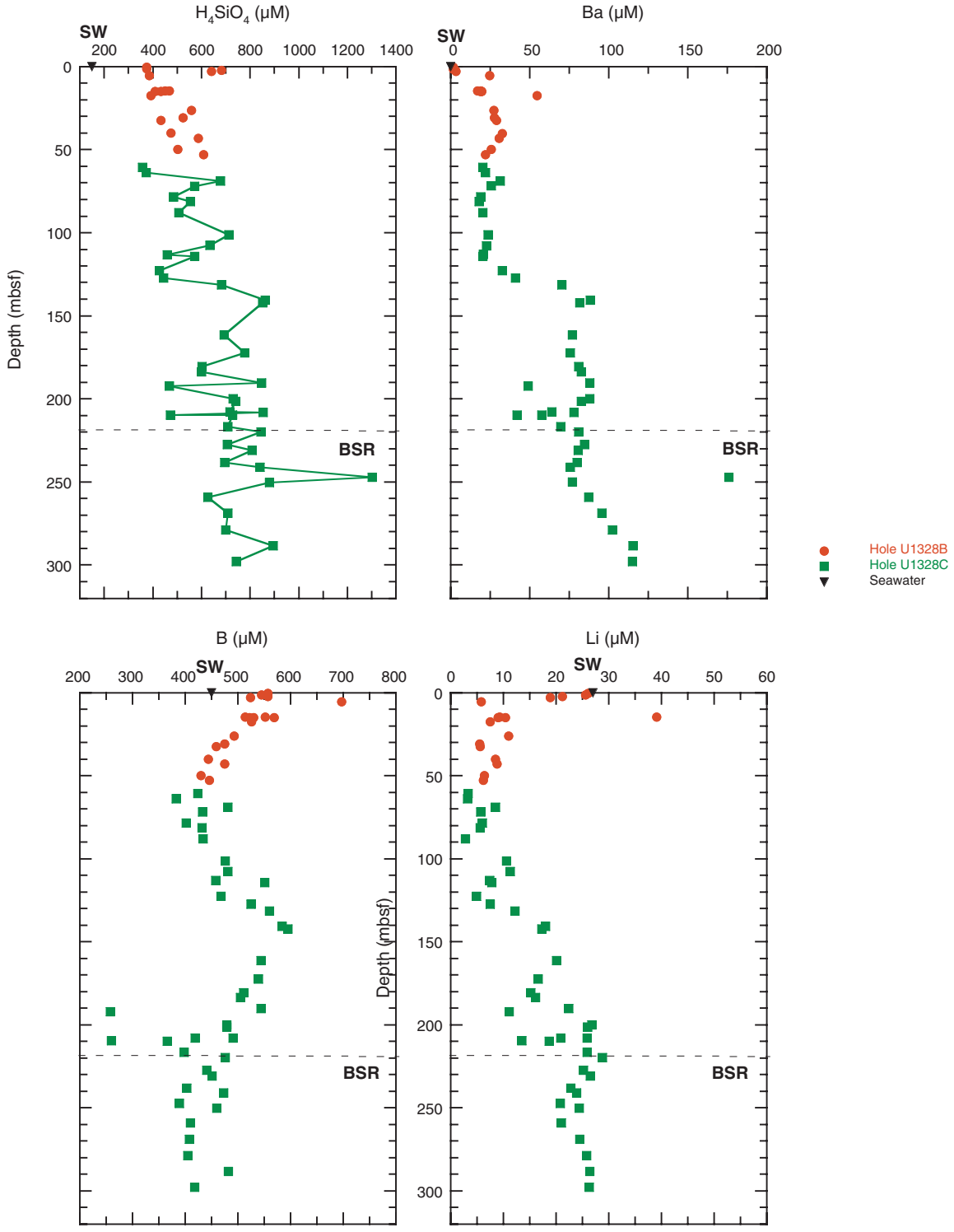

Figure F30. Concentrations of methane, ethane, and propane in headspace gas samples from Site U1328. BSR = bottom-simulating reflector.

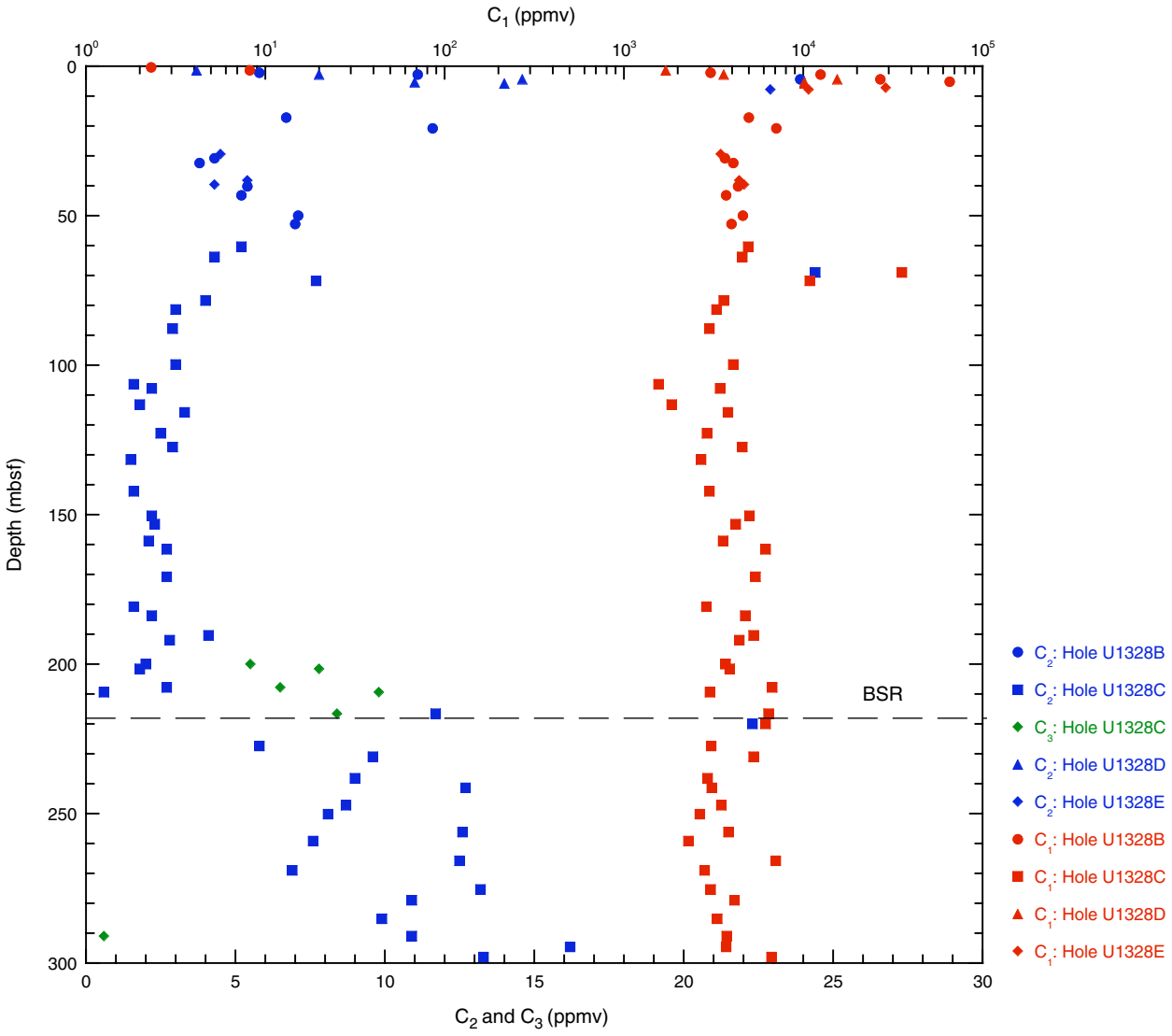

Figure F31. C_1/C_2 ratio vs. temperature at Site U1328. HS = headspace gas, VAC = void gas.

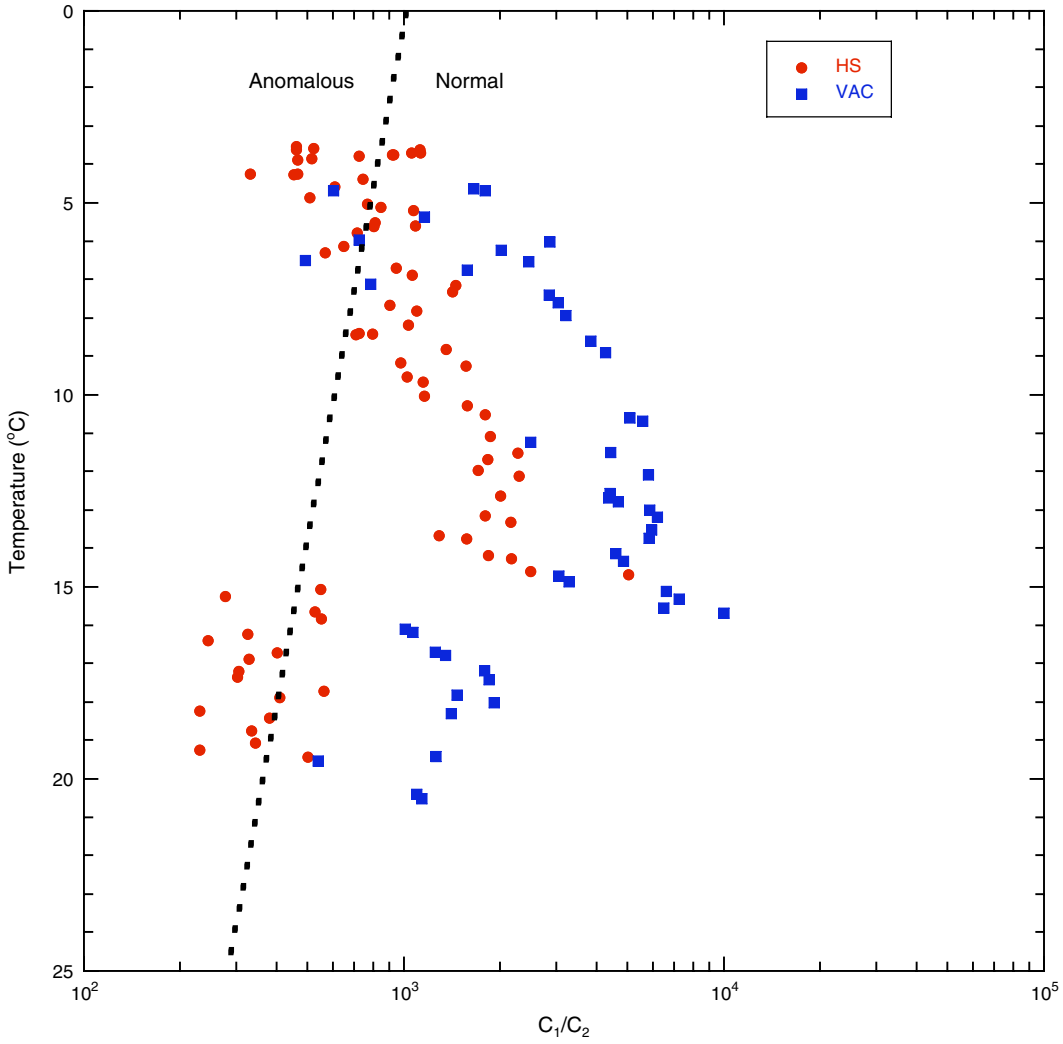

Figure F32. Concentrations of ethane, propane, *i*-butane, and *n*-butane in void gas samples from Site U1328. BSR = bottom-simulating reflector.

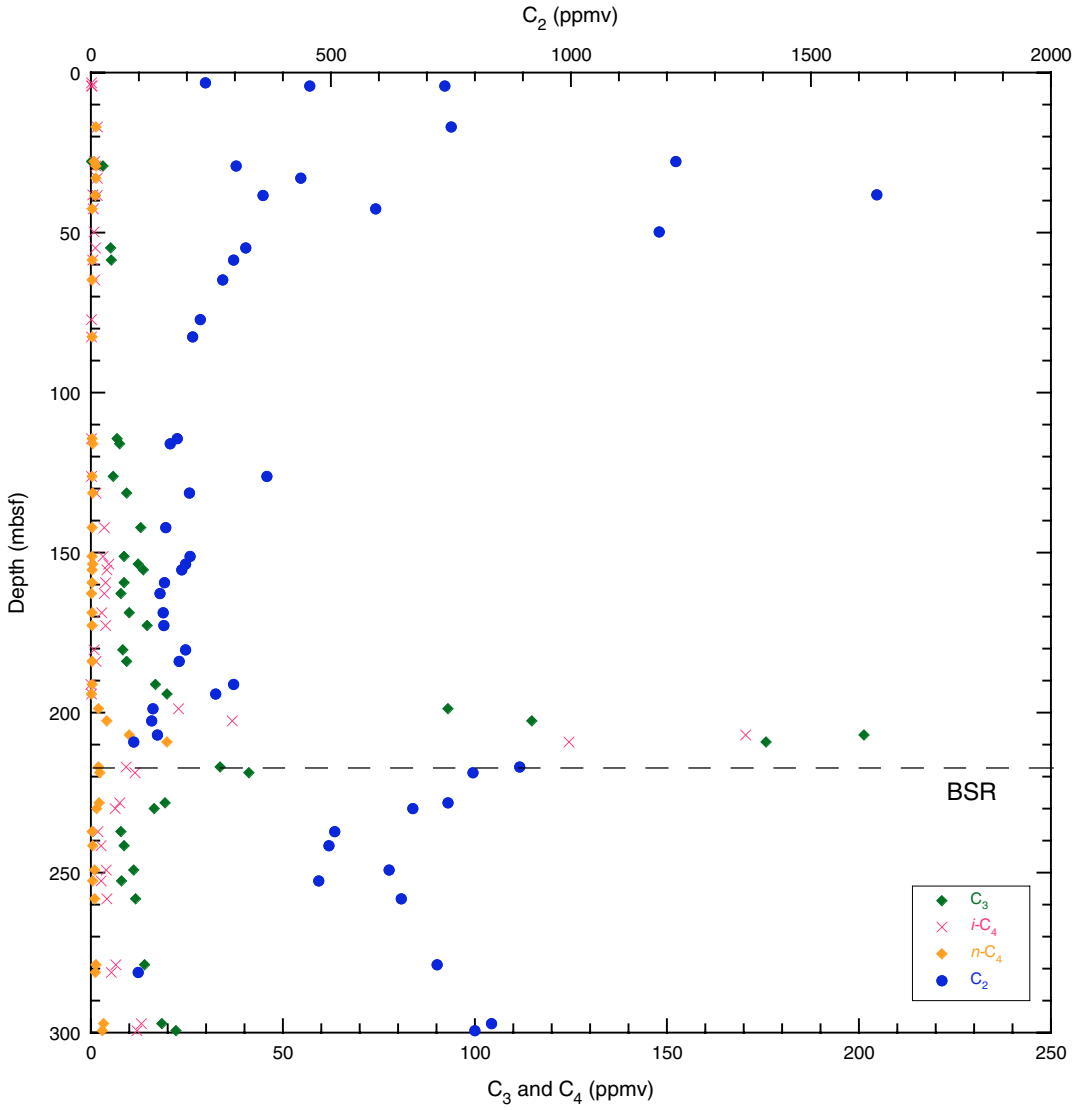

Figure F33. C_1/C_2 and i-C_4/n-C_4 ratios in void gas samples from Site U1328. BSR = bottom-simulating reflector.

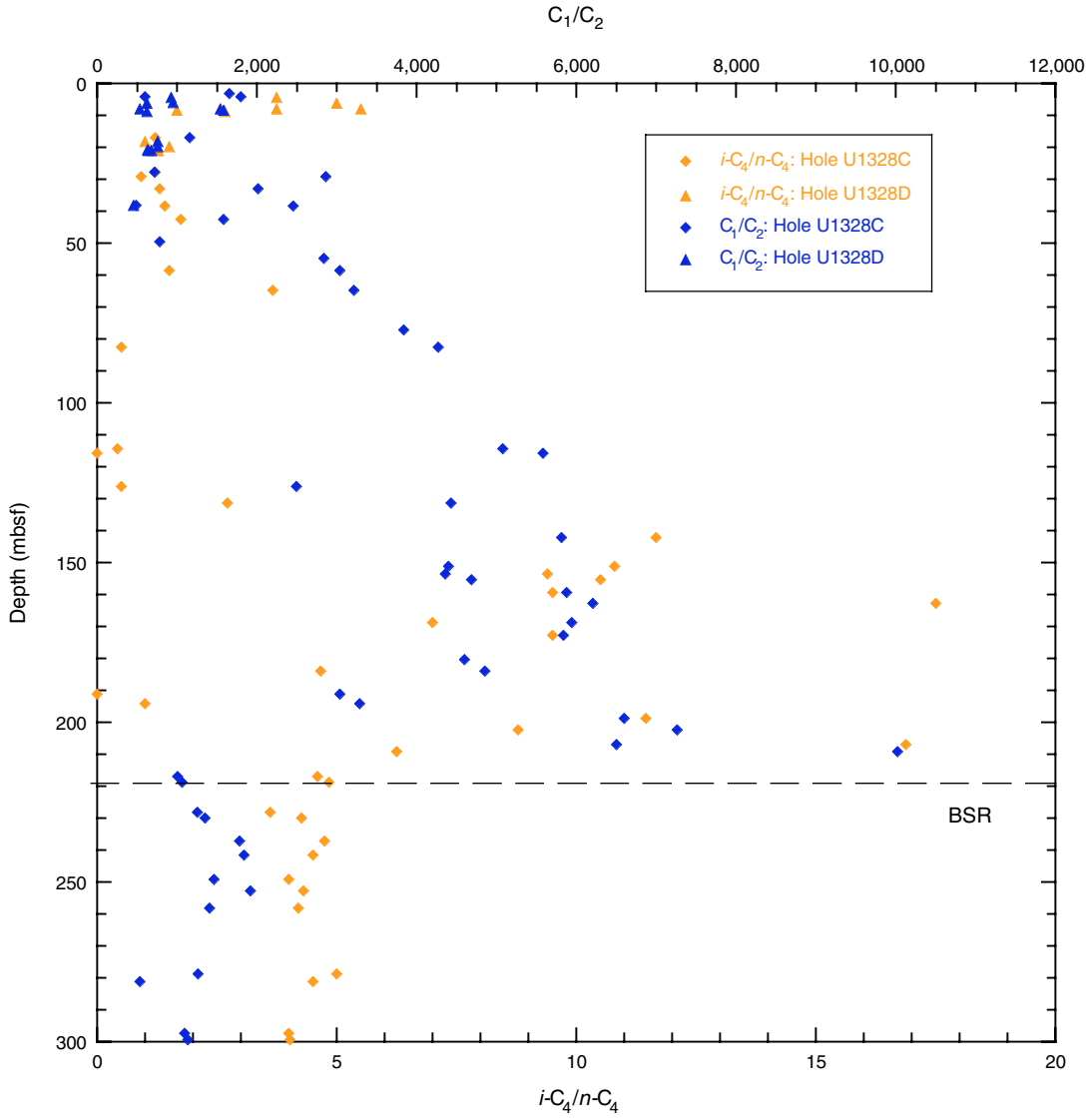

Figure F34. C_1/C_2 ratios in headspace gas (HS), void gas (VAC), gas hydrate gas (HYD), and Pressure Core Sampler (PCS) gas samples from Site U1328. BSR = bottom-simulating reflector.

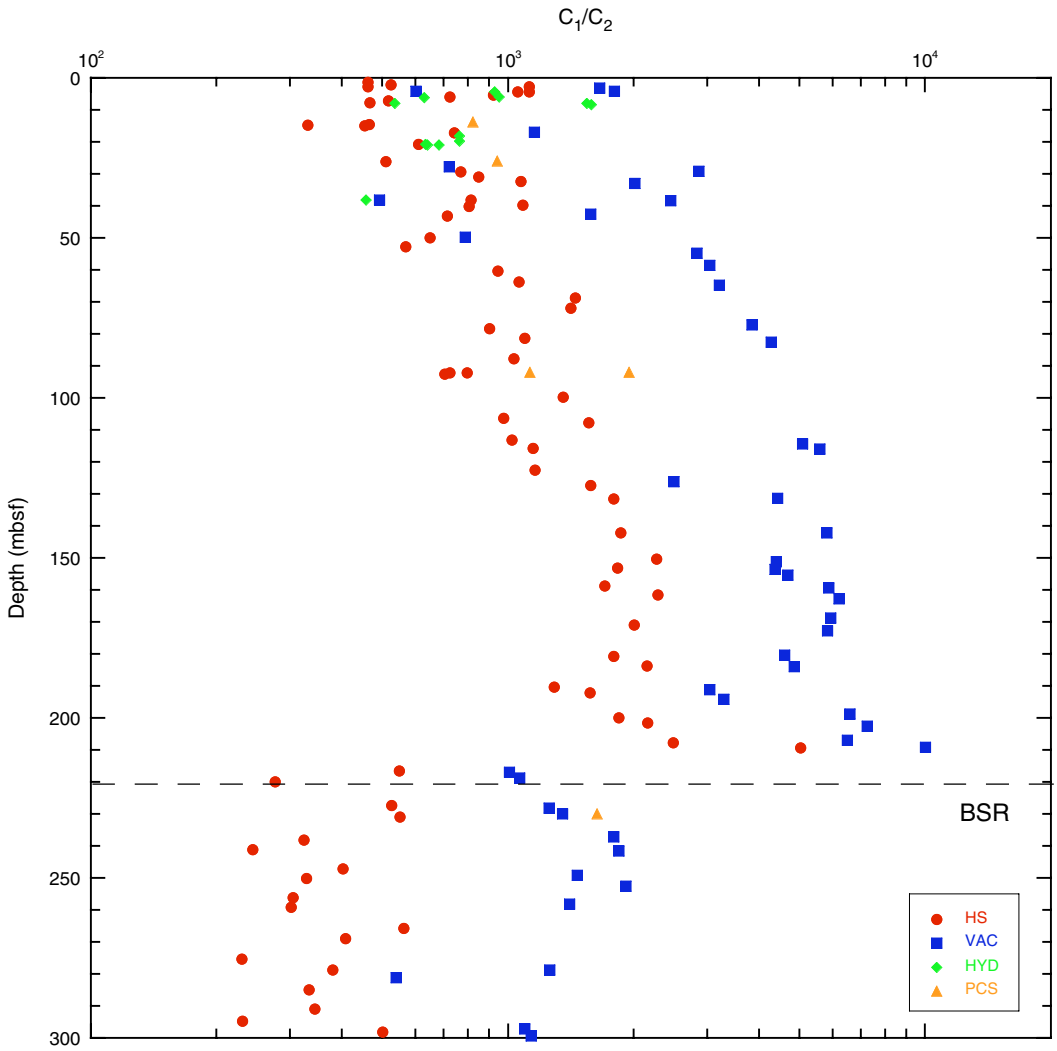

Figure F35. Contents of inorganic carbon (IC), calcium carbonate ($CaCO_3$), total organic carbon (TOC), total nitrogen (TN), and C/N ratios in sediments from Site U1328.

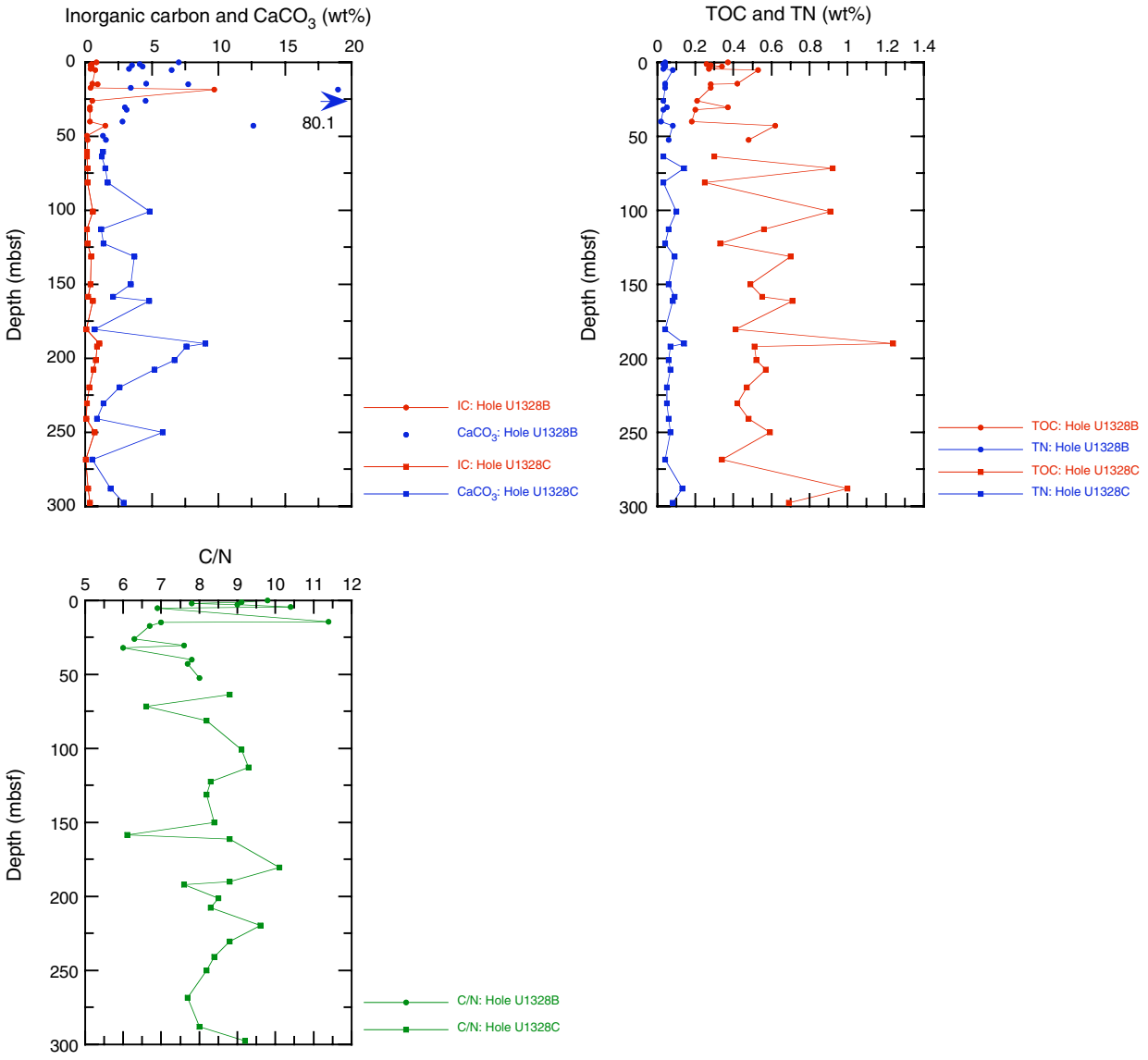

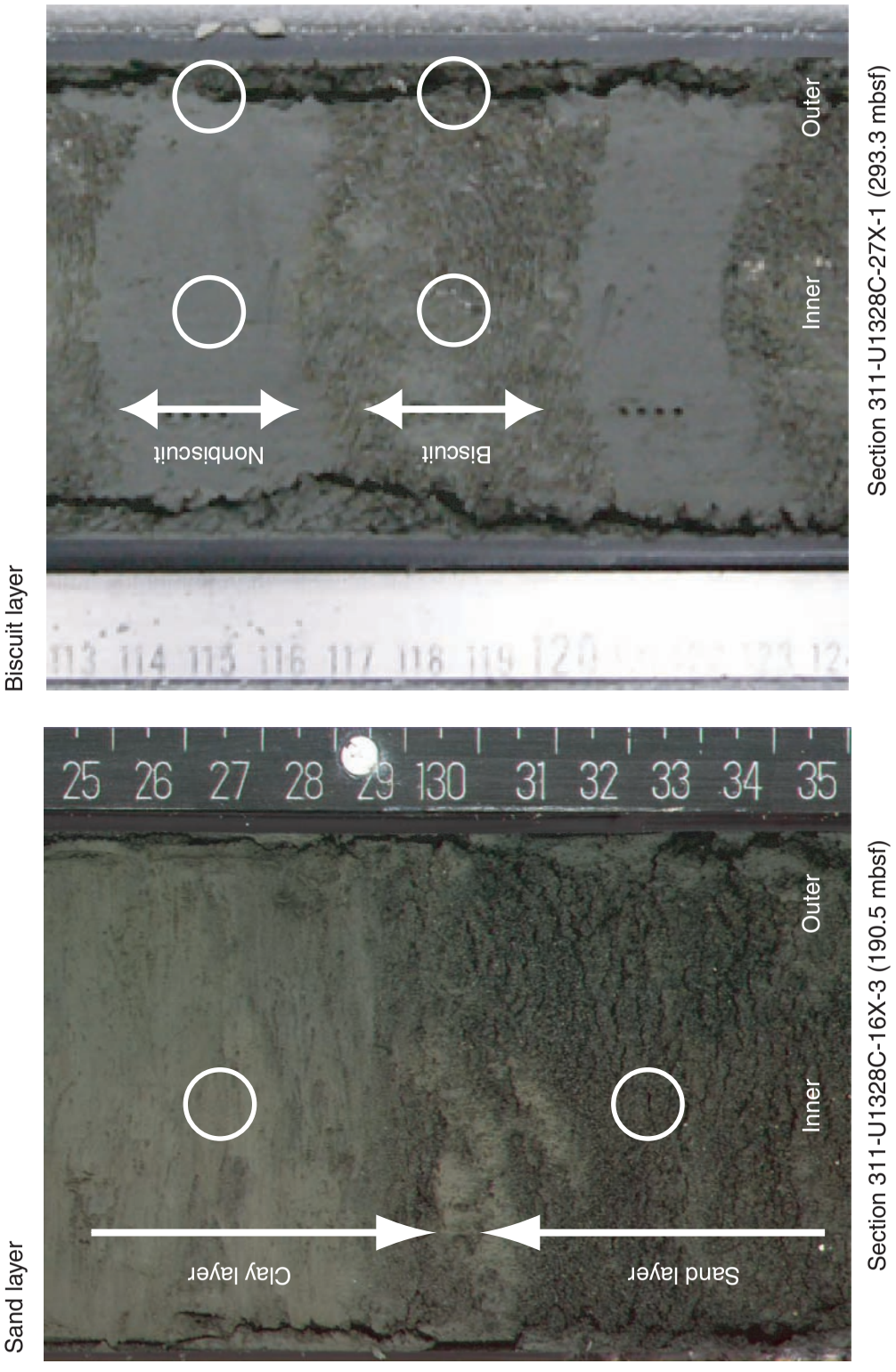

Figure F36. Sampling for fluorescent microsphere concentrations from Hole U1328C.

Figure F37. Overview of physical property data from Site U1328. Line in thermal conductivity plot shows regional trend from Davis et al., 1990. LWD = logging while drilling, MAD = moisture and density, MST = multisensor track, AVS = automated vane shear, BSR = bottom-simulating reflector.

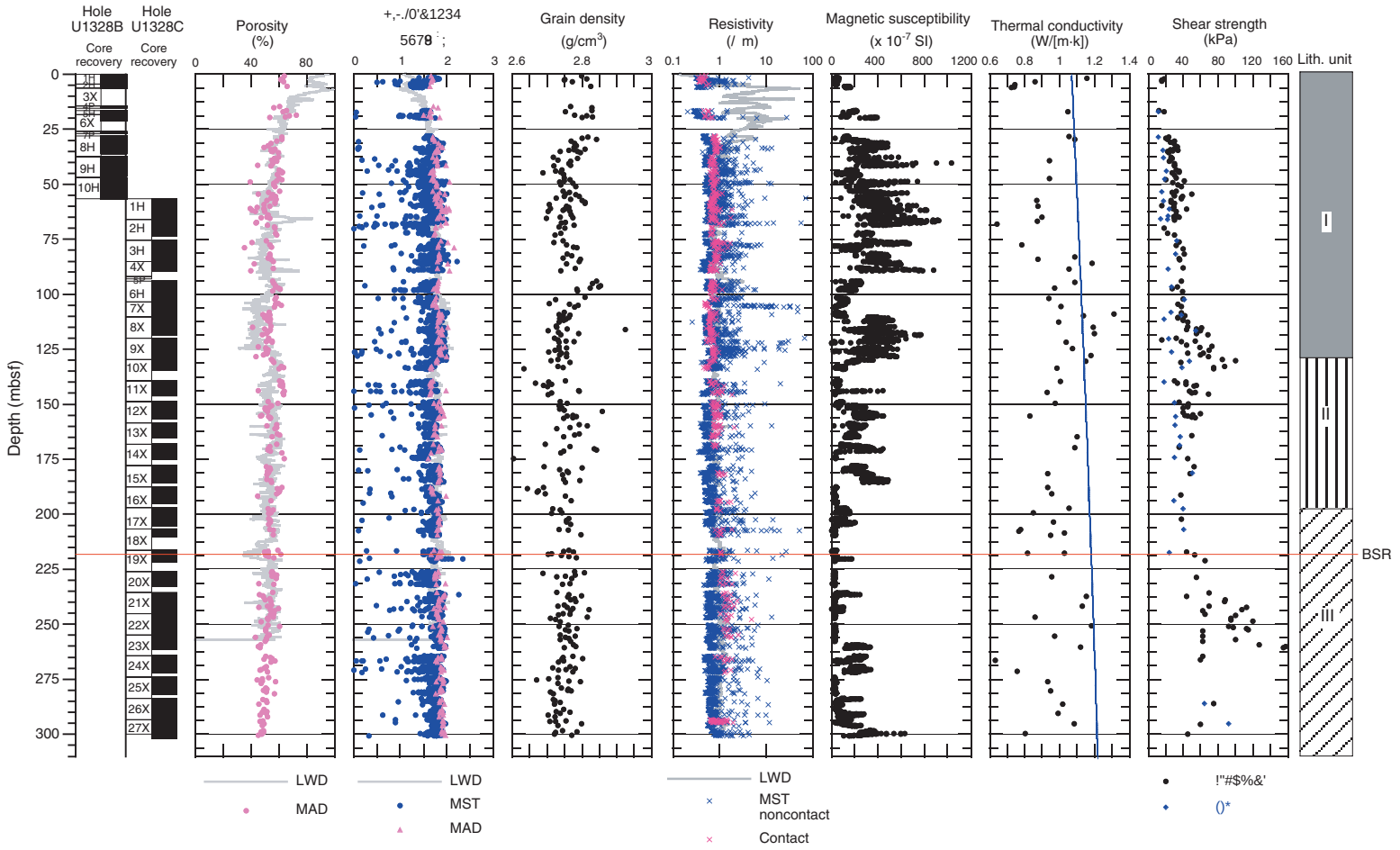

Figure F38. Combined infrared (IR) images of core liner temperature from Holes U1328B and U1328C, compared to logging-while-drilling/measurement-while-drilling (LWD/MWD) resistivity image and calculated pore water saturation from Hole U1327A. Core recovery and core handling time are also shown. BSR = bottom-simulating reflector. (This figure is also available in an **oversized format.**)

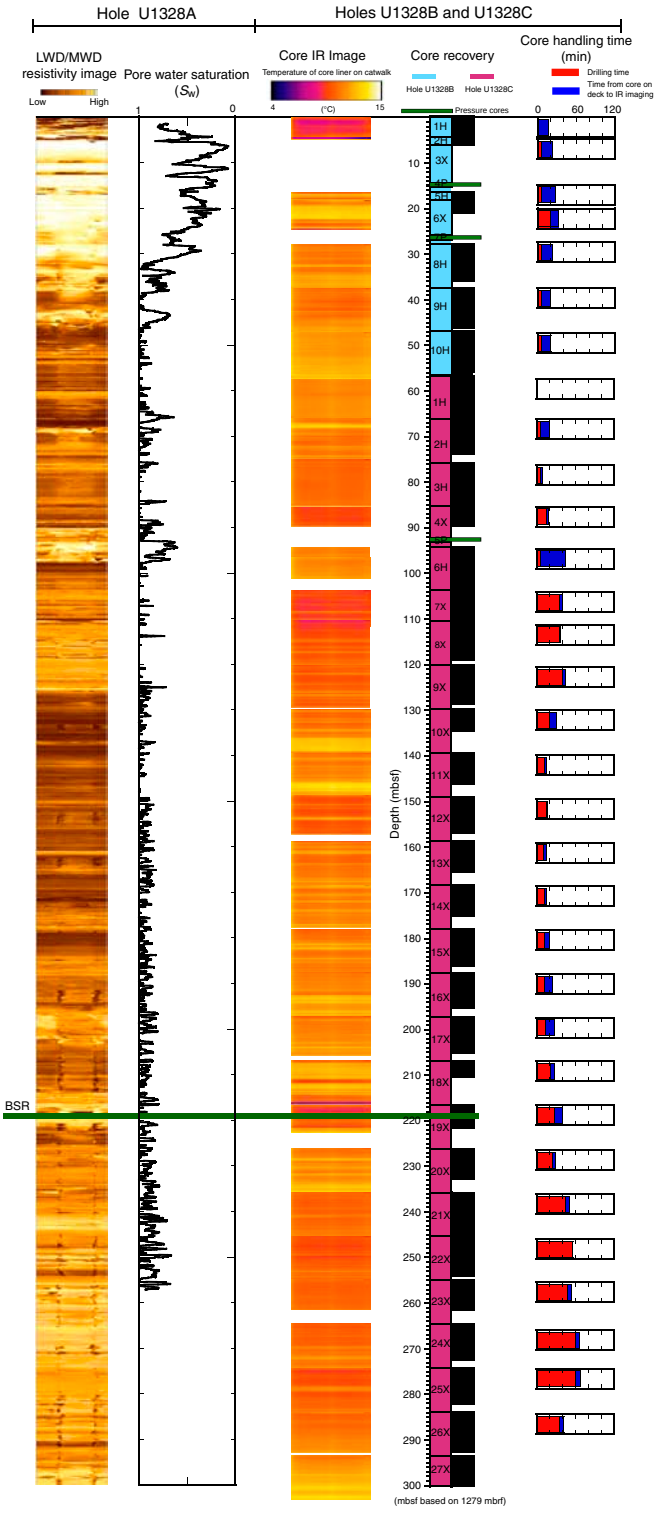

Figure F39. A. Portion of the IR image of Core 311-U1328C-19X taken on the catwalk. These images are used to quickly identify samples that may contain gas hydrate or fresh water released by gas hydrate dissociation during core recovery. **B.** IR images from several cores concatenated into an IR downhole profile. The presence of an image where there is no core recovery reflects the fact that voids in the core liner are compressed after the IR image is taken but prior to assignment of curated core lengths. As a result, the curated depth relative to the top of a core can be different from depth recorded on the catwalk IR image. **C.** Downhole temperature profile for Holes U1328B and U1328C based on concatenation of core liner temperatures averaged across each pixel row (see text for details). **D.** Detailed downhole temperature profiles for two segments of Hole U1328C. An approximate no–gas hydrate, no-void baseline is shown, as are anomalies that are interpreted to be caused by gas hydrate (negative anomalies) or voids (positive anomalies).

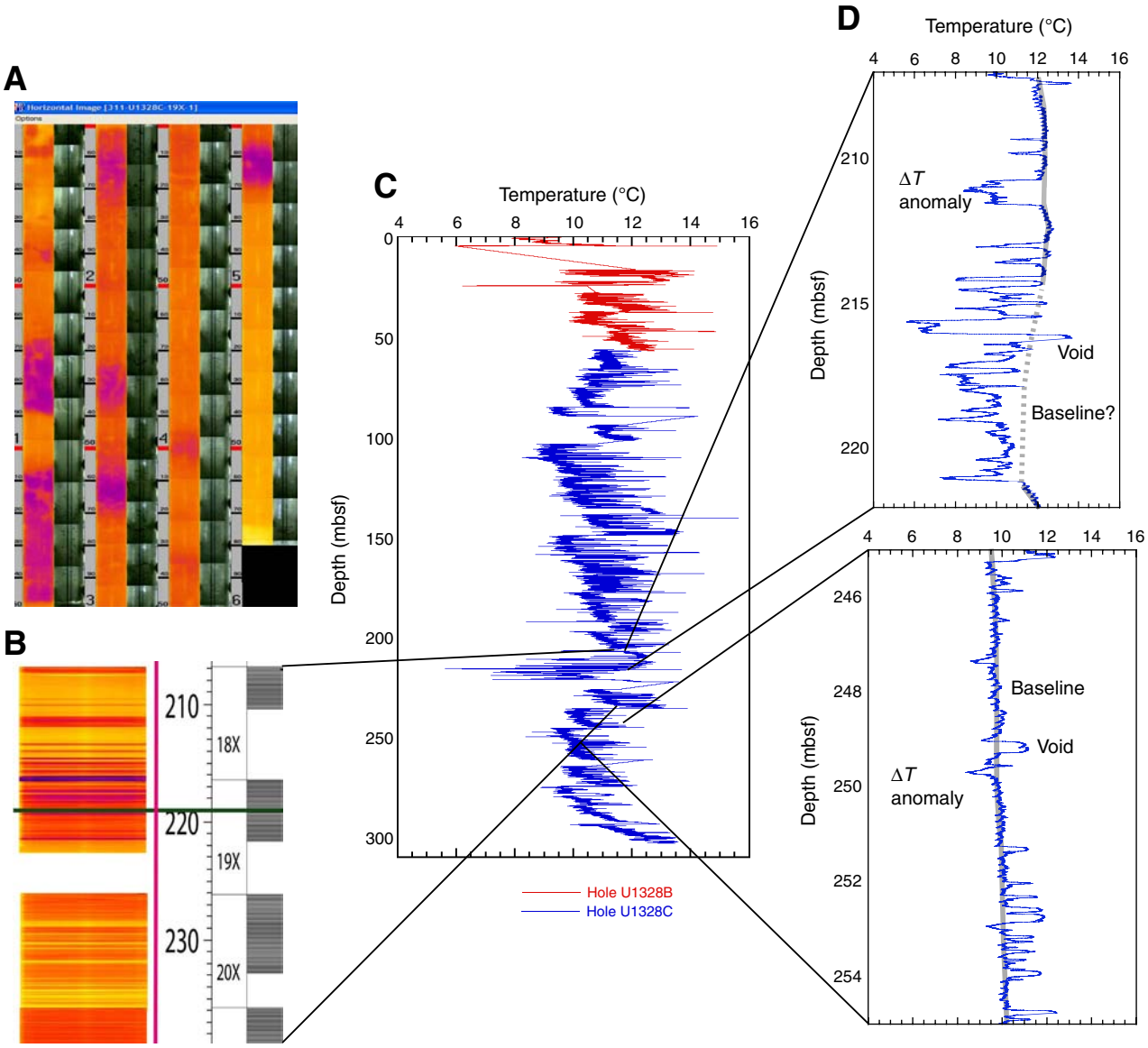

Figure F40. IR image and associated temperature profile of Sample 311-U1328C-18X-3, 72–82 cm.

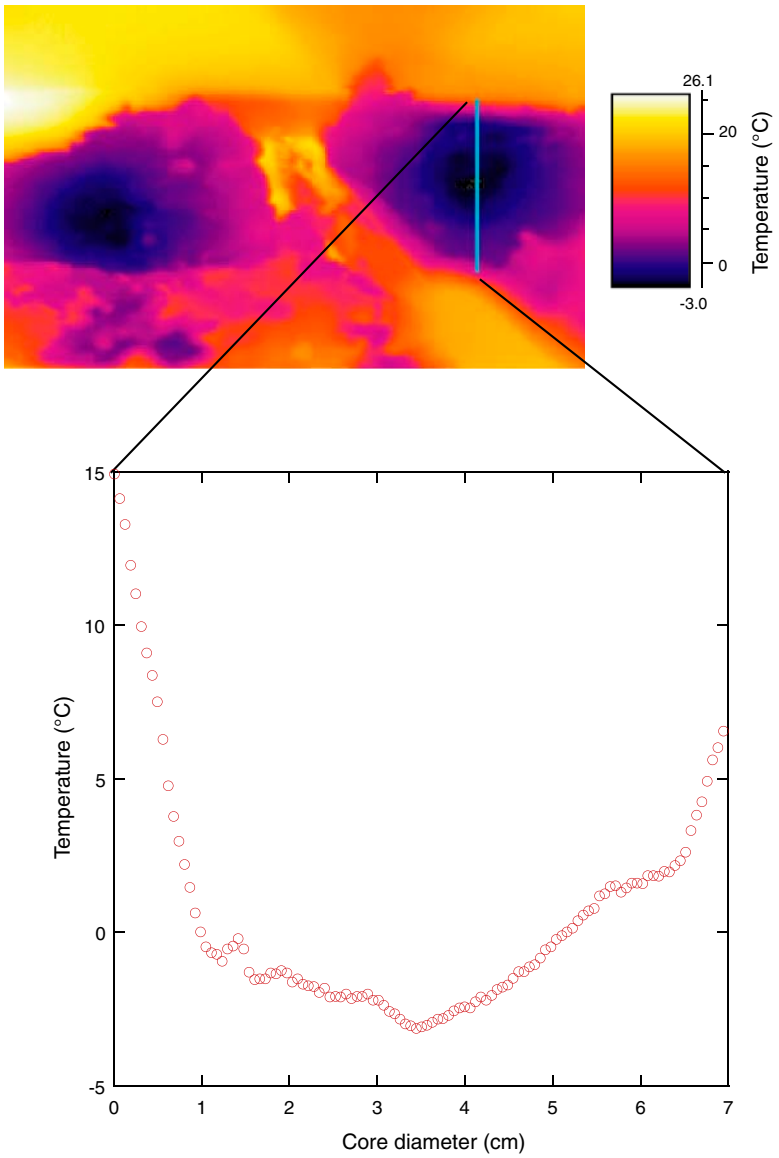

Figure F41. A. Moisture and density (MAD) porosity from Holes U1328B and U1328C compared to logging-while-drilling (LWD) porosity from Hole U1328A. **B.** MAD porosity compared to wireline logging porosity from Hole U1328C. **C.** Comparison of magnetic susceptibility from Sites U1328, U1329, and U1327.

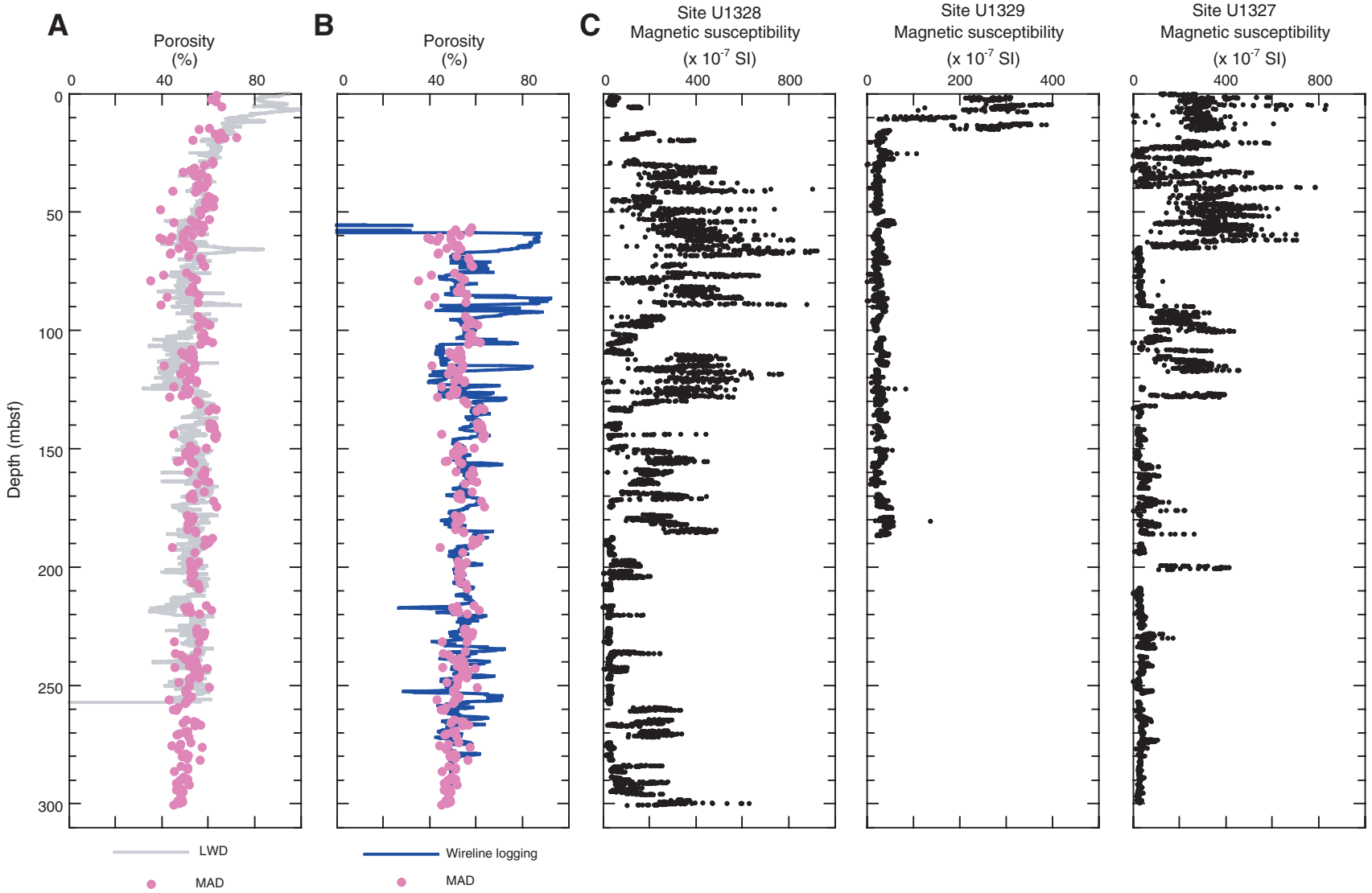

Figure F42. MAD porosity from advanced piston corer (APC) and extended core barrel (XCB) cores compared to porosity from pressures. Anomalously low porosity samples are thought to represent sand-rich horizons that have low porosity but probably have high relative permeability compared to the dominant clay lithology.

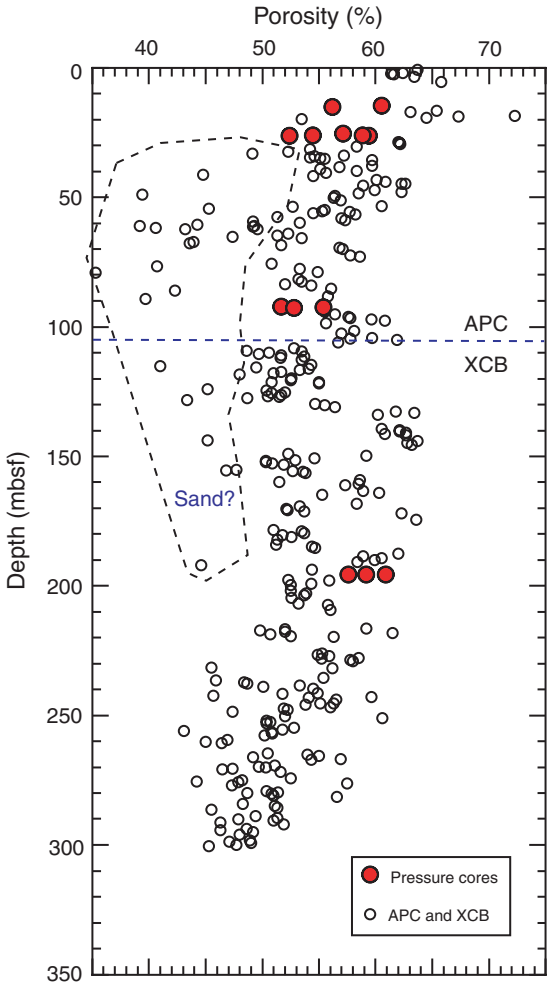

Figure F43. A. Comparison between automated vane shear (AVS) and handheld Torvane shear strength measurements. **B.** Overburden pressure calculated from MAD bulk density data. **C.** Ratio of Torvane shear strength to overburden pressure. This provides information on the degree of sediment underconsolidation or overconsolidation.

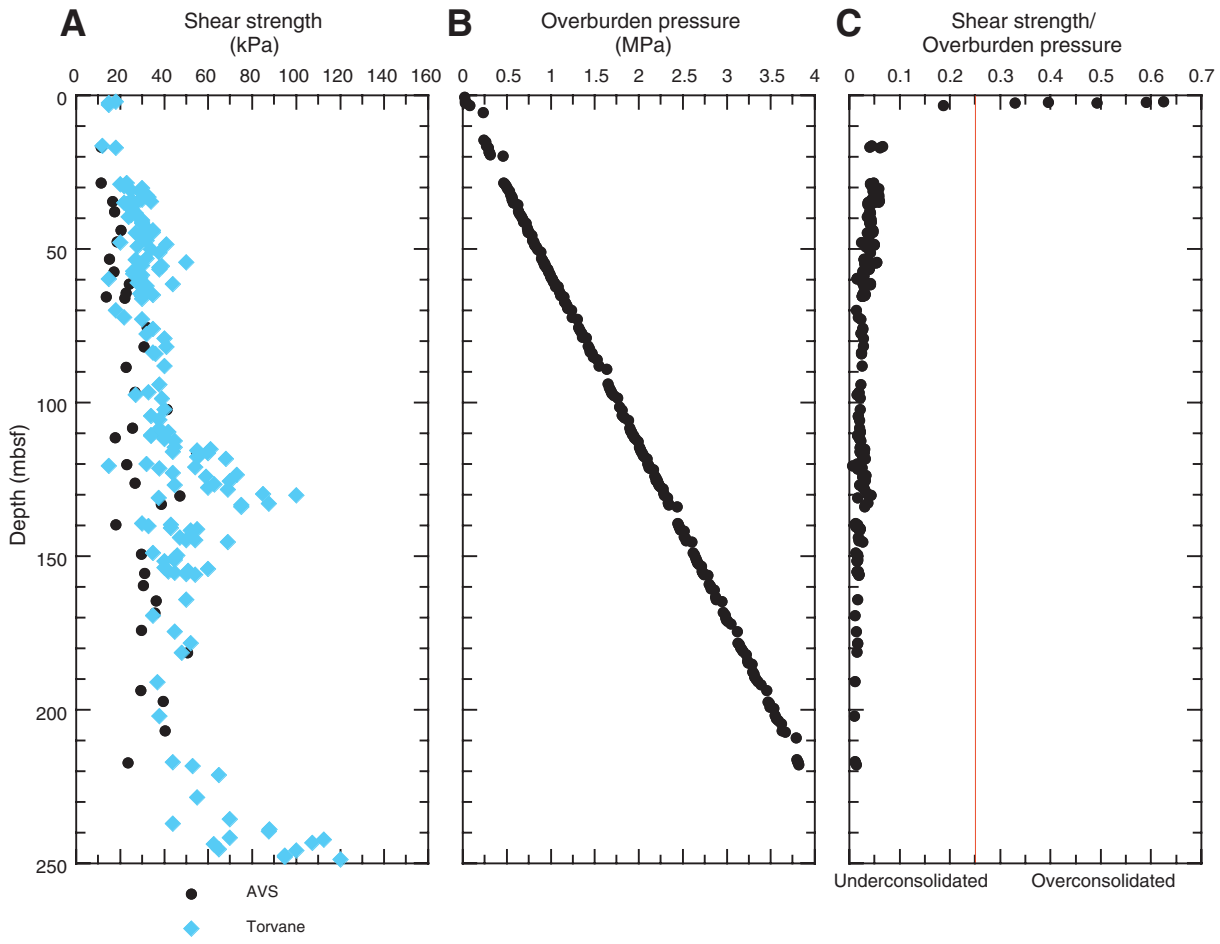

Figure F44. A. Comparison of pore water resistivity calculated from interstitial water salinity using equations developed by Fofonoff (1985) and bulk volume contact resistivity of sediments from Site U1328. Both sets of values have been corrected to 20°C. **B.** Formation factor (ratio of pore water resistivity to sediment resistivity). **C.** Comparison of porosity derived from moisture and density (MAD) measurements and Archie's equation (m = 1.36 and a = 1.58). (Continued on next page.)

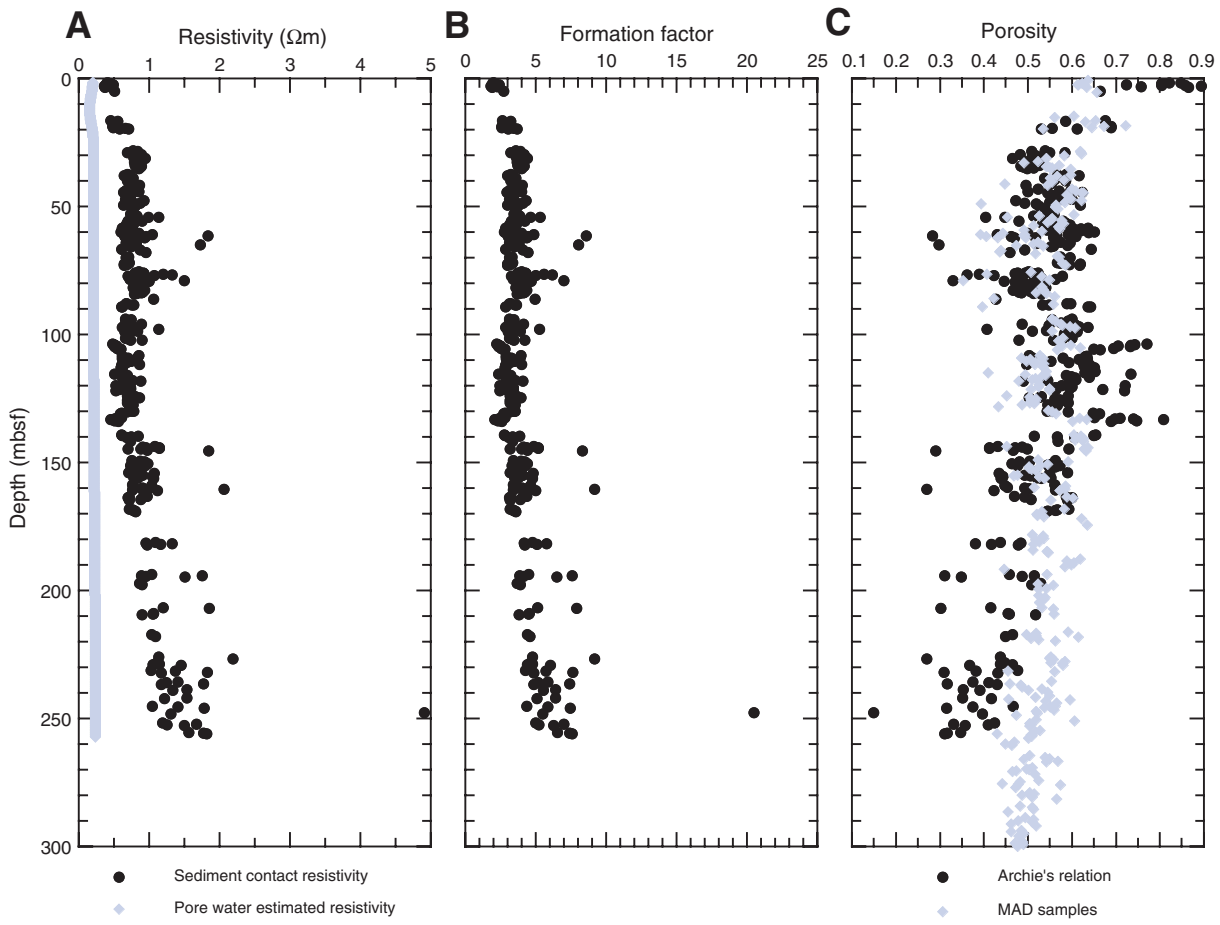

Figure F44 (continued). D. Formation factor vs. MAD porosity. A best-fit solution to Archie's equation gives Archie's parameters as m = 1.36 and a = 1.58. Solid circles = measurements included in the best-fit solution, open circles = sands, squares = outliers excluded from the analysis.

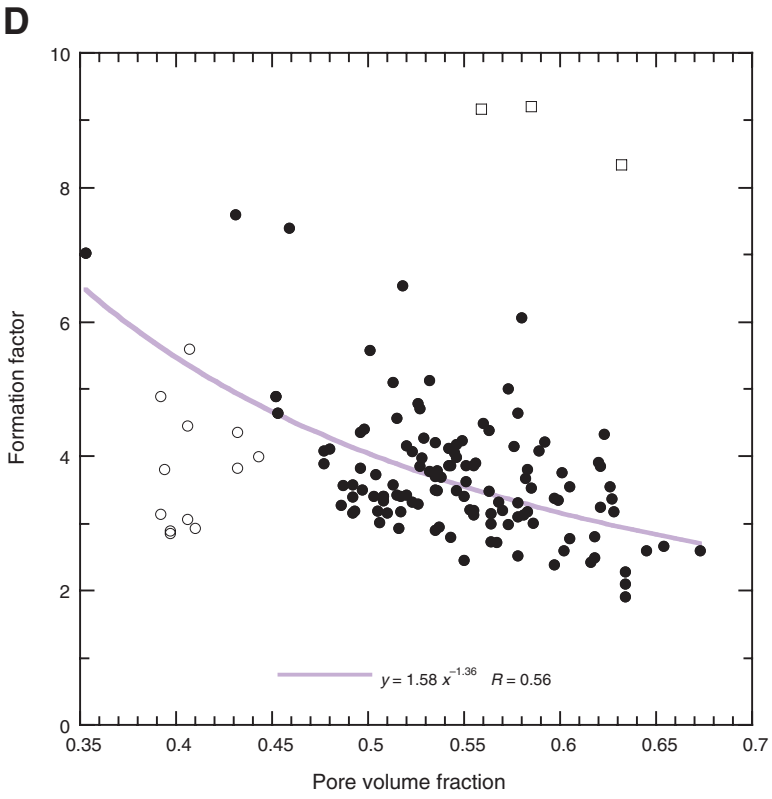

Figure F45. A. Advanced piston corer temperature tool (APCT16) and third-generation advanced piston corer temperature (APCT-3; APC3 in figure) tool in situ temperature measurements from Site U1328. (Continued on next page).

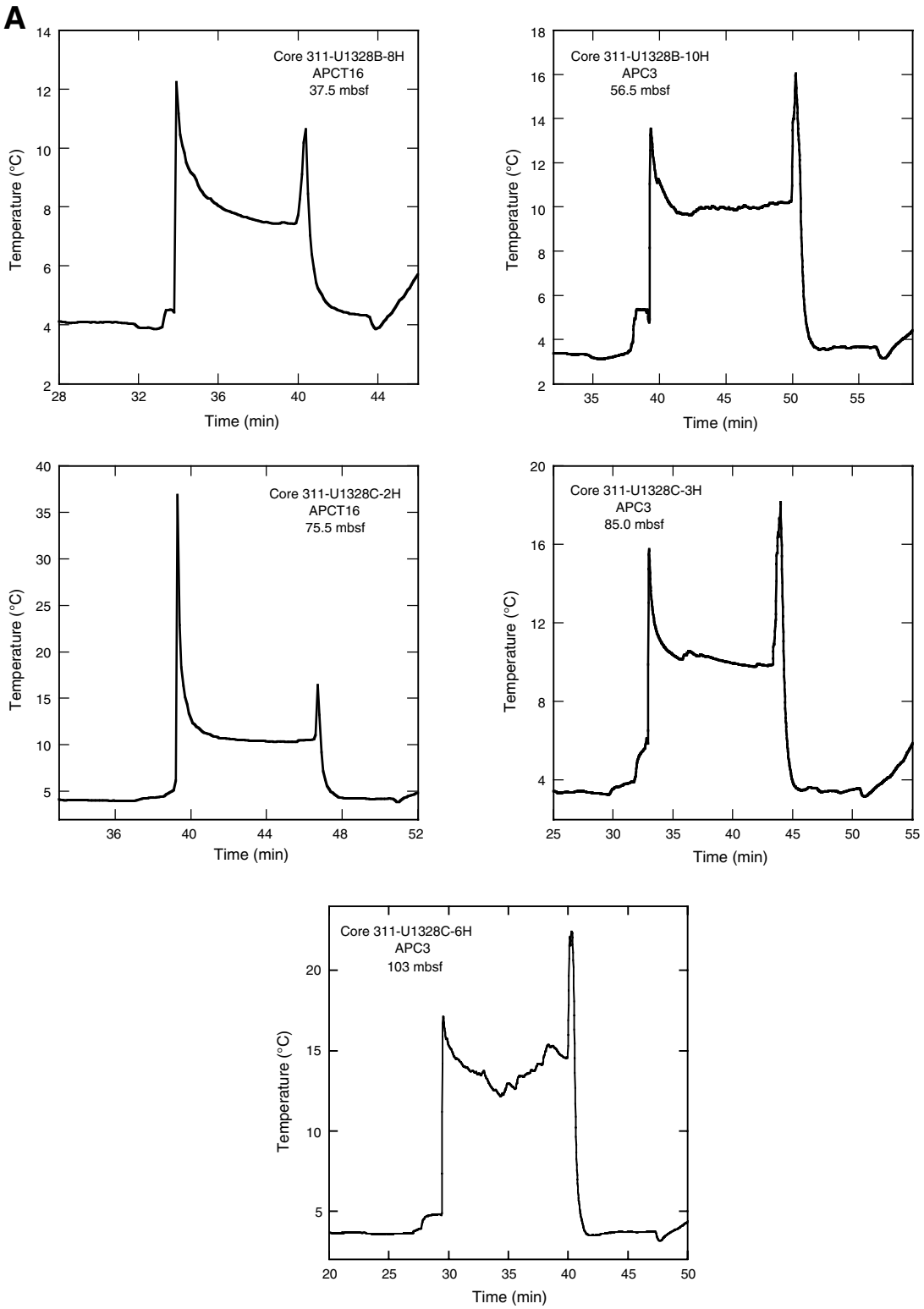

Figure F45 (continued). B. Davis-Villinger Temperature Probe (DVTP) temperature measurements from Site U1328. Both the upper (red) and lower (black) thermistors are shown.

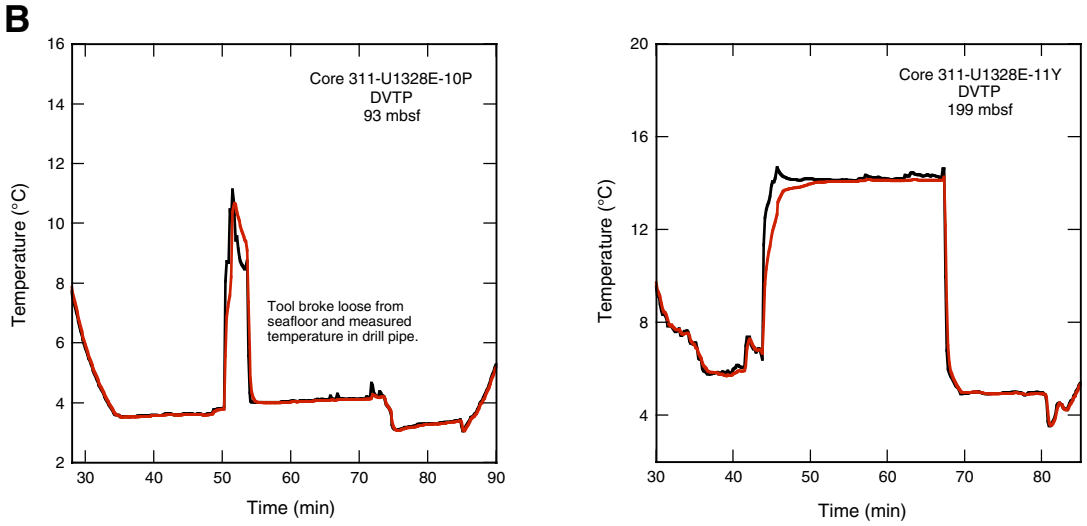

Figure F46. Apparent geothermal gradient at Site U1328 calculated from temperature data obtained during Expedition 311 and ODP Leg 146. See text for further discussion of uncertainties. The stability boundary for methane hydrate at hydrostatic pressure is shown (calculated using CSMHY; Sloan, 1998) for a seawater salinity of 3.5% and for an interstitial water salinity of 3% in the vicinity of the bottom-simulating reflector (BSR) (see **"Interstitial water geochemistry"**). BSR depth based on seismic data, base of gas hydrate stability zone (GHSZ) based on thermal gradient.

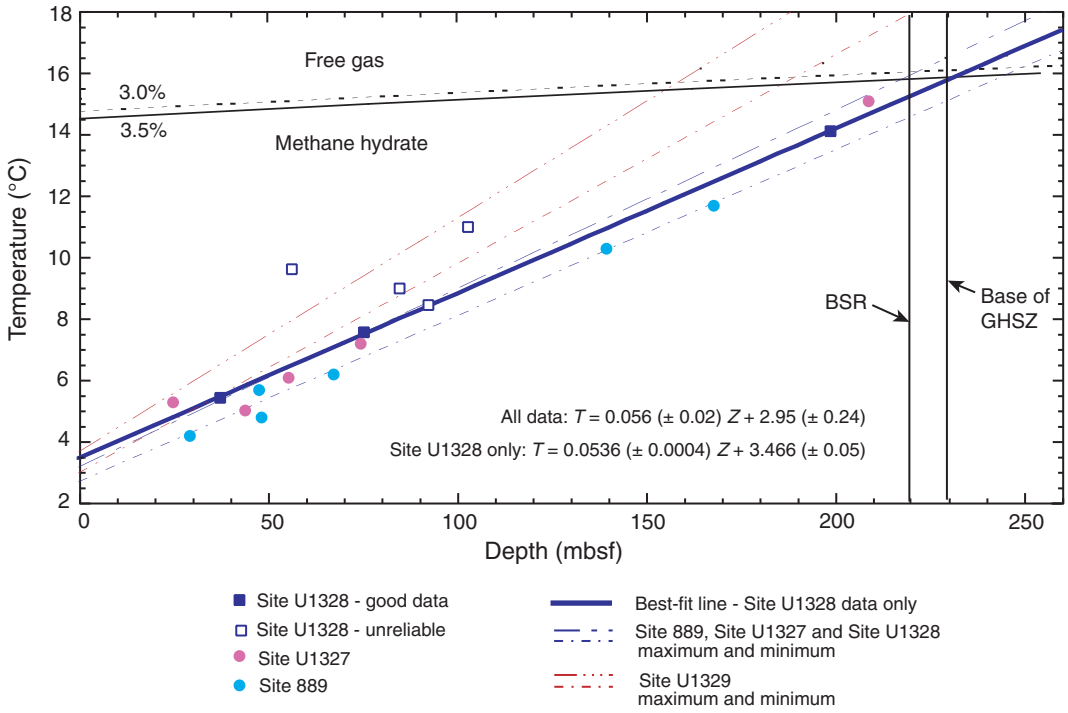

Figure F47. A. Advanced piston corer methane (APCM) tool pressure, temperature, and conductivity histories for Cores 311-U1328C-2H, 3H, and 6H.

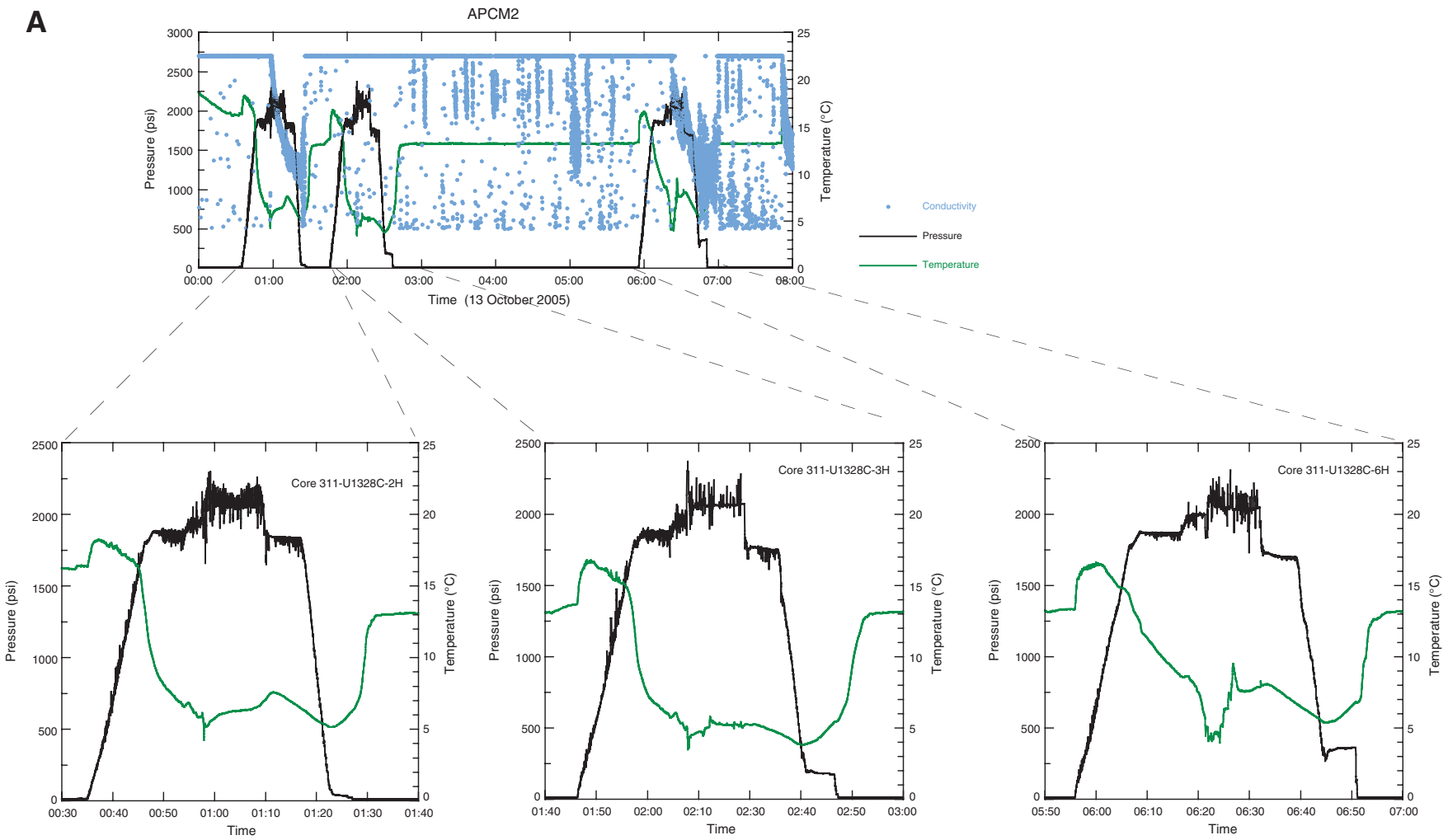

Figure F47 (continued). B. APCM pressure (green) and temperature (black) histories for Cores 311-U1328C-3H and 6H, compared with APCT-3 temperature (blue) histories for the same cores.

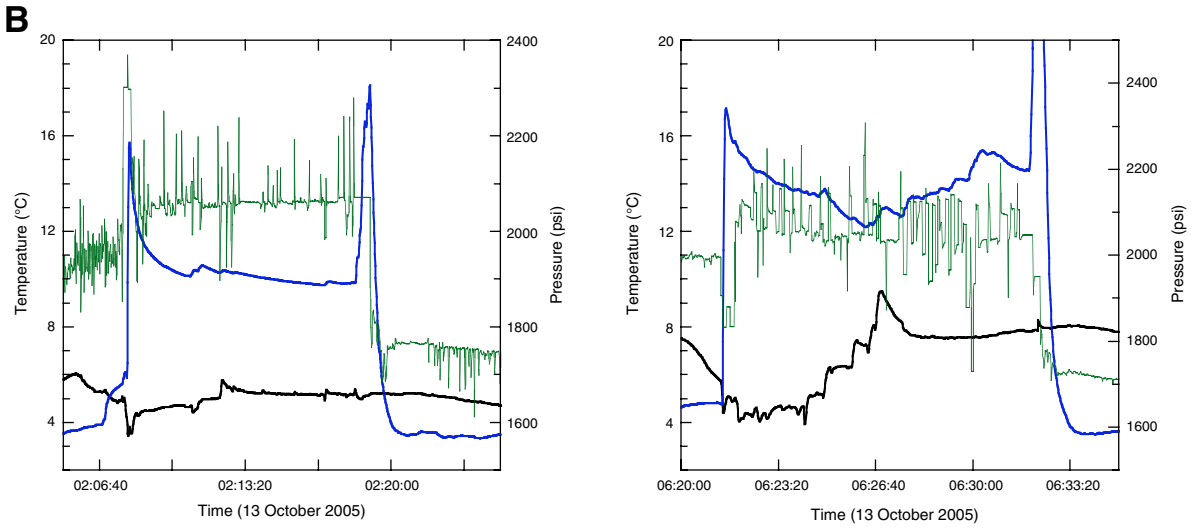

Figure F48. Paleomagnetic data after 20-mT alternating-field demagnetization from Site U1328.

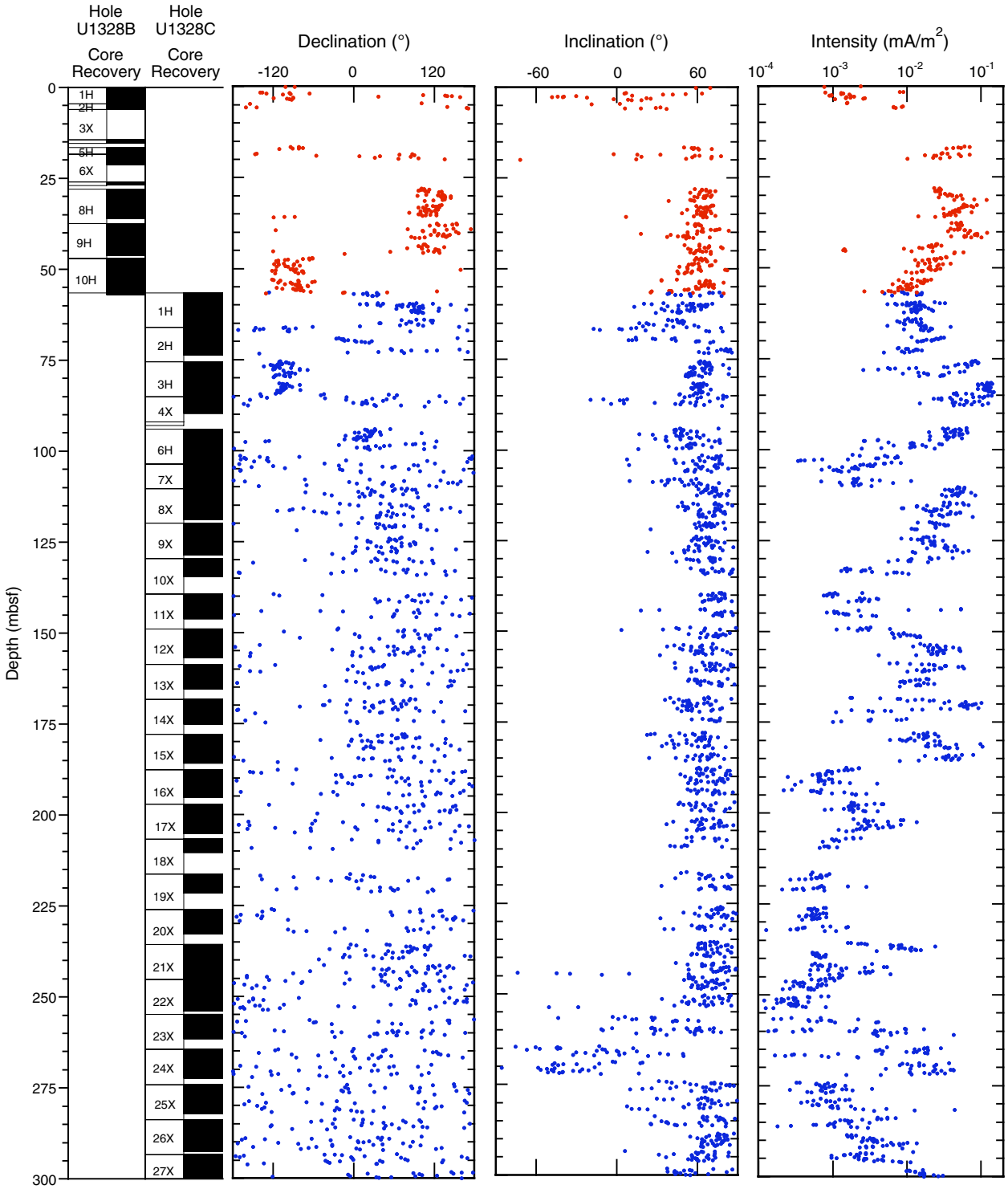

Figure F49. Temperature and pressure vs. elapsed time for each pressure core deployment as recorded by the corer's internal data logger. No data are available for Cores 311-U1328E-2Y and 12E. Deployment and recovery are shaded orange, operation at coring depth is shaded yellow, and autoclave immersion in the ice shuck is shaded blue. The ice shuck contained no ice when Core 311-U1328E-10P was immersed (shaded green). (Continued on next two pages).

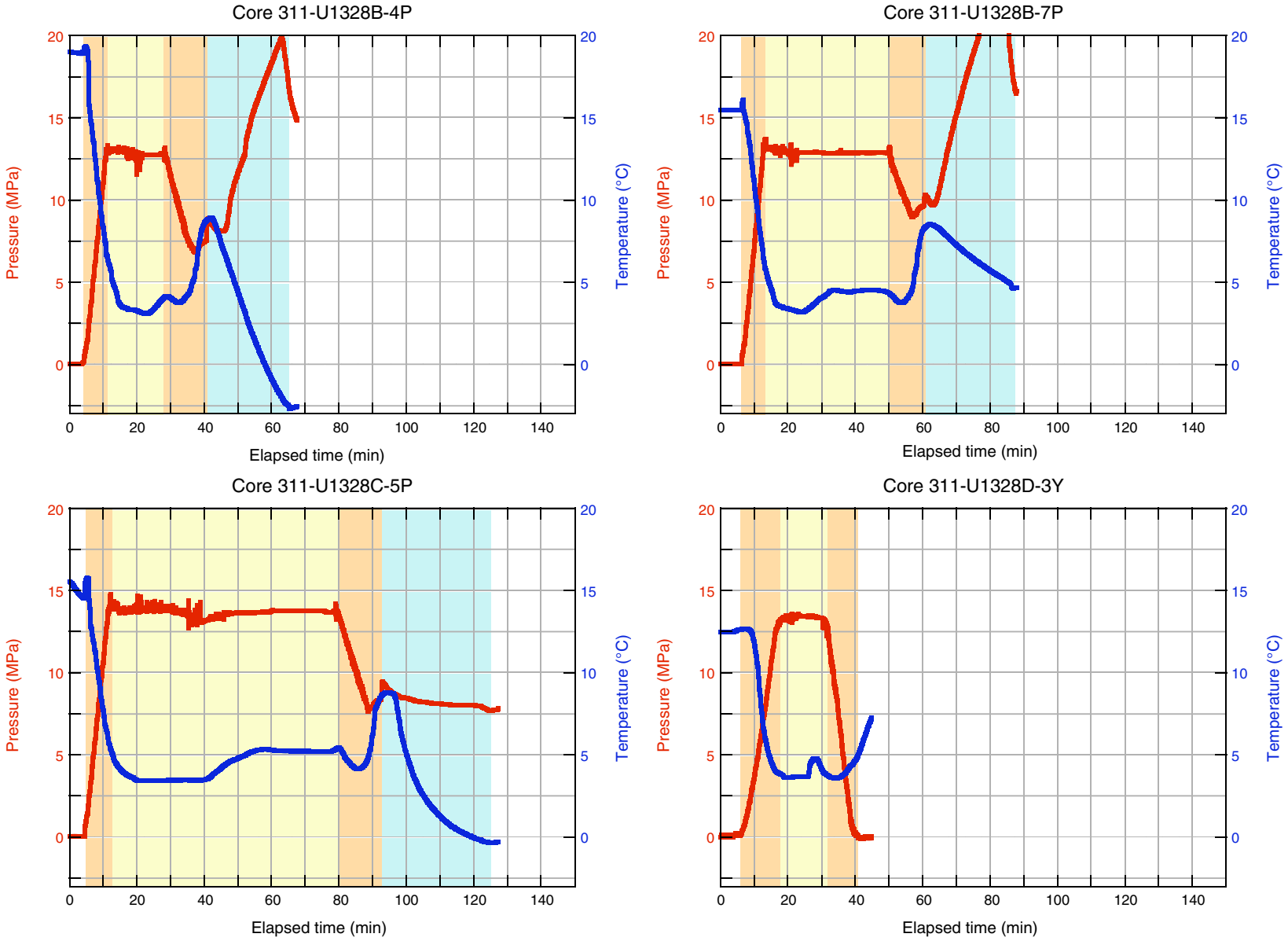

Figure F49 (continued). Temperature and pressure vs. time. (Continued on next page.)

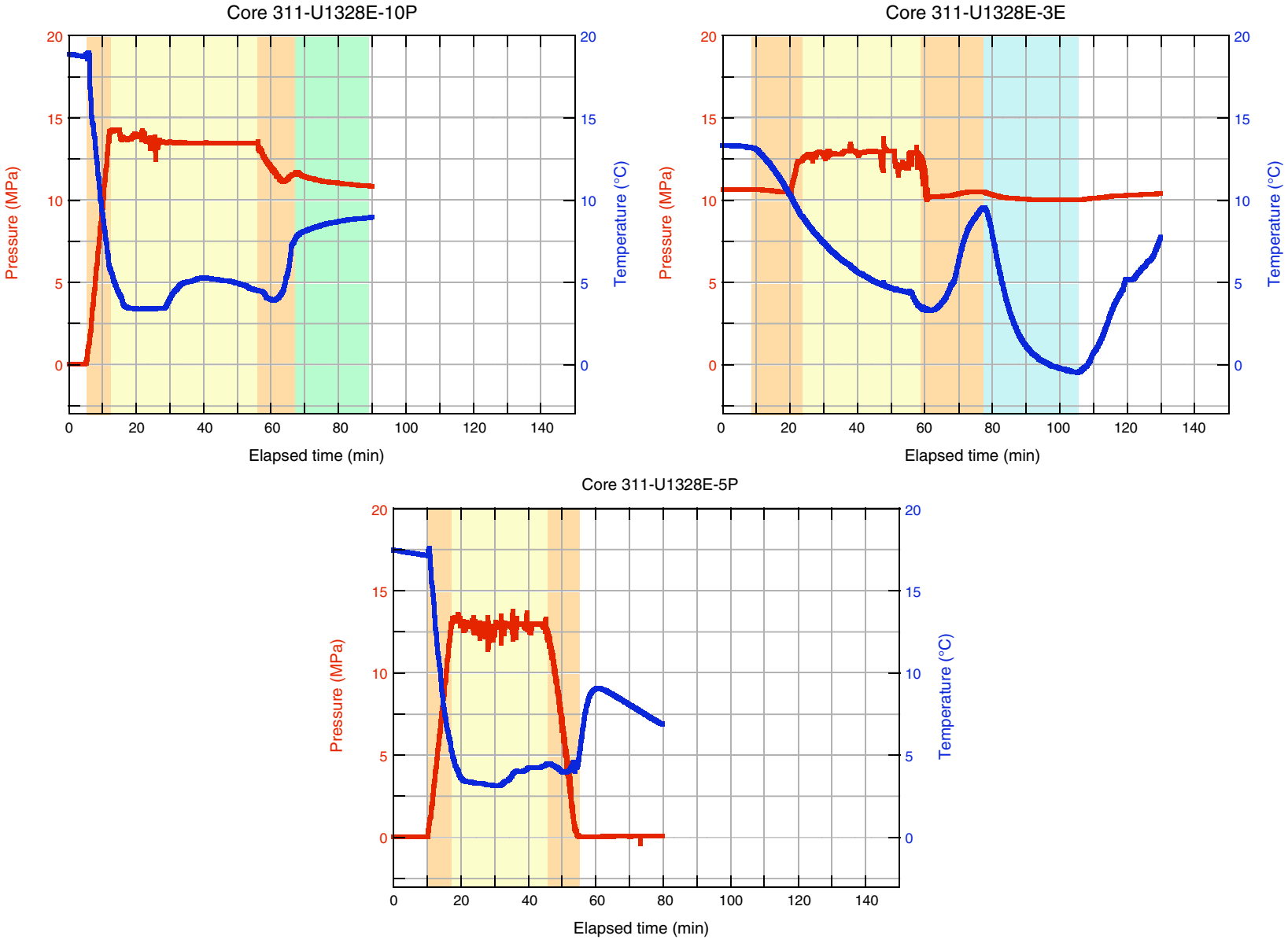

Figure F49 (continued). Temperature and pressure vs. time.

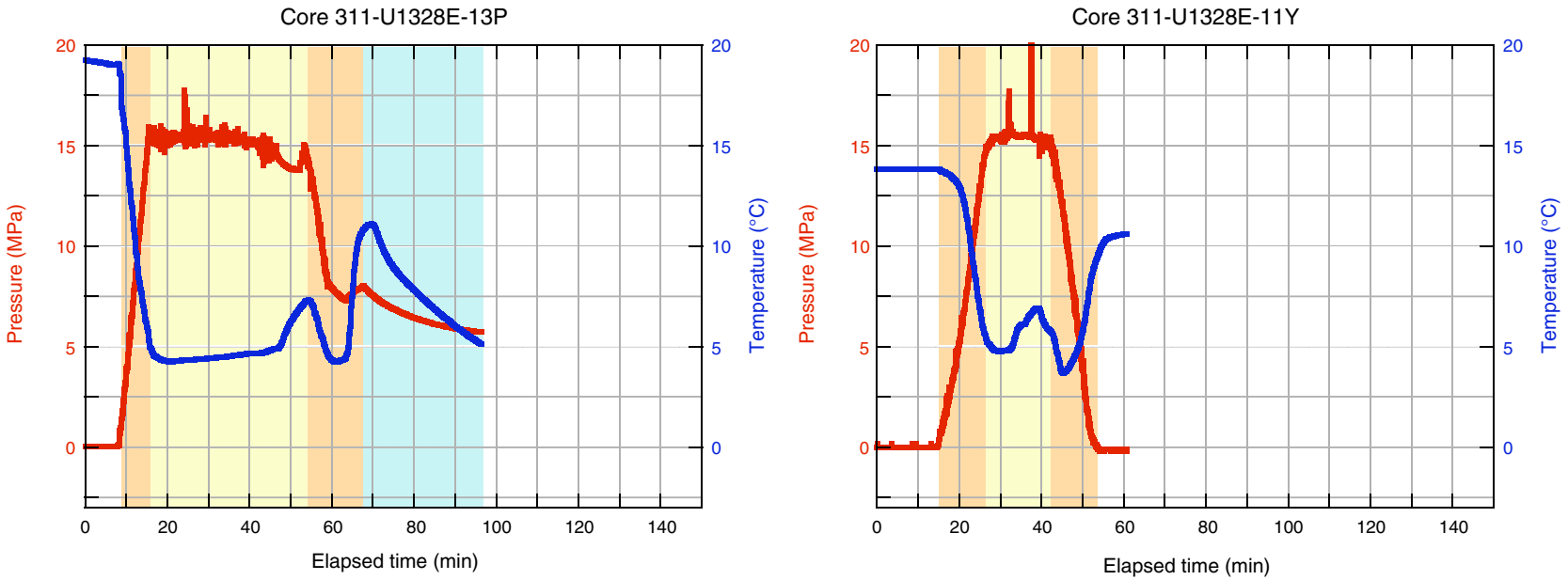

Figure F50. Temperature vs. pressure for all pressure core deployments, showing trajectories relative to gas hydrate stability at 30 and 55 ppt salinity (Xu, 2002, 2004). No data are available for Cores 311-U1328E-7Y and 12E. Circles = final temperature and pressure of autoclave prior to data logger removal, squares = pressure and temperature conditions in the cold laboratory van.

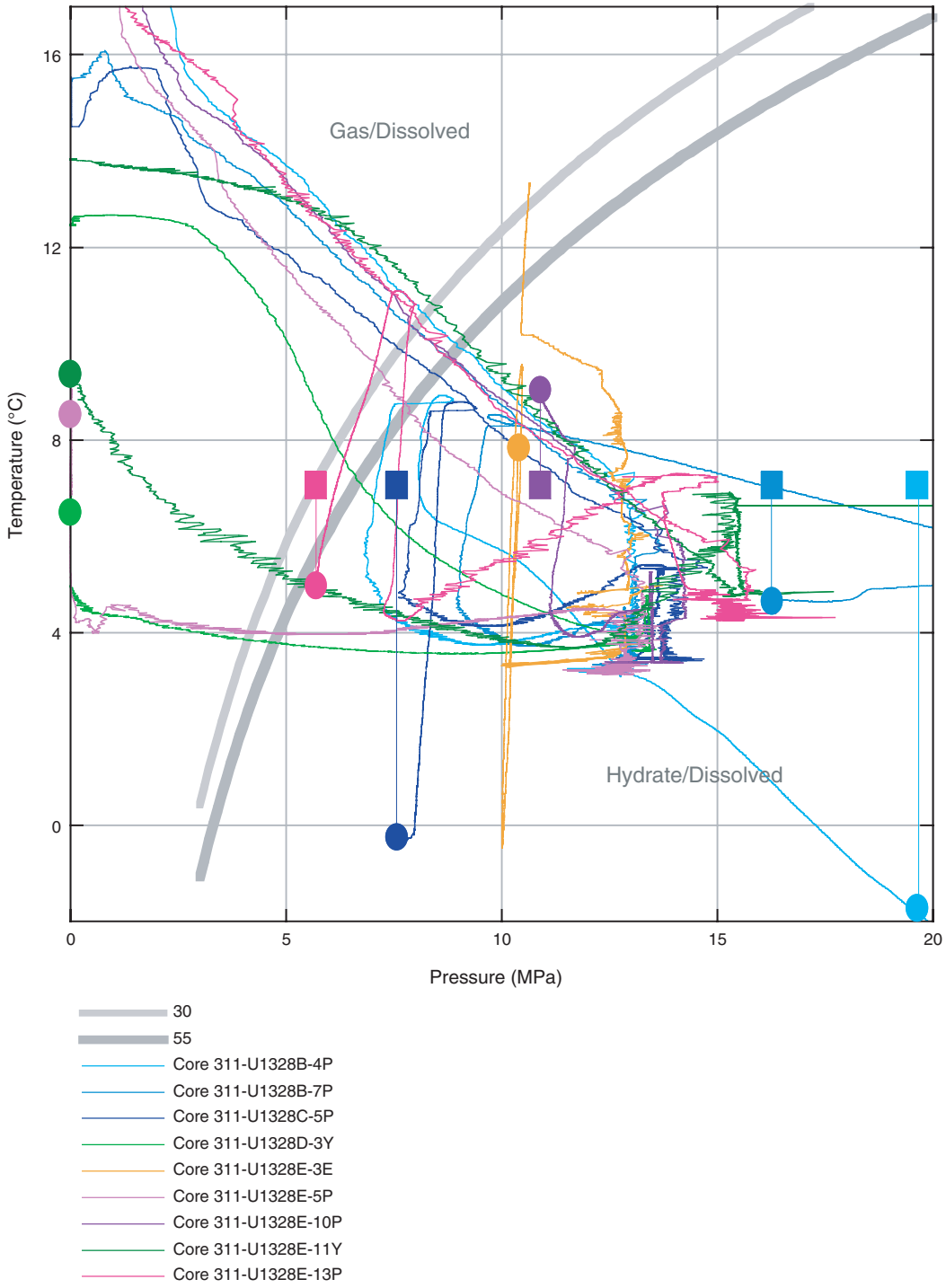

Figure F51. Methane phase diagram with total methane concentrations in the five degassed PCS cores at Site U1328. The seafloor temperature and thermal gradient were taken from **"In situ temperature profile,"** the salinity profile was taken from Table **T4,** and methane saturation was calculated according to Xu (2002, 2004). BSR = bottom-simulating reflector.

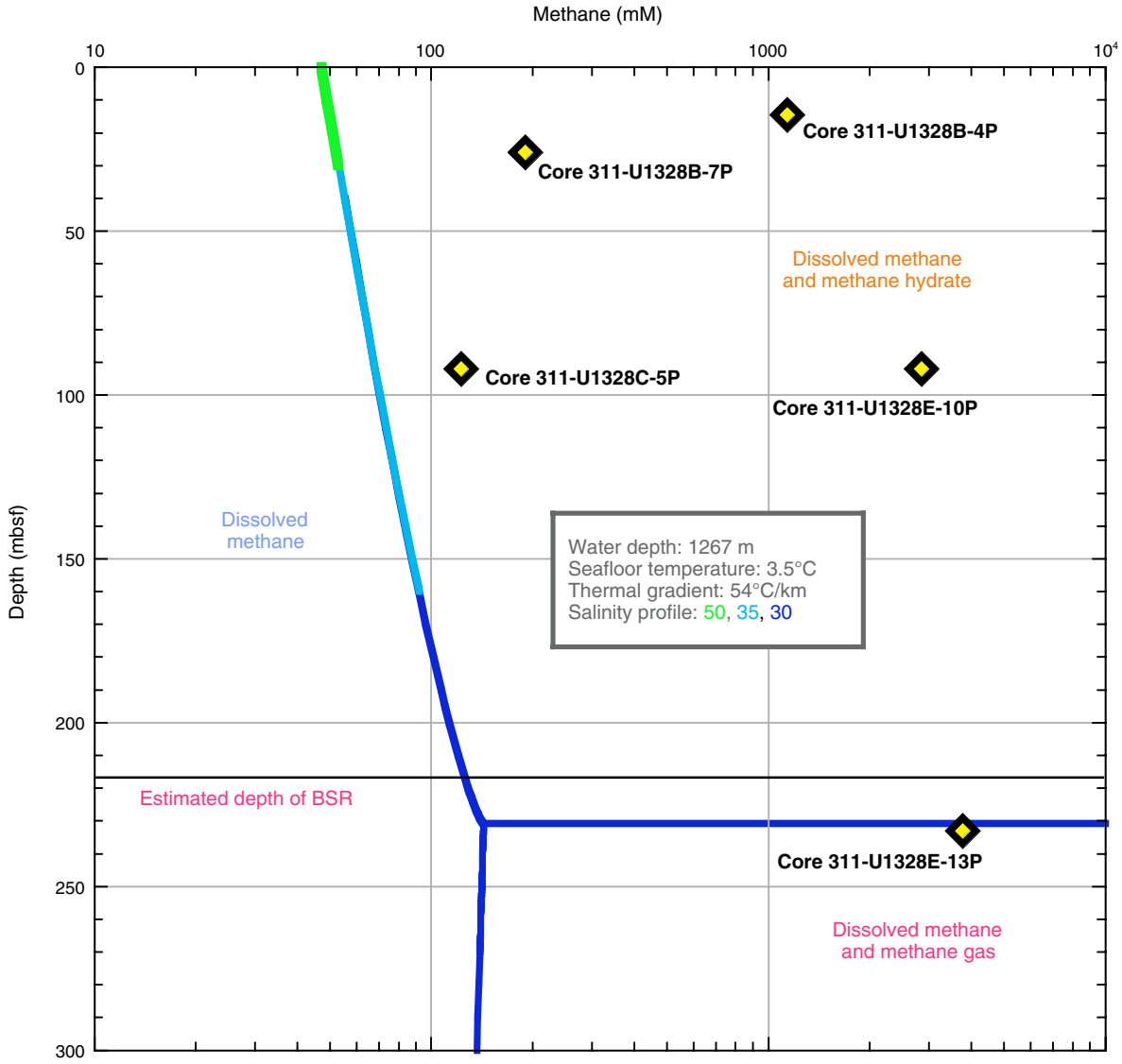

Figure F52. Pressure vs. released gas volume for PCS cores at Site U1328. Arrows = placement of gamma ray density scans. (Continued on next page).

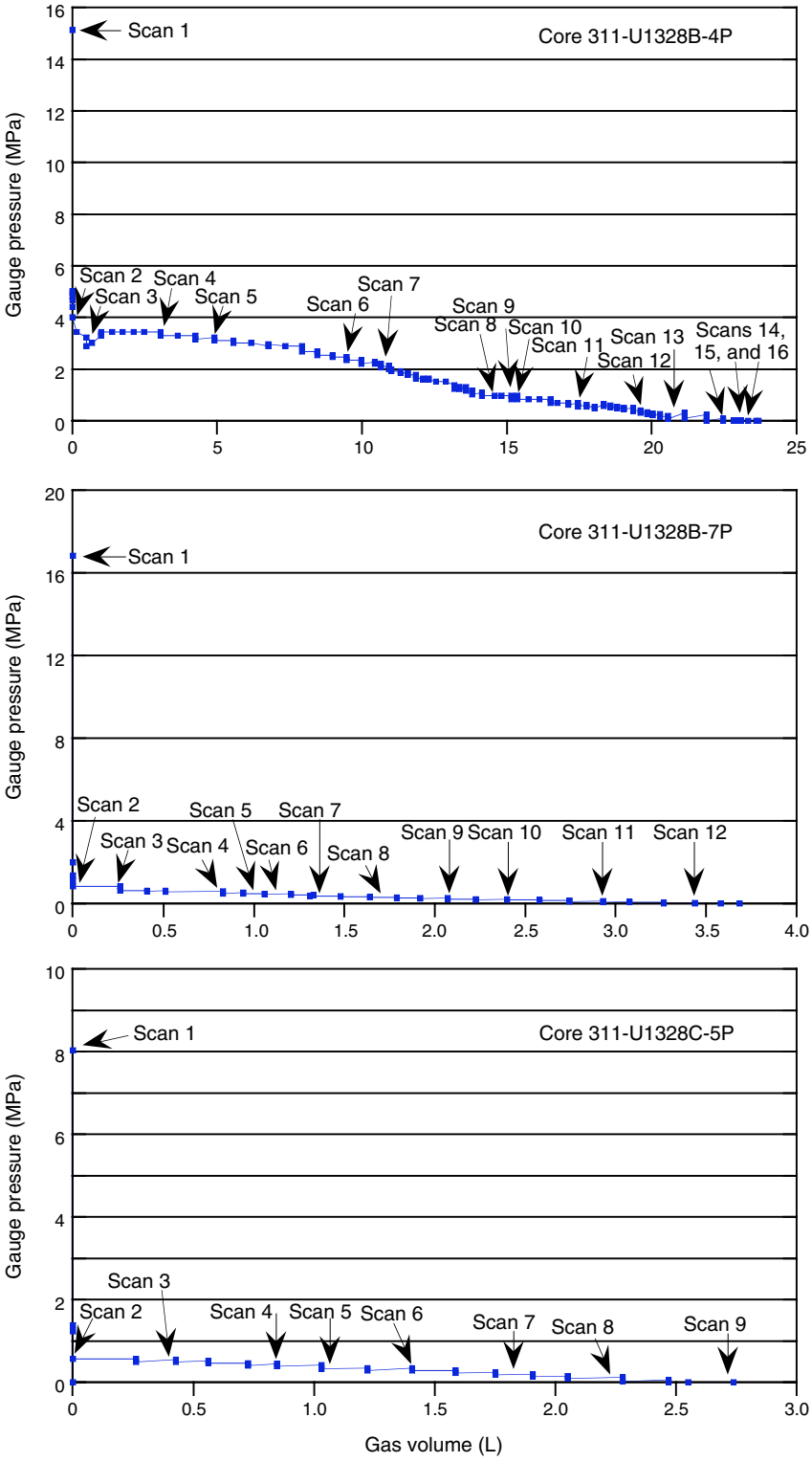

Figure F52 (continued). Pressure vs. released gas.

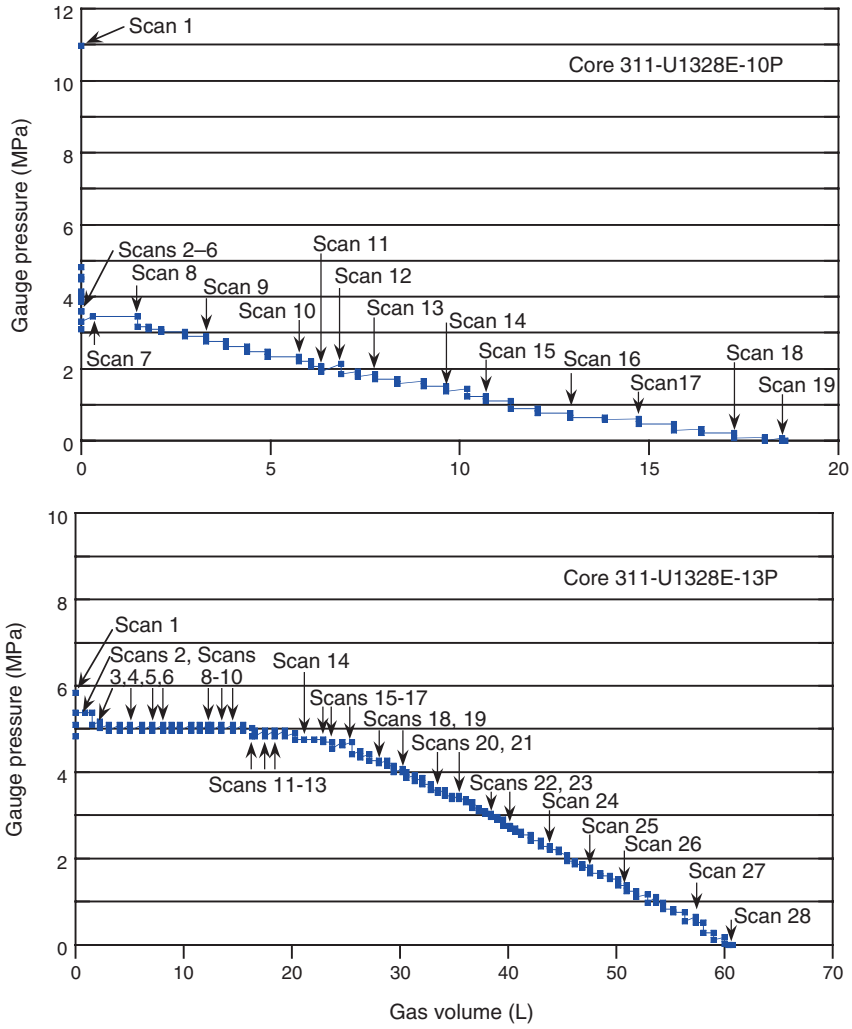

Figure F53. Summary of data collected from PCS cores at Site U1328, including gamma ray density scans collected during degassing, X-ray images collected before degassing, line scan images collected after degassing, and chlorinity data collected in selected zones. Gamma ray density scans are shown as differential density plots (i.e., as profiles from which the initial profile has been subtracted). **A.** Core 311-U1328B-4P. Arrows point to presumed gas hydrate veins imaged before depressurization and the gas voids they created after depressurization. (Continued on next four pages).

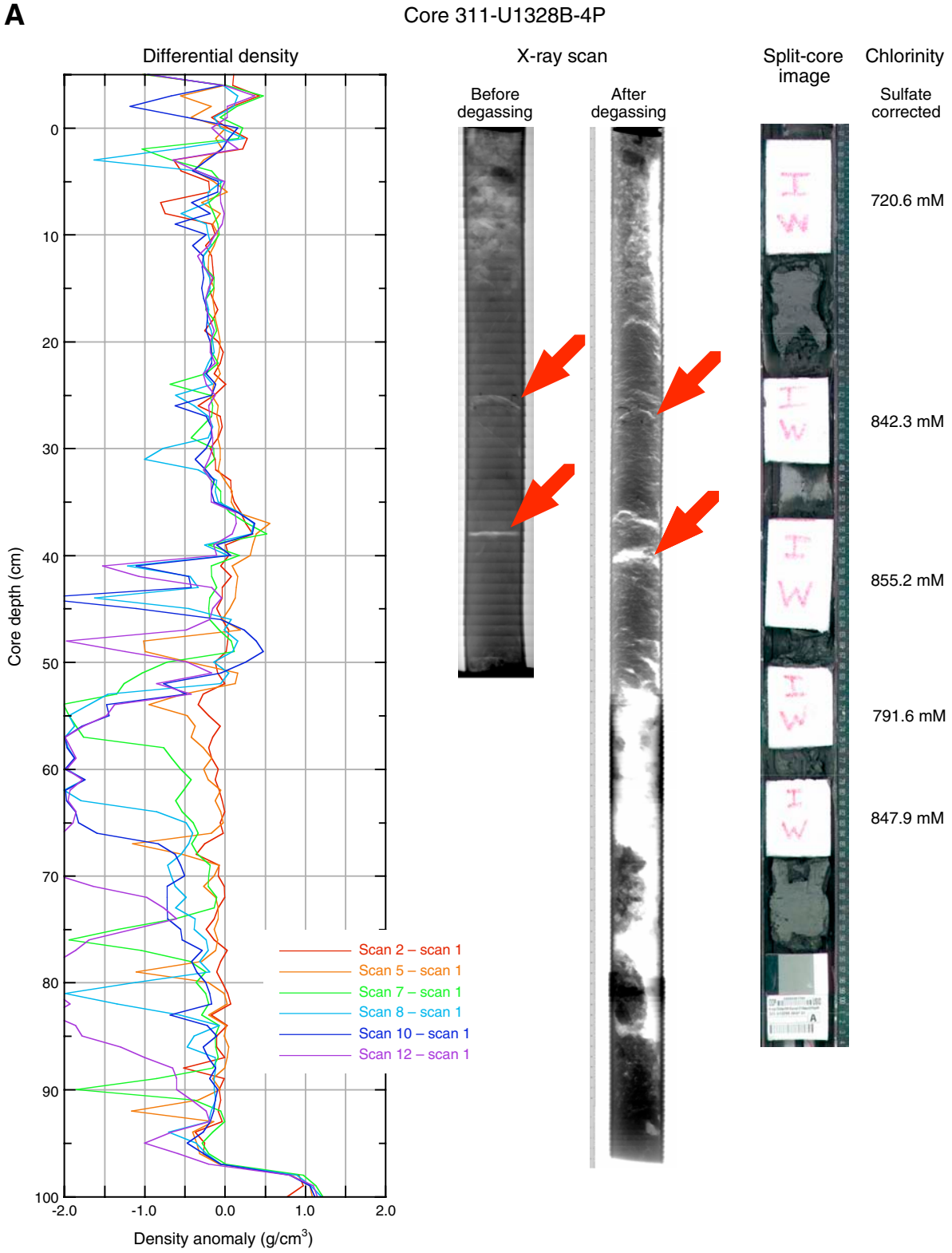

Figure F53 (continued). B. Core 311-U1328B-7P. Core elongated as it was extruded (dashed line). (Continued on next page.)

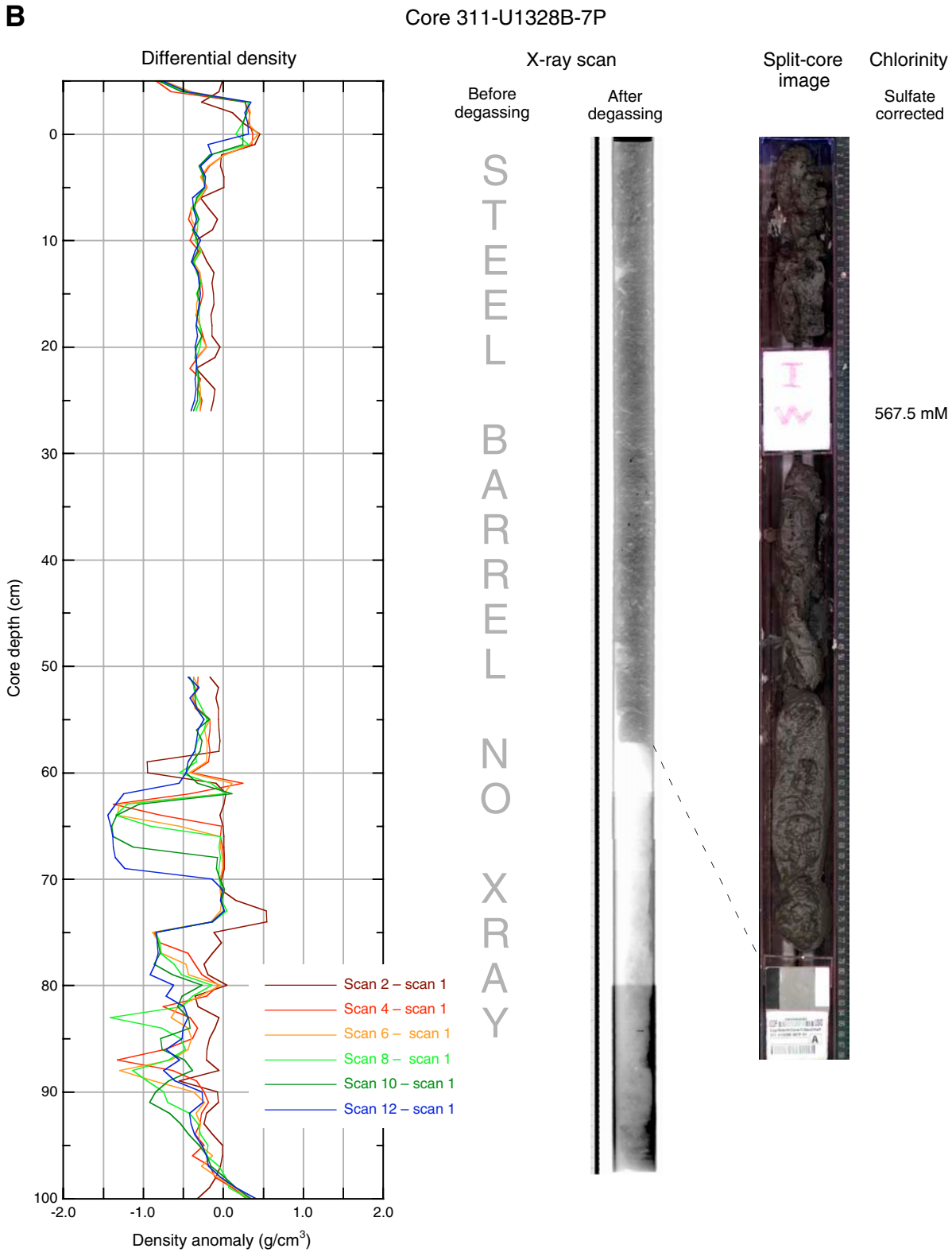

Figure F53 (continued). C. Core 311-U1328C-5P. (Continued on next page.)

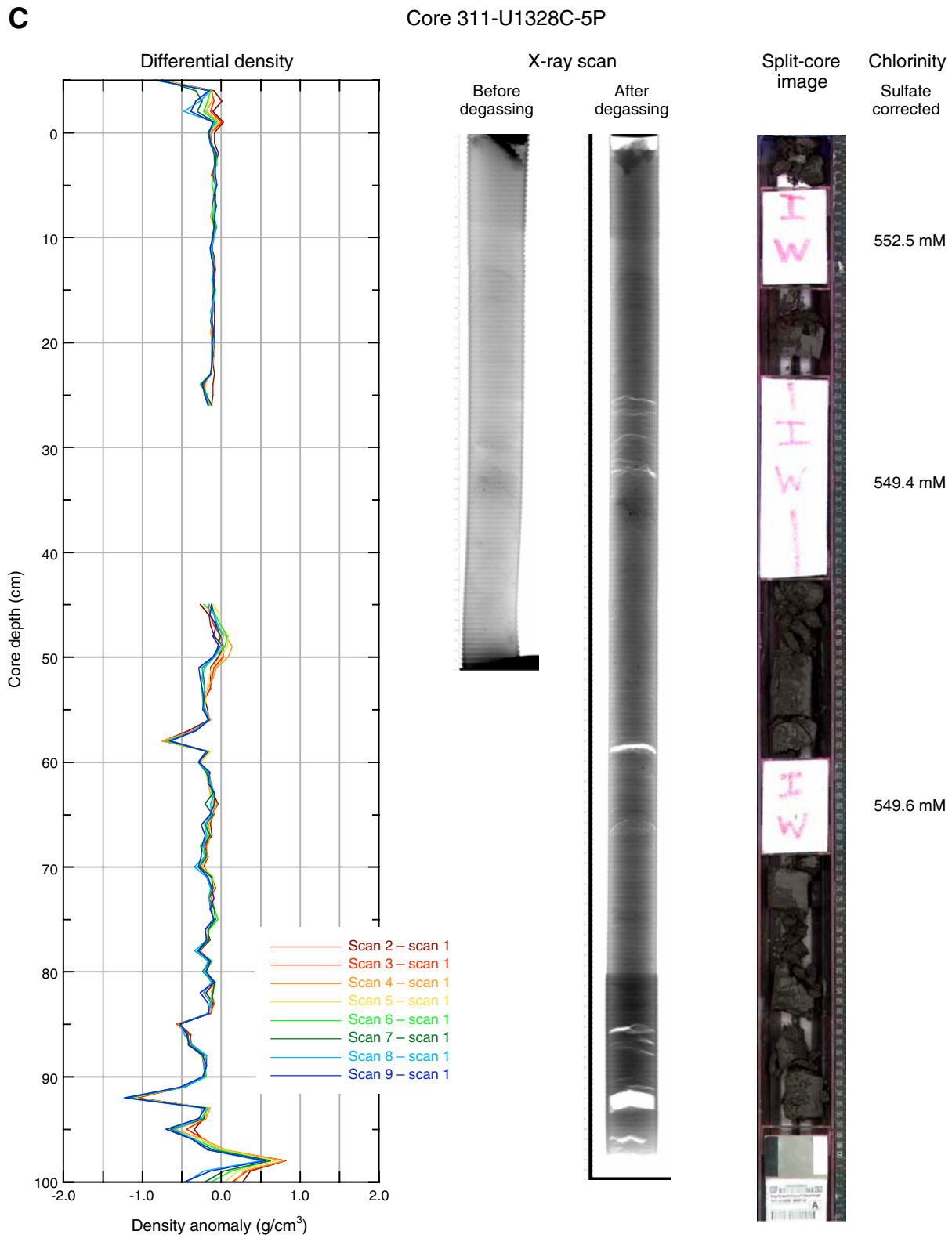

Figure F53 (continued). D. Core 311-U1328E-10P. (Continued on next page.)

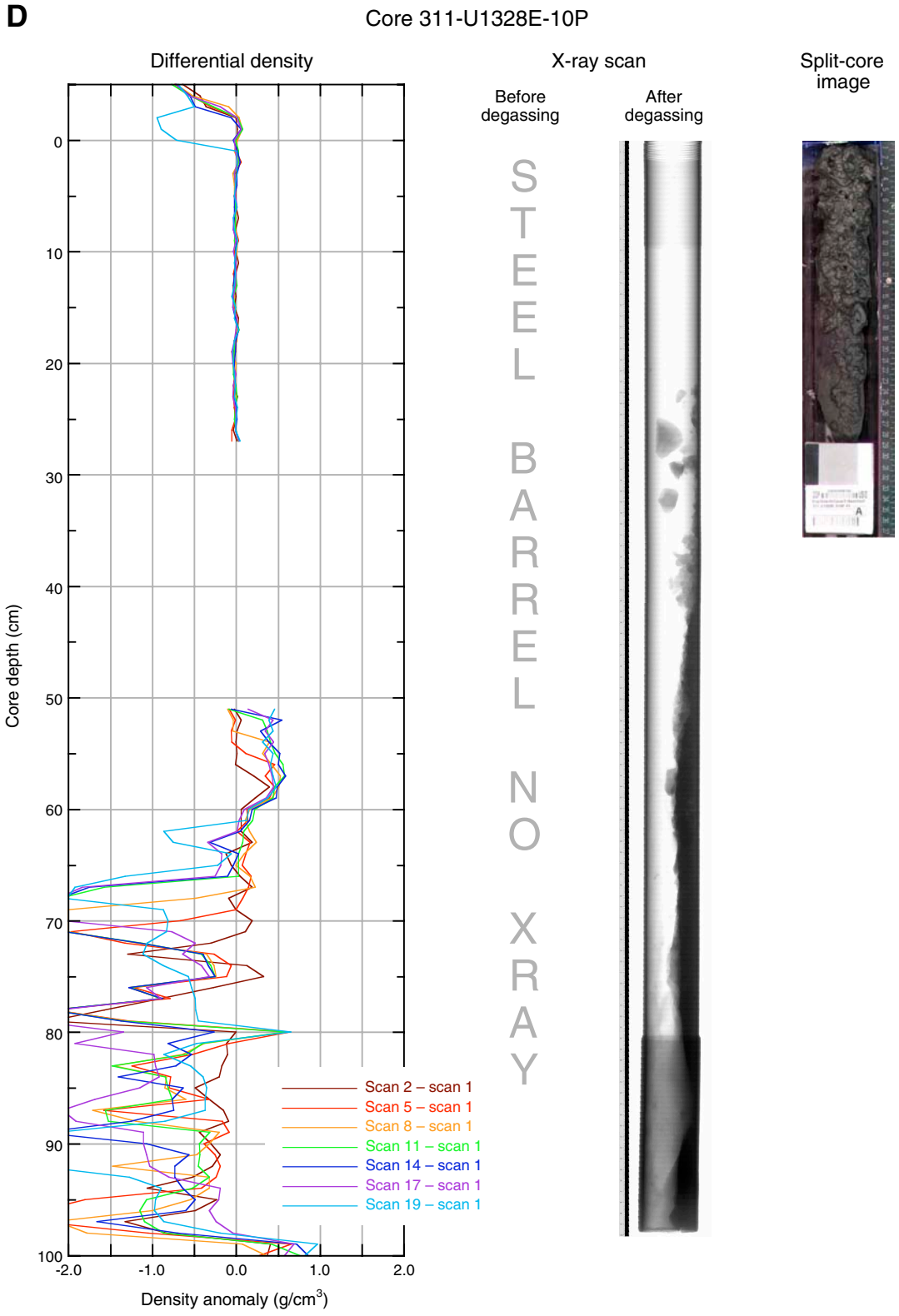

Figure F53 (continued). E. Core 311-U1328E-13P.

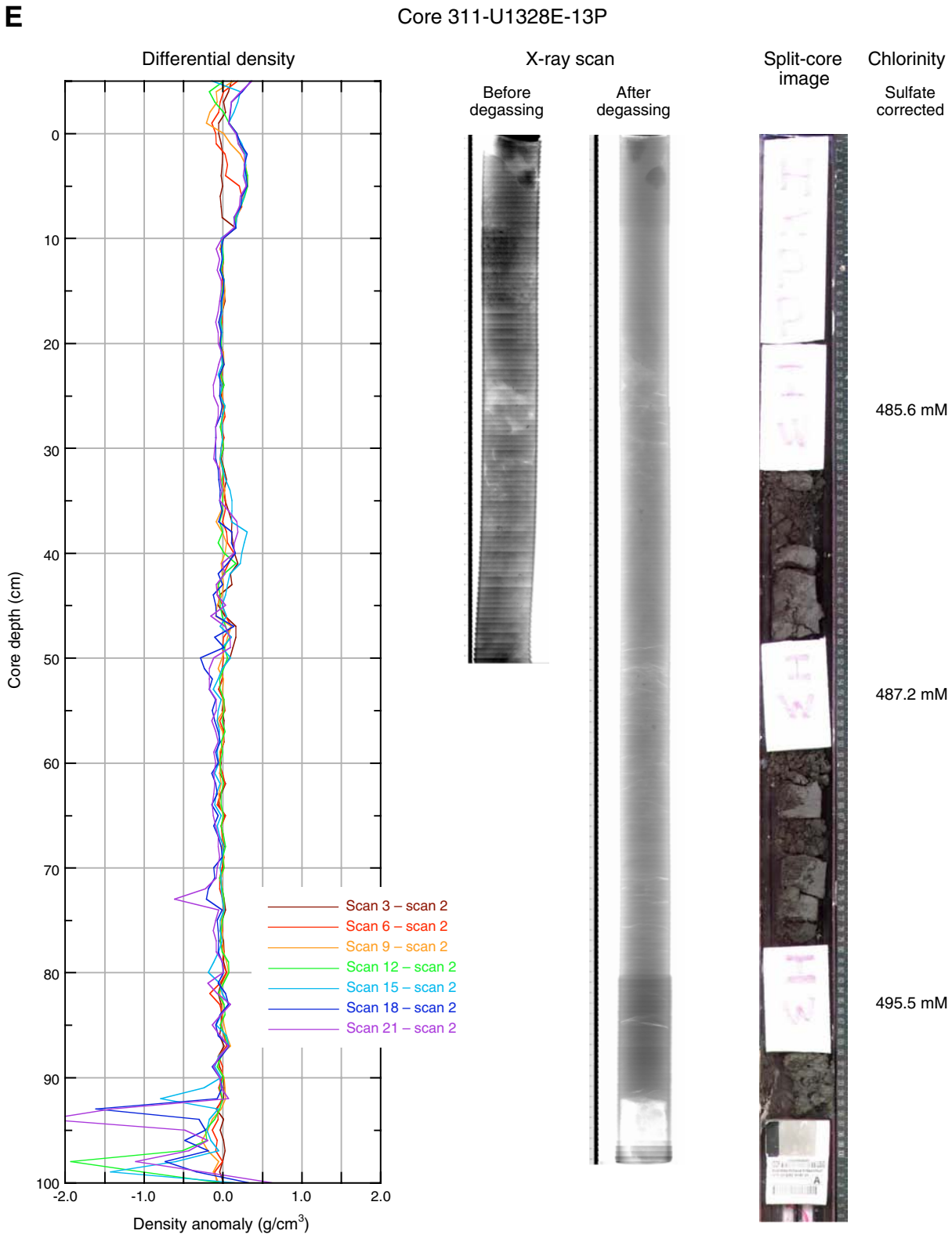

Figure F54. Repeated gamma ray density scans plotted as differential density profiles (i.e., the initial density profile has been subtracted from each of the subsequent profiles) taken during the degassing of Core 311-U1328B-4P showing movement of sediment and gas out of the bottom of the inner core barrel. X-ray images taken before and after degassing are shown on either side of the differential density profiles. *P* = pressure, cum. *V* = cumulative volume, Δ*V* = change in volume.

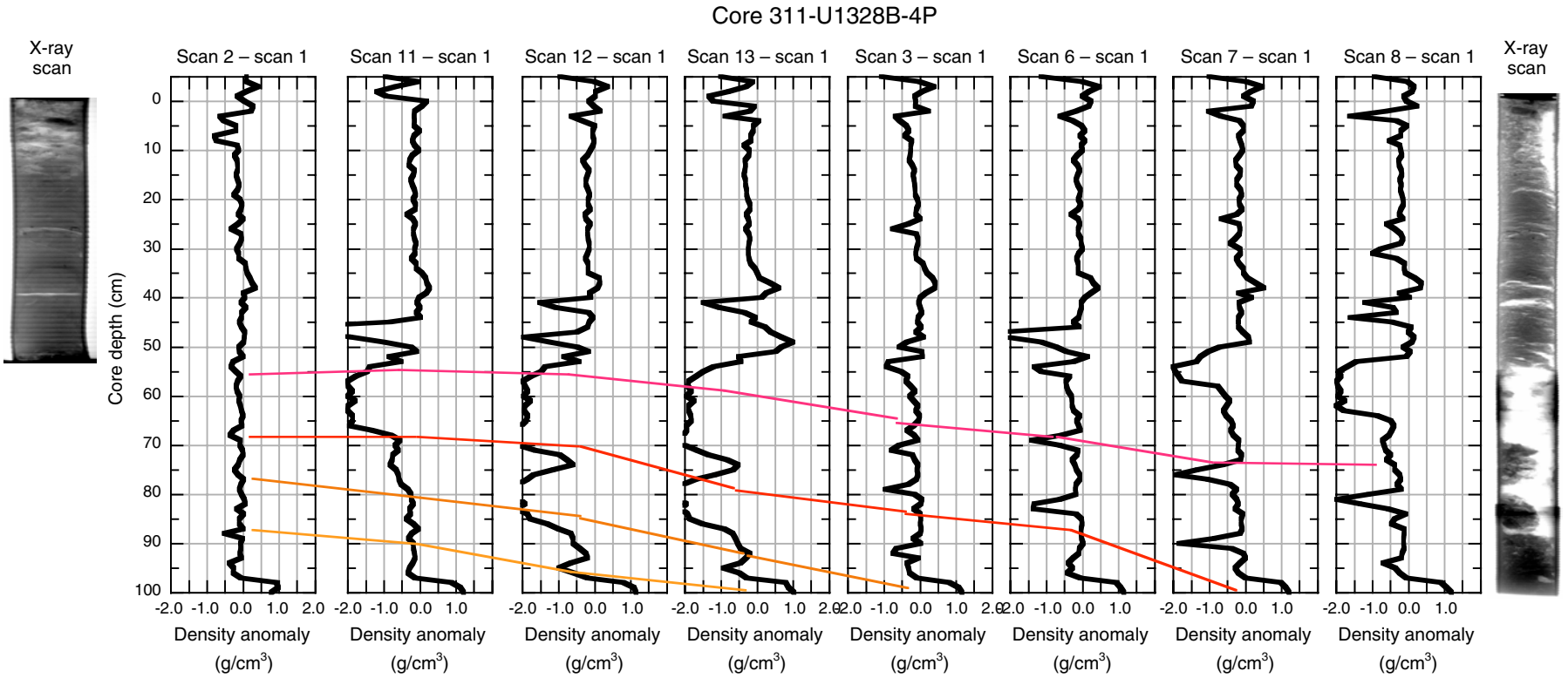

P (MPa)	44	30	25	15	0.97	0.69	0.41	0.17
cum. *V* (L)	0	0.7	9.8	12.6	14.6	17.5	19.6	21.9
Δ*V* (L)	--	0.7	9.1	2.8	2.0	2.9	2.1	2.3

Figure F55. Repeated gamma ray density scans taken during the degassing of Core 311-U1328E-10P showing movement of sediment and gas out of the bottom of the inner core barrel. The data are plotted as differential density profiles (i.e., as profiles from which the initial gamma ray density scan has been subtracted). Each successive profile is offset by 1 g/cm³. Top of sediment is at ~63 cm core depth and rises during the experiment. Excursions in the graphs between 30 and 50 cm core depth are an artifact created by the interaction between the PCS and the vertical multisensor core logger.

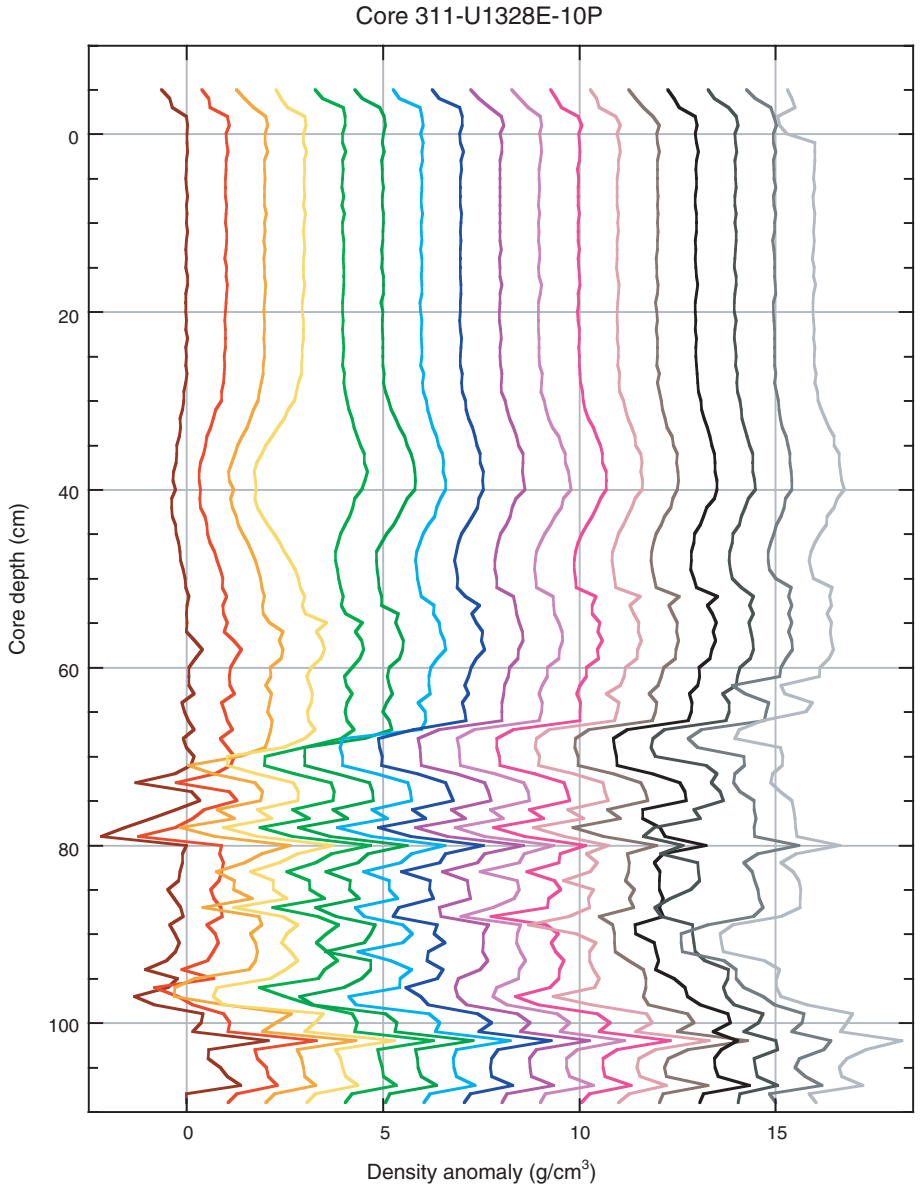

Figure F56. Monitoring and quality control LWD/MWD logs from Hole U1328A.

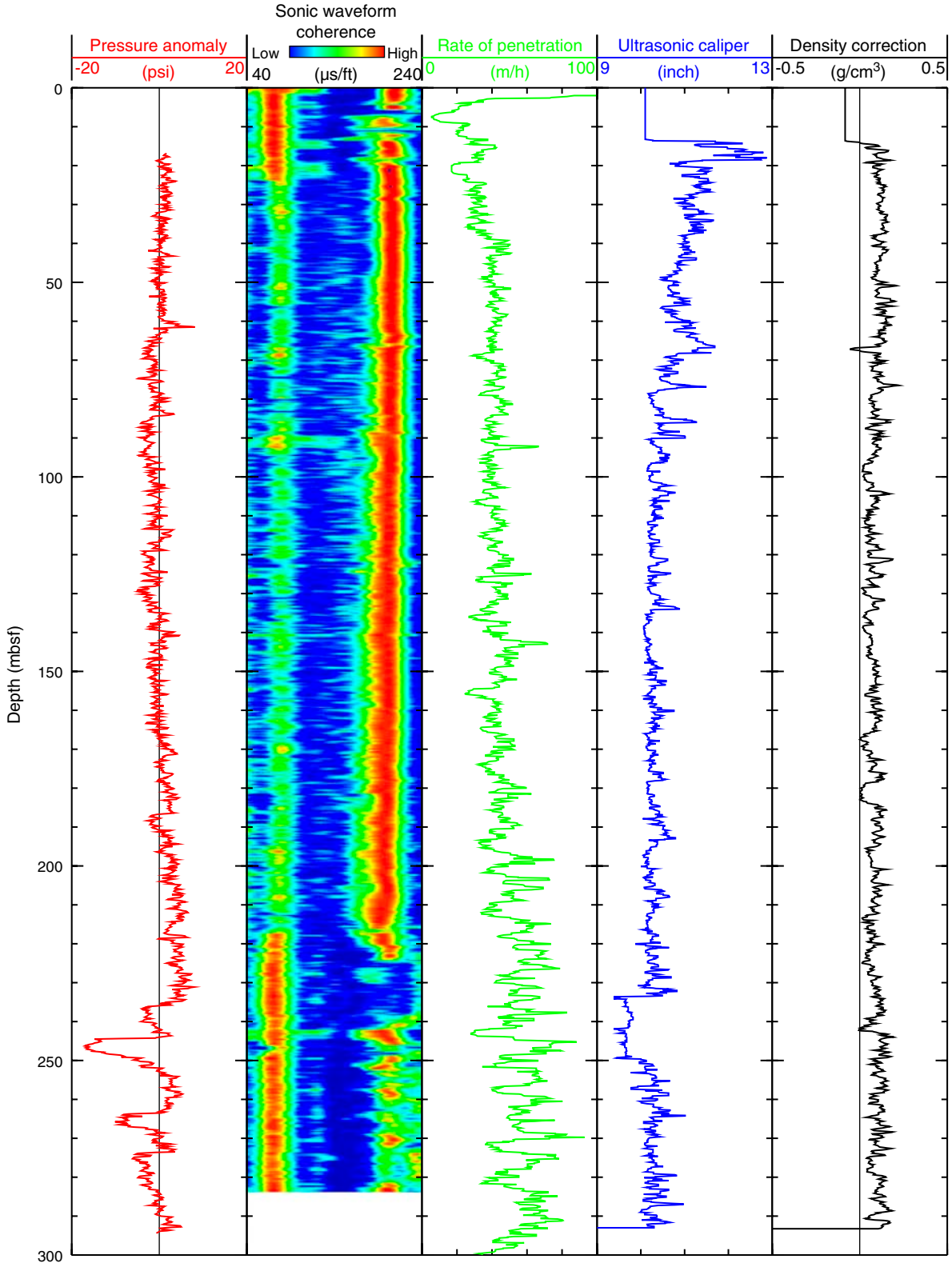

Figure F57. Summary of LWD data from Hole U1328A. avg. = average, P16B = phase-shift resistivity measured by the EcoScope tool at a source-receiver spacing of 16 inch (41 cm), A40B = attenuation resistivity measured by the EcoScope tool at a source-receiver spacing of 40 inch (102 cm), RAB = resistivity-at-the-bit image obtained by the GeoVISION tool.

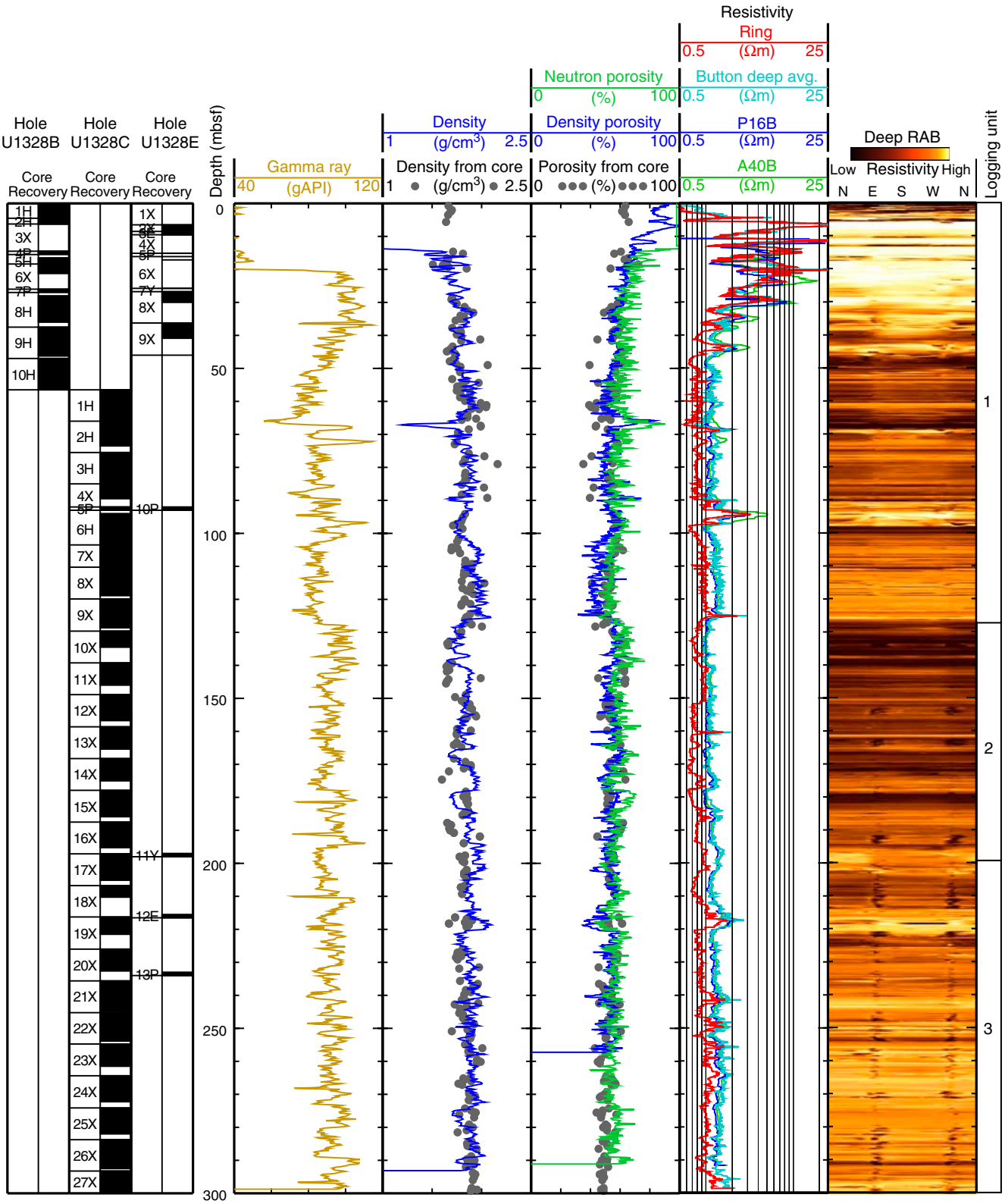

Figure F58. Summary of wireline logging data from Hole U1328C. FMS = Formation MicroScanner, V_P = *P*-wave velocity, V_S = *S*-wave velocity, SFLU = spherically focused resistivity.

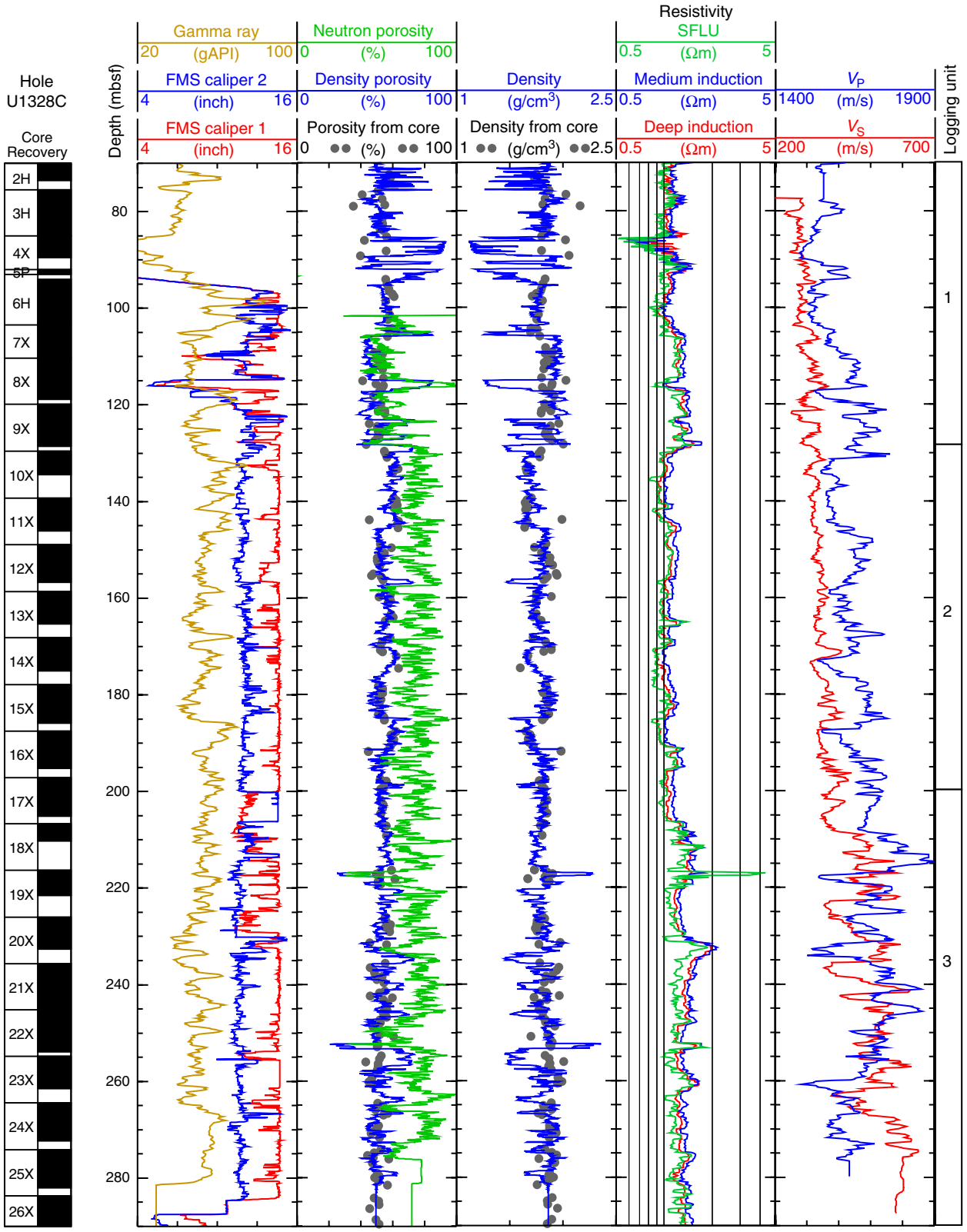

Figure F59. Sonic waveform data, *P*-wave velocity, and *S*-wave velocity obtained with the wireline Dipole Sonic Imager tool in Hole U1328C. SFLU = spherically focused resistivity, V_P = *P*-wave velocity, Mono. = monopole, UD = upper dipole, V_S = *S*-wave velocity, LD = lower dipole.

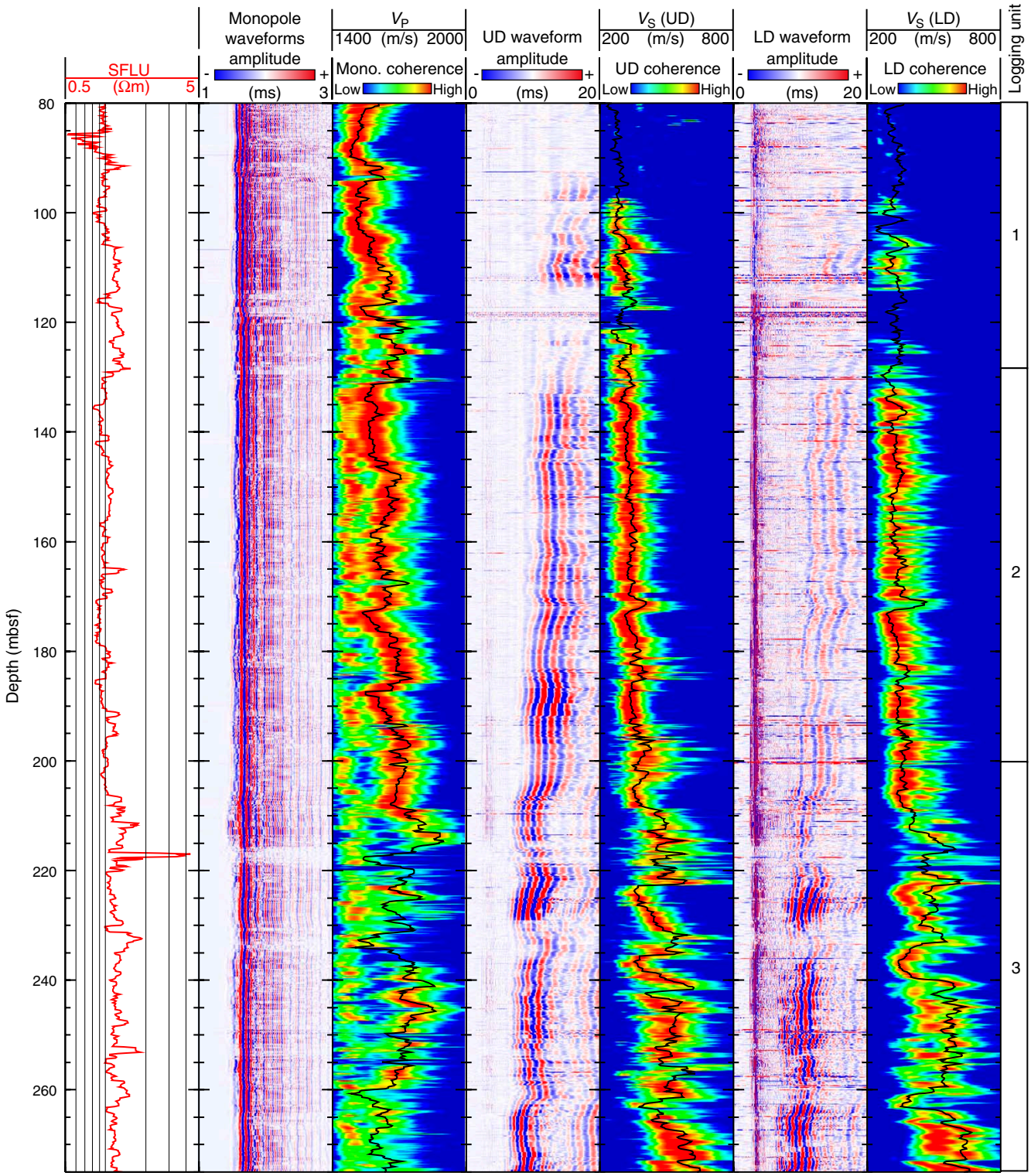

Figure F60. Comparison of logging-while-drilling (LWD; Hole U1328A) and wireline logging (WL; Hole U1328C data. por. = porosity, SFLU = spherically focused resistivity, P16B = phase-shift resistivity measured by the EcoScope tool at a source-receiver spacing of 16 inch (41 cm), avg. = average.

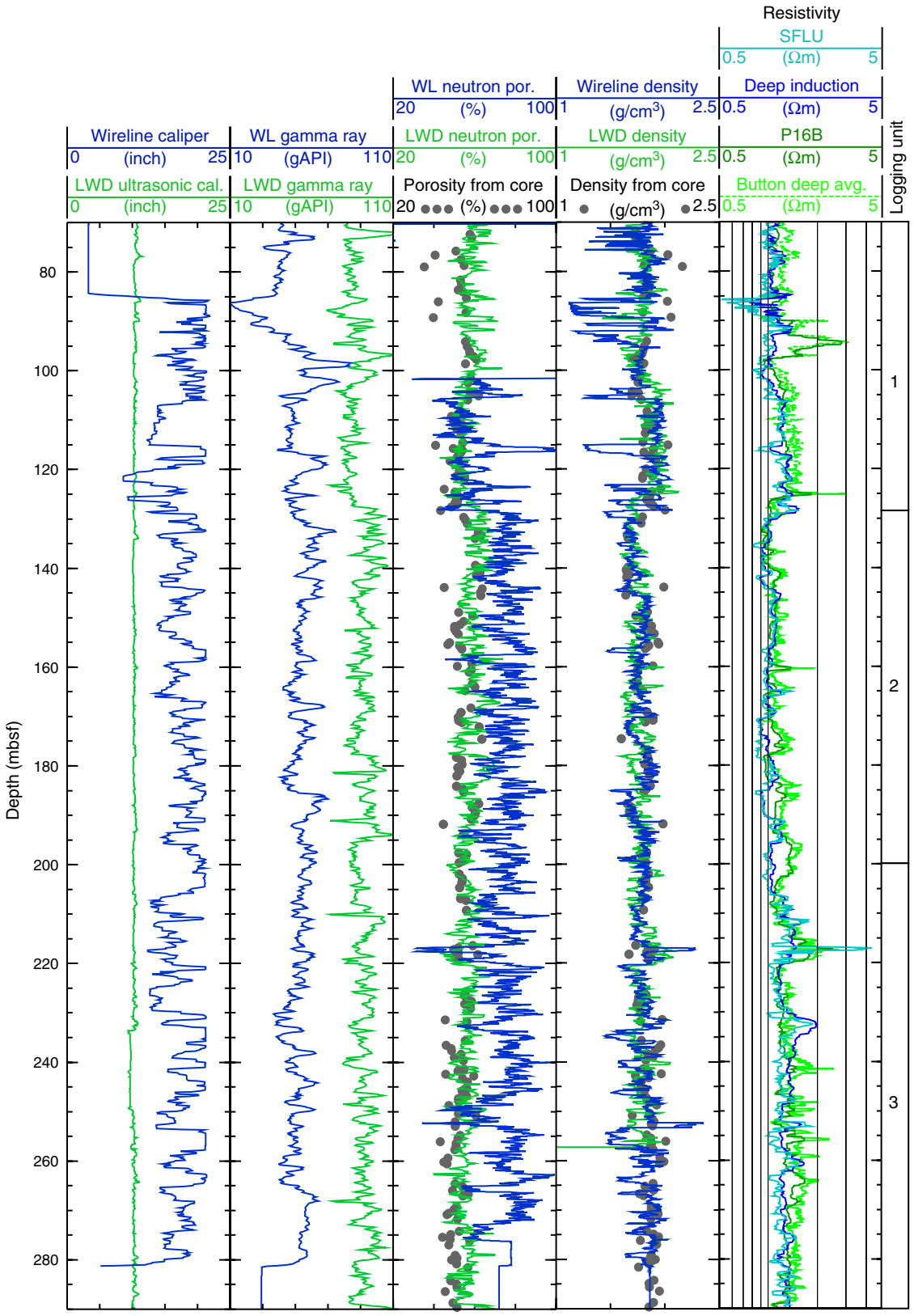

Figure F61. LWD image data from Hole U1328A. RAB = resistivity-at-the-bit image obtained by the GeoVISION tool.

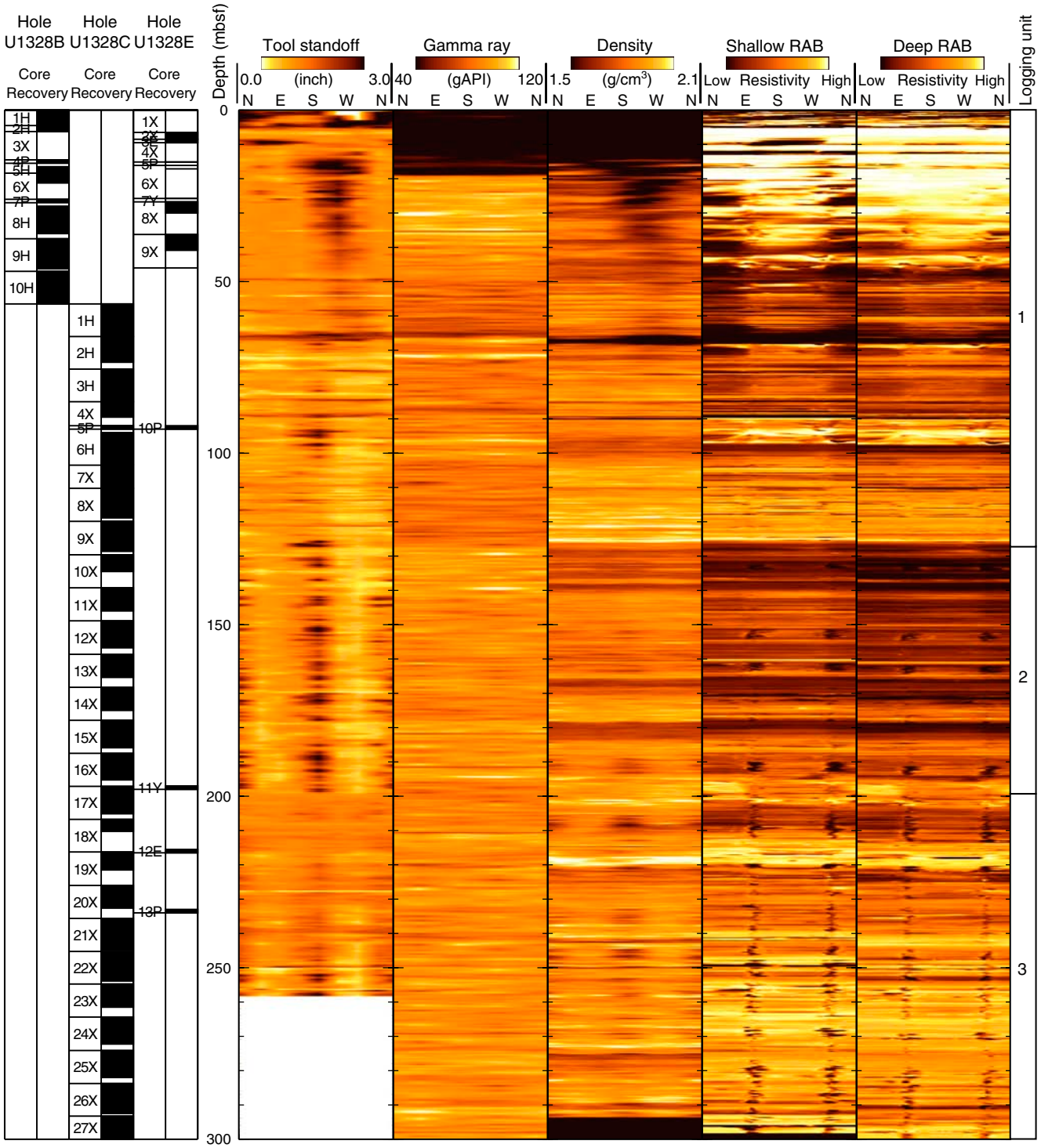

Figure F62. LWD resistivity images of gas hydrate–rich fractures in Hole U1328A. The fractures are nearly vertical, and have dips between 80° and 86°.

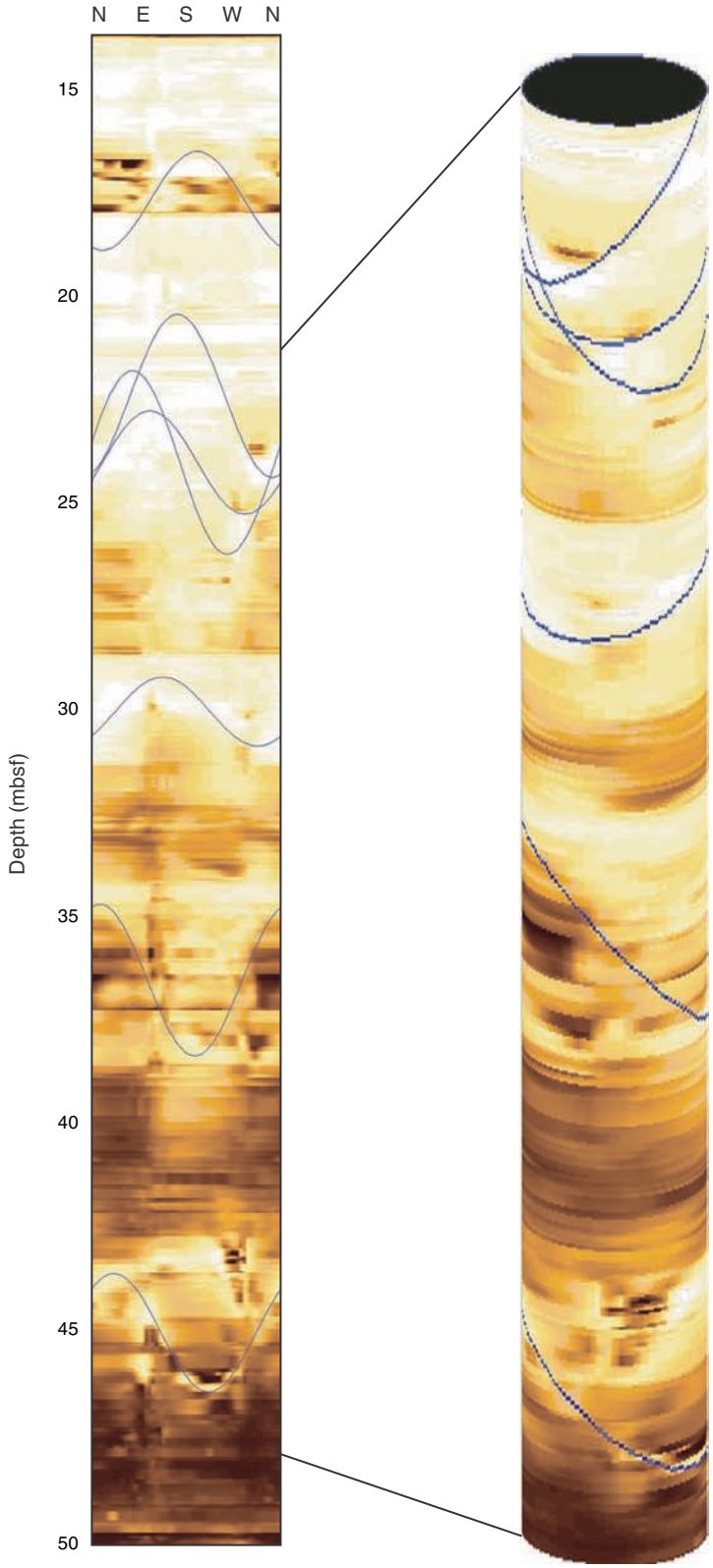

Figure F63. Comparison of LWD porosity logs with core-derived porosity data.

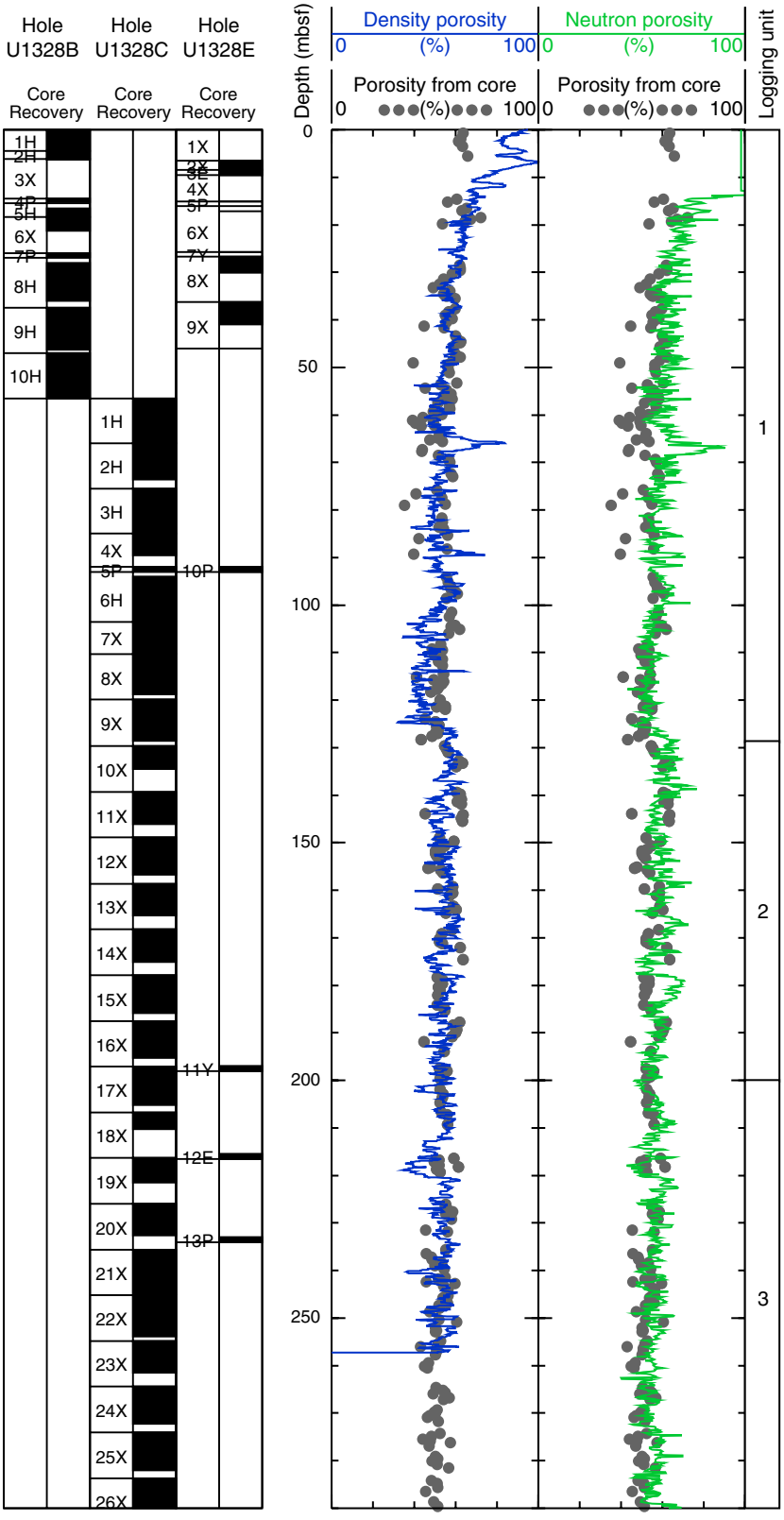

Figure F64. Water saturation from Archie's equation and from LWD porosity and resistivity logs. R_w = formation water resistivity, m = cementation coefficient, R_0 = computed formation resistivity for 100% water saturation, R_t = measured resistivity, S_w = water saturation, RAB = resistivity-at-the-bit image obtained by the GeoVISION tool.

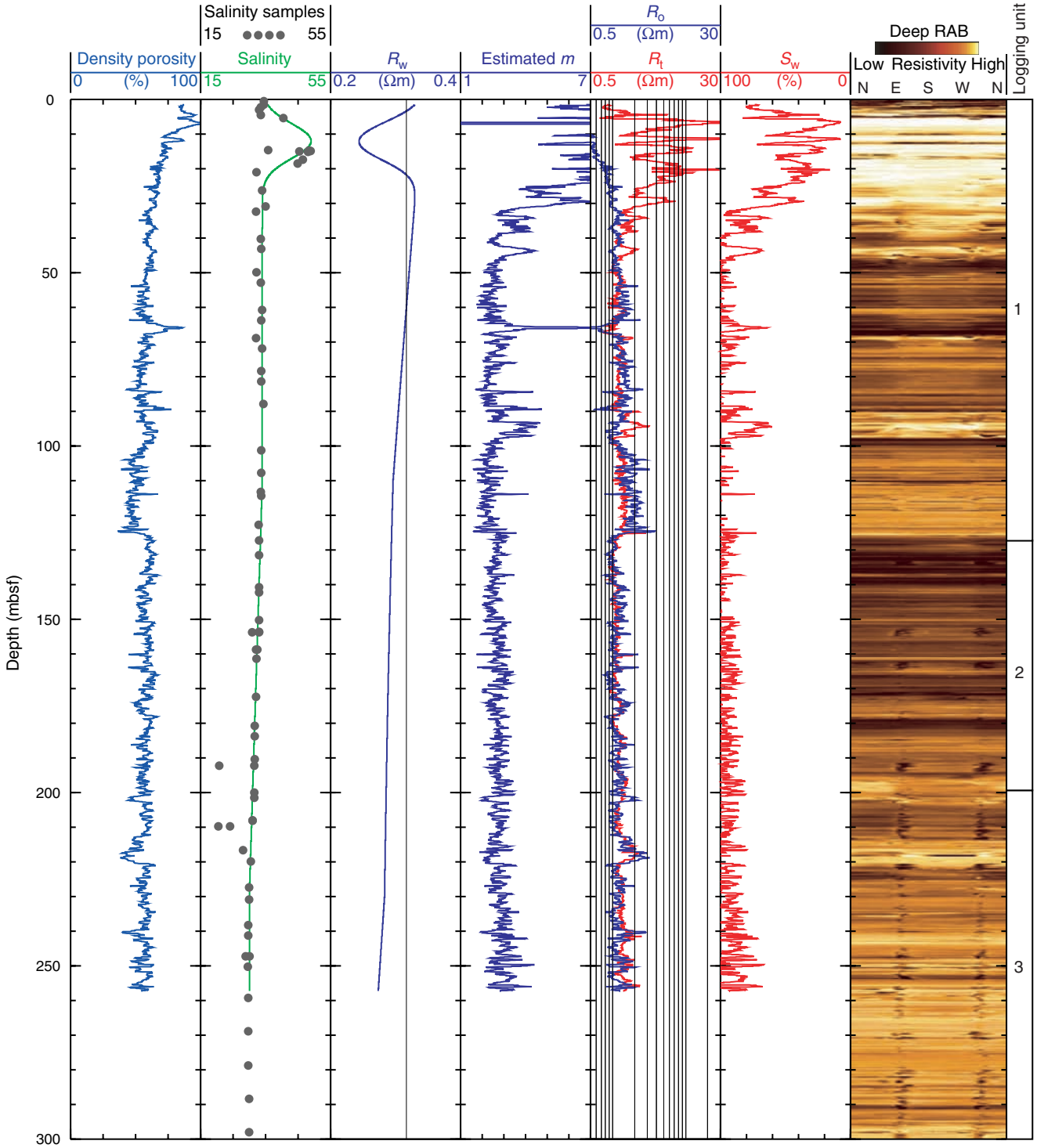

Figure F65. Comparison between LWD and wireline resistivity and infrared (IR) images from Holes U1328A and U1328C. IR images from the seafloor to 56.5 mbsf are from Hole U1328B, and IR images from 56.5 to 300 mbsf are from Hole U1328C. RAB = resistivity-at-the-bit image obtained by the GeoVISION tool, avg. = average, P16B = phase-shift resistivity measured by the EcoScope tool at a source-receiver spacing of 16 inch (41 cm), A40B = attenuation resistivity measured by the EcoScope tool at a source-receiver spacing of 40 inch (102 cm), SFLU = spherically focused resistivity, Med. = medium.

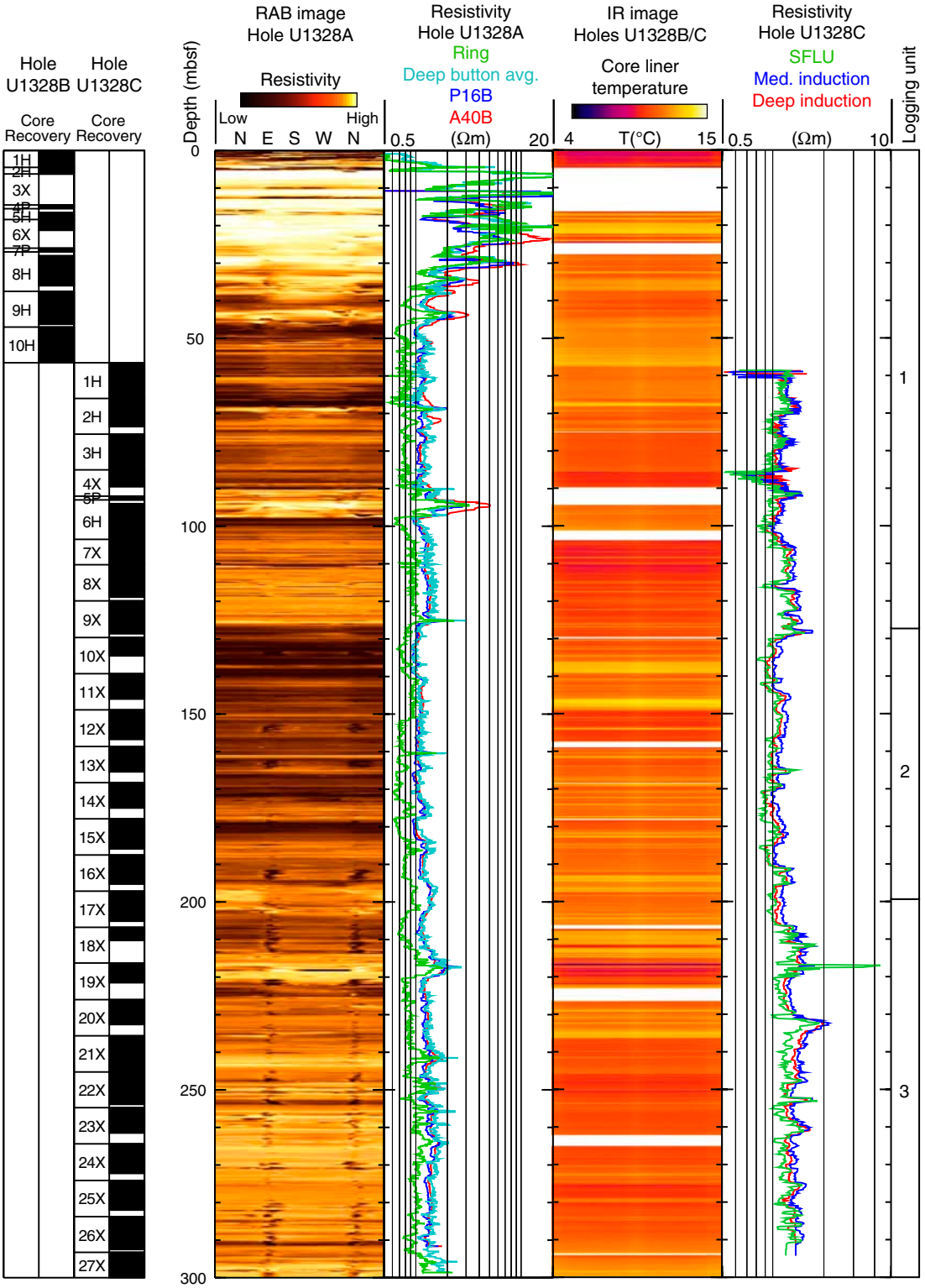

Figure F66. Stacked waveforms recorded at 35 stations by the Well Seismic Tool in the Hole U1328C vertical seismic profile. Red crosses = picked first break times.

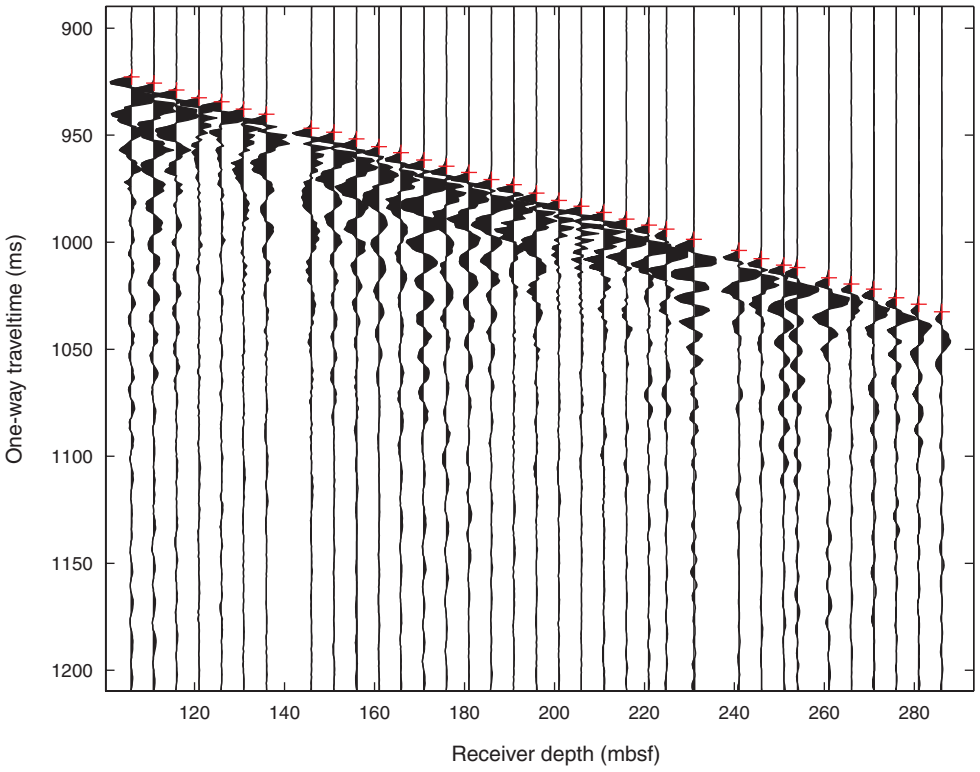

Figure F67. Time vs. depth plot of first break times in the Hole U1328C vertical seismic profile. The best-fit straight line indicates an average interval velocity (*V*) of 1645 m/s.

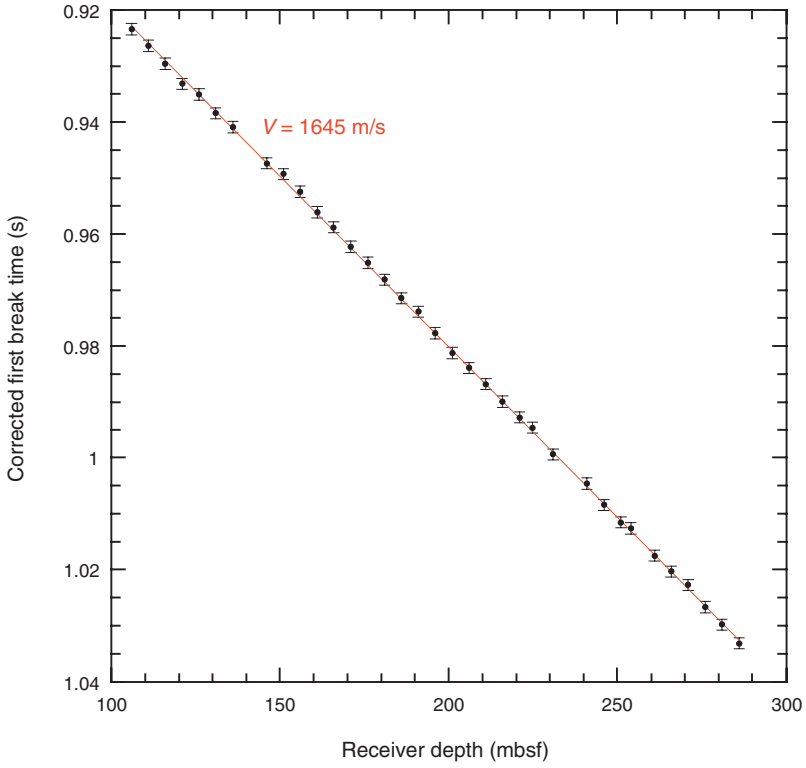

Figure F68. A. Interval velocity inversion of the first break times in the Hole U1328C vertical seismic profile. **B.** Comparison of the inversion results with the *P*-wave velocity sonic logs from Hole U1328C (red and blue). Dashed lines = ±1 posterior standard deviation.

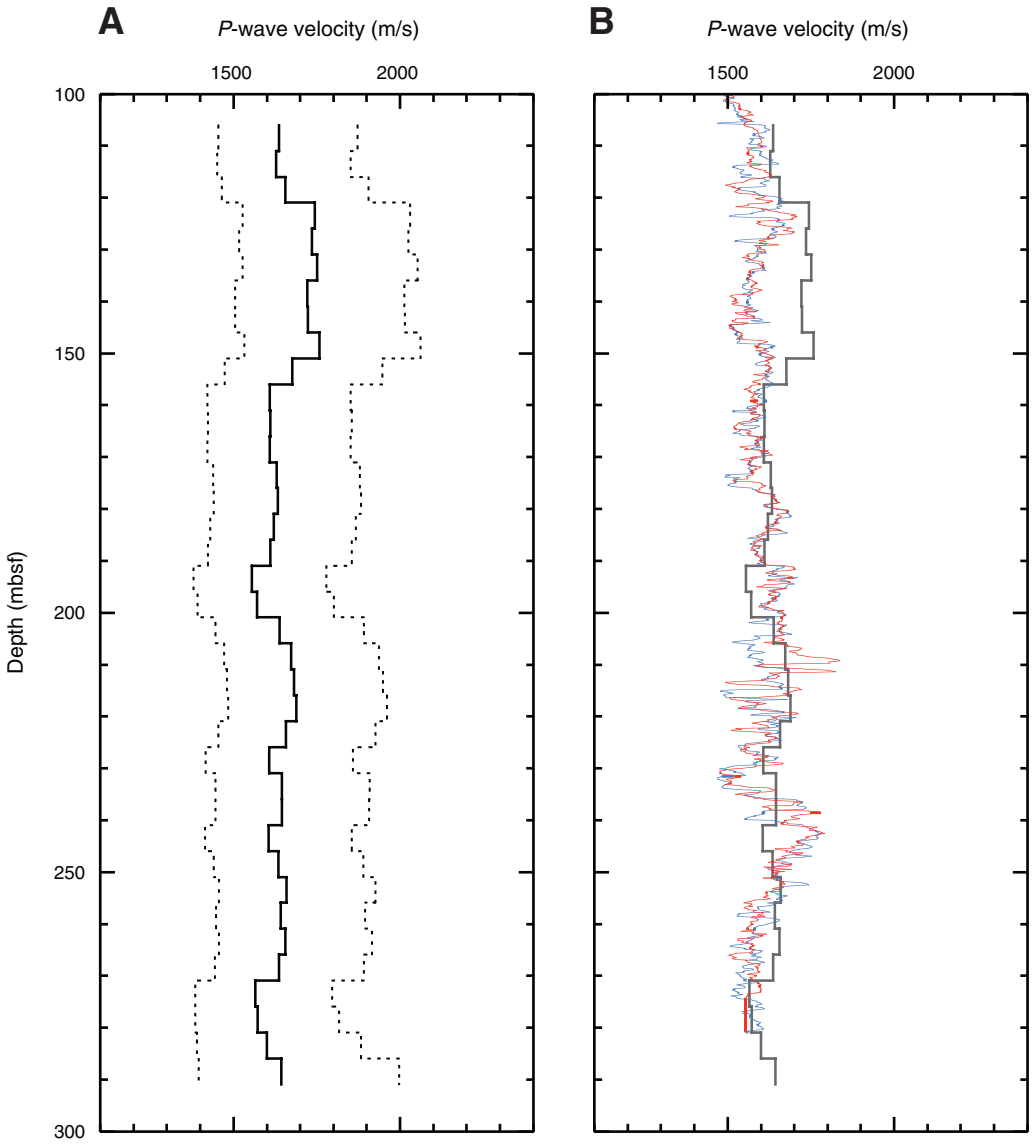

Table T1. Site U1328 coring summary. (See table note. Continued on next page.)

Hole U1328A
Latitude: 48°40.072′N
Longitude: 126°51.022′W
Seafloor (drill pipe measurement from rig floor, mbrf): 1279.0
Distance between rig floor and sea level (m): 10.9
Water depth (drill pipe measurement from sea level, m): 1268.1
Total penetration (mbsf): 300.0
Total drilled interval (m): 300.0; LWD/MWD

Hole U1328B
Latitude: 48°40.048′N
Longitude: 126°51.056′W
Seafloor (drill pipe measurement from rig floor, mbrf): 1279.0
Distance between rig floor and sea level (m): 11.2
Water depth (drill pipe measurement from sea level, m): 1267.8
Total penetration (mbsf): 56.5
Total drilled interval (m): 2

Hole U1328C
Latitude:48°40.057′N
Longitude: 126°51.044′W
Seafloor (drill pipe measurement from rig floor, mbrf): 1279.0
Distance between rig floor and sea level (m): 11.3
Water depth (drill pipe measurement from sea level, m): 1267.7
Total penetration (mbsf): 300.0
Total drilled interval (m): 57.5

Hole U1328D
Latitude: 48°40.067′N
Longitude: 126°51.020′W
Seafloor (drill pipe measurement from rig floor, mbrf): 1278.0
Distance between rig floor and sea level (m): 11.3
Water depth (drill pipe measurement from sea level, m): 1266.7
Total penetration (mbsf): 15.0

Hole U1328E
Latitude: 48°40.081′N
Longitude: 126°50.987′W
Seafloor (drill pipe measurement from rig floor, mbrf): 1276.0
Distance between rig floor and sea level (m): 11.3
Water depth (drill pipe measurement from sea level, m): 1264.7
Total penetration (mbsf): 235.0
Total drilled interval (mbsf): 186.0

Core, section	Date (Oct 2005)	Local time (h)	Top depth (mbsf)	Length (m) Cored	Length (m) Recovered	Recovery (%)	Comments
311-U1328A-							
		*****Drilled from 0.0 to 300.0 mbsf*****					LWD/MWD
311-U1328B-							
1H	11	1320	0.0	4.5	4.87	108.2	Fluorescent microspheres, APCM
2H	11	1425	4.5	1.7	1.72	101.2	Fluorescent microspheres, APCM
3X	11	1615	6.2	8.3	0.05	0.6	Fluorescent microspheres
4P	11	1720	14.5	1.0	0.77	77.0	
		*****Drilled from 14.5 to 16.5 mbsf*****					Overdrill pressure core
5H	11	1825	16.5	1.9	1.89	99.5	Fluorescent microspheres, APCM
6X	11	1945	18.4	7.6	2.81	37.0	Fluorescent microspheres
7P	11	2105	26.0	1.0	0.78	78.0	Sheared pin on OS
		*****Drilled from 26.0 to 28.0 mbsf*****					Overdrill pressure core
8H	11	2205	28.0	9.5	8.06	84.8	APCT, fluorescent microspheres, APCM
9H	11	2300	37.5	9.5	8.72	91.8	Fluorescent microspheres, APCM
10H	12	0025	47.0	9.5	9.98	105.1	APCT-3, DVTP, fluorescent microspheres, APCM
			Core totals:	54.5	39.65	72.8	
311-U1328C-							
1H	13	0015	56.5	9.5	9.62	101.3	Fluorescent microspheres
2H	13	0125	66.0	9.5	7.54	79.4	APCT; fluorescent microspheres, APCM
3H	13	0240	75.5	9.5	9.52	100.2	APCT-3, fluorescent microspheres, APCM
4X	13	0340	85.0	7.0	4.56	65.1	Fluorescent microspheres
5P	13	0510	92.0	1.0	0.96	96.0	Fluorescent microspheres
		*****Drilled from 92.0 to 94.0 mbsf*****					Overdrill of pressure core
6H	13	0650	94.0	9.5	9.30	97.9	APCT-3, fluorescent microspheres. APCM
7X	13	0900	103.5	6.8	6.72	98.8	Fluorescent microspheres

Table T1 (continued).

Core, section	Date (Oct 2005)	Local time (h)	Top depth (mbsf)	Length (m) Cored	Length (m) Recovered	Recovery (%)	Comments
8X	13	1010	110.3	9.6	8.53	88.9	Fluorescent microspheres
9X	13	1120	119.9	9.7	8.67	89.4	Fluorescent microspheres
10X	13	1210	129.6	9.7	4.87	50.2	Fluorescent microspheres
11X	13	1305	139.3	9.6	6.74	70.2	DVTPP at 148.9 mbsf; fluorescent microspheres
12X	13	1520	148.9	9.7	7.86	81.0	Fluorescent microspheres
13X	13	1600	158.6	9.6	6.74	70.2	Fluorescent microspheres
14X	13	1645	168.2	9.7	6.83	70.4	Fluorescent microspheres
15X	13	1730	177.9	9.6	7.93	82.6	Fluorescent microspheres
16X	13	1815	187.5	9.6	7.72	80.4	DVTPP at 197.1 mbsf; fluorescent microspheres
17X	13	2040	197.1	9.6	8.04	83.8	Fluorescent microspheres
18X	13	2140	206.7	9.6	3.57	37.2	Fluorescent microspheres
19X	13	2240	216.3	9.7	5.24	54.0	Fluorescent microspheres
20X	13	2350	226.0	9.6	6.66	69.4	Fluorescent microspheres
21X	14	0120	235.6	9.6	9.31	97.0	Fluorescent microspheres
22X	14	0300	245.2	9.6	8.70	90.6	Fluorescent microspheres
23X	14	0420	254.8	9.6	6.66	69.4	Fluorescent microspheres
24X	14	0555	264.4	9.7	7.88	81.2	Fluorescent microspheres
25X	14	0730	274.1	9.6	7.94	82.7	Fluorescent microspheres
26X	14	0835	283.7	9.6	8.76	91.2	Fluorescent microspheres
27X	14	1000	293.3	6.7	8.77	130.9	Fluorescent microspheres
			Core totals:	242.5	195.64	80.7	
311-U1328D-							
1X	15	2030	0.0	4.5	8.15	181.1	
2X	15	2215	4.5	9.5	1.88	19.8	
3Y	15	2325	14.0	1.0	0.00	0.0	
			Core totals:	15.0	10.0	66.9	
311-U1328E-							
1X	16	0125	0.0	6.5	0.00	0.0	
2X	16	0210	6.5	2.0	2.39	119.5	
3E	16	0350	8.5	1.0	0.00	0.0	
4X	16	0450	9.5	5.6	0.00	0.0	
5P	16	0600	15.1	1.0	0.00	0.0	
		*****Drilled from 15.1 to 17.1 mbsf*****					Overdrill pressure core
6X	16	0710	17.1	8.6	0.00	0.0	
7Y	16	0830	25.7	1.0	0.87	87.0	
8X	16	0930	26.7	9.6	3.35	34.9	
9X	16	1015	36.3	9.7	4.62	47.6	
		*****Drilled from 36.3 to 92.0 mbsf*****					
10P	16	1455	92.0	1.0	0.26	26.0	DVTP at 93 mbsf
		*****Drilled from 92.0 to 197.0 mbsf*****					
11Y	16	2055	197.0	1.0	0.90	90.0	DVTP at 198 mbsf
		*****Drilled from 197.0 to 215.5 mbsf*****					
12E	17	0130	215.5	1.0	0.00	0.0	
		*****Drilled from 215.5 to 233.0 mbsf*****					
13P	17	0450	233.0	1.0	0.94	94.0	
		*****Drilled from 233.0 to 234.0 mbsf*****					Overdrill pressure core
			Core totals:	49.0	13.33	27.2	

Note: LWD/MWD = logging while drilling/measurement while drilling, APCM = advanced piston corer methane tool, OS = over shot, APCT = advanced piston corer temperature tool, APCT-3 = third-generation advanced piston corer temperature tool, DVTP = Davis-Villinger Temperature Probe, DVTPP = Davis-Villinger Temperature-Pressure Probe.

Table T2. Occurrence of diatoms, Holes U1328B and U1328C. (**See table notes.** Continued on next page.)

Age	Diatom zone	Core, section	Depth (mbsf)	Abundance	Number of diatom valves/row × 100	Preservation	Marine diatoms: *Actinocyclus curvatulus* Janisch	*Actinocyclus oculatus* Jousé	*Coscinodiscus marginatus* Ehrenberg	*Coscinodiscus* spp.	*Cyclotella striata* (Kutzing) Grunow	*Neodenticula seminae* (Simonsen and Kanaya) Akiba and Yanagisawa	*Paralia sulcata* (Ehrenberg) Cleve	*Porosira gracilis* (Grunow) Jorgensen	*Proboscia curvirostris* (Jousé) Jordan and Priddle	*Stephanopyxis dimorpha* Schrader	*Stephanopyxis* spp.	*Thalassionema nitzschioides* H. and M. Peragallo	*Thalassiosira jouseae* Akiba	*Thalassiosira* spp.	*Thalassiothrix longissima* Cleve and Grunow	Miscellaneous	Nonmarine diatoms: *Aulacoseira granulata* (Ehrenberg) Simonsen s.l.	*Cyclotella* spp.	*Stephanodiscus* spp.	Miscellaneous	Total number of valves	Resting spores of *Chaetoceros* spp.	Marine and nonmarine diatoms ratio
		311-U1328B-																											
		1H-CC	4.75	VR	0.7	P	+			3	2	+	5			1	11	11		4		3	26		2	5	73	25	
		2H-CC	6.17	R	2.4	P				+			3			3	17	35		20	+	3	11	2	1	5	100	46	
		3X-CC	6.20	B																							0		
		5H-CC	18.24	VR	0.7	P	1			+	1						6	+		+	+	1	63		+		72	16	
		6X-CC	21.06	VR	0.4	P				+	+	+					8	2		1		1	25		+	1	38	8	
		8H-CC	35.98	VR	1.2	P				+							1					2	95	1	1		100	1	
	NPD12	9H-CC	46.12	R	2.5	P				1		1					7	1		1	+	3	82	2		2	100	11	
	N. seminae	10H-CC	56.88	VR	0.1	P				+		+					+	1		+		2	9				12	3	
		311-U1328C-																											
		1H-CC	66.07	VR	0.1	P											3	1		+			9				13	2	
Holocene–Pleistocene		2H-CC	73.49	C	6.0	M	3			1		13				3	29	14		16		7	12		1	1	100	184	
		3H-CC	84.92	VR	0.2	P	1			+			3				5	1		2		1	9	+		1	23	2	
		4X-CC	89.41	VR	0.2	P				+			1				2	3		+	+		10	1	+		17	7	
		6H-CC	103.20	R	2.0	P	+		+	3		+				15	32	9		9	+	5	18	3		6	100	66	
		7X-CC	110.07	VR	0.2	P				+		+			+	1	6	2		+	+	2	10	1			22	9	
		8X-CC	118.68	VR	0.1	P				+							3	+		+		1	4		+	1	9	10	
		9X-CC	128.73	B																									
		10X-CC	134.37	C	8.0	M	+			4		3			2	2	14	52		8		3	7	3		2	100	162	
	NPD11	11X-CC	145.94	R	2.2	P	+			1						1	13	4		3	+	1	62	6	3	6	100	22	
	P. curvirostris	12X-CC	156.64	C	6.0	P			+	+		2			1	4	13	30		8		2	32	5	1	2	100	174	
		13X-CC	165.24	VA	60.0	M	5			3		6			3	5	35	19		18	+	4	2	+	+		100	684	
		14X-CC	174.74	VA	72.0	G	+	+		2		13	1		3	5	19	29	+	14	+	8	3	3	+		100	849	
		15X-CC	185.73	A	60.0	M				+													76	23	1		100	—	
		16X-CC	195.12	R	1.5	P				+		2				6	22	12		7		2	39	3	5	2	100	76	

Table T2 (continued).

Age	Diatom zone	Core, section	Depth (mbsf)	Abundance	Number of diatom valves/row × 100	Preservation	Marine diatoms: *Actinocyclus curvatulus* Janisch	*Actinocyclus oculatus* Jousé	*Coscinodiscus marginatus* Ehrenberg	*Coscinodiscus* spp.	*Cyclotella striata* (Kutzing) Grunow	*Neodenticula seminae* (Simonsen and Kanaya) Akiba and Yanagisawa	*Paralia sulcata* (Ehrenberg) Cleve	*Porosira gracilis* (Grunow) Jorgensen	*Proboscia curvirostris* (Jousé) Jordan and Priddle	*Stephanopyxis dimorpha* Schrader	*Stephanopyxis* spp.	*Thalassionema nitzschioides* H. and M. Peragallo	*Thalassiosira jouseae* Akiba	*Thalassiosira* spp.	*Thalassiothrix longissima* Cleve and Grunow	Miscellaneous	Nonmarine diatoms: *Aulacoseira granulata* (Ehrenberg) Simonsen s.l.	*Cyclotella* spp.	*Stephanodiscus* spp.	Miscellaneous	Total number of valves	Resting spores of *Chaetoceros* spp.	Marine and nonmarine diatoms ratio
Holocene–Pleistocene	NPD11 *P. curvirostris*	17X-CC	205.04	R	2.0	P	1			1		10				7	16	9		14	+	6	31	2	+	3	100	58	
		18X-CC	210.12	A	15.8	M	4			7		6			3	7	22	15	1	8	4	18	5				100	189	
		19X-CC	221.39	VR	0.1	P											+			+			6	+			6	2	
		20X-CC	232.61	VR	0.2	P				+		1			1	1	4	1		+			6		3		17	5	
		21X-CC	244.86	R	2.4	P	+			+		2			+		9	2		7		3	69	4	2	2	100	7	
		22X-CC	253.80	R	2.4	P	+		+	+		7			+	13	57	3		3	+		14	3	+		100	122	
		23X-CC	261.36	VR	+	P				+													3				3	—	
		24X-CC	272.18	R	3.0	P	3			1		+		6	3	1	11	1	1	5	+	7	54	2	3	2	100	10	
	NPD10 *A. oculatus*	25X-CC	281.99	C	14.4	P	2	+	+	1		18			+	5	46	5		3	+	3	11	+	2	4	100	179	
		26X-CC	292.41	C	3.6	M	+			+		9			+	2	1			5		1	74	4	4		100	14	
		27X-CC	301.97	VR	0.8	P				1					1	8	24	+		5	+	1	41	1			82	23	

Notes: Abundance: VA = very abundant, A = abundant, C = common, R = rare, VR = very rare, B = barren. Preservation: G = good, M = moderate, P = poor. + = <1% and/or valve fragments, — = *Chaetoceros* spp. resting spores not present.

Table T3. Concentrations of solutes in interstitial waters, Site U1328. (See table notes. Continued on next page.)

Core, section, interval (cm)	Depth (mbsf)	Volume (mL)	pH	Alkalinity (mM)	Salinity	Cl (mM)	SO_4 (mM)	PO_4 (µM)	NH_4 (mM)	H_4SiO_4 (µM)	Cations (mM)					Trace elements (µM)			
											Na	K	Mg	Ca	Mg/Ca	Sr	Li	B	Ba
311-U1328B-																			
1H-1, 40–50	0.5	56.0	7.50	3.0	34.5	549.6	29.3	3.9	0.1	374.2	465.8	11.9	47.9	9.3	5.16	85.0	26.1	557.0	1.6
1H-1, 140–150	1.5	58.0	7.67	3.7	34.5	562.0	27.2	10.6	0.1	374.2	461.6	12.0	48.6	9.0	5.41	82.8	25.6	544.9	1.7
1H-2, 70–80	2.3	54.0	8.11	30.8	33.5	564.9	0.4	20.6	0.5	683.6	462.4	11.5	46.5	3.8	12.15	74.3	21.2	556.6	2.9
1H-2, 140–150	3.0	54.0	8.37	26.9	33.0	565.4	0.3	23.9	0.5	641.1	446.8	11.7	46.1	3.3	14.08	71.0	18.9	523.7	3.2
1H-3, 140–150	4.5	56.0	8.43	28.2	33.5	563.0	0.0	—	0.3	—	—	—	—	—	—	—	—	—	—
2H-1, 80–100	5.4	42.0	8.11	20.3	40.5	747.6	0.2	118.9	2.1	384.8	590.8	15.7	48.3	1.1	43.05	48.5	5.8	697.0	24.6
4P-1, 0–11	14.6	9.0	—	—	35.5	688.2	5.8	39.4	—	404.3	580.4	13.9	51.6	3.3	15.48	88.4	36.6	501.4	15.2
4P-1, 23–31	14.8	22.0	7.61	24.8	47.8	831.3	1.1	67.8	—	439.7	687.1	17.1	63.0	3.4	18.43	107.0	10.0	547.6	16.3
4P-1, 36–46	14.9	20.0	—	—	48.0	836.3	1.9	65.2	—	416.1	701.2	16.9	63.5	3.5	18.03	109.3	11.5	516.9	18.0
4P-1, 50–57	15.0	8.0	—	—	42.0	719.9	8.9	31.9	—	329.4	600.3	15.4	53.8	3.6	14.79	90.6	14.6	505.5	13.6
4P-1, 61–67	15.1	11.0	—	—	46.5	814.3	3.4	42.8	—	380.1	656.6	16.9	61.9	3.8	16.36	109.0	176.3	555.2	16.7
5H-1, 85–100	17.4	62.0	7.78	24.5	46.0	835.8	1.2	78.9	2.1	382.1	665.1	16.5	63.8	3.9	16.28	119.8	8.4	522.6	52.3
6X-1, 0–20	18.5	2.0	—	—	40.0	677.8	13.2	—	1.4	—	—	—	—	—	—	—	—	—	—
6X-2, 136–151	21.0	0.8	—	—	32.5	—	3.7	—	2.7	—	—	—	—	—	—	—	—	—	—
7P-1, 20–30	26.3	30.0	7.64	32.2	34.0	567.0	1.8	85.3	—	532.8	457.4	9.8	37.9	3.5	10.83	78.5	12.0	490.6	25.6
8H-2, 120–150	30.9	62.0	7.84	31.2	35.0	571.9	0.1	67.3	2.4	524.4	468.3	9.9	46.4	3.7	12.59	80.0	5.5	475.3	27.6
8H-3, 120–150	32.4	68.0	7.88	29.7	32.0	567.9	—	54.8	2.7	433.0	458.8	9.7	45.8	3.5	13.15	79.7	5.6	459.4	29.1
9H-2, 109–134	40.2	58.0	7.89	31.0	33.5	562.0	0.1	40.6	2.8	474.1	462.6	9.5	43.6	3.2	13.58	77.4	8.5	444.1	32.7
9H-4, 115–150	43.1	52.0	7.97	30.9	33.7	563.5	—	46.4	2.9	586.3	447.0	9.3	41.1	2.8	14.71	73.8	8.8	474.4	30.6
10H-2, 125–150	49.9	62.0	7.99	31.2	32.2	563.5	—	33.9	3.1	503.8	447.3	9.3	46.6	2.8	16.54	73.7	6.4	430.3	25.6
10H-4, 125–150	52.9	52.0	7.93	31.7	33.5	559.5	—	44.8	2.9	610.3	467.2	9.2	44.9	3.0	15.02	74.3	6.2	446.3	22.0
311-U1328C-																			
1H-3, 125–150	60.8	50.0	8.15	34.2	34.0	561.5	0.1	22.8	3.3	357.5	451.6	9.8	47.0	3.2	14.85	74.8	3.3	423.6	20.3
1H-5, 125–150	63.8	50.0	8.16	36.0	33.7	560.0	0.0	39.4	3.4	373.5	481.0	9.7	44.5	3.2	14.09	71.6	3.2	382.9	21.9
2H-2, 125–150	68.9	47.0	7.81	36.7	32.0	551.0	0.1	61.1	3.5	677.4	440.3	8.8	43.2	3.7	11.76	84.4	8.5	480.8	31.2
2H-4, 125–150	71.9	39.0	8.00	36.7	34.0	560.0	0.0	45.3	3.5	572.8	461.0	9.5	46.0	3.8	12.18	73.4	5.7	433.3	25.5
3H-2, 125–150	78.4	30.0	7.95	37.7	33.7	559.0	0.0	50.3	3.8	486.5	457.1	9.0	46.2	3.3	13.99	69.9	6.0	401.6	18.9
3H-4, 125–150	81.4	8.0	—	—	33.7	556.0	0.1	54.4	3.7	554.1	450.1	8.9	44.7	3.4	13.24	72.3	5.6	431.5	17.9
4X-2, 125–150	87.9	45.0	7.97	37.7	34.3	553.6	2.1	56.9	4.1	481.3	459.8	9.0	44.8	3.7	12.21	71.0	4.6	434.9	18.9
5P-1, 5–15	92.1	12.0	—	—	33.7	552.6	0.6	—	—	—	—	—	—	—	—	—	—	—	—
5P-1, 23–43	92.3	42.0	7.83	36.7	32.5	550.1	2.1	—	—	—	—	—	—	—	—	—	—	—	—
5P-1, 60–70	92.7	20.0	—	—	33.0	549.6	0.1	—	—	—	—	—	—	—	—	—	—	—	—
6H-7, 125–150	101.3	44.0	7.92	40.0	33.7	550.6	0.0	78.6	4.3	713.5	447.0	8.7	41.5	2.9	14.27	73.1	10.6	475.8	23.5
*7X-2, 120–150	106.4	—	—	—	—	—	—	—	—	—	—	—	—	—	—	—	—	—	—
7X-3, 115–140	107.8	7.0	—	—	33.7	552.6	0.2	61.1	4.5	635.1	465.3	9.2	42.8	2.8	15.21	74.8	11.3	480.5	22.5
8X-2, 120–150	113.2	24.0	—	—	33.5	547.0	0.9	50.3	5.1	449.5	458.2	9.8	41.7	3.4	12.30	77.5	8.0	457.9	20.0
8X-3, 97–118	114.4	20.0	7.98	42.8	33.7	548.0	0.3	53.6	5.1	568.0	428.1	8.9	42.0	3.2	13.26	77.2	8.0	549.7	20.1
9X-2, 110–140	122.7	36.0	8.04	42.3	33.0	544.0	1.2	45.3	5.8	416.5	474.8	10.5	41.2	3.7	11.06	81.7	5.8	467.5	31.3
9X-6, 40–71	127.3	22.0	—	—	33.0	542.0	0.2	59.4	5.6	443.1	457.0	9.7	41.3	3.7	11.23	82.5	7.5	524.4	40.9
10X-2, 22–52	131.5	40.0	7.84	47.5	33.0	543.0	0.2	88.1	5.8	683.8	485.4	9.8	42.5	4.8	8.87	88.3	12.2	560.2	70.3
11X-1, 120–150	140.7	52.0	7.77	48.8	33.0	541.0	0.3	107.3	6.2	855.2	478.8	10.1	39.8	4.9	8.17	92.9	18.0	582.7	87.6
11X-2, 120–150	142.2	42.0	7.68	48.3	33.0	540.0	0.5	108.1	6.3	839.7	480.0	10.0	42.3	5.0	8.44	91.4	17.5	592.3	80.3
12X-1, 120–150	150.3	40.0	7.78	47.2	33.0	538.0	0.1	63.9	6.0	—	457.9	9.8	39.9	4.8	8.27	—	—	—	—
*12X-3, 130–150	153.3	—	—	—	—	—	—	—	—	—	—	—	—	—	—	—	—	—	—
12X-4, 11–28	153.6	24.0	7.71	46.8	33.0	531.0	0.1	67.8	6.5	—	445.6	9.3	37.7	4.7	8.05	—	—	—	—
12X-4, 28–38	153.7	2.0	—	—	31.0	494.0	1.2	—	6.3	—	423.7	8.9	35.6	4.5	7.87	—	—	—	—
12X-4, 28–38	153.7	19.0	7.75	46.7	33.0	527.4	0.3	60.3	6.6	—	—	—	—	—	—	—	—	—	—

Table T3 (continued).

Core, section, interval (cm)	Depth (mbsf)	Volume (mL)	pH	Alkalinity (mM)	Salinity	Cl (mM)	SO_4 (mM)	PO_4 (µM)	NH_4 (mM)	H_4SiO_4 (µM)	Cations (mM)					Trace elements (µM)			
											Na	K	Mg	Ca	Mg/Ca	Sr	Li	B	Ba
13X-1, 0–10	158.7	20.0	—	—	32.5	534.8	0.0	82.3	5.8	—	451.5	9.2	36.5	4.8	7.67	—	—	—	—
13X-1, 10–20	158.8	14.0	—	—	32.0	533.0	0.2	56.1	6.4	—	—	—	—	—	—	—	—	—	—
13X-2, 120–150	161.4	14.0	—	—	32.2	532.8	0.1	61.9	6.8	692.7	435.1	9.5	32.3	4.1	7.83	84.8	20.1	543.7	77.1
14X-3, 120–150	172.4	40.0	7.91	38.5	32.0	532.3	0.2	83.1	6.6	778.1	443.3	9.7	31.9	4.8	6.60	84.2	16.6	538.4	75.7
15X-2, 117–147	180.7	45.0	7.72	36.0	31.7	531.3	0.0	103.1	6.1	601.5	427.2	9.6	30.5	3.8	8.06	83.0	15.2	510.7	80.8
15X-4, 115–150	183.7	32.0	7.84	34.2	31.7	530.8	0.0	103.9	6.0	599.9	433.9	9.5	28.4	3.7	7.73	82.2	16.1	504.6	82.6
16X-2, 120–150	190.4	32.0	7.81	32.0	31.7	530.8	0.3	80.6	6.0	841.0	444.0	9.7	28.5	3.1	9.23	80.5	22.4	542.8	87.3
16X-4, 21–28	192.2	9.0	—	—	22.5	379.3	3.8	27.8	5.2	426.7	317.3	7.3	17.9	2.0	9.02	49.7	13.2	282.8	42.5
16X-4, 28–39	192.3	7.0	—	—	31.5	525.8	0.0	44.4	6.4	—	—	—	—	—	—	—	—	—	—
17X-2, 120–150	200.0	40.0	8.02	30.2	31.5	531.8	0.0	47.3	5.8	731.3	453.1	10.2	27.8	2.7	10.16	82.5	26.8	478.9	88.0
17X-3, 120–150	201.5	40.0	7.92	28.9	31.5	530.8	0.0	50.6	5.7	741.9	443.0	9.7	27.3	2.5	10.99	78.7	26.0	479.1	82.7
18X-1, 120–130	208.0	10.0	—	—	31.0	433.7	0.3	37.8	5.1	712.5	356.1	7.9	19.8	1.9	10.55	64.1	21.0	419.8	63.4
18X-2, 0–25	208.1	26.0	—	—	31.0	517.4	0.2	69.5	5.5	854.5	435.8	9.4	26.6	2.4	11.32	77.9	25.9	491.1	77.9
18X-3, 67–72	209.7	8.0	—	—	20.5	347.6	0.2	—	4.1	472.9	280.9	6.5	15.4	1.3	11.50	43.5	13.5	259.6	42.1
18X-3, 72–82	209.8	16.0	7.98	24.4	24.0	411.0	0.0	44.5	4.6	728.9	343.4	7.2	19.5	1.7	11.70	57.6	18.7	365.9	57.7
19X-1, 20–40	216.6	9.0	—	—	28.0	487.7	0.5	50.3	4.9	709.1	408.6	8.9	23.6	1.8	13.31	72.8	25.9	398.0	69.8
19X-3, 120–150	219.9	30.0	7.95	27.3	30.5	520.9	0.5	58.7	5.4	833.9	429.0	9.2	25.0	2.0	12.41	81.4	28.7	475.2	79.8
20X-1, 120–150	227.4	28.0	—	—	30.0	513.0	0.7	59.5	5.3	694.4	438.3	9.6	27.4	2.3	12.03	81.4	25.3	441.5	82.6
20X-4, 120–150	230.9	50.0	7.98	28.6	30.0	515.4	1.0	56.2	6.8	787.1	424.7	9.1	26.8	2.3	11.76	79.2	26.5	450.5	77.8
21X-2, 122–150	238.2	16.0	—	—	29.7	505.0	0.3	—	6.8	690.7	416.8	9.1	26.8	2.9	9.28	78.9	22.9	403.0	79.3
21X-4, 120–150	241.2	36.0	8.08	28.9	30.0	504.5	2.1	53.7	5.3	793.0	421.0	8.9	27.4	3.0	9.14	83.0	24.1	470.8	70.2
22X-2, 51–61	247.3	3.0	—	—	31.7	519.9	15.0	42.0	—	702.1	415.0	9.3	26.3	3.1	8.38	80.3	24.0	420.9	84.4
22X-2, 51–61	247.3	8.0	—	—	30.0	501.6	0.2	—	6.0	—	—	—	—	—	—	—	—	—	—
22X-4, 120–150	250.2	34.0	7.84	29.9	29.7	498.6	1.0	42.8	5.3	855.9	409.7	8.7	27.2	3.0	9.02	80.3	24.5	459.2	74.3
23X-3, 120–150	259.2	15.0	—	—	29.7	490.7	0.0	27.0	5.6	626.7	407.8	8.4	26.2	3.6	7.20	79.9	21.0	410.4	87.3
24X-4, 0–40	268.9	29.0	7.99	33.1	29.7	494.6	1.6	24.5	5.8	709.1	407.8	8.6	26.7	4.3	6.19	81.9	24.5	408.3	95.5
25X-4, 0–40	278.8	11.0	—	—	29.7	496.1	0.5	18.7	6.6	691.5	410.4	8.6	26.4	4.3	6.21	82.6	25.8	405.3	100.5
26X-4, 0–30	288.4	47.0	7.78	37.3	30.0	498.6	0.8	27.0	6.6	875.0	411.8	8.1	26.8	4.6	5.80	85.9	26.5	480.6	112.1
27X-4, 0–50	298.0	40.0	8.06	32.5	30.0	496.1	0.5	13.7	6.8	732.6	403.5	8.6	26.5	4.7	5.65	84.1	26.3	418.9	112.9
311-U1328D-																			
**1X-1, 135–150	1.4	27.0	—	—	34.5	559.0	28.5	—	—	—	—	—	—	—	—	—	—	—	—
**1X-2, 135–150	2.9	13.0	—	—	34.5	559.0	28.2	—	—	—	—	—	—	—	—	—	—	—	—
**1X-3, 135–150	4.4	15.0	—	—	34.0	562.0	22.1	—	—	—	—	—	—	—	—	—	—	—	—
1X-4, 135–150	5.9	10.0	—	—	33.0	575.0	2.2	—	—	—	—	—	—	—	—	—	—	—	—
1X-5, 135–150	7.4	16.0	—	—	32.5	590.0	4.8	—	—	—	—	—	—	—	—	—	—	—	—
2X-1, 85–100	5.4	47.0	8.25	31.5	33.0	578.0	1.7	—	—	—	—	—	—	—	—	—	—	—	—
311-U1328E-																			
2X-1, 84–104	7.4	20.0	8.48	33.9	33.0	540.7	0.5	—	—	—	—	—	—	—	—	—	—	—	—
2X-1, 84–104	7.4	9.0	—	—	30.0	560.0	2.9	—	—	—	—	—	—	—	—	—	—	—	—
2X-2, 0–20	8.0	50.0	8.43	31.0	31.7	618.9	0.8	—	—	—	—	—	—	—	—	—	—	—	—
8X-2, 96–125	29.3	15.0	—	—	37.7	566.4	0.0	—	—	—	—	—	—	—	—	—	—	—	—
9X-2, 32–48	38.2	35.0	—	—	33.7	504.0	0.0	—	—	—	—	—	—	—	—	—	—	—	—
9X-4, 53–88	39.6	50.0	7.99	23.8	32.3	557.5	8.8	—	—	—	—	—	—	—	—	—	—	—	—
13P-1, 20–32	233.3	23.0	7.87	29.5	30.0	497.4	4.6	—	—	—	—	—	—	—	—	—	—	—	—
13P-1, 47–57	233.6	16.0	—	—	30.0	496.8	3.9	—	—	—	—	—	—	—	—	—	—	—	—
13P-1, 78–88	234.0	16.0	—	—	30.0	496.6	0.5	—	—	—	—	—	—	—	—	—	—	—	—

Notes: * = no interstitial water squeezed because of poor quality of sample, ** = analyzed for only a few elements because of extensive contamination with drill fluid. — = no data.

Table T4. Concentrations of solutes corrected for drill-fluid contamination in interstitial waters, Site U1328. (**See table notes.** Continued on next page.)

Core, section, interval (cm)	Depth (mbsf)	Volume (mL)	pH	Alkalinity (mM)	Salinity	Cl (mM)	SO_4 (mM)	PO_4 (µM)	NH_4 (mM)	H_4SiO_4 (µM)	Cations (mM)					Trace elements (µM)			
											Na	K	Mg	Ca	Mg/Ca	Sr	Li	B	Ba
311-U1328B-																			
1H-1, 40–50	0.5	56.0	7.50	3.0	34.5	549.6	29.3	3.9	0.1	374.2	465.8	11.9	47.9	9.3	5.16	85.0	26.1	557.0	1.6
1H-1,140–150	1.5	58.0	7.67	3.7	34.5	562.0	27.2	10.6	0.1	374.2	461.6	12.0	48.6	9.0	5.41	82.8	25.6	544.9	1.7
1H-2, 70–80	2.3	54.0	8.11	30.8	33.5	564.9	0.4	20.6	0.5	683.6	462.4	11.5	46.5	3.8	12.15	74.3	21.2	556.6	2.9
1H-2, 140–150	3.0	54.0	8.37	26.9	33.0	565.4	0.3	23.9	0.5	641.1	446.8	11.7	46.1	3.3	14.08	71.0	18.9	523.7	3.2
1H-3, 140–150	4.5	56.0	8.43	28.2	33.5	563.0	0.0	—	0.3	—	—	—	—	—	—	—	—	—	—
2H-1, 80–100	5.4	42.0	8.11	20.3	40.5	747.6	0.0	118.9	2.1	384.8	590.8	15.7	48.3	1.1	43.05	48.5	5.8	697.0	24.6
4P-1, 0–11	14.6	9.0	—	—	35.8	720.6	0.0	49.2	—	468.0	605.5	14.8	51.0	1.5	33.46	88.7	39.1	514.3	19.0
4P-1, 23–31	14.8	22.0	7.61	25.7	48.3	842.3	0.0	70.5	—	451.4	695.5	17.4	63.3	3.1	20.24	107.8	9.3	551.6	16.9
4P-1, 36–46	14.9	20.0	—	—	48.9	855.2	0.0	69.6	—	434.3	716.3	17.3	64.1	3.0	21.09	110.8	10.4	521.5	19.3
4P-1, 50–57	15.0	8.0	—	—	45.4	791.6	0.0	46.0	—	409.3	653.9	17.6	53.8	0.6	96.07	92.1	9.0	530.2	19.7
4P-1, 61–67	15.1	11.0	—	—	48.1	847.9	0.0	48.3	—	410.3	679.9	17.8	62.9	2.9	21.75	111.9	195.9	569.0	18.9
5H-1, 85–100	17.4	62.0	7.78	25.5	46.5	848.2	0.0	82.4	2.2	392.5	673.4	16.7	64.2	3.6	17.74	121.3	7.5	525.8	54.6
6X-1, 0–20	18.5	2.0	—	—	44.8	777.6	0.0	—	2.6	—	—	—	—	—	—	—	—	—	—
6X-2, 136–151	21.0	0.8	—	—	32.2	—	0.0	—	3.1	—	—	—	—	—	—	—	—	—	—
7P-1, 20–30	26.3	30.0	7.64	34.2	34.0	567.5	0.0	91.0	—	558.5	455.9	9.8	36.8	3.0	12.18	77.9	11.0	493.3	27.3
8H-2, 120–150	30.9	62.0	7.84	31.2	35.0	571.9	0.0	67.3	2.4	524.4	468.3	9.9	46.4	3.7	12.59	80.0	5.5	475.3	27.6
8H-3, 120–150	32.4	68.0	7.88	29.7	32.0	567.9	—	54.8	2.7	433.0	458.8	9.7	45.8	3.5	13.15	79.7	5.6	459.4	29.1
9H-2, 109–134	40.2	58.0	7.89	31.0	33.5	562.0	0.0	40.6	2.8	474.1	462.6	9.5	43.6	3.2	13.58	77.4	8.5	444.1	32.7
9H-4, 115–150	43.1	52.0	7.97	30.9	33.7	563.5	—	46.4	2.9	586.3	447.0	9.3	41.1	2.8	14.71	73.8	8.8	474.4	30.6
10H-2, 125–150	49.9	62.0	7.99	31.2	32.2	563.5	—	33.9	3.1	503.8	447.3	9.3	46.6	2.8	16.54	73.7	6.4	430.3	25.6
10H-4, 125–150	52.9	52.0	7.93	31.7	33.5	559.5	—	44.8	2.9	610.3	467.2	9.2	44.9	3.0	15.02	74.3	6.2	446.3	22.0
311-U1328C-																			
1H-3, 125–150	60.8	50.0	8.15	34.2	34.0	561.5	0.0	22.8	3.3	357.5	451.6	9.8	47.0	3.2	14.85	74.8	3.3	423.6	20.3
1H-5, 125–150	63.8	50.0	8.16	36.0	33.7	560.0	0.0	39.4	3.4	373.5	481.0	9.7	44.5	3.2	14.09	71.6	3.2	382.9	21.9
2H-2, 125–150	68.9	47.0	7.81	36.7	32.0	551.0	0.0	61.1	3.5	677.4	440.3	8.8	43.2	3.7	11.76	84.4	8.5	480.8	31.2
2H-4, 125–150	71.9	39.0	8.00	36.7	34.0	560.0	0.0	45.3	3.5	572.8	461.0	9.5	46.0	3.8	12.18	73.4	5.7	433.3	25.5
3H-2, 125–150	78.4	30.0	7.95	37.7	33.7	559.0	0.0	50.3	3.8	486.5	457.1	9.0	46.2	3.3	13.99	69.9	6.0	401.6	18.9
3H-4, 125–150	81.4	8.0	—	—	33.7	556.0	0.0	54.4	3.7	554.1	450.1	8.9	44.7	3.4	13.24	72.3	5.6	431.5	17.9
4X-2, 125–150	87.9	45.0	7.97	40.4	34.3	553.2	0.0	61.3	4.4	507.0	458.3	8.9	44.1	3.1	14.05	69.8	2.9	433.8	20.3
5P-1, 5–15	92.1	12.0	—	—	33.7	552.5	0.0	—	—	—	—	—	—	—	—	—	—	—	—
5P-1, 23–43	92.3	42.0	7.83	39.4	32.4	549.4	0.0	—	—	—	—	—	—	—	—	—	—	—	—
5P-1, 60–70	92.7	20.0	—	—	33.0	549.6	0.0	—	—	—	—	—	—	—	—	—	—	—	—
6H-7, 125–150	101.3	44.0	7.92	40.0	33.7	550.6	0.0	78.6	4.3	713.5	447.0	8.7	41.5	2.9	14.27	73.1	10.6	475.8	23.5
*7X-2, 120–150	106.4	—	—	—	—	—	—	—	—	—	—	—	—	—	—	—	—	—	—
7X-3, 115–140	107.8	7.0	—	—	33.7	552.6	0.0	61.1	4.5	635.1	465.3	9.2	42.8	2.8	15.21	74.8	11.3	480.5	22.5
8X-2, 120–150	113.2	24.0	—	—	33.5	546.6	0.0	51.8	5.3	458.7	457.5	9.8	41.3	3.2	13.04	77.2	7.4	458.1	20.6
8X-3, 97–118	114.4	20.0	7.98	43.2	33.7	547.9	0.0	54.1	5.1	572.4	427.5	8.9	41.9	3.1	13.55	77.1	7.8	550.7	20.3
9X-2, 110–140	122.7	36.0	8.04	44.1	32.9	543.3	0.0	47.2	6.1	428.2	474.5	10.5	40.7	3.4	11.87	81.5	4.9	468.3	32.7
9X-6, 40–71	127.3	22.0	—	—	33.0	542.0	0.0	59.4	5.6	443.1	457.0	9.7	41.3	3.7	11.23	82.5	7.5	524.4	40.9
10X-2, 22–52	131.5	40.0	7.84	47.5	33.0	543.0	0.0	88.1	5.8	683.8	485.4	9.8	42.5	4.8	8.87	88.3	12.2	560.2	70.3
11X-1, 120–150	140.7	52.0	7.77	49.2	33.0	540.8	0.0	108.3	6.2	861.8	478.8	10.1	39.7	4.8	8.23	92.9	18.0	584.0	88.4
11X-2, 120–150	142.2	42.0	7.68	49.1	33.0	539.7	0.0	109.9	6.4	851.6	480.0	10.0	42.1	4.9	8.57	91.5	17.3	594.8	81.7
12X-1, 120–150	150.3	40.0	7.78	47.2	33.0	538.0	0.0	63.9	6.0	—	457.9	9.8	39.9	4.8	8.27	—	—	—	—
*12X-3, 130–150	153.3	—	—	—	—	—	—	—	—	—	—	—	—	—	—	—	—	—	—
12X-4, 11–28	153.6	24.0	7.71	46.8	33.0	531.0	0.0	67.8	6.5	—	445.6	9.3	37.7	4.7	8.05	—	—	—	—
12X-4, 28–38	153.7	2.0	—	—	30.9	491.3	0.0	—	6.5	—	421.4	8.8	34.8	4.3	8.16	—	—	—	—
12X-4, 28–38	153.7	19.0	7.75	47.1	33.0	527.1	0.0	60.8	6.6	—	—	—	—	—	—	—	—	—	—
13X-1, 0–10	158.7	20.0	—	—	32.5	534.8	0.0	82.3	5.8	—	451.5	9.2	36.5	4.8	7.67	—	—	—	—

Table T4 (continued).

Core, section, interval (cm)	Depth (mbsf)	Volume (mL)	pH	Alkalinity (mM)	Salinity	Cl (mM)	SO_4 (mM)	PO_4 (µM)	NH_4 (mM)	H_4SiO_4 (µM)	Cations (mM)					Trace elements (µM)			
											Na	K	Mg	Ca	Mg/Ca	Sr	Li	B	Ba
13X-1, 10–20	158.8	14.0	—	—	32.0	533.0	0.0	56.1	6.4	—	—	—	—	—	—	—	—	—	—
13X-2, 120–150	161.4	14.0	—	—	32.2	532.8	0.0	61.9	6.8	692.7	435.1	9.5	32.3	4.1	7.83	84.8	20.1	543.7	77.1
14X-3, 120–150	172.4	40.0	7.91	38.5	32.0	532.3	0.0	83.1	6.6	778.1	443.3	9.7	31.9	4.8	6.60	84.2	16.6	538.4	75.7
15X-2, 117–147	180.7	45.0	7.72	36.0	31.7	531.3	0.0	103.1	6.1	601.5	427.2	9.6	30.5	3.8	8.06	83.0	15.2	510.7	80.8
15X-4, 115–150	183.7	32.0	7.84	34.2	31.7	530.8	0.0	103.9	6.0	599.9	433.9	9.5	28.4	3.7	7.73	82.2	16.1	504.6	82.6
16X-2, 120–150	190.4	32.0	7.81	32.3	31.7	530.5	0.0	81.3	6.1	847.3	443.7	9.7	28.3	3.0	9.36	80.5	22.4	543.7	88.1
16X-4, 21–28	192.2	9.0	—	—	20.7	352.2	0.0	31.9	5.9	468.5	292.7	6.8	12.4	0.7	18.02	44.1	11.1	257.5	48.9
16X-4, 28–39	192.3	7.0	—	—	31.5	525.8	0.0	44.4	6.4	—	—	—	—	—	—	—	—	—	—
17X-2, 120–150	200.0	40.0	8.02	30.2	31.5	531.8	0.0	47.3	5.8	731.3	453.1	10.2	27.8	2.7	10.16	82.5	26.8	478.9	88.0
17X-3, 120–150	201.5	40.0	7.92	28.9	31.5	530.8	0.0	50.6	5.7	741.9	443.0	9.7	27.3	2.5	10.99	78.7	26.0	479.1	82.7
18X-1, 120–130	208.0	10.0	—	—	31.0	432.4	0.0	38.2	5.1	718.4	354.8	7.9	19.4	1.8	10.89	63.9	20.9	419.5	64.1
18X-2, 0–25	208.1	26.0	—	—	31.0	517.4	0.0	69.5	5.5	854.5	435.8	9.4	26.6	2.4	11.32	77.9	25.9	491.1	77.9
18X-3, 67–72	209.7	8.0	—	—	20.5	347.6	0.0	—	4.1	472.9	280.9	6.5	15.4	1.3	11.50	43.5	13.5	259.6	42.1
18X-3, 72–82	209.8	16.0	7.98	24.4	24.0	411.0	0.0	44.5	4.6	728.9	343.4	7.2	19.5	1.7	11.70	57.6	18.7	365.9	57.7
19X-1, 20–40	216.6	9.0	—	—	28.0	487.7	0.0	50.3	4.9	709.1	408.6	8.9	23.6	1.8	13.31	72.8	25.9	398.0	69.8
19X-3, 120–150	219.9	30.0	7.95	27.7	30.4	520.3	0.0	59.6	5.5	845.0	428.2	9.2	24.5	1.9	13.07	81.3	28.8	475.7	81.0
20X-1, 120–150	227.4	28.0	—	—	29.9	511.9	0.0	60.9	5.5	706.9	437.3	9.6	26.8	2.1	12.84	81.3	25.2	441.3	84.5
20X-4, 120–150	230.9	50.0	7.98	29.5	29.9	513.9	0.0	58.1	7.0	809.0	422.8	9.1	25.8	2.0	12.97	79.0	26.5	450.6	80.5
21X-2, 122–150	238.2	16.0	—	—	29.7	504.5	0.0	—	6.9	696.0	416.2	9.1	26.5	2.8	9.43	78.8	22.8	402.5	80.1
21X-4, 120–150	241.2	36.0	8.08	31.0	29.7	500.4	0.0	57.7	5.7	842.1	416.4	8.8	25.4	2.4	10.48	82.7	23.9	472.4	75.6
22X-2, 51–61	247.3	3.0	—	—	28.8	477.4	0.0	87.3	0.0	1301.3	344.5	8.1	—	—	—	73.0	20.8	389.3	176.0
22X-2, 51–61	247.3	8.0	—	—	30.0	501.6	0.0	—	6.0	—	—	—	—	—	—	—	—	—	—
22X-4, 120–150	250.2	34.0	7.84	30.9	29.5	496.5	0.0	44.3	5.5	880.7	407.3	8.6	26.3	2.8	9.54	80.0	24.4	459.5	76.9
23X-3, 120–150	259.2	15.0	—	—	29.7	490.7	0.0	27.0	5.6	626.7	407.8	8.4	26.2	3.6	7.20	79.9	21.0	410.4	87.3
24X-4, 0–40	268.9	29.0	7.99	33.1	29.7	494.6	0.0	24.5	5.8	709.1	407.8	8.6	26.7	4.3	6.19	81.9	24.5	408.3	95.5
25X-4, 0–40	278.8	11.0	—	—	29.6	495.0	0.0	19.0	6.7	700.8	409.2	8.6	25.9	4.1	6.25	82.5	25.8	404.5	102.3
26X-4, 0–30	288.4	47.0	7.78	38.3	29.9	496.9	0.0	27.8	6.8	895.9	409.8	8.0	26.1	4.5	5.85	85.8	26.4	481.5	115.3
27X-4, 0–50	298.0	40.0	8.06	33.1	29.9	495.0	0.0	13.9	7.0	743.0	402.1	8.6	26.0	4.6	5.68	84.0	26.3	418.4	114.9
311-U1328D-																			
**1X-1, 135–150	1.4	27.0	—	—	34.5	559.0	28.5	—	—	—	—	—	—	—	—	—	—	—	—
**1X-2, 135–150	2.9	13.0	—	—	34.5	559.0	28.2	—	—	—	—	—	—	—	—	—	—	—	—
**1X-3, 135–150	4.4	15.0	—	—	34.0	562.0	22.1	—	—	—	—	—	—	—	—	—	—	—	—
1X-4, 135–150	5.9	10.0	—	—	33.0	575.0	2.2	—	—	—	—	—	—	—	—	—	—	—	—
1X-5, 135–150	7.4	16.0	—	—	32.1	596.1	0.0	—	—	—	—	—	—	—	—	—	—	—	—
2X-1, 85–100	5.4	47.0	8.25	33.4	32.9	579.2	0.0	—	—	—	—	—	—	—	—	—	—	—	—
311-U1328E-																			
2X-1, 84–104	7.4	20	8.48	34.5	33.0	540.3	0.0	—	—	—	—	—	—	—	—	—	—	—	—
2X-1, 84–104	7.4	9	—	—	29.5	560.1	0.0	—	—	—	—	—	—	—	—	—	—	—	—
2X-2, 0–20	8.0	50	8.43	31.8	31.6	620.6	0.0	—	—	—	—	—	—	—	—	—	—	—	—
8X-2, 96–125	29.3	15	—	—	37.7	566.4	0.0	—	—	—	—	—	—	—	—	—	—	—	—
9X-2, 32–48	38.2	35	—	—	33.7	504.0	0.0	—	—	—	—	—	—	—	—	—	—	—	—
9X-4, 53–88	39.6	50	7.99	33.1	31.4	556.9	0.0	—	—	—	—	—	—	—	—	—	—	—	—
13P-1, 20–32	233.3	23.0	7.87	34.8	29.2	485.6	0.0	—	—	—	—	—	—	—	—	—	—	—	—
13P-1, 47–57	233.6	16.0	—	—	29.3	487.2	0.0	—	—	—	—	—	—	—	—	—	—	—	—
13P-1, 78–88	234.0	16.0	—	—	29.9	495.5	0.0	—	—	—	—	—	—	—	—	—	—	—	—

Notes: The corrections are based on dissolved sulfate concentrations, assuming zero sulfate concentration below the sulfate/methane interface, which at this site occurs in the uppermost 2 m.
* = no interstitial water squeezed because of poor quality of sample, ** = analyzed for only a few elements because of extensive contamination with drill fluid. — = no data.

Table T5. Salinity, chloride, and sulfate corrected for sulfate concentrations in dissociated gas hydrate, Site U1328.

Core, section, interval (cm)	Depth (mbsf)	Volume (mL)	Salinity	Cl (mM)	SO_4 (mM)
311-1328B-					
2H-1, 0–5	4.5	0.4	2.7	17	0.1
2H-CC	6.1	1.5	0.5	18	0.1
5H-CC	18.3	< 0.3	—	14	1.1
6X-2, 136–151	20.9	~10	8.5	147	1.7
6X-CC	21.1	2.0	2.8	52	0.2
311-1328D-					
1X-CC	8.1	1.5	0.1	0.1	0.2
2X-CC	6.3	<0.3	—	39	0.4
311-1328E-					
2X-2, 60–70	8.5	1.5	0.2	23	0.0
2X-CC	8.8	0.8	1.0	18	0.0

Table T6. Headspace gas concentrations of hydrocarbons, Holes U1328B, U1328C, U1328D, and U1328E. (**See table note.** Continued on next page.)

Core, section, interval (cm)	Depth (mbsf)	C_1/C_2	C_1 (ppmv)	C_2 (ppmv)	$C_{2=}$ (ppmv)	C_3 (ppmv)	C_1 (mM)*
311-U1328B-							
1H-1, 50–55	0.5		2.3	0.0	0	0	0.0004
1H-2, 0–5	1.5		8.2	0.0	0	0	0.003
1H-2, 80–85	2.3	524	3,037	5.8	0	0	1.5
1H-3, 0–5	3.0	1,124	12,478	11.1	0	0	6.0
1H-4, 0–5	4.5	1,126	26,920	23.9	0	0	13.0
2H-1, 80–85	5.3	930	65,591	70.5	0	0	31.8
4P-1, 18–19	14.7	465	3,857	8.3	0	0	1.9
4P-1, 34–35	14.8	331	3,803	11.5	0	0	1.9
4P-1, 58–59	15.1	454	5,681	12.5	0	0	2.8
5H-1, 80–85	17.3	744	4,986	6.7	0	0	2.5
6X-2, 131–136	20.9	610	7,076	11.6	0	0	3.5
7P-1, 30–34	26.3	509	4,120	8.1	0	0	2.1
8H-3, 0–5	31.0	850	3,653	4.3	0	0	1.8
8H-4, 0–5	32.5	1,073	4,078	3.8	0	0	2.1
9H-3, 0–5	40.3	806	4,354	5.4	0	0.3	2.2
9H-5, 0–5	43.3	715	3,717	5.2	0	0	1.9
10H-3, 0–5	50.0	651	4,623	7.1	0	0	2.5
10H-5, 0–5	53.0	569	3,980	7.0	0	0	2.1
311-U1328C-							
1H-3, 110–115	60.5	946	4,919	5.2	0	0	2.7
1H-6, 0–5	63.9	1,062	4,566	4.3	0	0	2.5
2H-3, 0–5	69.0	1,450	35,374	24.4	0	0	19.9
2H-5, 0–5	72.0	1,418	10,915	7.7	0	0	6.2
3H-3, 0–5	78.5	905	3,619	4.0	0	0	2.1
3H-5, 0–5	81.5	1,097	3,290	3.0	0	0	1.9
4X-3, 0–5	88.0	1,032	2,992	2.9	0	0	1.8
5P-1, 15–18	92.2	725	3,842	5.3	0	0	2.3
5P-1, 43–46	92.4	798	5,425	6.8	0	0	3.3
5P-1, 70–73	92.7	707	3,961	5.6	0	0	2.4
6H-7, 0–5	99.9	1,357	4,070	3.0	0	0	2.5
7X-3, 0–5	106.5	977	1,563	1.6	0	0	1.0
7X-4, 0–5	107.9	1,561	3,434	2.2	0	0	2.2
8X-3, 0–5	113.3	1,024	1,843	1.8	0	0	1.2
8X-4, 145–150	115.9	1,150	3,794	3.3	0	0	2.5
9X-3, 0–5	122.8	1,161	2,902	2.5	0	0	2.0
9X-7, 0–5	127.5	1,578	4,577	2.9	0	0	2.9
10X-2, 52–57	131.6	1,792	2,688	1.5	0	0	1.5
11X-3, 0–5	142.3	1,867	2,988	1.6	0	0	1.7
12X-2, 0–5	150.4	2,274	5,002	2.2	0	0	2.9
12X-4, 0–5	153.4	1,832	4,213	2.3	0	0	2.4
13X-1, 20–25	158.8	1,704	3,578	2.1	0	0	2.1
13X-3, 0–5	161.6	2,288	6,179	2.7	0	0	3.6
14X-3, 0–5	171.0	2,008	5,422	2.7	0	0	3.1

Table T6 (continued).

Core, section, interval (cm)	Depth (mbsf)	C_1/C_2	C_1 (ppmv)	C_2 (ppmv)	$C_{2=}$ (ppmv)	C_3 (ppmv)	C_1 (mM)*
15X-3, 0–5	180.9	1,796	2,874	1.6	0	0	1.7
15X-5, 0–5	183.9	2,156	4,743	2.2	0	0	2.8
16X-3, 0–5	190.5	1,290	5,288	4.1	0	0	3.1
16X-4, 16–21	192.2	1,571	4,400	2.8	0	0	2.6
17X-3, 0–5	200.1	1,841	3,681	2.0	0	5.5	2.1
17X-4, 0–5	201.6	2,166	3,899	1.8	0	7.8	2.3
18X-1, 115–120	207.9	2,488	6,718	2.7	0	6.5	3.9
18X-3, 62–67	209.6	5,033	3,020	0.6	0	9.8	1.8
19X-1, 40–45	216.7	549	6,427	11.7	0	8.4	3.8
19X-4, 0–5	220.0	277	6,167	22.3	0	0	3.6
20X-2, 0–5	227.5	527	3,054	5.8	0	0	1.8
20X-5, 0–5	231.1	552	5,297	9.6	0	0	3.1
21X-3, 0–5	238.4	325	2,923	9.0	0	0	1.7
21X-5, 0–5	241.4	245	3,106	12.7	0	0	1.8
22X-3, 0–5	247.3	402	3,496	8.7	0	0	2.1
22X-5, 0–5	250.3	329	2,662	8.1	0	0	1.6
23X-2, 0–5	256.3	305	3,837	12.6	0	0	2.3
23X-4, 0–5	259.3	302	2,294	7.6	0	0	1.4
24X-2, 0–5	265.9	563	7,035	12.5	0	0	4.2
24X-4, 40–45	269.1	409	2,819	6.9	0	0	1.7
25X-2, 0–5	275.6	230	3,038	13.2	0	0	1.8
25X-4, 40–45	279.0	381	4,153	10.9	0	0	2.5
26X-2, 0–5	285.2	334	3,307	9.9	0	0	2.0
26X-6, 0–5	291.2	344	3,751	10.9	0	0.6	2.3
27X-2, 0–5	294.8	231	3,737	16.2	0	0	2.3
27X-4, 50–55	298.2	502	6,676	13.3	0	0	4.0
311-U1328D-							
1X-2, 0–5	1.5	461	1,707	3.7	0	0	0.8
1X-3, 0–5	3.0	461	3,598	7.8	0	0	1.7
1X-4, 0–5	4.5	1,057	15,434	14.6	0	0	7.5
1X-5, 0–5	6.0	725	10,150	14.0	0	0	4.9
2X-2, 0–5	5.5	922	10,140	11.0	0	0	4.9
311-U1328E-							
2X-1, 79–84	7.3	517	28,923	55.9	0	0	14.1
2X-2, 0–20	7.9	467	10,692	22.9	0	0	5.2
8X-3, 0–5	29.5	771	3,472	4.5	0	0	1.7
9X-3, 0–5	38.3	815	4,401	5.4	0	0	2.3
9X-5, 0–5	39.8	1,087	4,676	4.3	0	0	2.4

Note: * = dissolved residual methane obtained by the headspace equilibration method.

Table T7. Concentrations of light hydrocarbon and nonhydrocarbon gases in void gas samples, Holes U1328B, U1328C, U1328D, and U1328E.

Core, section, interval (cm)	Depth (mbsf)	C_1/C_2	$i\text{-}C_4/n\text{-}C_4$	Hydrocarbons (ppmv)							Volatiles (ppmv)			
				C_1	C_2	C_3	$i\text{-}C_4$	$n\text{-}C_4$	$i\text{-}C_5$	$n\text{-}C_5$	H_2S	CO_2	O_2	N_2
311-U1328B-														
1H-3, 34–35	3.3	1,658		395,927	239	0.0	0.2	0.0	0.0	0.0	23,470	4,375	NA	NA
2H-3, 126–127	4.3	1,800		822,516	457	0.0	0.4	0.0	0.0	0.0	45,491	7,384	23,636	103,010
5H-1, 47–48	17.0	1,158	1.2	869,390	751	0.0	1.7	1.4	3.9	1.2	0.0	3,139	31,299	121,027
8H-1, 0–5	28.0	724	1.2	882,201	1,219	0.2	1.1	0.9	3.1	1.1	0.0	1,391	27,536	100,571
8H-1, 119–120	29.2	2,867	0.9	869,599	303	3.2	1.3	1.4	2.4	1.2	0.0	6,316	29,591	123,441
8H-4, 60–61	33.1	2,015	1.3	882,277	438	0.0	1.7	1.3	1.8	0.9	0.0	5,588	25,117	99,257
9H-1, 111–112	38.6	2,460	1.4	882,714	359	1.2	1.7	1.2	2.3	1.0	0.0	5,654	25,485	102,217
9H-4, 91–92	42.7	1,582	1.8	939,154	594	0.0	0.7	0.4	0.0	3.1	0.0	3,794	3,129	14,941
10H-2, 126–127	49.8	790		934,450	1,184	0.0	0.8	0.0	0.0	0.0	0.0	1,401	1,714	13,715
10H-6, 44–45	54.9	2,841		917,302	323	5.3	1.2	0.0	0.0	0.0	0.0	6,892	6,188	28,695
311-U1328C-														
1H-2, 76–77	58.7	3,043	1.5	903,397	297	5.4	0.6	0.4	0.4	5.9	0.0	5,672	7,445	36,663
1H-6, 94–95	64.9	3,214	3.7	883,416	275	0.0	1.1	0.3	0.4	14.4	0.0	6,756	3,399	49,755
3H-2, 22–23	77.2	3,841		876,446	228	0.0	0.2	0.0	0.6	0.0	0.0	7,138	1,935	28,506
3H-5, 130–131	82.8	4,273	0.5	910,233	213	0.0	0.2	0.4	0.0	0.0	0.0	6,050	1,809	18,103
8X-3, 117–118	114.5	5,083	0.4	915,965	180	6.9	0.2	0.4	0.0	0.0	0.0	6,354	1,996	17,621
8X-5, 0–1	116.0	5,587		927,924	166	7.6	0.0	0.5	0.0	0.0	0.0	3,335	5,420	27,114
9X-5, 102–103	126.4	2,496	0.5	916,376	367	5.9	0.2	0.4	0.0	0.0	0.0	6,050	1,809	18,103
10X-2, 36–37	131.5	4,436	2.7	914,194	206	9.3	1.4	0.5	0.5	0.0	0.0	7,990	2,185	16,470
11X-3, 7–8	142.4	5,818	11.7	911,023	157	13.1	3.5	0.3	0.9	1.5	0.0	14,850	1,909	12,127
12X-2, 95–96	151.4	4,403	10.8	910,499	207	8.6	3.2	0.3	1.5	2.3	0.0	8,876	3,592	19,849
12X-4, 25–26	153.7	4,367	9.4	861,091	197	12.4	4.7	0.5	1.9	12.9	0.0	12,440	14,005	58,135
12X-5, 51–52	155.4	4,689	10.5	891,770	190	13.7	4.2	0.4	1.3	0.3	0.0	15,037	4,787	26,498
13X-1, 92–93	159.5	5,881	9.5	905,683	154	8.6	3.8	0.4	1.7	7.8	0.0	15,233	3,972	16,661
13X-3, 136–137	162.9	6,208	17.5	896,414	144	7.9	3.5	0.2	1.3	0.0	0.0	15,873	2,226	10,360
14X-1, 70–71	168.9	5,948	7.0	899,315	151	10.1	2.8	0.4	1.7	9.8	0.0	10,110	1,450	7,811
14X-4, 45–46	173.0	5,838	9.5	895,572	153	14.6	3.8	0.4	0.0	2.2	0.0	16,562	2,111	9,601
15X-2, 115–116	180.6	4,603		905,811	197	8.4	0.8	0.0	0.7	0.2	0.0	3,761	1,320	9,860
15X-5, 19–20	184.1	4,858	4.7	892,467	184	9.3	1.4	0.3	1.6	10.4	0.0	10,847	2,649	14,333
16X-3, 81–82	191.3	3,044	0.0	902,900	297	16.9	0.0	0.3	0.0	0.0	0.0	5,561	2,733	12,018
16X-5, 78–79	194.3	3,291	1.0	855,605	260	19.9	0.2	0.2	0.0	0.0	0.0	3,859	4,092	17,217
17X-2, 27–28	198.9	6,605	11.5	852,099	129	93.0	22.9	2.0	1.0	0.8	0.0	14,920	11,691	52,241
17X-4, 97–98	202.6	7,262	8.8	923,679	127	114.9	36.9	4.2	3.2	0.8	0.0	9,151	3,140	19,336
18X-1, 43–44	207.1	6,506	16.9	906,306	139	201.4	170.5	10.1	19.5	0.0	0.0	2,059	3,659	15,646
18X-3, 26–27	209.3	10,025	6.3	890,247	89	175.8	124.6	19.9	40.9	3.8	0.0	5,673	5,563	26,628
19X-2, 9–10	217.1	1,009	4.6	902,104	894	33.7	9.2	2.0	2.1	3.5	0.0	8,644	3,535	13,842
19X-3, 28–29	218.8	1,065	4.8	847,335	796	41.1	11.6	2.4	2.5	0.0	0.0	8,452	16,503	62,296
20X-3, 1–2	228.4	1,255	3.6	933,895	744	19.3	7.6	2.1	3.1	0.0	0.0	7,598	3,864	14,467
20X-4, 48–49	230.1	1,351	4.3	906,246	671	16.5	6.4	1.5	2.0	0.0	0.0	6,651	3,079	10,036
21X-2, 50–51	237.4	1,790	4.8	910,439	509	7.8	1.9	0.4	0.5	0.0	0.0	6,129	2,849	10,245
21X-5, 43–44	241.8	1,843	4.5	914,533	496	8.7	2.7	0.6	0.8	1.4	0.0	4,448	1,429	5,346
22X-4, 42–43	249.2	1,465	4.0	910,939	622	11.3	4.0	1.0	1.3	0.0	0.0	4,569	2,576	9,893
22X-6, 103–104	252.8	1,919	4.3	912,356	475	8.1	2.6	0.6	0.8	0.0	0.0	6,501	2,927	10,565
23X-3, 56–57	258.4	1,408	4.2	910,299	647	11.8	4.2	1.0	1.5	0.0	0.0	7,970	2,121	8,111
25X-4, 38–39	279.0	1,261	5.0	909,824	722	14.0	6.5	1.3	2.0	0.5	0.0	7,449	1,332	6,564
27X-3, 113–114	297.4	1,099	4.0	918,469	835	18.5	13.2	3.3	4.7	0.2	0.0	5,568	892	5,590
27X-5, 37–38	299.5	1,136	4.0	910,523	801	22.1	12.1	3.0	4.2	0.0	0.0	4,248	1,643	8,164
311-U1328D-														
1X-3, 121–122	4.2	602		444,109	737	0.0	0.2	0.0	0.0	0.0	1,302	2,017	95,318	405,762
311-U1328E-														
9X-2, 42–43	38.2	492		805,218	1637	0.0	0.5	0.0	0.0	0.0	0.0	1,512	31,524	119,974

Note: NA = not analyzed.

Table T8. Expected compositions of Structure I and Structure II gas hydrate formed from a source gas similar to that present below the BSR at Site U1328.

Component	Source gas	Structure I gas hydrate	Structure II gas hydrate	Void gas
Mole percent				
Methane	99.987	99.96	99.82	99.971
Ethane	0.01	0.04	0.04	0.014
Propane	0.002	0	0.09	0.016
i-butane	0.001	0	0.05	0.01
Molar ratios				
C_1/C_2	9998.7	2499	2495.5	7300 ± 1600
C_3/C_2	0.2	0	2.25	1.20 ± 0.57
i-C_4/C_2	0.1	0	1.25	0.73 ± 0.63

Notes: Compositions were calculated using the CSMHYD model of Sloan (1998) and assuming temperature and pressure conditions similar to those present near the projected BSR (15°C, 3.5% NaCl, and hydrostatic pressure). Void gas values are the observed data.

Table T9. Concentrations of light hydrocarbon and nonhydrocarbon gases from dissociated gas hydrate, Holes U1328C, U1328D, and U1328E.

Core, section, interval (cm)	Depth (mbsf)	C_1/C_2	*i*-C_4/*n*-C_4	Hydrocarbons (ppvm)							Volatiles (ppmv)			
				C_1	C_2	C_3	*i*-C_4	*n*-C_4	*i*-C_5	*n*-C_5	H_2S	CO_2	O_2	N_2
311-U1328C-														
2H-1, 5–6	4.60	930	3.8	803,565	864	7.3	1.5	0.4	0.4	0	0	680	8,780	30,976
2H-CC, 0–5	6.10	953	0	846,633	888	7.4	0.2	0	0	0	18,325	1,292	5,835	22,218
5H-CC, 5–10	18.30	765	1.0	810,363	1,059	0	1.4	1.4	0.5	1.3	0	941	53,449	200,560
6X-2, 23–24	19.80	765	1.5	862,710	1,127	0	1.5	1.0	2.3	0.9	0	2,445	27,707	100,625
6X-2, 135–136	20.90	635	1.1	881,605	1,389	6.7	1.2	1.1	1.7	1.0	0	1,063	29,289	103,691
6X-2, 150–151	21.10	684	1.3	868,093	1,269	0	1.8	1.4	2.2	1.1	0	1,167	32,722	118,142
6X-CC, 0–1	21.10	642	1.3	827,250	1,289	0	1.5	1.2	3.1	1.1	0	883	32,572	118,627
311-U1328D-														
1X-CC, 0–1	8.10	536	5.5	762,983	1,423	0	1.1	0.2	0.3	0	4,674	1,014	21,090	81,802
2X-CC, 0–1	6.30	630	5.0	494,148	784	0	1.0	0.2	0.6	0	10,339	840	3,814	18,824
311-U1328E-														
2X-2, 20–40	8.10	1,544	3.8	751,815	487	0	1.5	0.4	0.6	0	0	584	48,340	185,613
2X-2, 60–70	8.50	1,584	1.7	773,368	488	0	0.5	0.3	0.8	3.1	348	661	43,045	164,752
2X-CC, 0–10	8.80	630	2.7	494,148	784	0	0.8	0.3	0.7	0.6	0	0	5,929	19,167
9X-2, 48–50	38.30	456	0	907,908	1,989	0	0.4	0	0	0	0	781	11,482	41,377

Table T10. Composition of gas samples from PCS degassing experiments.

Core, section	Depth (mbsf)	C_1/C_2	*i*-C_4/*n*-C_4	Hydrocarbons (ppmv)							Volatiles (ppmv)			
				C_1	C_2	C_3	*i*-C_4	*n*-C_4	*i*-C_5	*n*-C_5	H_2S	O_2	N_2	CO_2
311-U1328B-														
4P	14.50	824	2.1	863,761	1,052	35	0.82	0.39	0.07	0.00	0.0	8,305	63,708	50
7P	26.00	984	1.0	704,767	696	1	1.66	1.70	1.08	1.05	0.0	9,341	171,010	296
311-U1328C-														
5P	92.00	2,109	0.6	631,813	337	165	0.09	0.14	0.00	0.00	0.0	25,957	339,770	669
311-U1328E-														
10P	92.00	1,030	3.2	867,639	844	0	1.40	0.44	0.37	0.00	0.0	4,818	40,748	78
13P	230.00	1,554	3.4	902,157	617	16	7.90	2.31	3.66	0.05	0.0	2,640	15,158	45

Table T11. Contents of inorganic carbon, $CaCO_3$ organic carbon, total organic carbon, and total nitrogen in sediment, Holes U1328B and U1328C.

Core, section, interval (cm)	Depth (mbsf)	Carbon (wt%)				Total nitrogen (wt%)	C/N
		Inorganic	$CaCO_3$	Total	Total organic		
311-U1328B-							
1H-1, 40–50	0.4	0.84	7.03	1.21	0.37	0.04	9.8
1H-1, 140–150	1.4	0.49	4.09	0.75	0.26	0.03	9.1
1H-2, 70–80	2.2	0.42	3.50	0.70	0.28	0.04	7.8
1H-2, 140–150	2.9	0.52	4.31	0.86	0.34	0.04	9.0
1H-3, 140–150	4.4	0.4	3.30	0.67	0.27	0.03	10.4
2H-1, 80–100	5.3	0.78	6.50	1.31	0.53	0.08	6.9
4P-1, 0–11	14.5	0.55	4.57	0.97	0.42	0.04	11.4
4P-1, 50–57	15.0	0.93	7.73	1.21	0.28	0.04	7.0
5H-1, 85–100	17.4	0.41	3.43	0.69	0.28	0.04	6.7
6X-1, 0–20	18.4	9.71	80.89	NA	NC	NA	NC
7P-1, 20–30	26.2	0.54	4.53	0.75	0.21	0.03	6.3
8H-2, 120–150	30.7	0.36	3.00	0.73	0.37	0.05	7.6
8H-3, 120150	32.2	0.38	3.13	0.58	0.20	0.03	6.0
9H-2, 109–134	40.1	0.34	2.81	0.52	0.18	0.02	7.8
9H-4, 115–150	43.0	1.52	12.63	2.14	0.62	0.08	7.7
10H-2, 125–150	49.8	0.16	1.36	NA	NC	NA	NC
10H-4, 125–150	52.8	0.18	1.54	0.66	0.48	0.06	8.0
311-U1328C-							
1H-3, 125–150	60.7	0.16	1.36	NA	NC	NA	NC
1H-5, 125–150	63.7	0.15	1.25	0.45	0.30	0.03	8.8
2H-4, 125–150	71.8	0.18	1.50	1.10	0.92	0.14	6.6
3H-4, 125–150	81.3	0.2	1.67	0.45	0.25	0.03	8.2
6H-7, 125–150	101.1	0.59	4.87	1.50	0.91	0.10	9.1
8X-2, 120–150	113.0	0.14	1.19	0.70	0.56	0.06	9.3
9X-2, 110–140	122.5	0.17	1.38	0.50	0.33	0.04	8.3
10X-2, 22–52	131.3	0.44	3.68	1.14	0.70	0.09	8.2
12X-1, 120–150	150.1	0.41	3.42	0.90	0.49	0.06	8.4
13X-1, 0–10	158.6	0.25	2.08	0.80	0.55	0.09	6.1
13X-2, 120–150	161.3	0.58	4.82	1.29	0.71	0.08	8.8
15X-2, 117–147	180.6	0.09	0.72	0.50	0.41	0.04	10.1
16X-2, 120–150	190.2	1.08	9.03	2.32	1.24	0.14	8.8
16X-4, 28–39	192.3	0.91	7.62	1.42	0.51	0.07	7.6
17X-3, 120–150	201.3	0.81	6.72	1.33	0.52	0.06	8.5
18X-2, 0–25	208.0	0.62	5.20	1.19	0.57	0.07	8.3
19X-3, 120–150	219.7	0.31	2.59	0.78	0.47	0.05	9.6
20X-4, 120–150	230.8	0.16	1.37	0.58	0.42	0.05	8.8
21X-4, 120–150	241.1	0.1	0.87	0.58	0.48	0.06	8.4
22X-4, 120–150	250.0	0.7	5.84	1.29	0.59	0.07	8.2
24X-4, 0–40	268.7	0.06	0.53	0.40	0.34	0.04	7.7
26X-4, 0–30	288.2	0.23	1.94	1.23	1.00	0.13	8.0
27X-4, 0–50	297.7	0.35	2.88	1.04	0.69	0.08	9.2

Note: NA = not analyzed; NC = not calculated.

Table T12. Perfluorocarbon tracer and fluorescent microsphere concentrations, Site U1328.

Core, section, interval (cm)	Depth (mbsf)	Detected PFT (ng/g sediment)		Detected particles (number/g sediment)		Comments
		Inner	Outer	Inner	Outer	
APC cores						
311-U1328B-						
1H-3, 0–5	3.00	0.0019	0.0114	ND	ND	High background PFT concentration
5H-2, 0–5	17.50	BDL	0.0018	BDL	1.83×10^5	
8H-3, 40–45	31.40	BDL	BDL	ND	ND	
9H-4, 0–5	41.80	BDL	BDL	ND	ND	
10H-4, 0–5	51.50	ND	ND	BDL	BDL	
311-U1328C-						
1H-5, 0–5	59.43	BDL	BDL	ND	ND	
3H-4, 0–5	80.00	BDL	BDL	ND	ND	
6H-7, 0–5	99.89	0.0049	0.0069	ND	ND	
XCB cores						
311-U1328C-						
16X-3, 127–128	191.77	ND	ND	4.31×10^5	ND	Clay layer; see Figure **F36**
16X-3, 133–134	191.83	ND	ND	BDL	ND	Sand layer; see Figure **F36**
20X-3, 32–33	228.67	ND	ND	BDL	1.88×10^5	Nonbiscuit
20X-3, 34–35	228.69	ND	ND	BDL	1.29×10^5	Biscuit
26X-5, 118–119	290.88	ND	ND	BDL	0.1×10^4	Sand layer
27X-1, 114–115	294.44	ND	ND	BDL	$>0.1 \times 10^4$	Nonbiscuit; see Figure **F36**
27X-1, 117–118	294.47	ND	ND	BDL	$>0.1 \times 10^4$	Biscuit; see Figure **F36**

Notes: PFT = perfluorocarbon tracers, APC = advanced piston corer, XCB = extended core barrel. ND = no data, BDL = below detection limit.

Table T13. Moisture and density, Holes U1328B, U1328C, U1328D, and U1328E. (Continued on next two pages.)

Core, section, interval (cm)	Depth (mbsf)	Density (g/cm^3)		Porosity (%)
		Bulk	Grain	
311-U1328B-				
1H-1, 70–72	0.70	1.67	2.80	63.7
1H-2, 48–50	1.98	1.70	2.81	62.4
1H-2, 93–95	2.43	1.69	2.75	61.4
1H-2, 103–105	2.53	1.69	2.75	61.6
1H-3, 45–47	3.45	1.66	2.77	63.4
2H-2, 10–12	5.60	1.64	2.83	65.8
4P-1, 17–19	14.67	1.71	2.77	60.5
4P-1, 69–71	15.19	1.81	2.83	56.2
5H-1, 8–10	16.58	1.65	2.83	65.4
5H-1, 55–57	17.05	1.66	2.75	63.1
6X-1, 10–12	18.50	1.51	2.76	72.3
6X-1, 41–44	18.81	1.61	2.81	67.3
6X-1, 90–92	19.30	1.67	2.83	64.5
6X-2, 21–23	19.76	1.85	2.80	53.5
8H-1, 56–58	28.56	1.71	2.82	62.0
8H-1, 108–110	29.08	1.70	2.80	62.1
8H-2, 6–8	29.56	1.71	2.84	62.2
8H-2, 86–88	30.36	1.75	2.77	58.3
8H-3, 38–40	31.38	1.83	2.78	54.2
8H-4, 4–6	32.54	1.86	2.78	52.3
8H-4, 67–69	33.17	1.92	2.78	49.1
8H-4, 144–146	33.94	1.79	2.81	57.2
8H-5, 22–24	34.22	1.82	2.78	54.6
8H-5, 57–59	34.57	1.82	2.76	54.2
8H-5, 96–98	34.96	1.82	2.79	55.1
8H-6, 4–6	35.04	1.79	2.74	55.5
8H-6, 56–58	35.56	1.74	2.80	59.7
9H-1, 26–28	37.76	1.71	2.72	59.7
9H-1, 83–85	38.33	1.79	2.79	56.8
9H-2, 5–7	39.02	1.79	2.73	55.1
9H-2, 74–76	39.71	1.75	2.77	58.3
9H-3, 20–22	40.51	1.80	2.76	55.6
9H-3, 98–100	41.29	1.99	2.77	44.8
9H-3, 136–138	41.67	1.80	2.72	54.5
9H-5, 7–9	43.38	1.71	2.74	60.1
9H-5, 76–78	44.07	1.69	2.72	60.9
9H-5, 133–135	44.64	1.67	2.74	62.6
9H-6, 2–4	44.83	1.65	2.69	62.3
9H-6, 85–87	45.66	1.73	2.75	58.9
10H-1, 22–24	47.22	1.72	2.75	59.9
10H-1, 86–88	47.86	1.68	2.77	62.3
10H-2, 4–6	48.54	1.74	2.75	58.5
10H-2, 51–53	49.01	2.06	2.74	39.4
10H-2, 95–97	49.45	1.79	2.78	56.4
10H-3, 21–23	50.21	1.77	2.74	56.3
10H-3, 114–116	51.14	1.78	2.78	56.9
10H-5, 26–28	53.26	1.70	2.75	60.5
10H-5, 70–72	53.70	1.85	2.76	52.7
10H-5, 139–141	54.39	1.97	2.75	45.3
10H-6, 28–30	54.75	1.81	2.78	55.5
10H-6, 96–98	55.43	1.82	2.79	55.3
10H-7, 7–9	55.54	1.75	2.750	57.7
10H-7, 73–75	56.20	1.80	2.73	54.5
311-U1328C-				
1H-1, 20–22	56.70	1.75	2.77	58.2
1H-1, 98–100	57.48	1.89	2.80	51.3
1H-2, 15–17	58.11	1.79	2.81	57
1H-2, 77–79	58.73	1.79	2.81	57.3
1H-2, 139–141	59.35	1.88	2.71	49.2
1H-3, 45–47	59.88	1.83	2.76	53.3
1H-3, 107–109	60.50	1.99	2.76	44.3
1H-4, 2–4	60.95	1.90	2.76	49.3
1H-4, 19–21	61.12	2.05	2.71	39.2
1H-4, 51–53	61.44	1.90	2.75	49.2
1H-4, 87–89	61.80	2.05	2.75	40.6
1H-4, 132–134	62.25	1.90	2.77	49.6
1H-4, 141–143	62.34	1.98	2.70	43.2
1H-6, 2–4	63.95	1.86	2.77	52.3
1H-6, 91–93	64.84	1.86	2.74	51.3
1H-6, 138–140	65.31	1.95	2.78	47.4
1H-7, 18–20	65.61	1.80	2.70	53.5
2H-1, 132–134	67.32	1.99	2.75	43.9
2H-2, 17–19	67.67	1.99	2.74	43.6
2H-2, 106–108	68.56	1.87	2.78	51.7
2H-3, 40–42	69.40	1.76	2.74	56.8
2H-3, 95–97	69.95	1.77	2.75	57.1
2H-5, 36–38	72.36	1.75	2.74	57.8
2H-5, 99–101	72.99	1.73	2.72	58.6
3H-1, 24–26	75.74	1.87	2.75	50.8
3H-1, 108–110	76.58	2.03	2.72	40.7
3H-2, 49–51	77.49	1.83	2.76	53.3
3H-3, 23–25	78.73	1.81	2.78	54.9
3H-3, 51–53	79.01	2.16	2.79	35.3
3H-5, 13–15	81.63	1.84	2.76	53.2
3H-5, 103–105	82.53	1.84	2.77	53.5
3H-6, 66–68	83.66	1.85	2.75	52.0
3H-7, 21–23	84.03	1.83	2.80	54.3
4X-1, 28–30	85.28	1.80	2.79	56.1
4X-1, 108–110	86.08	2.02	2.76	42.3
4X-3, 26–28	88.26	1.80	2.78	55.8
4X-3, 127–129	89.27	2.06	2.74	39.7
6H-1, 8–10	94.08	1.83	2.84	55.5
6H-1, 116–118	95.16	1.81	2.83	56.4
6H-2, 52–54	96.02	1.80	2.85	57.6
6H-2, 112–114	96.62	1.79	2.85	57.8
6H-3, 20–22	97.10	1.75	2.82	59.6
6H-3, 76–78	97.66	1.71	2.79	60.8
6H-5, 19–21	98.64	1.81	2.79	55.6
6H-8, 9–11	101.48	1.77	2.81	58.1
6H-8, 109–111	102.48	1.76	2.73	57.0
7X-1, 76–78	104.26	1.70	2.71	59.7
7X-1, 107–109	104.57	1.76	2.76	57.8
7X-2, 15–17	105.15	1.70	2.79	61.9
7X-2, 96–98	105.96	1.78	2.78	56.7
7X-4, 38–40	108.28	1.84	2.75	52.8
7X-4, 131–133	109.21	1.90	2.74	48.6
7X-5, 8–10	109.48	1.83	2.77	53.5
7X-5, 49–51	109.89	1.87	2.75	50.6
8X-1, 27–29	110.57	1.90	2.76	49.7
8X-1, 64–66	110.94	1.85	2.74	51.7
8X-1, 116–118	111.46	1.83	2.75	53.7
8X-2, 8–10	111.88	1.86	2.75	51.6
8X-2, 88–90	112.68	1.82	2.74	53.5
8X-4, 7–9	114.55	1.80	2.73	54.3
8X-4, 62–64	115.10	2.03	2.73	41.0
8X-4, 126–128	115.74	1.90	2.76	49.5
8X-5, 10–12	116.08	1.90	2.93	54.1
8X-5, 63–65	116.61	1.81	2.70	53.3
8X-5, 135–137	117.33	1.85	2.73	51.7
8X-6, 26–28	117.74	1.89	2.79	51.0
8X-6, 87–89	118.35	1.92	2.74	48.0
9X-1, 5–7	119.95	1.83	2.72	52.6
9X-1, 76–78	120.66	1.84	2.73	52.5
9X-1, 144–146	121.34	1.80	2.75	55.0
9X-2, 3–5	121.43	1.89	2.78	50.8
9X-2, 47–49	121.87	1.79	2.74	55.0
9X-4, 7–9	123.97	1.96	2.74	45.2
9X-4, 66–68	124.56	1.88	2.76	50.4
9X-4, 144–146	125.34	1.84	2.73	52.0
9X-5, 11–13	125.51	1.86	2.72	50.8
9X-5, 75–77	126.15	1.84	2.70	51.7
9X-5, 132–134	126.72	1.87	2.74	50.5
9X-6, 26–28	127.03	1.86	2.76	51.5

Table T13 (continued).

Core, section, interval (cm)	Depth (mbsf)	Density (g/cm^3)		Porosity (%)
		Bulk	Grain	
9X-7, 11–13	127.59	1.90	2.74	48.7
9X-7, 79–81	128.27	2.00	2.76	43.4
10X-1, 11–13	129.71	1.80	2.73	54.7
10X-1, 66–68	130.26	1.78	2.71	55.5
10X-1, 137–139	130.97	1.78	2.77	56.4
10X-3, 16–18	132.76	1.68	2.73	61.8
10X-3, 73–75	133.33	1.65	2.75	63.4
10X-3, 139–141	133.99	1.66	2.63	60.2
11X-1, 9–11	139.39	1.71	2.75	60.5
11X-1, 55–57	139.85	1.66	2.70	62.1
11X-1, 112–114	140.42	1.65	2.67	62.1
11X-2, 10–12	140.90	1.65	2.71	62.7
11X-2, 57–59	141.37	1.68	2.69	60.8
11X-2, 105–107	141.85	1.65	2.70	62.7
11X-4, 9–11	143.89	1.99	2.79	45.2
11X-4, 40–42	144.20	1.67	2.79	63.7
11X-5, 13–15	144.93	1.65	2.71	62.8
11X-5, 74–76	145.54	1.64	2.70	63.2
12X-1, 3–5	148.93	1.84	2.74	52.3
12X-1, 78–80	149.68	1.73	2.76	59.2
12X-2, 33–35	150.73	1.80	2.73	54.6
12X-2, 96–98	151.36	1.83	2.74	52.9
12X-2, 133–135	151.73	1.88	2.74	50.3
12X-3, 41–43	152.31	1.88	2.74	50.3
12X-3, 83–85	152.73	1.87	2.75	50.9
12X-3, 141–143	153.31	1.91	2.86	51.9
12X-5, 20–22	155.10	1.94	2.78	47.7
12X-5, 54–56	155.44	1.95	2.76	46.8
12X-5, 83–85	155.73	1.86	2.78	52.7
12X-6, 13–15	156.03	1.84	2.77	53.6
12X-6, 47–49	156.37	1.82	2.75	53.8
13X-1, 67–69	159.27	1.76	2.79	58.6
13X-1, 120–122	159.80	1.89	2.82	51.5
13X-2, 51–53	160.58	1.75	2.77	58.5
13X-2, 99–101	161.06	1.75	2.73	57.3
13X-4, 35–37	163.42	1.75	2.79	58.9
13X-4, 101–103	164.08	1.72	2.78	60.3
13X-5, 42–44	164.79	1.80	2.75	55.3
14X-1, 11–12	168.31	1.72	2.70	58.3
14X-1, 102–102	169.22	1.84	2.77	53.3
14X-2, 67–69	170.20	1.89	2.84	52.1
14X-2, 131–133	170.84	1.89	2.84	52.2
14X-3, 21–23	171.24	1.82	2.75	53.7
14X-3, 105–107	172.08	1.67	2.74	62.3
14X-5, 56–58	174.59	1.60	2.60	63.6
15X-1, 39–41	178.29	1.84	2.69	51.0
15X-1, 98–100	178.88	1.85	2.80	53.5
15X-2, 32–34	179.72	1.82	2.74	53.7
15X-2, 96–98	180.36	1.86	2.76	51.8
15X-3, 23–25	181.10	1.85	2.76	52.6
15X-3, 117–119	182.04	1.86	2.74	51.3
15X-5, 27–29	184.14	1.84	2.75	51.2
15X-5, 88–90	184.75	1.83	2.79	54.4
15X-6, 47–49	185.34	1.81	2.75	54.7
16X-1, 22–24	187.72	1.66	2.69	62.0
16X-1, 90–92	188.40	1.69	2.64	58.9
16X-2, 32–34	189.32	1.68	2.67	60.5
16X-2, 97–99	189.97	1.68	2.67	59.9
16X-3, 29–31	190.79	1.72	2.72	58.4
16X-3, 135–137	191.85	1.98	2.75	44.6
16X-5, 39–41	193.89	1.82	2.77	54.4
17X-1, 49–51	197.59	1.83	2.72	52.3
17X-1, 91–93	198.01	1.78	2.74	55.9
17X-2, 67–69	199.27	1.81	2.74	54.3
17X-2, 101–103	199.61	1.83	2.71	52.5
17X-4, 35–37	201.95	1.85	2.76	52.5
17X-4, 126–128	202.86	1.82	2.76	53.9
17X-5, 45–47	203.55	1.83	2.76	53.7
17X-6, 58–60	204.68	1.85	2.77	52.6
18X-1, 18–20	206.88	1.82	2.73	53.2
18X-1, 54–56	207.24	1.79	2.76	55.8
18X-3, 24–26	209.24	1.80	2.80	56.0
19X-1, 7–9	216.37	1.73	2.76	59.2
19X-1, 53–55	216.83	1.85	2.75	52.0
19X-2, 16–18	217.19	1.90	2.78	49.8
19X-2, 80–82	217.83	1.83	2.71	52.0
19X-2, 123–125	218.26	1.67	2.70	61.5
19X-3, 22–24	218.75	1.87	2.74	50.7
19X-3, 74–76	219.27	1.85	2.76	52.5
19X-3, 119–121	219.72	1.79	2.78	56.3
20X-1, 5–7	226.05	1.81	2.78	55.3
20X-1, 50–52	226.50	1.83	2.81	54.9
20X-1, 94–96	226.94	1.76	2.69	55.9
20X-2, 20–22	227.70	1.75	2.78	58.5
20X-2, 68–70	228.18	1.80	2.75	55.2
20X-3, 16–18	228.51	1.74	2.73	57.8
20X-3, 82–84	229.17	1.76	2.77	58.0
20X-5, 40–42	231.47	1.97	2.77	45.5
20X-5, 75–77	231.82	1.78	2.74	56.2
21X-1, 0–2	235.60	1.78	2.73	55.4
21X-1, 92–93	236.52	1.96	2.76	45.9
21X-2, 28–30	237.16	1.94	2.80	48.4
21X-2, 79–81	237.67	1.91	2.76	48.7
21X-3, 3–5	238.41	1.84	2.78	53.3
21X-3, 61–63	238.99	1.89	2.77	50.1
21X-3, 133–135	239.71	1.82	2.78	54.5
21X-5, 1–3	241.39	1.80	2.75	54.9
21X-5, 42–44	241.80	1.85	2.73	51.8
21X-5, 103–105	242.41	1.97	2.76	45.7
21X-6, 2–4	242.79	1.73	2.77	59.6
21X-6, 52–54	243.29	1.85	2.82	54.1
21X-6, 117–119	243.94	1.78	2.77	56.5
22X-1, 12–14	245.32	1.78	2.75	56.3
22X-1, 25–27	245.45	1.81	2.77	55.1
22X-1, 61–63	245.81	1.81	2.73	53.8
22X-2, 14–16	246.84	1.81	2.82	56.0
22X-3, 3–5	247.34	1.84	2.71	51.9
22X-3, 62–64	247.93	1.84	2.72	52.2
22X-3, 141–143	248.72	1.93	2.74	47.4
22X-5, 11–13	250.42	1.86	2.76	52.0
22X-5, 59–61	250.90	1.70	2.73	60.6
22X-6, 24–26	252.05	1.90	2.79	50.4
22X-6, 80–82	252.61	1.88	2.75	50.7
22X-7, 9–11	252.96	1.89	2.76	50.4
23X-1, 2–4	254.82	1.83	2.74	52.8
23X-1, 64–66	255.44	1.87	2.78	51.8
23X-1, 126–128	256.06	2.01	2.75	43.1
23X-2, 13–15	256.43	1.88	2.76	50.8
23X-2, 67–69	256.97	1.87	2.74	50.9
23X-2, 140–142	257.70	1.89	2.77	50.2
23X-4, 7–9	259.37	1.95	2.78	46.9
23X-4, 87–89	260.17	1.99	2.78	45.0
23X-5, 27–29	260.57	1.95	2.75	46.4
24X-1, 23–25	264.63	1.89	2.77	50.5
24X-1, 78–80	265.18	1.82	2.75	54.0
24X-1, 127–129	265.67	1.82	2.80	55.0
24X-2, 11–13	265.97	1.90	2.74	49.2
24X-2, 88–90	266.74	1.77	2.75	56.9
24X-2, 126–128	267.12	1.80	2.73	54.3
24X-4, 59–61	269.31	1.88	2.77	51.1
24X-4, 110–112	269.82	1.88	2.72	49.7
24X-4, 140–142	270.12	1.90	2.78	50.3
24X-5, 33–35	270.55	1.93	2.75	47.4
24X-6, 8–10	270.88	1.94	2.73	46.5
24X-6, 96–98	271.76	1.87	2.78	51.6
25X-1, 17–19	274.27	1.84	2.73	52.5

Table T13 (continued).

Core, section, interval (cm)	Depth (mbsf)	Density (g/cm^3)		Porosity (%)
		Bulk	Grain	
25X-1, 76–78	274.86	1.90	2.70	48.2
25X-1, 136–138	275.46	1.94	2.67	44.2
25X-2, 26–28	275.86	1.93	2.76	47.9
25X-2, 57–59	276.17	1.78	2.80	57.5
25X-2, 139–141	276.99	1.92	2.7	47.3
25X-4, 47–49	279.07	1.88	2.74	50.4
25X-4, 103–105	279.63	1.87	2.76	51.4
25X-4, 145–147	280.05	1.91	2.76	48.7
25X-5, 16–18	280.26	1.88	2.77	50.8
25X-5, 75–77	280.85	1.85	2.71	51.0
25X-6, 45–47	281.55	1.76	2.72	56.6
26X-1, 51–53	284.21	1.90	2.72	48.3
26X-1, 113–115	284.83	1.85	2.72	51.1
26X-2, 40–42	285.60	1.86	2.74	51.3
26X-2, 124–126	286.44	1.95	2.72	45.5
26X-4, 53–55	288.73	1.90	2.75	49.4
26X-4, 143–145	289.63	1.85	2.73	51.3
26X-5, 34–36	290.04	1.93	2.77	47.9
26X-5, 91–93	290.61	1.86	2.74	51.0
26X-6, 11–13	291.31	1.93	2.70	46.3
26X-6, 86–88	292.06	1.84	2.72	51.9
27X-1, 50–52	293.80	1.91	2.75	48.6
27X-1, 90–92	294.20	1.94	2.72	46.3
27X-1, 93–95	294.23	1.93	2.71	46.3
27X-2, 34–36	295.14	1.93	2.80	49.2
27X-2, 119–121	295.99	1.91	2.73	48.0
27X-4, 62–64	298.34	1.90	2.74	48.9
27X-4, 110–112	298.82	1.96	2.79	47.1
27X-5, 15–17	299.26	1.89	2.72	49.0
27X-5, 91–93	300.02	1.91	2.72	47.7
27X-6, 43–45	300.54	1.98	2.77	45.3
311-U1328D-				
1X-1, 58–60	0.58	1.69	2.79	62.1
1X-2, 11–13	1.61	1.70	2.79	61.7
1X-3, 39–41	3.39	1.57	2.77	68.4
1X-4, 44–46	4.94	1.61	2.78	66.6
1X-5, 48–50	6.48	1.59	2.73	66.5
2X-1, 14–16	4.64	1.65	2.82	65.1
2X-2, 25–27	5.75	1.66	2.76	63.6
311-U1328E-				
2X-1, 30–32	6.80	1.46	2.67	73.6
2X-1, 52–54	7.02	1.52	2.77	71.6
8X-1, 24–26	26.94	1.63	2.76	65.2
8X-1, 114–116	27.84	1.73	2.76	59.1
8X-2, 78–80	28.98	1.73	2.77	59.6
8X-3, 29–31	29.74	1.69	2.77	62.0
9X-1, 13–15	36.43	1.59	2.72	66.7
9X-1, 123–125	37.53	1.72	2.76	59.9
9X-2, 11–13	37.91	1.72	2.83	61.3
9X-3, 8–10	38.38	1.80	2.75	55.1
9X-3, 59–61	38.89	1.76	2.75	57.6
9X-4, 25–27	39.19	1.81	2.80	55.8
9X-5, 5–7	39.87	1.83	2.79	54.3
9X-5, 73–75	40.55	1.80	2.76	55.7

Table T14. Compressional wave velocity, Hole U1328B.

Core, section interval (cm)	Depth (mbsf)	Velocity (m/s)		
		PWS1	PWS2	PWS3
311-U1328B-				
1H-1, 65	0.65	1561.4		
1H-1, 65	0.65		1535.5	
1H-1, 65	0.65			1528.6
1H-2, 25	1.75	1535.5		
1H-2, 25	1.75		1535.5	
1H-2, 25	1.75			1510.4
1H-2, 56	2.06	1615.8		
1H-2, 56	2.06		1549.3	
1H-2, 56	2.06			1554.6
1H-2, 83	2.33			1480.1
1H-2, 87	2.37	1475.2		
1H-2, 134	2.84			1426.2
1H-3, 24	3.24			1381.1
1H-3, 42	3.42			1399.5

Table T15. Torvane shear strength, Holes U1328B and U1328C. (See table note. Continued on next page.)

Core, section, interval (cm)	Depth (mbsf)	Torvane shear strength (kPa)	Torvane size
311-U1328B-			
1H-2, 67–69	2.17	18	M
1H-2, 108–110	2.58	15	M
1H-3, 21–23	3.21	15	M
5H-1, 12–14	16.62	12	M
5H-1, 53–55	17.03	18	M
8H-1, 50–52	28.50	23	M
8H-1, 104–106	29.04	20	M
8H-2, 15–17	29.65	22	M
8H-2, 81–83	30.31	30	M
8H-3, 4–6	31.04	25	M
8H-3, 35–37	31.35	29	M
8H-4, 8–10	32.58	32	M
8H-4, 62–64	33.12	33	M
8H-4, 140–142	33.90	30	M
8H-5, 18–20	34.18	25	M
8H-5, 58–60	34.58	34	M
8H-5, 91–93	34.91	28	M
8H-6, 6–8	35.06	22	M
8H-6, 52–54	35.52	23	M
9H-1, 29–31	37.79	26	M
9H-1, 80–82	38.30	27	M
9H-2, 9–11	39.06	25	M
9H-2, 70–72	39.67	24	M
9H-3, 24–26	40.55	30	M
9H-3, 95–98	41.26	30	M
9H-3, 140–142	41.71	30	M
9H-5, 4–6	43.35	32	M
9H-5, 70–72	44.01	35	M
9H-5, 128–130	44.59	35	M
9H-6, 5–7	44.86	27	M
9H-6, 88–90	45.69	30	M
10H-1, 27–29	47.27	32	M
10H-1, 91.5–93.5	47.92	20	M
10H-2, 9–11	48.59	41	M
10H-2, 65–68	49.15	28	M
10H-3, 17–19	50.17	34	M
10H-3, 117–119	51.17	38	M
10H-5, 22–24	53.22	32	M
10H-5, 65–68	53.65	27	M
10H-6, 23–25	54.70	29	M
10H-5, 135–137	54.35	50	M
10H-6, 91–93	55.38	30	M
10H-7, 13–15	55.60	39	M
10H-7, 65–67	56.12	38	M
311-U1328C-			
1H-1, 13–15	56.63	38	M
1H-1, 78–80	57.28	26	M
1H-2, 17–19	58.13	26	M
1H-2, 73–76	58.69	30	M
1H-2, 136–138	59.32	29	M
1H-3, 32–34	59.75	15	M
1H-3, 97–99	60.40	29	M
1H-4, 5–7	60.98	28	M
1H-4, 53–55	61.46	44	M
1H-4, 129–131	62.22	32	M
1H-6, 5–7	63.98	32	M
1H-6, 77–79	64.70	29	M
1H-6, 133–135	65.26	30	M
1H-7, 10–12	65.53	30	M
1H-6, 100–102	64.93	35	M
2H-1, 27–29	66.27	30	M
2H-3, 92–94	69.92	18	M
2H-5, 31–33	72.31	22	M
2H-5, 100–102	73.00	30	M
3H-1, 59–61	76.09	35	M
3H-2, 77–79	77.77	32	M
3H-3, 81–83	79.31	40	M
3H-5, 36–38	81.86	41	M
3H-6, 73–75	83.73	35	M
3H-7, 47–49	84.29	36	M
4X-3, 16–18	88.16	40	M
6H-1, 14–16	94.14	38	M
6H-2, 124–126	96.74	33	M
6H-3, 61–63	97.51	27	M
6H-5, 29–31	98.74	39	M
6H-8, 85–87	102.24	40	M
7X-1, 94–96	104.44	34	M
7X-2, 69–71	105.69	38	M
7X-4, 62–64	108.52	38	M
7X-5, 26–28	109.66	42	M
8X-1, 31–33	110.61	34	M
8X-1, 61–63	110.91	34	M
8X-1, 121–123	111.51	40	M
8X-2, 15–17	111.95	40	M
8X-2, 81–83	112.61	45	M
8X-4, 14–16	114.62	45	M
8X-4, 72–74	115.20	61	M
8X-4, 130–132	115.78	55	M
8X-5, 18–20	116.16	44	M
8X-5, 55–57	116.53	60	M
8X-5, 127–129	117.25	56	M
8X-6, 32–34	117.80	55	M
8X-6, 87–89	118.35	68	M
9X-1, 10–12	120.00	32	M
9X-1, 81–83	120.71	15	M
9X-1, 129–131	121.19	54	M
9X-2, 10–12	121.50	38	M
9X-3, 21–23	123.01	44	M
9X-3, 76–78	123.56	73	M
9X-3, 133–135	124.13	59	M
9X-5, 15–17	125.55	70	M
9X-5, 124–126	126.64	63	M
9X-7, 14–16	127.62	60	M
9X-7, 83–85	128.31	69	M
9X-6, 13–15	126.90	45	M
10X-1, 19–21	129.79	85	M
10X-1, 62–64	130.22	100	S
10X-1, 142–144	131.02	37.5	S
10X-3, 23–25	132.83	87.5	S
10X-3, 70–72	133.30	75	S
10X-3, 134–136	133.94	75	S
11X-1, 14–16	139.44	30	M
11X-1, 63–65	139.93	43	M
11X-1, 105–107	140.35	33	M
11X-2, 5–7	140.85	43	M
11X-2, 52–54	141.32	55	M
11X-2, 99–101	141.79	52	M
11X-4, 14–16	143.94	47	M
11X-4, 91–93	144.71	54	M
11X-5, 7–9	144.87	50	M
11X-5, 63–65	145.43	69	M
12X-1, 11–13	149.01	35	M
12X-1, 83–85	149.73	46	M
12X-2, 29–31	150.69	45	M
12X-2, 88–90	151.28	45	M
12X-2, 129–131	151.69	40	M
12X-4, 46–49	153.86	40	M
12X-4, 77–79	154.17	60	M
12X-4, 136–138	154.76	51	M
12X-5, 16–18	155.06	42	M
12X-5, 49–51	155.39	45	M
12X-5, 91–93	155.81	50	M
12X-6, 13–15	156.03	54	M
13X-4, 114–110	164.21	50	M
14X-1, 128–130	169.48	35	M

Table T15 (continued).

Core, section, interval (cm)	Depth (mbsf)	Torvane shear strength (kPa)	Torvane size
14X-5, 67–69	174.70	45	M
15X-3, 64–66	181.51	48	M
15X-1, 54–56	178.44	52	M
16X-3, 64–66	191.14	37	M
17X-4, 59–61	202.19	38	M
19X-2, 12–14	217.15	44	M
19X-2, 128–130	218.31	53	M
19X-4, 118–120	221.21	65	M
20X-3, 25–27	228.60	55	M
21X-1, 6–8	235.66	70	M
21X-2, 33–35	237.21	44	M
21X-3, 55–57	238.93	88	M
21X-3, 126–128	239.64	87.5	S
21X-5, 34–36	241.72	70	S
21X-5, 99–101	242.37	112.5	S
21X-6, 55–57	243.32	107.5	S
21X-6, 107–109	243.84	62.5	S
22X-1, 19–21	245.39	65	S
22X-1, 69–71	245.89	100	S
22X-3, 9–11	247.40	95	S
22X-3, 68–70	247.99	95	S
22X-3, 137–139	248.68	120	S
22X-5, 55–57	250.86	92.5	S
22X-5, 122–124	251.53	97.5	S
22X-7, 4–6	252.91	62.5	S
22X-6, 32–34	252.13	112.5	S
22X-6, 76–78	252.57	115	S
23X-1, 61–63	255.41	62.5	S
23X-2, 63–65	256.93	100	S
23X-2, 137–139	257.67	62.5	S
23X-4, 15–17	259.45	127.5	S
23X-4, 78–80	260.08	157.5	S
23X-5, 32–34	260.62	155	S
24X-1, 27–29	264.67	62.5	S
24X-2, 18–20	266.04	60	S
26X-2, 97–99	286.17	75	S
27X-2, 76–78	295.56	60	S
27X-5, 84–86	299.95	45	S

Note: M = medium size (2.5 cm diameter), S = small size (1.9 cm diameter).

Table T16. AVS shear strength, Holes U1328B and U1328C.

Core, section, interval (cm)	Depth (mbsf)	Vane size	Shear strength (kPa)	
			Peak	Residual
311-U1328B-				
5H-1, 50	28.61	B	11.38	7.48
8H-1, 61	34.56	B	11.38	7.31
8H-5, 56	37.99	B	16.65	11.72
9H-1, 49	44.05	B	17.50	13.25
9H-5, 74	47.63	B	20.39	14.10
10H-1, 63	53.46	B	18.69	10.02
10H-5, 46	57.55	B	15.12	9.51
311-U1328C-				
1H-1, 105	61.38	B	17.33	12.74
1H-4, 45	64.36	B	24.12	18.86
1H-6, 43	65.75	B	22.77	20.05
1H-7, 32	66.14	B	13.76	11.21
2H-1, 14	75.70	B	22.26	18.69
3H-1, 20	81.80	B	32.28	25.14
3H-5, 30	88.57	B	30.92	25.82
4X-3, 57	96.66	B	22.77	17.16
6H-2, 116	102.29	B	26.67	15.46
6H-8, 90	108.29	B	41.28	16.48
7X-4, 39	109.56	B	25.48	16.14
7X-5, 16	111.43	B	38.06	24.46
8X-1, 113	116.58	B	17.84	13.42
8X-5, 60	120.22	B	54.70	34.32
9X-1, 32	126.25	B	23.11	20.56
9X-5, 85	130.43	B	26.84	19.88
10X-1, 83	133.20	B	47.23	32.62
10X-3, 60	139.89	B	38.73	27.69
11X-1, 59	149.32	B	18.18	13.42
12X-1, 42	155.60	B	29.73	24.12
12X-5, 70	159.70	B	31.09	26.33
13X-1, 110	164.67	B	30.58	24.80
13X-5, 30	168.62	B	36.53	26.84
14X-1, 42	174.08	B	35.85	30.58
14X-5, 5	181.37	B	29.56	10.36
15X-3, 50	193.85	B	50.63	16.65
16X-5, 35	197.41	B	29.39	17.16
17X-1, 31	206.93	B	39.58	17.84
18X-1, 23	217.35	B	40.60	15.29
19X-2, 32	286.00	B	23.61	18.86
26X-2, 80	295.33	B	64.22	15.12
27X-2, 53		B	92.42	16.99

Notes: B = medium vane size. AVS values calibrated for spring constant used to calculate shear strength.

Table T17. Contact resistivity, Holes U1328B and U1328C. (Continued on next two pages.)

Core, section, interval (cm)	Depth (mbsf)	Resistivity (Ωm)
Parallel		
311-U1328B-		
1H-1, 62	0.62	0.515
1H-1, 62	0.62	0.512
1H-1, 73	0.73	0.419
1H-2, 15	1.65	0.348
1H-2, 25	1.75	0.401
1H-2, 35	1.85	0.418
1H-2, 45	1.95	0.463
1H-2, 65	2.15	0.427
1H-2, 85	2.35	0.421
1H-2, 100	2.50	0.474
1H-2, 110	2.60	0.487
1H-2, 125	2.75	0.421
1H-2, 135	2.85	0.385
1H-3, 7	3.07	0.362
1H-3, 20	3.20	0.391
1H-3, 40	3.40	0.449
1H-3, 55	3.55	0.374
2H-1, 7	4.57	0.591
2H-1, 46	4.96	0.510
5H-1, 10	16.60	0.455
5H-1, 23	16.73	0.595
5H-1, 37	16.87	0.558
5H-1, 57	17.07	0.580
6X-1, 42	18.82	0.482
6X-1, 62	19.02	0.484
6X-1, 87	19.27	0.489
6X-2, 7	19.62	0.662
6X-2, 21	19.76	0.709
6X-2, 37	19.92	0.587
8H-1, 10	28.10	0.778
8H-1, 32	28.32	0.796
8H-1, 42	28.42	0.772
8H-1, 52	28.52	0.836
8H-1, 94	28.94	0.753
8H-1, 110	29.10	0.694
8H-2, 7	29.57	0.719
8H-2, 17	29.67	0.897
8H-2, 40	29.90	0.824
8H-2, 57	30.07	0.834
8H-2, 71	30.21	0.781
8H-2, 87	30.37	0.815
8H-2, 104	30.54	0.750
8H-3, 8	31.08	0.783
8H-3, 20	31.20	0.946
8H-3, 37	31.37	0.828
8H-4, 6	32.56	0.872
8H-4, 23	32.73	0.875
8H-4, 40	32.90	0.794
8H-4, 69	33.19	1.036
8H-4, 100	33.50	1.014
8H-4, 118	33.68	0.884
8H-4, 132	33.82	0.813
8H-5, 6	34.06	0.801
8H-5, 22	34.22	0.895
8H-5, 38	34.38	0.896
8H-5, 60	34.60	0.883
8H-5, 83	34.83	0.873
8H-5, 97	34.97	0.827
8H-6, 5	35.05	0.876
8H-6, 17	35.17	0.809
8H-6, 37	35.37	0.859
8H-6, 57	35.57	0.798
9H-1, 6	37.56	0.690
9H-1, 28	37.78	0.723
9H-1, 47	37.97	0.645
9H-1, 68	38.18	0.715
9H-1, 85	38.35	0.711
9H-2, 6	39.03	0.777
9H-2, 35	39.32	0.780
9H-2, 57	39.54	0.733
9H-2, 74	39.71	0.607
9H-2, 95	39.92	0.691
9H-3, 5	40.36	0.715
9H-3, 20	40.51	0.726
9H-3, 35	40.66	0.644
9H-3, 50	40.81	0.633
9H-3, 70	41.01	0.746
9H-3, 93	41.24	0.653
9H-3, 105	41.36	0.670
9H-3, 121	41.52	0.755
9H-3, 137	41.68	0.868
9H-5, 8	43.39	0.805
9H-5, 45	43.76	0.674
9H-5, 62	43.93	0.715
9H-5, 76	44.07	0.800
9H-5, 100	44.31	0.858
9H-5, 115	44.46	0.636
9H-5, 135	44.66	0.761
9H-6, 3	44.84	0.679
9H-6, 27	45.08	0.918
9H-6, 71	45.52	0.719
9H-6, 85	45.66	0.690
9H-6, 107	45.88	0.739
10H-1, 6	47.06	0.669
10H-1, 23	47.23	0.716
10H-1, 41	47.41	0.669
10H-1, 64	47.64	0.821
10H-1, 87	47.87	0.926
10H-1, 108	48.08	0.751
10H-2, 6	48.56	0.755
10H-2, 25	48.75	0.874
10H-2, 46	48.96	0.815
10H-2, 66	49.16	0.771
10H-2, 96	49.46	0.641
10H-3, 9	50.09	0.801
10H-3, 24	50.24	0.746
10H-3, 41	50.41	0.727
10H-3, 63	50.63	0.718
10H-3, 93	50.93	0.707
10H-3, 103	51.03	0.767
10H-3, 142	51.42	0.768
10H-5, 8	53.08	0.737
10H-5, 27	53.27	0.761
10H-5, 43	53.43	0.729
10H-5, 70	53.70	0.826
10H-5, 101	54.01	0.880
10H-5, 121	54.21	1.140
10H-5, 139	54.39	0.995
10H-6, 9	54.56	0.780
10H-6, 30	54.77	0.851
10H-6, 48	54.95	0.746
10H-6, 70	55.17	0.841
10H-6, 97	55.44	0.756
10H-7, 9	55.56	0.754
10H-7, 27	55.74	0.702
10H-7, 39	55.86	0.906
10H-7, 57	56.04	0.772
10H-7, 73	56.20	0.708
311-U1328C-		
1H-1, 5	56.55	0.691
1H-1, 20	56.70	0.786
1H-1, 36	56.86	0.731
1H-1, 64	57.14	0.676
1H-1, 97	57.47	0.765
1H-2, 4	58.00	0.714
1H-2, 14	58.10	0.685
1H-2, 29	58.25	0.667
1H-2, 53	58.49	0.815
1H-2, 64	58.60	0.619
1H-2, 78	58.74	0.639
1H-2, 100	58.96	0.660
1H-2, 121	59.17	0.722
1H-2, 131	59.27	0.766
1H-3, 21	59.64	0.640
1H-3, 40	59.83	0.606
1H-3, 66	60.09	0.599
1H-3, 87	60.30	0.617
1H-3, 106	60.49	0.856
1H-4, 4	60.97	0.682
1H-4, 14	61.07	0.673
1H-4, 20	61.13	1.048
1H-4, 27	61.20	0.652
1H-4, 37	61.30	0.845
1H-4, 48	61.41	0.727
1H-4, 53	61.46	0.676
1H-4, 63	61.56	1.841
1H-4, 73	61.66	0.835
1H-4, 80	61.73	0.656
1H-4, 89	61.82	0.953
1H-4, 97	61.90	0.718
1H-4, 106	61.99	0.738
1H-4, 116	62.09	0.764
1H-4, 133	62.26	0.819
1H-4, 141	62.34	0.934
1H-6, 3	63.96	0.711
1H-6, 23	64.16	0.629
1H-6, 43	64.36	0.676
1H-6, 56	64.49	0.816
1H-6, 93	64.86	0.701
1H-6, 116	65.09	1.728
1H-6, 126	65.19	0.686
1H-6, 142	65.35	0.810
1H-7, 6	65.49	0.739
1H-7, 20	65.63	0.749
1H-7, 38	65.81	0.675
2H-1, 5	66.05	0.699
2H-1, 14	66.14	0.798
2H-1, 32	66.32	0.673
2H-1, 45	66.45	0.847
2H-1, 73	66.73	0.609
2H-1, 97	66.97	0.875
2H-1, 130	67.30	1.251
2H-2, 13	67.63	0.982
2H-2, 61	68.11	0.961
2H-2, 105	68.55	1.077
2H-3, 40	69.40	0.658
2H-3, 66	69.66	0.711
2H-3, 95	69.95	0.708
2H-3, 105	70.05	0.676
2H-3, 129	70.29	0.674
2H-5, 10	72.10	0.723
2H-5, 37	72.37	0.710
2H-5, 59	72.59	0.642
2H-5, 80	72.80	0.679
2H-5, 101	73.01	0.644
3H-1, 8	75.58	0.855
3H-1, 30	75.80	0.878
3H-1, 50	76.00	0.805
3H-1, 66	76.16	0.869
3H-1, 69	76.19	0.915
3H-1, 73	76.23	0.723
3H-1, 87	76.37	0.929
3H-1, 92	76.42	0.817
3H-1, 99	76.49	1.199

Table T17 (continued).

Core, section, interval (cm)	Depth (mbsf)	Resistivity (Ωm)
3H-1, 104	76.54	1.080
3H-1, 110	76.60	0.928
3H-1, 120	76.70	1.326
3H-1, 128	76.78	1.698
3H-1, 145	76.95	0.904
3H-2, 10	77.10	1.073
3H-2, 32	77.32	0.705
3H-2, 51	77.51	0.792
3H-2, 77	77.77	0.825
3H-2, 101	78.01	0.791
3H-3, 10	78.60	0.732
3H-3, 31	78.81	0.907
3H-3, 51	79.01	1.504
3H-3, 71	79.21	0.999
3H-3, 91	79.41	0.927
3H-3, 115	79.65	0.831
3H-3, 135	79.85	0.879
3H-3, 145	79.95	1.185
3H-5, 15	81.65	0.810
3H-5, 35	81.85	0.770
3H-5, 64	82.14	0.802
3H-5, 105	82.55	0.900
3H-5, 120	82.70	0.940
3H-5, 130	82.80	0.846
3H-6, 6	83.06	1.000
3H-6, 26	83.26	0.845
3H-6, 46	83.46	0.908
3H-6, 66	83.66	0.890
3H-6, 76	83.76	0.849
3H-7, 22	84.04	0.827
3H-7, 37	84.19	0.815
3H-7, 50	84.32	0.792
4X-1, 25	85.25	0.861
4X-1, 50	85.50	0.779
4X-1, 83	85.83	0.672
4X-1, 104	86.04	0.645
4X-1, 124	86.24	1.061
4X-1, 141	86.41	0.766
4X-3, 10	88.10	0.673
4X-3, 30	88.30	0.651
4X-3, 50	88.50	0.756
4X-3, 60	88.60	0.697
4X-3, 97	88.97	0.843
4X-3, 120	89.20	0.619
4X-3, 128	89.28	0.891
4X-3, 134	89.34	0.659
6H-1, 10	94.10	0.669
6H-1, 35	94.35	0.744
6H-1, 55	94.55	0.747
6H-1, 75	94.75	0.682
6H-1, 95	94.95	0.811
6H-1, 115	95.15	0.675
6H-1, 140	95.40	0.785
6H-2, 7	95.57	0.709
6H-2, 29	95.79	0.679
6H-2, 50	96.00	0.889
6H-2, 71	96.21	0.659
6H-2, 93	96.43	0.757
6H-2, 113	96.63	0.664
6H-2, 133	96.83	0.635
6H-3, 10	97.00	0.645
6H-3, 30	97.20	0.655
6H-3, 50	97.40	0.619
6H-3, 70	97.60	0.697
6H-4, 41	98.31	0.684
6H-4, 50	98.40	0.767
6H-4, 8	97.98	1.134
6H-5, 20	98.65	0.835
6H-5, 40	98.85	0.768
6H-6, 8	99.08	0.653
6H-6, 9	99.09	0.627
6H-6, 80	99.80	0.697
6H-8, 10	101.49	0.670
6H-8, 48	101.87	0.704
6H-8, 83	102.22	0.906
6H-8, 97	102.36	0.739
6H-8, 111	102.50	0.782
7X-1, 40	103.90	0.478
7X-1, 60	104.10	0.502
7X-1, 84	104.34	0.510
7X-1, 104	104.54	0.539
7X-1, 124	104.74	0.511
7X-1, 144	104.94	0.557
7X-2, 15	105.15	0.483
7X-2, 40	105.40	0.538
7X-2, 62	105.62	0.549
7X-2, 79	105.79	0.601
7X-2, 99	105.99	0.583
7X-4, 15	108.05	0.629
7X-4, 34	108.24	0.851
7X-4, 55	108.45	0.674
7X-4, 75	108.65	0.623
7X-4, 95	108.85	0.627
7X-4, 115	109.05	0.838
7X-4, 135	109.25	0.700
7X-5, 10	109.50	0.621
7X-5, 30	109.70	0.657
7X-5, 50	109.90	0.645
7X-5, 60	110.00	0.638
8X-1, 7	110.37	0.724
8X-1, 27	110.57	0.749
8X-1, 50	110.80	0.683
8X-1, 64	110.94	0.681
8X-1, 87	111.17	0.632
8X-1, 116	111.46	0.632
8X-1, 142	111.72	0.863
8X-2, 11	111.91	0.629
8X-2, 35	112.15	0.613
8X-2, 55	112.35	0.587
8X-2, 75	112.55	0.631
8X-2, 91	112.71	0.577
8X-2, 111	112.91	0.601
8X-4, 8	114.56	0.600
8X-4, 28	114.76	0.611
8X-4, 57	115.05	0.630
8X-4, 77	115.25	0.637
8X-4, 108	115.56	0.513
8X-4, 128	115.76	0.722
8X-4, 148	115.96	0.693
8X-5, 12	116.10	0.665
8X-5, 27	116.25	0.635
8X-5, 47	116.45	0.675
8X-5, 64	116.62	0.668
8X-5, 80	116.78	0.618
8X-5, 99	116.97	0.663
8X-5, 119	117.17	0.708
8X-5, 137	117.35	0.625
8X-6, 8	117.56	0.652
8X-6, 27	117.75	0.682
8X-6, 46	117.94	0.661
8X-6, 70	118.18	0.768
8X-6, 89	118.37	0.886
8X-6, 109	118.57	0.666
9X-1, 6	119.96	0.712
9X-1, 23	120.13	0.527
9X-1, 40	120.30	0.604
9X-1, 58	120.48	0.676
9X-1, 77	120.67	0.621
9X-1, 94	120.84	0.737
9X-1, 125	121.15	0.683
9X-1, 146	121.36	0.737
9X-2, 5	121.45	0.737
9X-2, 13	121.53	0.583
9X-2, 48	121.88	0.530
9X-4, 9	123.99	0.751
9X-4, 23	124.13	0.690
9X-4, 42	124.32	0.801
9X-4, 62	124.52	0.808
9X-4, 96	124.86	0.861
9X-4, 122	125.12	0.766
9X-4, 144	125.34	0.743
9X-5, 10	125.50	0.725
9X-5, 31	125.71	0.695
9X-5, 47	125.87	0.714
9X-5, 77	126.17	0.739
9X-5, 100	126.40	0.959
9X-5, 115	126.55	0.720
9X-5, 135	126.75	0.693
9X-6, 9	126.86	0.731
9X-6, 26	127.03	0.744
9X-7, 10	127.58	0.775
9X-7, 24	127.72	0.733
9X-7, 49	127.97	0.749
9X-7, 69	128.17	0.826
10X-1, 12	129.72	0.750
10X-1, 32	129.92	0.755
10X-1, 48	130.08	0.778
10X-1, 68	130.28	0.696
10X-1, 89	130.49	0.663
10X-1, 117	130.77	0.614
10X-1, 139	130.99	0.596
10X-3, 18	132.78	0.545
10X-3, 34	132.94	0.557
10X-3, 50	133.10	0.515
10X-3, 73	133.33	0.458
10X-3, 117	133.77	0.509
10X-3, 140	134.00	0.568
10X-3, 7	132.67	0.613
11X-1, 7	139.37	0.611
11X-1, 32	139.62	0.617
11X-1, 52	139.82	0.847
11X-1, 77	140.07	0.744
11X-1, 101	140.31	0.679
11X-2, 8	140.88	0.659
11X-2, 26	141.06	0.679
11X-2, 54	141.34	0.939
11X-2, 78	141.58	1.228
11X-2, 100	141.80	0.742
11X-4, 9	143.89	1.079
11X-4, 29	144.09	0.914
11X-4, 51	144.31	0.959
11X-4, 53	144.33	1.145
11X-4, 73	144.53	1.143
11X-4, 93	144.73	0.886
11X-5, 6	144.86	0.701
11X-5, 29	145.09	0.794
11X-5, 49	145.29	0.973
11X-5, 76	145.56	1.843
12X-1, 5	148.95	0.744
12X-1, 24	149.14	0.679
12X-1, 47	149.37	0.758
12X-1, 65	149.55	0.876
12X-1, 81	149.71	0.935
12X-2, 14	150.54	0.790
12X-2, 34	150.74	0.885
12X-2, 54	150.94	0.687
12X-2, 68	151.08	0.790

Table T17 (continued).

Core, section, interval (cm)	Depth (mbsf)	Resistivity (Ωm)
12X-2, 83	151.23	0.741
12X-2, 98	151.38	0.950
12X-2, 118	151.58	0.840
12X-2, 132	151.72	0.758
12X-2, 10	150.50	0.982
12X-2, 30	150.70	0.776
12X-4, 38	153.78	0.858
12X-4, 57	153.97	0.713
12X-4, 79	154.19	0.785
12X-4, 99	154.39	1.076
12X-4, 119	154.59	1.051
12X-4, 138	154.78	0.824
12X-5, 11	155.01	0.910
12X-5, 22	155.12	0.867
12X-5, 35	155.25	0.879
12X-5, 55	155.45	0.896
12X-5, 75	155.65	1.050
12X-5, 85	155.75	0.769
12X-5, 97	155.87	0.785
12X-6, 6	155.96	0.780
12X-6, 15	156.05	0.845
12X-6, 33	156.23	1.066
12X-6, 48	156.38	0.824
13X-1, 35	158.95	0.731
13X-1, 53	159.13	1.040
13X-1, 81	159.41	0.832
13X-1, 111	159.71	0.866
13X-1, 129	159.89	1.023
13X-1, 147	160.07	0.914
13X-1, 13	158.73	0.767
13X-2, 13	160.20	0.765
13X-2, 34	160.41	0.891
13X-2, 54	160.61	2.063
13X-2, 72	160.79	0.764
13X-2, 90	160.97	0.856
13X-2, 106	161.13	1.122
13X-4, 16	163.23	0.976
13X-4, 34	163.41	0.917
13X-4, 54	163.61	0.724
13X-4, 78	163.85	0.703
13X-4, 100	164.07	0.718
13X-4, 119	164.26	0.788
13X-5, 8	164.45	0.883
13X-5, 28	164.65	0.759
13X-5, 45	164.82	0.721
13X-5, 62	164.99	0.666
14X-1, 6	168.26	0.718
14X-1, 26	168.46	0.877
14X-1, 46	168.66	0.762
14X-1, 65	168.85	0.772
14X-1, 85	169.05	0.804
14X-1, 116	169.36	0.811
15X-3, 12	180.99	0.897
15X-3, 32	181.19	1.094
15X-3, 63	181.50	0.955
15X-3, 102	181.89	1.323
15X-3, 116	182.03	1.021
15X-3, 118	182.05	1.167
15X-3, 136	182.23	0.973
16X-5, 8	193.58	0.960
16X-5, 28	193.78	1.040
16X-5, 48	193.98	1.048
16X-5, 68	194.18	0.890
16X-5, 80	194.30	1.754
16X-5, 100	194.50	0.959
16X-5, 122	194.72	1.509
17X-1, 10	197.20	0.861
17X-1, 30	197.40	0.860
17X-1, 50	197.60	0.863
17X-1, 70	197.80	0.906
17X-1, 90	198.00	0.887
17X-1, 111	198.21	1.045
18X-1, 10	206.80	1.201
18X-1, 30	207.00	1.852
18X-1, 50	207.20	0.973
18X-1, 56	207.26	0.972
18X-1, 59	207.29	0.810
18X-1, 108	207.78	1.036
18X-3, 10	209.10	1.065
18X-3, 30	209.30	1.055
18X-3, 50	209.50	0.898
19X-2, 19	217.22	1.042
19X-2, 48	217.51	1.045
19X-2, 97	218.00	1.093
19X-2, 124	218.27	1.068
20X-1, 41	226.41	1.215
20X-1, 87	226.87	2.190
20X-1, 20	226.20	1.141
20X-3, 8	228.43	1.110
20X-3, 35	228.70	1.147
20X-3, 64	228.99	1.057
20X-3, 88	229.23	1.452
20X-5, 13	231.20	1.023
20X-5, 56	231.63	1.376
20X-5, 92	231.99	1.832
20X-5, 117	232.24	1.172
21X-1, 15	235.75	1.410
21X-1, 49	236.09	1.245
21X-1, 94	236.54	1.773
21X-1, 122	236.82	1.173
21X-3, 9	238.47	1.451
21X-3, 36	238.74	1.536
21X-3, 62	239.00	1.337
21X-3, 104	239.42	2.366
21X-3, 135	239.73	1.743
21X-5, 11	241.49	1.301
21X-5, 33	241.71	2.082
21X-5, 67	242.05	1.537
21X-5, 93	242.31	1.222
21X-5, 130	242.68	1.801
22X-1, 14	245.34	1.051
22X-1, 36	245.56	1.412
22X-1, 78	245.98	1.786
22X-1, 123	246.43	1.547
22X-3, 16	247.47	1.435
22X-3, 51	247.82	4.914
22X-3, 85	248.16	1.313
22X-3, 129	248.60	1.476
22X-6, 9	251.90	1.195
22X-6, 42	252.23	1.675
22X-6, 67	252.48	1.256
22X-6, 94	252.75	1.505
23X-1, 14	254.94	2.527
23X-1, 38	255.18	1.344
23X-1, 72	255.52	1.566
23X-1, 98	255.78	1.771
23X-1, 128	256.08	1.820
24X-1, 40	264.80	1.136
24X-1, 45	264.85	0.817
24X-1, 80	265.20	1.018
24X-1, 114	265.54	1.511
24X-1, 142	265.82	1.270
24X-2, 13	265.99	1.870
24X-2, 40	266.26	1.490
24X-2, 125	267.11	1.297
24X-6, 12	270.92	1.735
24X-6, 50	271.30	1.359
24X-6, 108	271.88	1.261
27X-1, 13	293.43	0.867
27X-1, 16	293.46	0.622
27X-1, 20	293.50	1.445
27X-1, 24	293.54	0.662
27X-1, 27	293.57	1.103
27X-1, 29	293.59	0.659
27X-1, 34	293.64	0.873
27X-1, 38	293.68	0.715
27X-1, 43	293.73	0.824
27X-1, 45	293.75	0.660
27X-1, 50	293.80	0.753
27X-1, 55	293.85	0.689
27X-1, 58	293.88	1.397
27X-1, 60	293.90	0.695
27X-1, 64	293.94	1.295
27X-1, 66	293.96	0.777
27X-1, 69	293.99	1.020
27X-1, 72	294.02	0.706
27X-1, 77	294.07	1.461
27X-1, 79	294.09	0.741
27X-1, 82	294.12	0.915
27X-1, 87	294.17	0.658
27X-1, 90	294.20	1.455
27X-1, 94	294.24	0.740
27X-1, 99	294.29	0.962
27X-1, 101	294.31	0.745
27X-1, 104	294.34	0.893
27X-1, 108	294.38	0.723
27X-1, 111	294.41	1.103
27X-1, 114	294.44	0.739
27X-1, 118	294.48	0.944
27X-1, 120	294.50	0.745
27X-1, 125	294.55	1.072
27X-1, 129	294.59	0.730
27X-1, 133	294.63	1.277
27X-1, 136	294.66	0.785
27X-1, 139	294.69	1.956
27X-1, 145	294.75	1.020
27X-1, 147	294.77	1.064
Perpendicular		
311-U1328C-		
4X-3, 10	88.10	0.687
4X-3, 30	88.30	0.620
4X-3, 50	88.50	0.785
4X-3, 60	88.60	0.665
4X-3, 97	88.97	0.714
4X-3, 120	89.20	0.611
4X-3, 128	89.28	0.875
4X-3, 134	89.34	0.629

Table T18. Thermal conductivity, Holes U1328B, U1328C, and U1328E.

Core, section, interval (cm)	Depth (mbsf)	Thermal conductivity (W/[m·K])			
		Average	1	2	3
311-U1328B-					
1H-2, 40	1.90	1.155	1.156	1.152	1.157
1H-3, 52	3.52	0.858	0.851	0.856	0.866
1H-4, 13	4.63	0.742	0.787	0.734	0.705
2H-2, 32	5.82	0.739	0.691	0.739	0.787
2H-2, 45	5.95	0.724	0.715	0.728	0.728
5H-1, 40	16.90	1.048	1.042	1.057	1.044
8H-1, 20	28.20	1.052	1.036	1.057	1.064
10H-1, 45	47.45	0.940	0.940	0.941	0.940
311-U1328C-					
1H-1, 81	57.31	0.869	0.859	0.869	0.880
1H-3, 64	60.07	0.874	0.877	0.874	0.870
1H-6, 97	64.90	0.898	0.898	0.898	0.897
2H-1, 82	66.82	0.871	0.861	0.873	0.880
2H-2, 59	68.09	0.641	0.639	0.641	0.644
3H-2, 44	77.44	0.783	0.787	0.781	0.780
3H-6, 13	83.13	1.088	1.097	1.090	1.078
3H-7, 29	84.11	0.876	0.876	0.875	0.877
4X-1, 92	85.92	1.187	1.198	1.186	1.177
4X-3, 53	88.53	1.054	1.058	1.051	1.052
6H-1, 68	94.68	1.089	1.097	1.096	1.075
6H-3, 24	97.14	0.970	0.966	0.961	0.983
6H-8, 61	102.00	0.937	0.935	0.938	0.938
7X-2, 57	105.57	1.008	1.012	1.006	1.005
7X-4, 108	108.98	1.311	1.331	1.291	1.312
7X-5, 39	109.79	1.136	1.129	1.140	1.139
8X-2, 85	112.65	0.993	0.996	0.993	0.990
8X-4, 55	115.03	1.193	1.186	1.195	1.197
8X-6, 39	117.87	1.200	1.205	1.201	1.193
9X-2, 49	121.89	1.038	1.035	1.041	1.039
9X-4, 80	124.70	1.073	1.077	1.070	1.072
9X-7, 26	127.74	1.179	1.186	1.165	1.187
10X-1, 75	130.35	1.151	1.152	1.155	1.146
10X-3, 113	133.73	0.985	0.985	0.982	0.987
11X-1, 38	139.68	1.006	1.005	1.005	1.008
11X-4, 80	144.60	0.929	0.932	0.930	0.924
12X-1, 67	149.57	0.975	0.975	0.979	0.97
12X-5, 42	155.32	0.830	0.829	0.828	0.834
13X-5, 44	164.81	1.101	1.106	1.096	1.100
14X-2, 10	169.63	1.089	1.102	1.078	1.086
15X-3, 74	181.61	0.930	0.932	0.933	0.924
16X-1, 24	187.74	0.933	0.942	0.931	0.926
16X-3, 30	190.80	0.955	0.959	0.957	0.948
17X-1, 29	197.39	1.054	1.051	1.055	1.056
17X-2, 75	199.35	0.849	0.848	0.845	0.854
17X-5, 57	203.67	0.964	0.962	0.966	0.965
18X-1, 20	206.90	0.776	0.759	0.792	0.777
18X-1, 107	207.77	0.765	0.769	0.763	0.764
18X-2, 64	208.64	1.027	1.026	1.027	1.029
18X-3, 49	209.49	0.950	0.942	0.955	0.952
19X-2, 64	217.67	1.027	1.026	1.027	1.029
19X-2, 67	217.70	0.815	0.822	0.816	0.808
20X-3, 10	228.45	0.956	0.958	0.958	0.953
21X-2, 50	237.38	1.154	1.152	1.156	1.155
21X-5, 35	241.73	1.129	1.127	1.136	1.125
22X-2, 13	246.83	0.859	0.854	0.852	0.871
22X-5, 46	250.77	1.183	1.185	1.181	1.184
23X-1, 57	255.37	0.970	0.975	0.973	0.961
23X-5, 23	260.53	1.122	1.114	1.128	1.125
24X-2, 54	266.40	0.629	0.631	0.629	0.628
24X-6, 64	271.44	0.758	0.758	0.759	0.758
25X-2, 52	276.12	0.930	0.933	0.928	0.930
25X-5, 33	280.43	0.948	0.950	0.947	0.947
26X-2, 121	286.41	1.019	1.026	1.017	1.015
26X-5, 66	290.36	0.992	0.994	0.991	0.992
27X-2, 45	295.25	1.084	0.958	1.151	1.144
27X-5, 70	299.81	0.803	0.787	0.811	0.810
311-U1328E-					
8X-3, 23	29.68	1.087	1.087	1.097	1.078
9X-4, 34	39.28	0.941	0.928	0.945	0.949

Table T19. In situ temperature, Holes U1328B, U1328C, and U1328E.

Core	Depth (mbsf)	Temperature (°C)		Thermal conductivity (W/[m·K])	Calibration correction (°)	Temperature tool	Solution reliability
		Corrected	Uncorrected				
311-U1328B-							
8H	37.5	5.45	6.42	1.1	–0.97	APCT16	Good
10H	56.5	10*	10	1.1	0	APCT-3	Poor (heave)
10H–11H	56.5	ND	ND	ND	ND	DVTPP3	No data
311-U1328C-							
2H	75.5	7.57	8.54	1.1	–0.97	APCT16	Good
3H	85.0	9	9	1.1	0	APCT-3	Poor
6H	103.5	11	11	1.1	0	APCT-3	Poor (heave)
11X–12X	148.9	ND	ND	ND	ND	DVTPP3	No data
16X–17X	197.1	ND	ND	ND	ND	DVTPP3	No data
311-U1328E-							
10P–11Y	93.0	8.47	8.47	1.1	0	DVTP	Poor (heave)
11Y–12E	198.0	14.13	14.13	1.1	0	DVTP	Very good

Notes: * = measurements severely affected by heave are estimated to only the nearest degree. ND = not determined. APCT = advanced piston corer temperature tool, APCT-3 = third-generation advanced piston corer temperature tool, DVTPP = Davis-Villinger Temperature-Pressure Probe, DVTP = Davis-Villinger Temperature Probe.

Table T20. Summary of pressure coring operations at Site U1328.

Core	Core-top depth (mbsf)	Length recovered* (cm)	Length curated (cm)	Pressure at core depth (MPa)	Pressure recovered (MPa)		Comments
					Logged†	Gauge‡	
311-U1328B-							
4P	14.5	98	77	12.9	15.1	5.0	Unusual pressure rise while in ice shuck
7P	26.0	98	78	13.0	16.8	2.0	Unusual pressure rise while in ice shuck
311-U1328C-							
5P	92.0	98	96	13.7	8.0	1.4	Normal operation
311-U1328D-							
3Y	14.0	0	0	12.9	0	—	No evidence of penetration
311-U1328E-							
3E	8.5	0	0	12.8	4.0	4.0	Side valve leaked; gas hydrate in outer barrel
5P	15.1	0	0	12.9	0	—	Actuator did not stroke after four attempts
7Y	25.7	87	87	13.0	0	—	Large wireline tension during coring
10P	92.0	35	26	13.7	11.0	4.8	Normal operation
11Y	197.0	90	90	14.7	0	—	Large wireline tension during coring
12E	215.5	0	0	14.9	0	—	Bit left bottom during coring; shattered liner
13P	233.0	98	94	15.0	5.8	5.4	Normal operation

Notes: Water depth at Site U1328 is 1267 mbsl. P = Pressure Core Sampler (PCS), Y = Fugro Percussion Corer (FPC), E = HYACE Rotary Corer (HRC). * = based on X-ray imaging and gamma ray density profiling prior to degassing. † = last pressure recorded before data logger disconnected from corer autoclave. Temperature 2°–4°C unless otherwise noted. ‡ = pressure measured when autoclave pressure transducer connected to computer (PCS cores) or external gauge (PCS, FPC, HRC cores). Pressure measured at 7°C unless otherwise noted. — = no data.

Table T21. In situ conditions of PCS cores recovered from Site U1328.

Core	Depth (mbsf) Top	Depth (mbsf) Bottom	Temperature (°C)	Pressure (MPa)	Salinity	Methane saturation (mM)
311-U1328B-						
4P	14.5	15.5	4.3	12.9	44.0	50.2
7P	26.0	27.0	4.9	13.0	34.0	52.6
311-U1328C-						
5P	92.0	93.0	8.5	13.7	33.1	68.3
311-U1328E-						
10P	92.0	93.0	8.5	13.7	33.0	68.3
13P	233.0	234.0	16.1	15.0	30.0	142.3

Note: Salinity was analyzed in interstitial water samples from Cores 311-U1328B-4P, 7P, 311-U1328C-5P, and 311-U1328E-13P and extrapolated from adjacent XCB cores for Core 311-U1328E-10P (Table T1). Temperature was calculated from sediment depth assuming a seafloor temperature of 3.5°C and a thermal gradient of 54°C/km. Pressure was calculated from sediment and water depth. Methane saturation was calculated based on sediment and water depth, seafloor temperature, thermal gradient, and salinity according to Xu (2002, 2004).

Table T22. Results from degassing experiments at Site U1328.

Core	Total volume of gas released (mL)	Total volume of methane released (mL)	Average concentration of released gas components (%)* C_1	C_2†	CO_2	N_2	C_1/C_2†	Total volume of water released (mL)	Salinity of released water	Temperature during degassing (°C)	Air pressure during degassing (MPa)
311-U1328B-											
4P	23,700	21,461	90.9	0.1052	BD	7.9	824	202	32.2	7.1 ± 0.5	0.1015
7P	3,685	2,509	75.6	0.0696	BD	20.4	984	504	32.0	7.3 ± 0.5	0.1011
311-U1328C-											
5P	2,740	1,741	69.6	0.0337	BD	23.4	2109	315	31.8	7.3 ± 0.5	0.1012
311-U1328E-											
10P	18,600	17,434	94.9	0.0844	BD	3.7	1030	342	32.0	7.0 ± 0.4	0.1015
13P	61,575	59,905	97.9	0.0617	BD	0.7	1554	0	NA	6.9 ± 03	0.1011

Notes: * = excludes initially released gas increments that are diluted by dead volume of manifold system. † = obtained for selected samples from each core using methods described in "Organic geochemistry" in the "Methods" chapter (see Table T10). BD = below detection.

Table T23. Characteristics of PCS cores used for mass balance calculations, Site U1328.

Core	Core length recovered (m)	Sediment volume in inner core barrel (mL)	Porosity (%)	Pore water volume in inner core barrel (mL)	Volume of water in outer core barrel (mL)	Sediment extruded with outer core barrel water, dry weight (g)	Headspace volume in outer core barrel (mL)	Salinity of water in outer core barrel
311-U1328B-								
4P	0.98	1436	58	839	2145	160	819	—
7P	0.98	1436	50	715	3140	309	0	—
311-U1328C-								
5P	0.98	1436	53	766	2885	155	79	33
311-U1328E-								
10P	0.35	513	53	273	3640	161	0	32
13P	0.98	1436	48	692	2425	127	539	—

Note: — = no data.

Table T24. Mass balance calculations based on degassing experiments, Site U1328.

Core	Depth (mbsf) Top	Depth (mbsf) Bottom	Total C_1 released (10^{-3} mole)	C_1 concentration (mM) Total	At laboratory conditions Dissolved*	At laboratory conditions Free†	In situ Dissolved‡	In situ Nondissolved	In situ nondissolved C_1 as percentage of pore volume if present as Free gas	In situ nondissolved C_1 as percentage of pore volume if present as Gas hydrate	Potential pore water freshening caused by gas hydrate decomposition Water release (mL)	Potential pore water freshening caused by gas hydrate decomposition Freshening (%)
311-U1328B-												
4P	14.5	15.5	955	1140	2.2	1138	50.2	1090	19.5	14.9	99	12
7P	26.0	27.0	135	190	2.1	188	52.6	137	2.4	1.9	11	1.5
311-U1328C-												
5P	92.0	93.0	92.3	123	2.7	121	68.3	54.9	0.9	0.7	4.5	0.6
311-U1328E-												
10P	92.0	93.0	781	2858	2.7	2855	68.3	2790	47.7	38.0	82	30
13P	233.0	234.0	2612	3775	1.5	3773	142.3	3633	58.1	49.5	272	56

Notes: * = obtained by HS analysis of extruded sediment core (Table T6). † = calculated based on the total amount of C_1 released during the degassing experiment and the pore water volume recovered by the PCS. ‡ = methane saturation of pore water (Table T21).

Table T25. Receiver depths, measured first break times, and first break times corrected for horizontal source offset and gun depth in the vertical seismic profile, Hole U1328C.

Receiver depth (mbrf)	Receiver depth (mbsf)	First break time (s) Uncorrected	First break time (s) Corrected
1385.0	106.0	0.922726	0.923457
1390.0	111.0	0.925680	0.926413
1395.0	116.0	0.928887	0.929622
1400.0	121.0	0.932469	0.933206
1405.0	126.0	0.934396	0.935135
1409.9	130.9	0.937760	0.938501
1415.0	136.0	0.940194	0.940936
1425.0	146.0	0.946704	0.947450
1430.0	151.0	0.948589	0.949336
1435.0	156.0	0.951710	0.952459
1440.0	161.0	0.955393	0.956145
1444.9	165.9	0.958120	0.958873
1450.0	171.0	0.961569	0.962324
1455.0	176.0	0.964446	0.965203
1460.0	181.0	0.967412	0.968171
1465.0	186.0	0.970717	0.971478
1470.0	191.0	0.973159	0.973921
1475.0	196.0	0.977021	0.977786
1480.0	201.0	0.980530	0.981297
1485.0	206.0	0.983184	0.983952
1490.0	211.0	0.986078	0.986848
1495.0	216.0	0.989200	0.989972
1500.0	221.0	0.992029	0.992802
1503.9	224.9	0.993825	0.994599
1510.0	231.0	0.998619	0.999396
1520.0	241.0	1.003820	1.004600
1525.0	246.0	1.007640	1.008422
1530.0	251.0	1.010730	1.011514
1533.0	254.0	1.011790	1.012574
1540.0	261.0	1.016660	1.017447
1545.0	266.0	1.019500	1.020288
1550.0	271.0	1.021920	1.022710
1555.0	276.0	1.025910	1.026702
1560.0	281.0	1.028990	1.029783
1565.1	286.1	1.032320	1.033115